MODELING AND CONTROL OF THERMOACOUSTIC INSTABILITIES

THÈSE N^{O} 2800 (2003)

PRÉSENTÉE À LA FACULTÉ SCIENCES ET TECHNIQUES DE L'INGÉNIEUR

Institut des sciences de l'énergie

SECTION DE GÉNIE MÉCANIQUE

ÉCOLE POLYTECHNIQUE FÉDÉRALE DE LAUSANNE

POUR L'OBTENTION DU GRADE DE DOCTEUR ÈS SCIENCES

PAR

Bruno SCHUERMANS

M.Sc. in Mechanical Engineering, Delft University of Technology, Pays-Bas
et de nationalité belge

acceptée sur proposition du jury:

Prof. P.A. Monkewitz, directeur de thèse
Prof. A.P. Dowling, rapporteur
Prof. R. Longchamp, rapporteur
Prof. C.O. Paschereit, rapporteur

Lausanne, EPFL
2003

Remerciements

Ce travail de doctorat a été mené au Laboratoire de Mécanique des Fluides (LMF) de l'Ecole Polytechnique Fédérale de Lausanne (EPFL), les travaux présentés ont été effectués dans les laboratoires de ALSTOM (Switzerland) Ltd.

Je souhaite exprimer toute ma gratitude à Monsieur le Professeur Peter A. Monkewitz pour avoir encadré mon travail, pour m'avoir guidé et conseillé, et pour m'avoir fait profité de ses immenses connaissances en mécanique des fluides.

Je tiens à remercier tout particulièrement Dr. Oliver Paschereit, pour m'avoir permis de réaliser ce travail au sein d'ALSTOM, et pour les nombreuses discussions intéressantes sur le sujet de la thermoacoustique.
Je souhaite également exprimer mes remerciements aux personnes suivantes:
Professeur Wolfgang Polifke et Dr. Klaus Döbbeling, pour m'avoir accueilli dans le département, au début de la thèse.
Professeur Ephraim Gutmark, qui m'a encouragé à commencer ce travail.
Valter Bellucci pour son conseil avisé au sujet de l'acoustique et de la thermoacoustique et pour sa disponibilité, Dr. Dariusz Nowak pour les calculs FEM, François Meili pour les mesures de fonctions de transfert.
Dr. Felix Guethe pour les images de flammes et de sa technologie pour mesurer les oscillations de concentration de carburant.
Dr. Peter Flohr et Martin Zajadatz pour les nombreuses discussions fructueuses sur le sujet des instabilitées de la combustion.
Dr. Andrew Paice, Dr. Andreas Poncet et Dr. Eduardo Gallestey pour leur conseils au sujet du contrôle actif.
Wolgang Weisenstein, David Yaki et Christian Motz, pour leur support dans la partie expérimentale de cette thèse.
Je remercie bien sûr tous les étudiants qui ont contribué à ce travail : Jan van der Linden, Daniel Gstoehl, Peter Bauckhage, Ulrich Kwan, Bart van Roon, Daniel Campos -Delgado, Rebecca Cutri-Kohart, Tina Kholwad, Karin Kramer, Daniel Visser et Jonathan Reynolds.
Je désire enfin remercier tout particulièrement mon épouse, Anne Marie, qui m'a toujours soutenu dans les bons comme les moments difficiles. Sans elle cette thèse n'aurait pas pu être réalisée.

Résumé

Nous proposons dans ce travail une méthode de modélisation et de réglage des instabilités thermoacoustiques dues à la combustion. Le modèle s'applique au brûleur utilisant un pré-mélange air-combustible riche en comburant.

Pour un système thermoacoustique complexe un réseaux de modules peut être utilisé. Chaque modules ou sous-systèmes comportent alors un modèle obtenu de façon analytique, ou numérique ou provenant de techniques expérimentales.

La dynamique d'un tel système est obtenu expérimentalement, on en déduit la fonction de transfert sous forme matricielle.

En effet la fonction de transfert d'une combustion à pré-mélange est déterminée, à pression atmosphérique, pour un brûleur de turbine à gaz. Et ceci est réalisé pour plusieurs régimes opératoires. Un modèle analytique du comportement dynamique de la zone de réaction en est alors déduit. Dans ce modèle, on considère que la fluctuation de libération de chaleur provient de la fluctuation, d'une part de la fraction massique de combustible et d'autre part de la vitesse dans la flamme. Il en résulte un bon accord avec les résultats expérimentaux.

Pour une géométrie tridimensionnelle complexe de la chambre de combustion, la propagation d'ondes est modélisée à l'aide de la méthode d'expansion modale. Les modes acoustiques utilisés par l'expansion modale peuvent alors être obtenus analytiquement pour des géométries simples, ou pour une géométrie très complexe de façon numérique par élément finis. L'expansion modale est ensuite représentée dans un espace d'états afin d'obtenir un modèle numérique très efficace et aussi très robuste.

Le modèle thermoacoustique du réseau de modules regroupe les espace d'états de sous-systèmes en un seul. Ce système peut être analysé par une représentation temporelle ou fréquentielle. L'analyse de la stabilité en ressort directement et ne requière pas d'itération. D'autre part des éléments non linéaires peuvent être facilement insérés et simulés en fonction du temps. Cette nouvelle méthode est ensuite validée par une comparaison avec des solutions analytiques d'un système thermoacoustique simple fourni par la littérature, ainsi que par une comparaison avec un programme par élément finis et finalement avec des mesures expérimentales. Dans tout les cas une excellante correspondance des résultats est obtenue.

En introduisant des éléments non linéaires dans un système annulaire, un champs de rotation acoustique est simulé, ceci correspond également aux observations expérimentales. Ce résultat et alors vérifié de façon analytique.

Sur la base du réseau obtenu, un réglage a été développé en utilisant l'optimisation H_∞. Les

résultats du contrôle, testés par simulation et sur un stand d'essai comportant un brûleur, révèlent une suppression de plus de $25dB$ du niveau acoustique. Le contrôleur adaptable développé sur le model d'un algorithme génétique ne demande pas la connaissances entière du processus de combustion. Les testes effectués sur le réglage adaptif montrent des performances similaires au réglage H_∞.
Un système de réglage active pour une configuration de plusieurs brûleurs est également développé. L'insertion du réglage dans la simulation démontre le bon fonctionnement de cette méthode.

Abstract

This work deals with modeling and control of thermoacoustic combustion instabilities in lean premixed combustion systems. Because of the complex interactions present in thermoacoustic systems, a network modeling approach is used. The model of each network element or subsystem is obtained analytically, numerically, or by making use of experimental techniques.
The dynamics of a network system are determined experimentally by making use of a transfer matrix measurement technique. The transfer functions of a premixed flame have been determined experimentally on an atmospheric combustion test facility with a full-scale gas turbine burner, for a wide variety of operating conditions. An analytical model of the dynamic behavior of the reaction zone was made. In this model, the heat release fluctuations are assumed to be caused by fluctuations of the mass fraction of fuel and by fluctuations in the burning velocity. The model proved to be in good agreement with experimental results.
Wave propagation in complex three-dimensional geometries is modeled by making use of a modal expansion technique. The modes used for the modal expansion can be obtained analytically for relatively simple geometries, or numerically (finite element method) for geometries of any complexity. By representing the modal expansion in state-space, a very numerically efficient and robust model is obtained. The thermoacoustic network model combines the state-space representations of the sub-systems in one system. The system can be analyzed in the time domain or in the frequency domain. The stability analysis is straightforward and does not require a numerical search. Non linear elements can easily be incorporated in the time domain simulation. This novel method has been validated by comparison with analytic solutions of simple thermoacoustic systems found in literature, by comparison with Finite Element codes, and by comparison with experimental results. An excellent agreement was found for all comparisons. When including non-linear elements in an annular system, a rotating acoustic field is predicted, which corresponds to experimental observations. This result has been verified analytically. Based on network models, a model based controller has been obtained using H_∞ optimization. This controller has been tested in simulation and experiment on a single burner rig and proved to suppress acoustic levels by more than $25dB$. An adaptive controller, based on a genetic algorithm, has been developed that does not require any knowledge about the system. This controller has been tested and proved to have similar performance as the model-based controllers. An active control system for multi-burner configurations has been developed and proved to perform well in simulations.

Nomenclature

Notation

p^*	complex conjugate of p
$\|p\|$	absolute value of p
$\|p\|_1^2$	jump relation between position 1 and 2
$\|P\|_\infty$	infinity norm of transfer function P
$\mathbf{P}^\dagger$	Moore-Penrose pseudo inverse of $\mathbf{P}$
$\bar{p}$	mean value of quantity
p'	acoustic fluctuation of quantity
p_j	p at location j
$\hat{p}$	Fourier transform of p domain
f_j	Riemann-invariant travelling in the downstream direction at location j
g_j	Riemann-invariant travelling in the upstream direction at location j

Greek

α	real part of Laplace coefficient $\alpha = \Re\{s\} = \Im\{-\omega\}$ $\omega \in \mathbb{C}$
γ	ratio of specific heats C_p/C_v
$\delta\{\cdot\}$	Dirac delta
δ_n	Kronecker delta
ζ	loss coefficient
ρ	density
μ	dynamic viscosity
η	modal value, eigen value
ψ	mode shape, eigen function
θ	spatial angle
σ_x	standard deviation of x
ϕ	phase angle
τ	convective time lag
ω	angular frequency
ξ	probability density

Latin lower case

c	speed of sound
e	specific internal energy
f_s, g_s	source terms
f	downstream travelling Riemann invariant or source at a boundary
g	upstream travelling Riemann invariant
h_f	specific reaction enthalpy
h	volume source
i	imaginary unit $\sqrt{-1}$
k	wave number ω/c
m	azimuthal (circumferential) mode number
n	axial mode number
p	pressure
s	specific entropy, Laplace operator $s = i\omega$, $s \in \mathbb{C}$
u	velocity, velocity in x-direction
v	velocity in y-direction
x	axial position, state vector
y_f	fuel concentration
z	waveform $z = e^{-i\frac{\omega L}{c}}$

Latin upper case

A	area
C_p	specific heat at constant pressure
C_v	specific heat at constant volume
G	Green's function
L	length
L_{red}	reduced length
M	Mach number $M = u/c$
Q	heat release (per unit area)
S	surface
S_f	flame speed
R	universal gas constant, Reflection coefficient
V	volume

Latin cursive

$\mathcal{F}\{\cdot\}$	Fourier transform
$\mathcal{H}\{\cdot\}$	Heaviside function
$\mathcal{L}\{\cdot\}$	Laplace transform
$\mathcal{S}_{\overline{x,y}}$	cross power spectral density estimate between signal x and y

Matrices

$\mathbf{A}, \mathbf{B}, \mathbf{C}, \mathbf{D}$	state space matrices
$\hat{\mathbf{n}}$	unit vector normal to boundary
$\mathbf{x}$	spatial coordinate $\mathbf{x} = (x, y, z)$

Contents

List of Figures

List of Tables

Chapter 1

Introduction

1.1 Background

1.1.1 Gas Turbine Combustors

Although the approach for modeling and control used throughout this work is generic, the focus will be on combustion in gas turbine combustion chambers. Because of environmental regulations there has been a tendency for the last two decades to reduce the levels of emissions of nitrous oxides (NO_x) in gas turbines. Formation of NO_x has an exponential dependence on the (local) temperature in the combustion zone. Because of this exponential dependence on the local temperature, a uniform temperature in the reaction zone is desired to achieve low emission levels. This uniform temperature requires that the air and fuel are well mixed before entering the reaction zone. This type of combustion is referred to as lean premix combustion. Because of the trade off between high efficiency and low NO_x emissions in modern industrial gas turbines, nearly all air that is delivered by the compressor is premixed with fuel. This is in contrast with older types of industrial gas turbines, where a substantial amount of the air is mixed with the hot reaction products in order to reduce the hot gas temperature to allowable levels and to cool the combustion chamber liners. The combination of a lean premixed flame and convectively cooled combustion chambers has led to the rise of another problem: combustion driven oscillations, or thermoacoustic instabilities. The absence of by-pass air in convectively cooled combustion systems results in a decrease of acoustic damping and hence an increase in pulsation amplitudes. The mechanism of thermoacoustic instabilities due to premixed flames will be discussed in this work.

1.1.2 Thermoacoustic Instabilities

A thermoacoustic system is characterized by an interaction between the acoustic field and periodic heat release. This interaction is a feedback interaction that may become unstable under certain conditions. These instabilities are unwanted in gas turbines, because they may lead to large acoustic pressure levels, which can cause component damage. The driving mechanism behind thermoacoustic instabilities was already recognized in the nineteenth century by Lord

Rayleigh [108]: if the pressure fluctuation and heat release fluctuations are in phase, the oscillations are enhanced. Or, in his phrasing: "*If heat be periodically communicated to, and abstracted from, a mass of air vibrating (for example) in a cylinder bounded by a piston, the effect produced will depend upon the phase of the vibration at which the transfer of heat takes place. If heat be given to the air at the moment of greatest condensation, or be taken from it at the moment of greatest rarefaction, the vibration is encouraged. On the other hand, if heat be given at the moment of greatest rarefaction, or abstracted at the moment of greatest condensation, the vibration is discouraged*".

The relation to combustion instabilities can be seen as follows: a small perturbation of the flow velocity will cause a perturbation of the heat released by the flame. This heat release fluctuation will cause a perturbation of the volume expansion in the flame. This periodic volume expansion propagates as a sound wave through the combustion chamber, reflects on the boundaries and propagates back to the flame, where it causes an (acoustic) velocity perturbation. In this way, a feedback mechanism between heat release and the acoustic field is formed. An analogy between the acoustic cycle and the thermodynamic cycle in a piston engine can be made: if heat is added periodically to the cycle at the moment where pressure is maximum (piston up), the engine delivers work. If heat is added when the pressure is minimum (piston down), the engine will slow down.

The phenomenon of thermoacoustic instabilities has been encountered in solid and liquid fuelled rocket engines in aero-engine after burners, ramjets, gas turbines and in industrial or household combustion furnaces. Because these instabilities occur in such a variety of combustion systems, it may be clear that the physical mechanism responsible for the interaction between heat release and the acoustic field may be very different. Nonetheless, the conditions leading to instability will invariantly be given by Rayleigh's criterion.

A good insight in the mechanism of thermoacoustic instabilities can be obtained by investigating an example. Consider a flame stabilized in a straight duct as shown in Figure 1.1. The acoustic properties of the pieces of duct upstream and downstream of the flame are defined by the duct's impedance. The acoustic impedance is defined as the ratio of acoustic pressure and velocity and is denoted by $Z = \frac{p'}{u'}$. As will be discussed later in this work, the fluctuating heat release is mainly affected by the acoustic velocity. Because of the volume expansion associated with the heat release, it will act as a source term for the acoustic velocity. The dependence of the heat release on the acoustic velocity is given by a transfer function: F. The volume expansion is proportional to the heat release, and this proportionality is given by a constant k: $\Delta u' = k\,Q' = k\,F\,u'$. In Figure 1.1, the inter-dependence of the impedances and the flame transfer function is given in a block diagram.

The impedances only dependent on the tube geometry and may be combined in one transfer function (G) representing the geometry of the system: $G = \frac{-Z_{do}}{Z_{up}+Z_{do}}$. The thermoacoustic system is then represented by the block diagram of Figure 1.2, which clearly shows the feedback loop between the combustion chamber acoustics and the heat release process.

If no combustion were to take place, this would correspond to $F = 0$ in Figure 1.2, and the dynamics of the system would be entirely described by G. Such a system will be referred to as a "classical acoustic" system. If no acoustic losses are present in the volume or on the boundaries

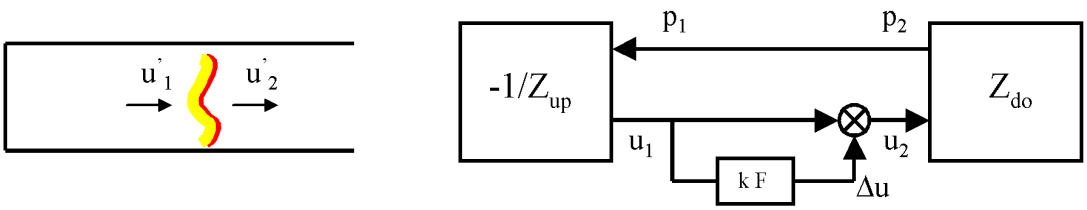

Figure 1.1: Left: Flame stabilised in a tube. Right: Corresponding thermoacoustic block diagram.

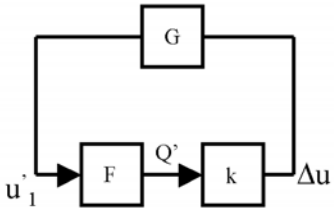

Figure 1.2: Feedback cycle between heat release and combustion chamber acoustics.

of the ducts, then G is a pure acoustic resonator. Its frequency response consists of a series of peaks that reach infinite values. Such a system is neither stable nor unstable, but is on a limit of stability: a finite perturbation at one of the resonance frequencies will not grow nor decay, but will be maintained infinitely. This is characterized by eigenvalues of the system that are completely imaginary. From this point of view it is not very surprising that a slight modification of the system (by making F non-zero) will render the system stable or unstable. Generally, it is not an easy task to find the appropriate model for the flame (F). In this work, analytical methods and experimental techniques will be combined to derive this model. There are several analytical and numerical methods to model the wave propagation in the volume (G). However, the models obtained by most of these methods are inconvenient to use in a stability analysis, or when developing active control strategies. In this work an approach has been developed in which a model G of geometries of any complexity can be obtained in a straight-forward, modular approach. The model is represented in state-space, thus stability is easily assessed and this representation is very useful for deriving active control strategies.

1.1.3 Thermoacoustic Modeling

Dynamic models of thermoacoustic systems can be used to predict the acoustic behavior of combustion systems. These models are of great importance because they lead to better understanding of combustion instabilities, and can be used as a basis for the design of active control systems. The most difficult part of thermoacoustic modeling is to describe the process of interaction between periodic heat release and the acoustic field. Several modeling techniques have been proposed by different researchers. Depending on the physical system under consideration, some approaches are more favorable then others. If the zone of heat release is compact, i.e., the geometrical extent is small with respect to the wave length, then a *network approach* is generally most suitable. In such an approach, the heat release zone is treated as a discontinuity of the acoustic field. This facilitates modeling, because the interaction between combustion and acoustics can essentially be treated as a zero-dimensional process. If the heat release zone is not compact, then methods should be used that take into account the spatial dependence of the acoustic field within the reaction zone. This is generally done by using modal expansion techniques like the Galerkin method.

In an analytical investigation by Merk [76], the combustion system is represented as a network of acoustic elements and a stability analysis is made. The unsteady motion of the flame is accounted for by allowing fluctuations of the flame speed. In a combined experimental and theoretical investigation performed by Becker and Günter [11] the dynamics of the entire combustion system are modeled, the transfer function of the combustion process is described by a simple delay-lag, or lead-lag model. The coefficients of the flame model are then fit to the experimental data obtained from two pressure transducers. The theoretical analysis by Boa-Teh Chu [20] of a planar premixed flame is very similar to the flame modeling approach that is used in this work: the flame is considered as a propagating discontinuity in a reactive medium. His analysis allows for fuel mass fraction variations, flame speed fluctuations and entropy fluctuations. An overview of modeling techniques relevant to liquid propellant rockets is given in a paper by Luigy Crocco [26]. The theoretical analysis includes non-linear stability analysis, waves in annular combustion systems and interaction with shock waves. It is a very interesting work. The reviewer's comments at the end of the paper (although dating from the late 1960's) are worth reconsidering for present day analysis.

Numerous papers of Culick [29, 28, 27, 134] and references therein are based on a generic framework to model, analyze, and control thermoacoustic systems. The approach includes effects of mean flow and non-linear acoustic wave propagation. The governing equations are expanded in modal series, making use of Greens functions. The solution of the system is similar to the Galerkin method but is iterated, in order to correct for the change in mode shapes due to the combustion process and interactions with mean flow.

A combined experimental and analytical analysis of thermoacoustic instabilities in afterburners is performed by Bloxsidge, Dowling, and Langhorne in 1988 [66, 15]. The theoretical flame model accounts for displacement of the flame surface. A fit to experimental data is performed in order to obtain an empirical linear model for the dependence of heat release fluctuations on the acoustic velocity. A similar analysis is reported by Dowling in 1997 [33], but now including

non-linear effects. The system is represented as a linear network, the non linearity acts as a static saturation of the heat release. The amplitudes of the limit cycle are calculated by making use of a describing function technique [1].

Another paper by Dowling [32], gives an overview about different thermoacoustic modeling techniques, the underlying assumptions and their consequences made in the different techniques are discussed. More recent papers of Dowling and her co-workers focus on the inclusion of mixture fraction fluctuations and flame speed fluctuations in the flame models [54], thermoacoustic modeling in annular gas turbine combustion systems [126, 3] and on determination of flame transfer function by means of Computational Fluid Dynamics [138].

An overview of physical mechanisms and their mathematical description, possibly responsible for thermoacoustic oscillations in premixed gas turbine combustion systems is given by Keller (1995) [61]. Special attention is paid to the role of entropy waves, mixture fraction oscillations and forced oscillations due to flow instabilities. An earlier paper by the same author focuses on low frequency instability due to entropy fluctuations [60].

In a theoretical work by A.L. Ni [84], the stability of a planar flame front relative to two-dimensional perturbations is discussed. The dependence of the flame velocity on pressure perturbations is considered as an important mechanism leading to instability. A paper by the same author deals with a thermoacoustic model of a sequential combustor [85]. In this model the flame dynamics are described by an ignition delay model.

A very simple model describing the interaction between the acoustic field and heat release is given by Lang, Poinsot and Candel [65]. Because of its simplicity, this representation provides good insight in the basic mechanism leading to instability and means to control this instability.

Poinsot, Trouvé, Veynante, Candel and Esposito (EM2C, CNRS) analyzed, in detail, the acoustic and fluid dynamic aspects of combustion leading to instability of a dump combustor [100]. Based on phased locked images, they propose a mechanism for vortex driven instabilities. A similar approach is used by Yu, Trouvé and Daily [136].

Peracchio and Proscia [97] model the acoustics of a combustion system as modal expansion, the heat release couples with the acoustic quantities via dynamic motion of the flame surface and via fluctuations of the fuel mass fraction in the mixture. Amplitudes of non-linear limit cycles are predicted via a method very similar to the describing function analysis. The describing function is obtained experimentally from a steady relation between mean flow velocity and heat release.

Near extinction instabilities of a diffusion flame are studied in a theoretical work of Papas and Monkewitz [89]. The diffusion and reaction terms are modeled in a flame region of finite thickness. This method enables one to describe different modes of instability near extinction.

Lieuwen [72] models the acoustic field in terms of propagating Riemann invariants and specifying impedances at the boundaries. The flame region is modeled as a jump condition with unsteady heat release. The heat release is dependent of equivalence ratio fluctuations via a static reaction rate law. Convective time for equivalence ratio waves is taken into account, and because the flame is assumed to have spatial extent, an integral over distributed time delays is taken. The

[1] Describing function analysis is an approximate method (the non-linearity being approximated by a finite order Fourier expansion) to analyze non-linear systems in the frequency domain. In control theory, this method is typically applied to predict amplitudes of limit cycles[125].

eigenvalues of the resulting system are evaluated numerically, stability maps are made and were in reasonable agreement with experimental data.
The influence of equivalence ratio fluctuations convecting with mean flow is described by Sattelmayer (2000) [115] as well. He considers that the convection of mixture fraction waves should not be described by a single time delay, but by a distribution of time delays. An estimate of the time delay distribution is obtained by investigation of the velocity field. In a stability analysis, the spread of time delays was found to make the system more stable. A similar analysis is performed by Polifke et. al. [103]. However, in this approach particle tracing is used to obtain the time delay distribution.
Polifke et. al. [102, 101], derived a model for combustion instabilities that does not depend on periodic heat release. They observed experimentally that the pressure drop across a premixed, swirl stabilized burner, depends non-monotonically on the mean flow velocity. This tendency was assumed to be the result of a complex interaction between the swirling flow and the (steady) combustion process. Thus, the derivative of the pressure drop with respect to the mean flow velocity was negative under certain conditions. This derivative was then considered as a loss coefficient for the acoustic field. The occurrence of instabilities is then explained by the negative loss coefficient. It is remarkable that this implies that such a system can be unstable without fulfilling Rayleigh's criterion. More recent work focuses on acoustic modeling of annular combustion chambers. Evesque and Polifke [35] derive a low order model in the frequency domain for multi burner annular configurations. A time-domain model is demonstrated by Pankiewitz and Sattelmayer [88].
Najm and Ghoniem (1995) [82] performed a numerical simulation of a dump combustor using the random vortex method. Periodic heat release associated with periodic vortical structures were found to be responsible for thermoacoustic instability. Fleifil, Annaswamy, Ghoniem and Ghoniem [36] derived a model that relates the periodic heat release to fluctuations in the flame front area in a similar manner as in [33]. The acoustic field is described in terms of propagating Riemann invariants. The flame model is then, somewhat artificially, cast in a time lag model. In a later report [5], the acoustic field is expressed in a modal expansion using the Galerkin method. The flame model is essentially the same but represented in a more straightforward manner. The resulting feedback model is of low order and is described as rational polynomials in the Laplace coefficient, and is therefore suitable for control design (see the literature overview in Chapter 6 for application of their model to controller design).
Baldini et. al. model the reaction zone of a premixed flame in a one-dimensional way. The relevant thermodynamic and chemical quantities in the reaction zone are then expressed as low order polynomials as a function of the axial coordinate. By expressing the dynamic equations (in space and time) as functions of the polynomial coefficients, a low order ordinary differential equation is obtained. This (non-linear) flame model is then coupled to the combustion chamber acoustics. Time domain simulations indicated that the system was linearly unstable and exhibited limit cycle behavior. It is quite remarkable and interesting that such a system becomes unstable because neither flame area fluctuations nor equivalence ratio fluctuations are captured in this model.
A number of papers by Krebs, Walz, Hoffmann and Walz et. al., focus on acoustics in annular

gas turbine combustion systems. The influence of temperature distributions in the combustion chamber, and of impedances at burner locations, is assessed numerically in [132]. A similar, but more extensive analysis is performed in [64]. In this work, measured burner impedances (without combustion) are included in the Finite Element analysis. Results are compared with measured mode shapes and frequencies in a gas turbine combustion chamber. A time lag model with distributed time delays is validated in [63]. The time delay distribution is obtained by CFD, the transfer function between heat release and velocity fluctuations is determined experimentally on a single burner test rig.
Apart form the previously mentioned contributions by Keller, Polifke and Ni, research interest at ALSTOM (former ABB and ABB-ALSTOM) focused on:

- detailed experimental analysis of combustion instabilities
- experimental determination of transfer matrices
- analytic thermoacoustic flame models
- models for wave propagation in three-dimensional geometries
- active control of combustion instabilities

The fluid dynamic structure of combustion instabilities has been investigated experimentally by means of phase locked imaging of the heat release process in a flame, together with water-channel flow investigations. An important outcome of this work performed by Paschereit, Gutmark and Weissenstein [92, 94] is that hydrodynamic flow instabilities observed in non reacting flow have similar structure and similar Strouhal numbers as the combustion instabilities. The method to obtain transfer matrices of flames experimentally has been discussed in detail in by Paschereit, Polifke and Schuermans et. al. [95, 118, 90]. Analytic flame transfer functions have been derived and compared to the experimentally obtained flame transfer functions [118, 117, 12, 37].
In this dissertation, a network model is used and the combustion zone is considered as a discontinuity. The acoustic wave propagation is either modeled using a modal expansion technique or described in terms of propagating waves. The advantage of a model that describes the propagating waves is that the mean flow effect can be included in a straightforward manner. The modal expansion technique used in this work does not take into account mean flow effects, but has the advantage that it is numerically much more efficient, while the mean flow effect proved to be negligible for the systems under consideration in this work. Note that the mean flow effects are taken into account on the boundaries and in the burner model. This is very important when considering acoustic damping, because acoustic losses are mainly due to dissipation on the boundaries and because of conversion of acoustic energy into vorticity at the burner exit. The modes required for the modal expansion can either be obtained analytically or from a finite element analysis. When using modes from finite element analysis, geometries of any complexity can be modeled. The modal expansion approach is not restricted to one-dimensional acoustics and therefore very usefull when modelling multi-burner combustion systems. The reaction zone is modeled as a moving discontinuity, heat release fluctuations in this discontinuity are caused

by acoustic fluctuations of the fuel to air ratio. The propagation velocity of the discontinuity (the flame velocity) is considered to be dependent on the fuel to air ratio fluctuations. The time delay between fuel injection and fuel consumption is taken into account as a distribution of transport delay times. Because these delay times are not known a-priori they are obtained by assuming a normal distribution of delay times, and by fitting the mean and standard deviation of this distribution to measured flame transfer functions. The burner transfer function is considered as an area discontinuity with mean flow. Such a model is mainly described by two quantities: the "reduced length" which is a measure for the potential drop across the burner, and a "loss coefficient" which is a measure for the acoustic dissipation in the burner. These two quantities are obtained as well by curve fits to experimentally obtained transfer functions. The models of all these sub-systems are represented as state-space representations and interconnected to obtain the model of the entire network system. A linear stability analysis can be performed by solving for the eigenvalues of the homogeneous system. This is a straightforward procedure because the system is represented in state-space. A time-domain analysis can be also be performed, allowing for inclusion of non-linear saturation of the heat release. This model is very computational efficient: even for very complex systems, all eigenvalues can be calculated within seconds. This novel time domain network approach is a perfect basis for development of active combustion control strategies.

1.1.4 Active Control

One method to reduce acoustic pulsation amplitudes is by means of Active Instability Control (AIC). A large number of papers exist on this topic, an overview is given in [10] and in chapter 6. In active control, a flow parameter is modulated continuously in order to reduce pulsation levels in combustion systems. Closed loop active control relies on the principles of anti-sound. It is realized by measuring the acoustic fluctuation, passing this signal to a controller and feeding the resulting signal back to an actuator. In small scale facilities loudspeakers can be used to modulate the airflow. Because of pressure levels, size and life time requirements this is not an option in gas turbines. Because of the chemical energy content of the fuel, the effect of fuel flow modulation is much stronger than airflow modulation. Therefore, fuel flow modulation with fast actuation valves is generally preferred in industrial applications. From a controls point of view, AIC is very challenging: it is very difficult to obtain satisfactory performance because of large model uncertainties, large time delays, large noise levels and limited actuator power (saturation). On the other hand, it has been shown experimentally that extremely simple control strategies prove to be very effective. The reason is that the control objectives for AIC are: stability and disturbance rejection. The disturbances are generally present in very narrow frequency bands (resonance) thus the controller only needs to realize the desired objective in these narrow bands. It is therefore much more challenging to realize AIC for a system with low amplitude broadband pulsation behavior, than for a system with high amplitude narrow peaks in the frequency spectrum. The active control algorithm can be either model-based or adaptive. Model-based AIC has the advantage that it generally has better performance, provided of course that a good model is available (which is generally not the case). Adaptive control has the advantage that no model is required at all, and that the controller adapts automatically to changes of the system. In this work, both approaches are used.

1.2 Dissertation Overview

In this work a theoretical and experimental analysis of modeling and control of thermoacoustic systems is given. In order to prevent these instabilities, it is useful to have a model that predicts the behavior of the real system. This model can then be used to predict under what conditions the system becomes unstable and design changes can be made accordingly. A different approach is to make use of active control. In active control, a certain control parameter (such as the mass flow of fuel) is modulated in order to interfere with the system and cancel the oscillation. In feedback active control, the signal of a sensor that measures an acoustic quantity such as the acoustic pressure, is sent to a control algorithm. This algorithm generates a signal that controls an actuator that modulates the control parameter. When designing an active control system it is useful to have a dynamic model of the system. This model can be used to derive the control laws (model based control), or to test control algorithms that are self-adaptive. Thermoacoustic systems, as they are encountered in gas turbine combustion chambers, are typically of very complex nature, because they are the result of an interaction between several physical mechanisms. These mechanisms involve acoustic wave propagation, unsteady combustion, generation of mixture fraction waves, entropy waves, a strong turbulence field and large-scale fluid dynamic structures. Because these mechanisms interact on a broad range of length and time scales, it is very difficult (if not impossible) to derive a physical model from first principles. This is why in this work a "systems approach" is used to model the thermoacoustic phenomena in combustion systems. The underlying idea is to represent the entire system as a network of sub-systems. The division in subsystems is then chosen such that each sub-system can be represented in a simplified manner. In gas turbines, for example, the zone of heat release is small with respect to the wavelength. It is thus convenient to model this heat release zone as a spatial discontinuity, because the spatial dependence of the governing equations in the heat release zone can then be neglected, which simplifies the analysis considerably. It is thus natural to concentrate the heat release zone in one subsystem and the wave propagation in the volumes in other subsystems.

This modular network approach is also convenient because it allows different modeling techniques in the different network elements. This work demonstrates how the Finite Element Method, analytical methods and experimental methods can be used to describe the dynamics of the subsystems, and how to combine the sub-systems into one system interconnecting the different sub-systems.

The governing equations relevant to different subsystems will be derived and discussed in Chapter 2. Relations will be given for acoustic wave propagation, with or without convective terms and with or without periodic heat addition. Acoustic relations for wave propagation through annular geometries with mean flow are derived. A modal expansion of the acoustic field will be derived using Greens functions. This expansion is used later to obtain state-space models of combustion chamber geometries. As mentioned before, the combustion zone can be considered as zero-dimensional for low frequencies. Relations for one-dimensional acoustic jump conditions relevant to premixed flames are therefore derived. The mean flow has only a weak effect on wave propagation for small Mach number flows. However, the effect of the mean flow can be

considerable on the boundaries of the system and in strong area discontinuities. Because the burner (without combustion) can be considered an area discontinuity with mean flow, this will be discussed as well in Chapter 2. All relations are derived starting from the conservation equations of mass, energy, momentum, and a state equation. Then, assumptions are made that are appropriate for the specific problem. After linearization, the acoustic relations are obtained. In addition, an acoustic energy balance is derived for acoustic systems with periodic heat addition.

Several mechanisms may cause unsteady heat release in the combustion zone and therefore drive the system to instability. One of these mechanisms is due to the periodic change of area of the heat release zone. Other mechanisms are based on periodic heat release due to interaction of periodic vortical structures with the flame front. In this work, a model for premixed flames has been derived that is based on the heat release associated with the periodic fluctuations of the fuel mass fraction in the fuel-air mixture. This model, although zero-dimensional in nature, includes three-dimensional effects due to the local flow field and flame shape. This model and a comparison with experimental results is derived and discussed in Chapter 4.

A model of a subsystem can be obtained experimentally by a method referred to as the transfer matrix measurement technique. The transfer matrix relates all acoustic quantities on the input to the output of the element in a linear manner. For elements that are very difficult to model, such as the complex interaction in the combustion zone, a model based on a measured transfer matrix may be used. Such a measured transfer matrix can be included directly in the network system, or may be used to gain understanding in the physical mechanisms in the sub-system. The measured transfer matrix has been used to validate the analytical models obtained for the heat release zone. After a thorough analysis of the validity of the measurement technique, the experimental method was automated. A discussion of the transfer matrix measurement technique is given in Chapter 3. The principles of this measurement technique were not developed in the course of this work, but were the result of previous work. However, during this work the method has been improved by applying a better cross correlation technique, an error analysis has been made and the method has been validated. Moreover, the forcing, data acquisition and data processing has been fully automated. In this way the transfer matrix of a full scale gas turbine burner has been measured for a wide range of operating conditions, and proved in good agreement with the derived flame model.

Special attention will be paid to multi-burner annular combustion chambers as they are encountered in modern gas turbines. It has proven to be very useful to model the (three-dimensional) wave propagation in the combustion chamber using a modal expansion technique and by making use of a state-space representation. By expressing all elements as state-space systems, the stability analysis of the interconnected systems is straightforward, time domain simulations can be performed and non-linear system dynamics can easily be included. Moreover, this way of representing the system is computationally very effective and robust. The network modeling has been validated by comparison with analytical models, finite element results from commercial software packages, and with results found in literature. The network modeling approach and its application and validation are discussed in Chapter 5. Also in this chapter, is a discussion of stability analysis of thermoacoustic systems. An atmospheric single-burner test facility with a

full scale gas turbine burner has been modeled using this approach and proved to give excellent agreement with experimental results. An interesting outcome of the time-domain simulations of annular combustion systems is that under certain conditions the acoustic field starts rotating. This has also been observed experimentally. An analytical investigation of the non-linear dynamics underlying this mechanism has been performed.
The test facility has been equipped with pressure transducers and a fuel flow actuator in order to test active control strategies. The active control strategies are discussed in Chapter 6. Two different strategies have been developed, simulated and tested. One strategy was to use a controller that is model based. A network model of the combustion system was made using measured transfer matrices. Control laws were derived based on this model. The control laws have been obtained making use of H_∞ optimization. H_∞ optimization is a mathematical method to obtain the transfer function of a controller that minimizes the peak in the frequency spectrum of the controlled system. These controllers have been tested successfully in simulation and experiment. The disadvantage of a model-based controller is that the effectiveness of the controller strongly depends on the accuracy of the model. The second strategy does not make use of a model at all. In this method, a very generic control law is used. The controller has some parameters that have to be tuned in order to reduce the acoustic amplitudes. The tuning of these parameters was done by making use of an evolution strategy (or genetic algorithm). This method has been tested as well and proved as effective as the model-based controller. The control laws obtained for single burner configurations cannot be applied directly to multi-burner configurations. Multi-burner configurations are governed by more complex (higher order) dynamics and it is therefore more difficult to obtain a robust control law. The controller is no longer described by a single transfer function, but by a transfer matrix that has as many inputs as sensors and as many outputs as actuators. A technique has been developed to significantly reduce the effort to obtain a controller for such systems. This technique makes use of modal decomposition (or spatial filtering) and modal recombination in order to obtain low-order control laws. The technique proved very efficient in simulation, but has not been tested experimentally.

1.3 Objective

The goal of this work is to model and control the thermoacoustic dynamics of premixed combustion systems. This work specifically applies to gas turbine combustion systems with turbulent, premixed, swirl-stabilized flames.

Chapter 2

Relevant Acoustic Theory

2.1 Wave Equation

In this chapter, the equations for acoustic wave propagation in fluids will be derived. A similar derivation of the acoustic wave equation can be found in any basic acoustics text book, it is repeated here in order to emphasis and analyze the underlying assumptions that have been made in these derivations. Although these assumptions generally hold for classical acoustic problems such as propagation of small amplitude sound waves in air at ambient pressure and temperature, care has to be taken when using the equations to describe wave propagation under conditions encountered in a gas turbine combustion chamber. Starting from the conservation of mass, equation of motion, energy conservation and the equation of state, the following relations are found:

Continuity

$$\frac{\partial \rho}{\partial t} + \nabla \cdot (\rho \mathbf{u}) = \mathcal{W} \tag{2.1}$$

Momentum

$$\rho[\frac{\partial \mathbf{u}}{\partial t} + \mathbf{u} \cdot \nabla \mathbf{u}] + \nabla p = \mathcal{F} \tag{2.2}$$

Energy

$$\rho T[\frac{\partial \mathbf{s}}{\partial t} + \mathbf{u} \cdot \nabla \mathbf{s}] = \mathcal{S} \tag{2.3}$$

State

$$p = p(\rho, s) \tag{2.4}$$

In which $\mathcal{W}$ contains the mass source terms, $\mathcal{F}$ represents external body forces and viscous effects and $\mathcal{S}$ represents heat addition and viscous effects. In absence of viscosity: $\mathcal{S} = \dot{Q}$, in which $\dot{Q}$ is the heat flux. The sources $\mathcal{W}$, $\mathcal{F}$ and $\mathcal{S}$ are not independent: they depend on each other and on T, ρ and u. In [29], the wave equation is derived taking into account the contribution of all source terms. The equations become rather complex and the final equation requires an iterative procedure to be solved. In this work, a different approach is used, the entire system is considered to consist of different sub-systems that are coupled. In this section, acoustic relations will be derived for a medium without viscous dissipation, no external body

forces, no mass addition and no heat input. These assumptions are clearly not valid for a gas turbine combustion chamber. However, as will be discussed in section 5 the contribution of the sources will be taken into account in other subsystems. In this way, the combustion process can be represented as an interface separating the fresh mixture and the hot reaction products. The heat addition to the system takes place at this interface. The acoustic field on both sides of the interface does not need to contain a heat release source term because this is already taken into account at the interface. With $\mathcal{W}$, $\mathcal{F}$ and $\mathcal{S}$ set to zero, the wave equation can be obtained in a straightforward way. Expressing the equation of state as:

$$\frac{Dp}{Dt} = (\frac{\partial p}{\partial \rho})_s \frac{D\rho}{Dt} + (\frac{\partial p}{\partial s})_\rho \frac{Ds}{Dt}, \tag{2.5}$$

for isentropic conditions this yields:

$$\frac{Dp}{Dt} = (\frac{\partial p}{\partial \rho})_s \frac{D\rho}{Dt} = c^2 \frac{D\rho}{Dt}, \tag{2.6}$$

In which the speed of sound is defined by: $c^2 = (\frac{\partial p}{\partial \rho})_s$.
In acoustics, "small" fluctuations of pressure and density with respect to the mean values are considered. If the fluctuations are sufficiently small, Eq. 2.1 and 2.2 can be linearized around their mean values in order to describe the acoustic relations. The speed of sound is a quantity that depends on the density and is thus generally not a constant. However, the effect of speed of sound fluctuations depends on the second order [127] of the density fluctuations and can therefore be neglected for small amplitudes.
If the acoustic amplitudes are large, the linearity assumption will not hold. The quadratic terms will become large, and this will be manifested by the occurrence of non-linear harmonics: multiples of the excitation frequencies will be excited. The relative amount of harmonic distortion for weak non-linear wave propagation in an infinite tube is given by [127]:

$$\frac{A_1}{A_0} \;=\; \frac{1}{2}\,\epsilon\,\frac{\omega}{c}\,L \tag{2.7}$$

In which A_0 and A_1 are the amplitudes of the first and second harmonic, ϵ is the ratio of the non steady pressure amplitudes of the wave and the mean steady pressure, and L is the length of wave propagation. The non-linearity is caused by the dependence of the speed of sound on density fluctuations. A second, usually more important, effect is that the velocity fluctuations are not small anymore with respect to the speed of sound, thus the group velocity depends on the level of the fluctuations. For typical values of mean pressure, temperature, length scale, and for typical amplitudes and frequencies, the nonlinear distortion will be very weak and can safely be neglected.
Expressing pressure and density as the sums of their mean parts and fluctuating parts ($p = \bar{p} + p'$ and $\rho = \bar{\rho} + \rho'$), assuming zero mean flow ($u' = 0 + u'$), and substituting this into Eq. 2.1 and 2.2 and retaining only first order quantities yields:
acoustic continuity

$$\frac{\partial \rho'}{\partial t} + \bar{\rho}\,\nabla \cdot \mathbf{u}' = 0 \tag{2.8}$$

acoustic momentum

$$\bar{\rho}\frac{\partial \mathbf{u}'}{\partial t} + \nabla p' = 0 \tag{2.9}$$

Tthe mean density and speed of sound in the acoustic momentum and continuity equations is constant in time but can have spatial gradients: $\rho = \rho(\mathbf{x})$.
By taking the time derivative of Eq. 2.8,

$$\frac{\partial^2 \rho'}{\partial t^2} + \bar{\rho}\,\nabla\cdot\frac{\partial \mathbf{u}'}{\partial t} = 0 \tag{2.10}$$

and the spatial derivative of Eq. 2.9,

$$\bar{\rho}\,\nabla\frac{\partial \mathbf{u}'}{\partial t} + \nabla^2 p' = 0 \tag{2.11}$$

In the last equation, a spatial uniform density has been assumed. Combining Eqs. 2.10 and 2.11, the wave equation is obtained:

$$\frac{\partial^2 \rho'}{\partial t^2} - \nabla^2 p' = 0. \tag{2.12}$$

By linearizing Eq. 2.6, a relation between the acoustic pressure and acoustic density is obtained: $p' = c^2\rho'$. By making use of this relation, a more convenient expression of the wave equation is obtained:

$$\frac{\partial^2 p'}{\partial t^2} - c^2\nabla^2 p' = 0. \tag{2.13}$$

Note that it would have been more correct to use $\bar{c}$ rather than c in Eq. 2.13. However, for ease of notation, the symbol c will be used for the mean value of the speed of sound.
In a combustion system, the assumption of uniform density will generally not hold (it implies a uniform temperature and thus a uniform speed of sound). The spatial variance of the temperature in a practical combustion system is generally small compared to its mean. Because the speed of sound depends on the square root of the temperature, the error in the speed of sound is $\sqrt{1+\frac{\Delta T}{T}} - 1$. The spatial temperature distribution in the combustor can be assumed to be well below 10%, this would cause an error in the speed of sound of less than 5%.

2.2 Wave Equation Including Fluctuating Heat Release

When heat is periodically added to the medium, the isentropic relation between pressure and density fluctuations (Eq. 2.6) may not be used because the second term in Eq. 2.5 will not vanish. Under the assumption of zero mean flow, this term can be written as:

$$(\frac{\partial p}{\partial s})_\rho \frac{Ds}{Dt} = (\frac{\partial p}{\partial s})_\rho \frac{\partial s}{\partial t} = (\frac{\partial p}{\partial T}\,\frac{\partial T}{\partial s})_\rho \frac{\partial s}{\partial t} = (\frac{\partial p}{\partial T}\,T\frac{\partial T}{\partial Q})_\rho \frac{1}{T}\frac{\partial Q}{\partial t} = \frac{R}{C_v}\frac{\partial Q}{\partial t} = (\gamma-1)\frac{\partial Q}{\partial t} \tag{2.14}$$

Use has been made here of: $\partial s = \frac{\partial Q}{T}$, $\left(\frac{\partial Q}{\partial T}\right)_\rho = \rho C_v$ and of $\frac{p}{\rho T} = R$.

Thus, if heat release fluctuations are present, the relation between acoustic pressure and density is obtained by substituting Eq. 2.14 into Eq. 2.5 and linearizing the result. Making use of the definition of the speed of sound, the following relation is obtained:

$$\frac{\partial p'}{\partial t} = c^2 \frac{\partial \rho'}{\partial t} + (\gamma - 1)\dot{Q}' \tag{2.15}$$

This can be considered a correction to the acoustic state equation due to the presence of heat release.
After substitution into the wave equation (Eq. 2.12) the wave equation with non-steady heat release source term is obtained:

$$\frac{\partial^2 p'}{\partial t^2} - c^2 \nabla^2 p' = (\gamma - 1)\frac{\partial \dot{Q}'}{\partial t}. \tag{2.16}$$

Note that in deriving this equation it is assumed that no gradients of the mean flow quantities are present. This is rather unrealistic in the presence of combustion because the mean heat release will introduce a mean temperature difference across the flame. Nevertheless, this equation is useful because it provides good insight into the thermoacoustic phenomenon. However, the equation in this form will not be used in this work to model the thermo-acoustic interaction. A more rigorous derivation of the wave equation with heat release source term, mean flow, temperature gradients and without small amplitude restriction is given in an analysis by Candel et. al. [19] and by Culick [29].

2.3 Convective Wave Equation

In this section, relations for the wave equation in the presence of a constant, uniform mean flow will be derived. This is done by using a coordinate transformation in Eq. 2.12. The velocity field is thus considered to be a superposition of a constant mean flow ($\bar{\mathbf{u}}$) and a fluctuating (acoustic) part ($\mathbf{u}'$). Note that $\mathbf{u}'$ is not required to be small compared to $\bar{\mathbf{u}}$.

$$\tilde{\mathbf{x}} = \mathbf{x} + \bar{\mathbf{u}}t \tag{2.17}$$

$$\tilde{t} = t \tag{2.18}$$

The relation between the differential operators in both coordinate systems is then:

$$\nabla = \frac{\partial \tilde{t}}{\partial \mathbf{x}}\frac{\partial}{\partial \tilde{t}} + \frac{\partial \tilde{\mathbf{x}}}{\partial \mathbf{x}}\tilde{\nabla} = \tilde{\nabla} \tag{2.19}$$

$$\frac{\partial}{\partial t} = \frac{\partial \tilde{t}}{\partial t}\frac{\partial}{\partial \tilde{t}} + \frac{\partial \tilde{\mathbf{x}}}{\partial t}\tilde{\nabla} = \frac{\partial}{\partial t} + \bar{\mathbf{u}} \cdot \tilde{\nabla} \tag{2.20}$$

Substituting Eq. 2.19 and Eq. 2.20 into the wave equation (Eq. 2.12) yields the *convective wave equation*:

$$(\frac{\partial}{\partial t} + \bar{\mathbf{u}} \cdot \nabla)^2 p' - c^2 \nabla^2 p' = 0, \tag{2.21}$$

where for ease of notation the tildes have been dropped.
This equation is separable in the usual coordinate systems. For coordinates ($\mathbf{x} = \xi_1, \xi_2, \xi_3$) solutions exist of type $F_1(\xi_1)F_2(\xi_2)F_3(\xi_3)$. Each of these solutions is called a mode. If the boundaries of the volume are applied at surfaces ξ_i = constant, equations F_i are decoupled. This means that the acoustic field retains its shape in a direction parallel to this boundary. From a mathematical point of view, it is very convenient to choose a coordinate system in which the boundary conditions are imposed on planes at ξ_i =constant. This is because the solutions then form a complete basis by which any other solutions can be represented [111].
Applying the same coordinate transformation to Eq. 2.9 yields the *acoustic convective momentum equation*:

$$\rho(\frac{\partial}{\partial t} + \bar{\mathbf{u}} \cdot \nabla)\mathbf{u}' + \nabla p' = 0 \tag{2.22}$$

Solution in One Dimension

Evaluating the convective wave equation in one dimension yields a very compact solution in terms of up-stream and down-stream traveling waves, or characteristics. These waves originate mathematically as integration constants (or Riemann invariants) when solving the wave equation. Expressing the acoustic pressure with separated space and time dependence and considering the dependence on frequency ω and on wave number k:

$$p' = \hat{p}\, e^{i\,\omega\, t - ik\, x} = \hat{p}(s, \kappa)\, e^{s\, t + \kappa\, x}, \tag{2.23}$$

in which $s = i\,\omega$ is the temporal Laplace coefficient, and $\kappa = -i\,k$ its spatial equivalent.
Substituting this expression for p' into the convective wave equation:

$$(s + u\,\kappa)^2\, p' - c^2\, \kappa^2\, p' \tag{2.24}$$

and solving for κ, yields two solutions:

$$\kappa_\pm = \frac{\pm s}{c \mp u} \tag{2.25}$$

The expression for the acoustic pressure is then a linear combination of these two solutions:

$$p'(x,t) = C_+ e^{s\, t + \kappa_+\, x} + C_- e^{s\, t + \kappa_-\, x} \tag{2.26}$$

In which $C_\pm$ are two integration constants. This is a general solution of the homogeneous one-dimensional acoustic wave equation with mean flow. The value of these integration constants (or Riemann invariants) depends on the boundary and initial conditions of the given problem. Note that the integration constants $C_\pm$ are frequency dependent (dependent on s). This solution can be interpreted as the sum of two waves traveling in opposite directions. This can best be seen by substituting the relation for the wave number (2.25) into Eq. 2.26:

$$p'(x,t) = C_+ e^{s(t + \frac{x}{c-u})} + C_- e^{s(t - \frac{x}{c+u})} \tag{2.27}$$

Thus C_+ propagates upstream with a velocity $c-u$, while C_- propagates downstream with velocity $c+u$. For ease of notation, the upstream traveling wave, or Riemann invariant, is termed g, while the downstream traveling component is denoted as f. A subscript indicates its axial position: $f_j = \frac{1}{\rho\, c}\, C_- e^{s(t-\frac{x_j}{c+u})} = f_o\, e^{s(t-\frac{x_o-x_j}{c+u})}$ and similar for g. Thus the acoustic pressure can be written as: $p' = \rho\, c\, (f+g)$, the choice of the scaling factor ρc will become apparent from next equation.
The acoustic velocity can be obtained by substituting the solution for the wave number (Eq. 2.25) and the pressure (Eq. 2.27) into the momentum equation (Eq. 2.22):

$$\rho(\frac{\partial}{\partial t} + u\frac{\partial}{\partial x})u' + \frac{\partial}{\partial x}p' = 0 \tag{2.28}$$

$$\rho(s + u\,\kappa)u' + \kappa p' = 0 \tag{2.29}$$

$$u' = \frac{p'}{\rho}\frac{-1}{\frac{s}{\kappa}+u} \tag{2.30}$$

$$= \frac{-1}{\rho}\left\{\frac{1}{\frac{s}{\kappa_+}+u}\, C_+ e^{s\,t+\kappa_+\,x} + \frac{1}{\frac{s}{\kappa_-}+u} C_- e^{s\,t+\kappa_-\,x}\right\} \tag{2.31}$$

$$= \frac{-1}{\rho}\left\{\frac{1}{c}\, C_+ e^{s\,t+\kappa_+\,x} - \frac{1}{c} C_- e^{s\,t+\kappa_-\,x}\right\} \tag{2.32}$$

$$= f - g \tag{2.33}$$

Thus, very simple relations are found between Riemann invariants and the acoustic pressure and velocity:

$$\begin{bmatrix} \frac{\hat{p}}{\rho c} \\ \hat{u} \end{bmatrix} = \begin{bmatrix} 1 & 1 \\ 1 & -1 \end{bmatrix} \begin{bmatrix} \hat{f} \\ \hat{g} \end{bmatrix}, \tag{2.34}$$

$$\begin{bmatrix} \hat{f} \\ \hat{g} \end{bmatrix} = \frac{1}{2} \begin{bmatrix} 1 & 1 \\ 1 & -1 \end{bmatrix} \begin{bmatrix} \frac{\hat{p}}{\rho c} \\ \hat{u} \end{bmatrix}. \tag{2.35}$$

The relation between Riemann invariants at two positions in a straight, one-dimensional duct with mean flow can be expressed using Eq. 2.27:

$$\begin{bmatrix} \hat{f}_j \\ \hat{g}_j \end{bmatrix} = \begin{bmatrix} e^{-s\frac{x_j-x_i}{c+u}} & 0 \\ 0 & e^{s\frac{x_j-x_i}{c-u}} \end{bmatrix} \begin{bmatrix} \hat{f}_i \\ \hat{g}_i \end{bmatrix}. \tag{2.36}$$

With Eqns. 2.34-2.36 a conversion between the Riemann invariants and acoustic pressures and velocities can be performed at any location in a duct. These properties will be used in section 3 where the Riemann invariants will be estimated from multiple pressure signals.
In one-dimensional acoustics, the ratio between Riemann invariants is refered to as a *reflection coefficient* R, for the upstream side:

$$R(\omega) = \frac{\hat{f}(\omega)}{\hat{g}(\omega)}, \tag{2.37}$$

and for the downstream side:

$$R(\omega) = \frac{\hat{g}(\omega)}{\hat{f}(\omega)}. \tag{2.38}$$

The name *reflection coefficient* is somewhat misleading because it is not really a coefficient, but a (complex valued) frequency dependent function. Similary, impedances can be defined as the ratio between acoustic pressure and acoustic velocity. The acoustic velocity is generally taken to be orthogonal to the bounding surface and pointing out of the volume:

$$Z(\omega) = \frac{\hat{p}}{\rho c\, \hat{u}} \tag{2.39}$$

For one-dimensional acoustics with a global coordinate system, the relations for the upstream side become:

$$Z_{up}(\omega) = \frac{\hat{p}(\omega)}{-\rho c\, \hat{u}(\omega)}, \tag{2.40}$$

and for the downstream side:

$$Z_{down}(\omega) = \frac{\hat{p}(\omega)}{\rho c\, \hat{u}(\omega)}. \tag{2.41}$$

Note that the conversion between impedance and reflection coefficients can be made as follows:

$$\begin{aligned} Z_{up} &= \frac{1}{\rho\, c} \frac{R_{up}+1}{R_{up}-1} \\ Z_{do} &= -\frac{1}{\rho\, c} \frac{R_{do}+1}{R_{do}-1} \\ R_{up} &= -\frac{Z_{up}-1}{Z_{up}+1} \\ R_{do} &= \frac{Z_{do}-1}{Z_{do}+1} \end{aligned} \tag{2.42, 2.43}$$

The factor ρc is referred to as the characteristic impedance.

2.4 Convective Wave Equation for Annular Ducts

Many modern gas turbines have annular combustion chambers. Therefore, special attention will be paid to wave propagation in annular channels. In typical combustion chamber geometries the difference between the inner and outer diameters of the annulus is small compared with the mean diameter of the annulus. Therefore, a Cartesian system of coordinates is chosen where: x is the axial coordinate, y the azimuthal coordinate and z the radial coordinate, as depicted in Fig. 2.1. Thus the annular volume is approximated by a rectangular volume being periodic in the azimuthal direction [1]

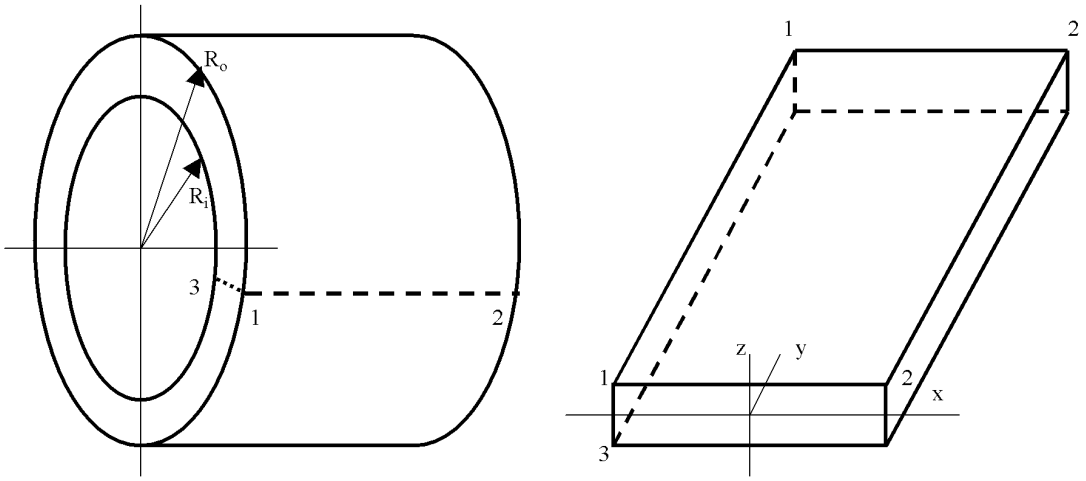

Figure 2.1: System of coordinates for annular ducts.

For a mode defined by the wave numbers k_x, k_y, k_z, the acoustic pressure can be expressed as a Fourier integral:

$$\frac{p'(t,x,y,z)}{\rho c} \equiv \int_{-\infty}^{\infty} \hat{p}(\omega)\ e^{i\omega t - ik_x x - ik_y y - ik_z z} d\omega. \tag{2.44}$$

with $p' \in \mathbb{R}$ and $\hat{p} \in \mathbb{C}$ and thus $\hat{p}(-\omega) = \hat{p}^*(\omega)$, in which $*$ denotes the complex conjugate. Note that according to this definition, $\hat{p}(\omega)$ is the Fourier transform of $p'(t)$ scaled by the characteristic impedance ρc. Substituting Eq. 2.44 into Eq. 2.21, assuming a uniform mean-flow in axial direction and solving for k_x yields:

$$k_x^{\pm} = \frac{-kM \pm \sqrt{(M^2-1)(k_y^2+k_z^2)+k^2}}{1-M^2} \tag{2.45}$$

The general solution of the wave equation in the Cartesian coordinate system is given by:

[1] An exact representation of the acoustic field in an annulus can be obtained using cylindrical coordinates, the difference is, however, minimal. Use of Cartesian coordinates avoids the use of Bessel functions.

$$p(x,y,z,t) = (C_1 e^{-ik_x} + C_2 e^{+ik_x x})(e^{-ik_y y} + C_3 e^{+ik_y y})(e^{-ik_z z} + C_4 e^{+ik_z z}) e^{+i\omega t}, \tag{2.46}$$

in which $C_{1,2,3,4}$ are integration constants.
Because of periodicity in the azimuthal (y) direction:

$$p(x,y,z) = p(x, y + \pi D, z), \tag{2.47}$$

and

$$\frac{\partial p(x,y,z)}{\partial y} = \frac{\partial p(x, y + \pi D, z)}{\partial y}, \tag{2.48}$$

with D the (average) diameter of the annulus. Substituting the periodicity conditions in the solution of the wave equation and solving for k_y yields:

$$k_y = \frac{2n}{D} \qquad\qquad n \in \mathbb{Z} \tag{2.49}$$

The wave number in the radial direction can be found by applying rigid wall boundary conditions. These conditions imply that fluid velocity in the direction normal to the wall is zero at the wall. Because,

$$\mathbf{u} = \frac{1}{i\rho k} \nabla p \tag{2.50}$$

it follows that in the radial direction:

$$\frac{\partial p(x,y,z=0)}{\partial z} = \frac{\partial p(x,y,z=h)}{\partial z} = 0, \tag{2.51}$$

with h denoting the height of the annulus.
Substituting these boundary conditions into equation 2.46 yields:

$$C_4 = 1; \qquad\qquad k_z = \frac{m\pi}{h} \qquad\qquad m \in \mathbb{N} \tag{2.52}$$

Because C_4 is solved for, the dependence of the acoustic pressure on the radial direction is given by:

$$p'(x,y,z,t) = p(x,y,t) cos(\frac{m\pi}{h} z). \tag{2.53}$$

Thus, the pressure distribution in the radial direction for $m \neq 0$ is always such that a maximum of the absolute value is found on the annulus walls, and a minimum halfway between the walls. In the azimuthal direction such a fixed distribution does not exist, because the value of C_3 is not known a-priori. If the boundary condition in the longitudinal direction is independent of the y-coordinate, then the distribution of the pressure amplitudes in the y-direction can only be obtained if the excitation of the system is known.
Assuming harmonic time dependence: $p' = \hat{p}\, e^{+i\omega t}$, the general solution of the wave equation in an annular duct is thus:

$$\frac{\hat{p}}{\rho c} = \sum_{m=0}^{M} \sum_{n=0}^{N} (r_{++} + r_{+-} + r_{-+} + r_{--}) cos(\frac{m\pi}{h} z) \tag{2.54}$$

with

$$r_{\pm\pm} = R_{\pm\pm}^{(n,m)} e^{-ik_x^{\pm}x - i\frac{\pm 2n}{D}y} \tag{2.55}$$

$$k_x^{\pm} = \frac{\frac{-\omega}{c}M \pm \sqrt{(M^2-1)((\frac{\pm 2n}{D})^2 + (\frac{m\pi}{h})^2) + (\frac{\omega}{c})^2}}{1-M^2} \tag{2.56}$$

Because the mode $n = 0$ has a uniform distribution in the y-direction, and is thus independent of the y-coordinate, Eq. 2.54 can be written as:

$$\frac{\hat{p}}{\rho c} = \sum_{m=0}^{\infty}\{F\ e^{-ik_x^{+}x} + G\ e^{-ik_x^{-}x} + \sum_{n=1}^{N}(r_{++} + r_{+-} + r_{-+} + r_{--})\}cos(\frac{m\pi}{h}z) \tag{2.57}$$

The terms $r_{\pm\pm}$ can be physically interpreted as four waves traveling in up- and down- stream directions with positive and negative senses of rotation.
Relations for the acoustic velocities can be obtained by substituting Eq. 2.54 into Eq. 2.22. Considering mean flow in the axial direction only, u'_x, u'_y and u'_z can be solved for by making use of the fact that the velocity field and the pressure field have the same space and time dependence.

$$\hat{u}_x = \sum_{m=0}^{\infty}\sum_{n=0}^{\infty}\{\frac{k_x^{+}}{k - Mk_x^{+}}(r_{++} + r_{+-}) + \frac{k_x^{-}}{k - Mk_x^{-}}(r_{-+} + r_{--})\}cos(\frac{m\pi}{h}z) \tag{2.58}$$

$$\hat{u}_y = \sum_{m=0}^{\infty}\sum_{n=1}^{\infty}\{\frac{2n/D}{k - Mk_x^{+}}(r_{++} - r_{+-}) + \frac{2n/D}{k - Mk_x^{-}}(r_{-+} - r_{--})\}cos(\frac{m\pi}{h}z) \tag{2.59}$$

$$\hat{u}_z = \sum_{m=1}^{\infty}\sum_{n=0}^{\infty}\{\frac{m\pi/h}{k - Mk_x^{+}}(r_{++} - r_{+-}) + \frac{m\pi/h}{k - Mk_x^{-}}(r_{-+} - r_{--})\}cos(\frac{m\pi}{h}z) \tag{2.60}$$

As can be seen, the azimuthal velocity (v') is zero for $n = 0$, which is consistent with plane wave theory. The axial velocity ($\hat{u}$) can be rewritten as:

$$\begin{aligned}\hat{u}_x \;=\; & \sum_{m=1}^{\infty}\Bigg\{\frac{k_x^{+}}{k - Mk_x^{+}}F\ e^{-ik_{x+}x} + \frac{k_x^{-}}{k - Mk_x^{-}}G\ e^{-ik_{x-}x} + \\ & + \sum_{n=1}^{\infty}\Big(\frac{k_x^{+}}{k - Mk_x^{+}}(r_{++} + r_{+-}) + \frac{k_x^{+}}{k - Mk_x^{+}}(r_{-+} + r_{--})\Big)\Bigg\}cos(\frac{m\pi}{h}z)\end{aligned} \tag{2.61}$$

2.5 Acoustic Energy Conservation

When analyzing thermoacoustic systems such as gas turbines, it is very important to consider the acoustic energy balance of the system. The acoustic energy balance is closely related to the stability of the system. If the net flow of acoustic energy into the system (averaged over space and time) is positive, acoustic energy is accumulated which will result in continuously increasing acoustic amplitudes. In this case, the system is said to be unstable. The acoustic energy balance will be derived here for a system with zero mean flow. This is, however, a dangerous assumption. In a combustion chamber, mean flow will always be present. Although the effect of the mean flow on wave propagation may often be neglected, the effect on the boundaries and especially on the energy balance can not be neglected. The energy balance with mean flow (but without heat release) can be found in [111]. However, in order to get insight into the general behavior of thermoacoustic systems, it is useful to investigate the simplified energy balance, without mean flow. This balance can easily be obtained by making use of the acoustic continuity and momentum equation and substituting the non-isentropic relation between acoustic pressure and density (Eq. 2.15):

acoustic continuity

$$\frac{\partial \rho'}{\partial t} + \bar{\rho}\nabla \cdot \mathbf{u}' = (\gamma - 1)\dot{Q}' \tag{2.62}$$

acoustic momentum

$$\bar{\rho}\frac{\partial \mathbf{u}'}{\partial t} + \nabla p' = 0 \tag{2.63}$$

Multiplying the continuity equation by $\frac{p'}{\bar{\rho}}$, and the momentum equation by $\mathbf{u}'$, and taking the sum of these two results yields (after some manipulation):

$$\frac{1}{2c^2\bar{\rho}}\frac{\partial (\rho')^2}{\partial t} + \frac{\bar{\rho}}{2}\frac{\partial (u')^2}{\partial t} + \nabla\cdot(\rho'\mathbf{u}') = \frac{p'}{\rho c^2}(\gamma - 1)\dot{Q}' \tag{2.64}$$

Which can be recognized to be an energy balance [111]. This can be written more conveniently as:

$$\begin{aligned} \frac{\partial \mathcal{E}}{\partial t} + \nabla \cdot \mathcal{I} &= (\gamma - 1)\frac{p'\dot{Q}'}{\rho c^2}, \\ \mathcal{E} &= \frac{p'^2}{2c^2\bar{\rho}} + \frac{\bar{\rho}\mathbf{u}'^2}{2}, \\ \mathcal{I} &= p'\mathbf{u}'. \end{aligned} \tag{2.65}$$

In which $\mathcal{E}$ will be referred to as the acoustic energy density, and $\mathcal{I}$ the acoustic energy flux. From this expression the Rayleigh criterion can easily be understood: if heat release and pressure are in phase, the right-hand side of Eq. 2.65 becomes positive, and thus the energy density will increase locally. On the other hand, if the heat release is out of phase with pressure, the energy density decreases locally. In order to investigate the energy flows of a system, Eq. 2.65 has to be integrated over the volume:

$$\frac{d}{dt}\int\int\int_V \mathcal{E}\, d\mathbf{x} = \int\int\int_V (\gamma - 1)\frac{p'\dot{Q}'}{\rho c^2} d\mathbf{x} - \oint_S \mathcal{I}\cdot\mathbf{n}\, d\mathbf{x}_S. \tag{2.66}$$

In which the normal ($\mathbf{n}$) points out of the volume.
By considering harmonic fluctuations, this expression can be given a frequency domain interpretation. To do so, the acoustic pressure is expressed as: $p'(t) = \frac{1}{2}\hat{p}e^{i\,\omega\,t} + \frac{1}{2}\hat{p}^* e^{-i\,\omega\,t}$, and similar for the acoustic velocity and heat release rate. Substituting this relation into Eq. 2.66 and integrating over one period of oscillation ($T = \frac{2\pi}{\omega}$) yields:

$$\begin{aligned}
\Delta\mathcal{E} &= \frac{1}{T}\int_{t-T}^{t}\int\int\int_V \mathcal{E}\,d\mathbf{x}\,dt \\
&= \frac{1}{4T}\int_{t-T}^{t}\int\int\int_V \frac{(\gamma-1)}{\rho c^2}(\hat{p}e^{i\,\omega\,t} + \hat{p}^* e^{-i\,\omega\,t})(\hat{\dot{Q}}e^{i\,\omega\,t} + \hat{\dot{Q}}^* e^{-i\,\omega\,t})d\mathbf{x}\,dt + \\
&\quad -\frac{1}{4T}\int_{t-T}^{t}\oint_S (\hat{p}e^{i\,\omega\,t} + \hat{p}^* e^{-i\,\omega\,t})(\hat{u}e^{i\,\omega\,t} + \hat{u}^* e^{-i\,\omega\,t})\cdot n\; d\mathbf{x}_S\,dt \\
&= \frac{1}{4}\int\int\int_V \frac{(\gamma-1)}{\rho c^2}(\hat{p}\hat{\dot{Q}}^* + \hat{p}^*\hat{\dot{Q}})d\mathbf{x} - \frac{1}{4}\oint_S (\hat{p}\hat{u}^* + \hat{p}^*\hat{u})\cdot n\; d\mathbf{x}_S. \qquad (2.67)
\end{aligned}$$

The relation between the acoustic pressure and velocity can be expressed as an impedance: $Z(\omega) = \frac{\hat{p}}{\hat{u}\cdot n}$. In a similar manner, the relation between heat release rate and acoustic pressure can be expressed as a transfer function $F_{Qp} = \frac{\hat{\dot{Q}}}{\hat{p}}$. Note that linearity is assumed when expressing the relation as transfer functions. Substituting these relations into Eq. 2.67 the following expression is obtained for the energy increment over one period of oscillation:

$$\Delta\mathcal{E} = \frac{1}{2}\frac{(\gamma-1)}{\rho c^2}\int\int\int_V |\hat{p}|^2\Re(F_{Qp})d\mathbf{x} - \frac{1}{2}\oint_S |\hat{p}|^2\Re(\frac{1}{Z_{up}})\,d\mathbf{x}_S. \qquad (2.68)$$

The real part of the impedance of a boundary is always positive if no external energy addition takes place on the boundary. Thus the second part of the right hand side of equation 2.68 is always a loss term. The first term will add energy to the system if the real part of F_{Qp} is positive (if the absolute value of the phase is smaller than $\pi/2$), this term will dissipate energy if the real part is negative (if the absolute value of the phase is larger than $\pi/2$). The system is unstable if $\Delta\mathcal{E}$ is positive.

2.6 Modal Expansion Using Green's Function

The response to acoustic sources on the boundary or within a volume can be expressed conveniently by making use of Green's functions and modal expansion. The derivation given here follows the approach described in [79, 78]. This representation will later prove to be very useful in obtaining acoustic input-output relations of a volume. These acoustic transfer functions, will form the basis of the acoustic network models.
Starting from the wave equation with a heat release rate source term ($\dot{Q}$), but in absence of mean flow (Eq. 2.16), and writing the contribution of the heat release rate as $h = -(\gamma - 1)\frac{\partial \dot{Q}'}{\partial t}$:

$$\begin{aligned} c^2\nabla^2 p' - \alpha\,\frac{\partial p'}{\partial t} - \frac{\partial^2 p'}{\partial t^2} &= h, \\ \hat{\mathbf{n}}\cdot\nabla p' &= -f, \\ f(t<0) &= 0, \\ h(t<0) &= 0. \end{aligned} \tag{2.69}$$

In which $f(t)$ is a source on the boundary and $h(t)$ a source in the volume. The unit vector ($\hat{n}$) points out of the volume, perpendicular to the boundary. Note that a damping term (α) has been introduced, this term accounts for dissipation of acoustic energy.
After applying the Fourier transform to 2.69:

$$\begin{aligned} c^2\nabla^2 \hat{p} - i\,\alpha\,\omega\hat{p} + \omega^2\hat{p} &= \hat{h} \\ \hat{\mathbf{n}}\cdot\nabla\hat{p} &= -\hat{f} \end{aligned} \tag{2.70}$$

A solution can be obtained by making use of Green's function. The Green's function is a solution of Eq. 2.69 in which $f = 0$ and $h = \delta(\mathbf{x} - \mathbf{x_0})\delta(t - t_0)$. The Dirac delta function $\delta(\mathbf{x} - \mathbf{x_0})$ is a function which is zero for all values of $\mathbf{x}$ and for all instances of time except at $\mathbf{x} = \mathbf{x_0}, t = t_0$, where it is infinite. Thus the Green's function $G(\mathbf{x}|\mathbf{x}_0, t)$ can be considered as the response of the system at $\mathbf{x}$ to an impulse in space and time at $(\mathbf{x_0}, t_0)$. The Green's function can, for example, be used to analyze how an acoustic (impulse) disturbance introduced at one point in the volume at $t = 0$ evolves in space and time. However, the applications of Green's function reach much farther than this. This can be understood by considering that *any* function $h(t, \mathbf{x})$ can be considered as an infinite sum of impulses in space and time: $h(t, \mathbf{x}) = \int_V \int_{t_0}^{\infty} h(x_0, t_0)\delta(t - t_0)\delta(\mathbf{x} - \mathbf{x_0})d\,t_0 d\,\mathbf{x_0}$. This makes clear that *any* solution of Eq. 2.69 can be expressed as an integral of infinite impulse responses. To demonstrate this, the derivation presented in [79] is used, it starts with the wave equation with an impulse at $h = \delta(\mathbf{x} - \mathbf{x_0})\delta(t - t_0)$:

$$c^2\nabla^2 G(\mathbf{x}, t|\mathbf{x}_0, t_0) - \alpha\,\frac{\partial G(\mathbf{x}, t|\mathbf{x}_0, t_0)}{\partial t} - \frac{\partial^2 G(\mathbf{x}, t|\mathbf{x}_0, t_0)}{\partial t^2} = \delta(\mathbf{x} - \mathbf{x_0})\delta(t - t_0), \tag{2.71}$$

$$\hat{\mathbf{n}}\cdot\nabla G(\mathbf{x}, t|\mathbf{x}_0, t_0) = 0, \tag{2.72}$$

Upon Fourier transformation:

$$c^2\nabla^2\hat{G}(\mathbf{x}|\mathbf{x}_0) - i\,\omega\alpha\hat{G}(\mathbf{x}|\mathbf{x}_0) + \omega^2\hat{G}(\mathbf{x}|\mathbf{x}_0) = \delta(\mathbf{x}-\mathbf{x_0})\,e^{-i\omega t_0} \quad (2.73)$$

$$\hat{\mathbf{n}}\cdot\nabla\hat{G}(\mathbf{x}|\mathbf{x}_0) = 0 \quad (2.74)$$

Note that the Fourier transform of a Dirac delta was introduced in this step: $\mathcal{F}\{\delta(t-t_0)\} = e^{-i\,\omega t_0}$. The usual way to proceed is to multiply Eq. 2.70 with $G(\mathbf{x}|\mathbf{x}_0)$, subtract Eq. 2.73 multiplied by $\hat{p}(\mathbf{x})$ and integrate over the volume:

$$\int\int\int_V c^2(\hat{G}\nabla^2\hat{p}-\hat{p}\nabla^2 G)d\mathbf{x}+\int\int\int_V(\omega^2+i\,\omega\alpha)(\hat{G}\hat{p}-\hat{p}\hat{G})d\mathbf{x} = \int\int\int_V(\hat{G}\,\hat{h}-\hat{p}\delta(\mathbf{x}|\mathbf{x}_0)\,e^{-i\omega t_0})d\mathbf{x} \quad (2.75)$$

In this step it becomes apparent why the Fourier transforms of Eqns. 2.73 and 2.69 have been taken: the multiplication operation can be done in the frequency domain only, because in the time domain, a convolution integral should have been evaluated. Because G and p are scalar functions, $\hat{G}\,\hat{p} = \hat{p}\,\hat{G}$ and, therefore, the second term on the left hand side vanishes. Green's second theorem can now be applied to the first term and, by making use of the properties of an integral over Dirac's delta, Eq. 2.75 can be written as:

$$\oint_S c^2(\hat{G}(\mathbf{x}|\mathbf{x}_0)\nabla\hat{p} - \hat{p}\nabla\hat{G}(\mathbf{x}|\mathbf{x}_0))\cdot\hat{n}\,d\mathbf{x_s} = \int\int\int_V \hat{G}(\mathbf{x}|\mathbf{x}_0)h(\mathbf{x})d\mathbf{x} - \hat{p}(\mathbf{x}_0)\,e^{-i\omega t_0} \quad (2.76)$$

Substituting the boundary conditions $\hat{\mathbf{n}}\cdot\nabla\hat{p} = -\hat{f}$ and $\hat{\mathbf{n}}\cdot\nabla G(\mathbf{x}|\mathbf{x}_0) = 0$ into Eq. 2.76 yields:

$$\hat{p}(\mathbf{x}_0) = e^{-i\omega t_0}\int\int\int_V \hat{G}(\mathbf{x}|\mathbf{x})\hat{h}(\mathbf{x})d\,\mathbf{x_0} + e^{-i\omega t_0}\oint_S c^2\,\hat{G}(\mathbf{x_s}|\mathbf{x}_0)\hat{f}(\mathbf{x_s})d\mathbf{x_s} \quad (2.77)$$

Because the delay $e^{-i\omega t_0}$ multiplies both terms in Eq. 2.77, the value of t_0 can, without loss of generality, be set to zero.
As demonstrated in [78], the Green's function satisfies a reciprocity condition: $G(\mathbf{x},t|\mathbf{x}_0,t_0) = G(\mathbf{x}_0,-t_0|\mathbf{x},-t)$. The Fourier transform of G is obtained as:

$$\hat{G}(\mathbf{x}|\mathbf{x}_0) = \int_{-\infty}^{\infty} G(\mathbf{x},t|\mathbf{x}_0,t_0)e^{-i\omega t}d\,t \quad (2.78)$$

$$= \int_{-\infty}^{\infty} G(\mathbf{x}_0,-t_0|\mathbf{x},-t)e^{-i\omega t}d\,t \quad (2.79)$$

$$= \hat{G}(\mathbf{x}_0|\mathbf{x}) \quad (2.80)$$

And thus, in the frequency domain, the reciprocity condition reduces to: $\hat{G}(\mathbf{x}|\mathbf{x}_0) = \hat{G}(\mathbf{x}_0|\mathbf{x})$. Hence a solution for $\hat{p}$ in the domain V is obtained:

$$\hat{p}(\mathbf{x}) = \int\int\int_V \hat{G}(\mathbf{x}|\mathbf{x}_0)h(\mathbf{x}_0)d\mathbf{x_0} + \oint_S c^2\,\hat{G}(\mathbf{x_s}|\mathbf{x}_0)\hat{f}(\mathbf{x_s})d\mathbf{x_{0,s}}. \quad (2.81)$$

In order to make this equation useful, an expression for G has to be found. A convenient way to proceed is to express G in an *eigenfunction expansion*. The eigenfunctions (modal functions)

are orthogonal and form a complete set. Therefore, any function that fulfills the homogeneous boundary conditions can be expressed as a linear combination of the eigenfunctions:

$$G(\mathbf{x}|\mathbf{x}_0, t) = \sum_{n=0}^{\infty} \eta_n(t)\psi_n(\mathbf{x}), \tag{2.82}$$

or, in the frequency domain.

$$\hat{G}(\mathbf{x}|\mathbf{x}_0, \omega) = \sum_{n=0}^{\infty} \eta_n(\omega)\psi_n(\mathbf{x}). \tag{2.83}$$

With eigenfunctions (ψ_n) satisfying:

$$c^2\nabla^2\psi + \omega^2\psi = 0, \tag{2.84}$$

$$\hat{\mathbf{n}} \cdot \nabla\psi = 0, \tag{2.85}$$

and

$$\int\int\int_V \psi_m(\mathbf{x})\psi_n(\mathbf{x})d\mathbf{x} = \Lambda\delta_{mn}. \tag{2.86}$$

In which δ_{mn} is the Kronecker delta, it is unity for $m = n$ and zero if $m \neq n$. Note that because the original problem (Eq. 2.69) is causal, $\eta_n(t < t_0) = 0$.
Substituting the modal expansion of Green's function into Eq. 2.73, multiplying by ψ_m and integrating over the volume yields:

$$\int\int\int_V c^2\,\psi_m \sum_{n=0}^{\infty} \eta_n\nabla^2\psi_n d\mathbf{x_0} + (\omega^2 - i\,\omega\alpha)\int\int\int_V \psi_m \sum_{n=0}^{\infty} \eta_n\psi_n d\mathbf{x_0} = \int\int\int_V \psi_m(\mathbf{x})\delta(\mathbf{x}-\mathbf{x}_0)d\mathbf{x_0} \tag{2.87}$$

Substituting $c^2\nabla^2\psi_n = -\omega_n^2\psi_n$ (Eq. 2.84), making use of the properties of an integral over the Dirac delta and of the properties of an orthogonal function (Eq. 2.86), then solving for η_n yields:

$$\eta_n = \frac{1}{\Lambda}\frac{\psi_n(\mathbf{x_0})}{\omega^2 - i\,\omega\alpha - \omega_n^2} \tag{2.88}$$

Substituting this result into Eq. 2.83, $\hat{G}$ can be written as:

$$\hat{G}(\mathbf{x}|\mathbf{x}_0) = \sum_{n=0}^{\infty} \frac{\psi_n(\mathbf{x})\psi_n(\mathbf{x_0})}{\Lambda(\omega^2 - i\,\omega\alpha - \omega_n^2)} \tag{2.89}$$

And, finally, the pressure fluctuations can be expressed as a function of the eigenfunctions, eigenfrequencies and sources by substitution of Eq. 2.89 into Eq. 2.81:

$$\hat{p}(\mathbf{x}) = \sum_{n=0}^{\infty} \frac{\psi_n(\mathbf{x})}{\Lambda(\omega^2 - i\,\omega\alpha - \omega_n^2)} \left\{ \int\int\int_V \psi_n(\mathbf{x}_0)\hat{h}(\mathbf{x}_0)d\mathbf{x_0} + \oint_S c^2\,\psi(\mathbf{x}_s)\hat{f}(\mathbf{x_s})d\mathbf{x_{0,s}} \right\}. \tag{2.90}$$

So, if the sources in a volume are known, Eq. 2.89 can be used to calculate the acoustic pressure in the volume. The eigenfunctions and frequencies can be obtained analytically for simple geometries, or numerically (e.g. Finite Element Method) for more complex systems. Note that the eigenvalues of Eq. 2.90 are all stable if $\alpha > 0$ (positive damping) thus $\Im\omega < 0$ (the inverse Fourier transform of Eq. 2.90) may then be used [57] to obtain the time domain signal ($p(t)$) from $\hat{p}(\omega)$. Note that this also implies that Eq. 2.90 is causal [57]. The solution is straightforward if the sources do not depend on the acoustic field. Therefore, it is useful to make a distinction between *dependent* and *independent* acoustic sources. An independent source is not affected by the acoustic field and can be considered as an external [2], independent input.

In thermoacoustic systems, a heat-release source term will be present. This source term will generally have a *dependent* and an *independent* part. The independent part of the heat release is caused by turbulent processes that are invariant to acoustic perturbations. The heat release that depends on the acoustic field is the cause of thermoacoustic instabilities. The dependence of the heat release fluctuations on the acoustic field is described by the flame transfer function.

2.6.1 State-Space Representation

In Eq.2.90, the sum over an infinite number of modes is taken. Depending on the frequency range of interest, a limited number of modes is sufficient to represent the system. For N modes, the order of the differential equation Eq.2.90 is $2\,N$. A differential equation of any order can be represented as a system of first order differential equations. These state-space systems, as they are termed, will then have as many dynamic variables (states) as the order of the original system. It will be demonstrated here how a system like Eq.2.90 can be treated as a state space system. Equation. 2.88 can be written in the time domain as:

$$-\ddot{\eta}_n = \alpha\,\dot{\eta}_n + \omega_n^2\,\eta_n + \frac{\psi_n(\mathbf{x_0})}{\Lambda}, \tag{2.91}$$

in which the dot represents a time derivative and the double dot the second time derivative. The equivalent first order system (or state space representation) is given by:

$$\frac{\partial}{\partial t}\begin{bmatrix} \eta_n \\ \dot{\eta}_n \end{bmatrix} = \begin{bmatrix} 0 & 1 \\ -\omega_n^2 & -\alpha_n \end{bmatrix}\begin{bmatrix} \eta_n \\ \dot{\eta}_n \end{bmatrix} + \frac{1}{\Lambda}\begin{bmatrix} 0 \\ -\psi_n(\mathbf{x_0}) \end{bmatrix}, \tag{2.92}$$

or, for modes up to N:

[2] The word external should be interpreted from a systems point of view, it has no geometrical interpretation!

$$\frac{\partial}{\partial t}\begin{bmatrix}\eta_0\\ \dot\eta_0\\ \eta_1\\ \dot\eta_1\\ \vdots\\ \eta_N\\ \dot\eta_N\end{bmatrix} = \begin{bmatrix} 0 & 1 & & & & & & \\ -\omega_0^2 & -\alpha_n & & & & & & \\ & & 0 & 1 & & & & \\ & & -\omega_1^2 & -\alpha_n & & & & \\ & & & & \ddots & & & \\ & & & & & & 0 & 1 \\ & & & & & & -\omega_N^2 & -\alpha_n \end{bmatrix}\begin{bmatrix}\eta_0\\ \dot\eta_0\\ \eta_1\\ \dot\eta_1\\ \vdots\\ \eta_N\\ \dot\eta_N\end{bmatrix} + \frac{1}{\Lambda}\begin{bmatrix}0\\ -\psi_0(\mathbf{x_0})\\ 0\\ -\psi_1(\mathbf{x_0})\\ \vdots\\ 0\\ -\psi_N(\mathbf{x_0})\end{bmatrix}. \tag{2.93}$$

The vector $\vec{\eta} = [\eta_0\, \dot\eta_0 \cdots \eta_N\, \dot\eta_N]^T$ is referred to as the state vector. Using similar notation for the mode functions: $\vec{\psi}(\mathbf{x}) = -[\psi_0(\mathbf{x})\ 0\ \cdots\ \psi_N(\mathbf{x})\, 0]$ and $\vec{\psi}^*(\mathbf{x_s}) = [0\ \frac{\psi_0(\mathbf{x_s})}{\Lambda_0}\ \cdots\ 0\ \frac{\psi_N(\mathbf{x_s})}{\Lambda_N}]$, the Green's function up to mode N can simply be expressed as:

$$\hat{G}(\mathbf{x}|\mathbf{x}_0, t) = \vec{\psi}(\mathbf{x})\,\vec{\eta} \tag{2.94}$$

This equation, together with Eq. 2.93 is the state space representation of the Green's function, it is exactly equal to Eq. 2.89 for $N = \infty$.

This representation of the Green's function will be used to express Eq. 2.90 in state-space. In order to avoid the integrals, the source terms are spatially discretised. The discrete points where the sources are applied are gathered in a vector and are denoted as: $\vec{\mathbf{x}}_s$ for sources on the boundary, and $\vec{\mathbf{x}}_0$ for sources within the volume. Here, only surface integrals will be considered (the volume integrals can be treated in the same manner). The integral in Eq. 2.90 for one mode then reduces to $c^2\,\psi(\vec{\mathbf{x}}_s)\,f(\vec{\mathbf{x}}_s^T)\cdot a_f(\vec{\mathbf{x}}_s^T)$, in which a_f is the area associated with the discrete point. For an exact representation, the vector $\vec{\mathbf{x}}_s$ is of infinite length. For practical applications, a finite length vector will be used. The discretization should then be chosen such that it is small compared to the largest wave length. All modes can now be combined in matrices $\mathbf{\Psi}$, then by making use of Eqs. 2.94 and 2.93, the relation for the acoustic pressure (Eq. 2.90) as a function of sources on the boundary can be written as:

$$\frac{\partial}{\partial t}\vec{\eta}(t) = \mathbf{A}\,\vec{\eta}(t) + c^2\,\mathbf{\Psi}^*(\vec{\mathbf{x}}_s^T)\,f_a(\vec{\mathbf{x}}_s^T, t) \tag{2.95}$$

$$p'(\vec{\mathbf{x}}^T, t) = \mathbf{\Psi}(\vec{\mathbf{x}}^T)\,\vec{\eta}(t), \tag{2.96}$$

in which $f_a = a_f \cdot f$, and $\mathbf{A}$ is the square matrix in Eq. 2.93.

2.7 Area Disconitinuities

In this section, the acoustic relations across a compact area change or discontinuity are derived. Such an element is of special importance because the burner can be regarded (from an acoustic point of view) as an area discontinuity, provided the frequency range of interest is sufficiently low (to ensure compactness). In order to simplify the analysis, incompressibility of the fluid is assumed. In an acoustic network approach, several elements are interconnected. When interconnecting two elements, the area of the two "interconnection surfaces" should be equal. If these areas are not equal, appropriate correction for the area change should be used. In a first approximation, continuity of mass and pressure could be applied. Which, in a linearized approach would yield the static equations: $|| Au' ||_1^2 = 0$ and $|| p' ||_1^2 = 0$. Later, it will be shown that this approximation is valid for very low frequencies. For higher frequencies, the inertia of the fluid in the "area change element" should be taken into account. Writing the momentum equation without external forces as:

$$\frac{\partial \mathbf{u}}{\partial t} = -\mathbf{u} \cdot \nabla \mathbf{u} - \frac{1}{\rho} \nabla p \tag{2.97}$$

Making use of the relation $\mathbf{u} \cdot \nabla \mathbf{u} = \frac{1}{2} \nabla \mathbf{u^2} + \omega \times \mathbf{u}$, the momentum equation is written as:

$$\frac{\partial \mathbf{u}}{\partial t} = -\frac{1}{2} \nabla \mathbf{u^2} - \omega \times \mathbf{u} - \frac{1}{\rho} \nabla p. \tag{2.98}$$

Assuming irrotational flow ($\omega \times \mathbf{u} = 0$) and thus defining the velocity as the gradient of the potential function $\mathbf{u} = \nabla \varphi$, yields:

$$\frac{\partial \nabla \varphi}{\partial t} = -\frac{1}{2} \nabla \mathbf{u^2} - \frac{1}{\rho} \nabla p. \tag{2.99}$$

For incompressible flow, the density is constant, thus integration yields (for the one-dimensional case):

$$\frac{\partial || \varphi ||_1^2}{\partial t} = -\frac{1}{2} || u^2 ||_1^2 - \frac{1}{\rho} || p ||_1^2. \tag{2.100}$$

The potential drop can be written as the integral over the velocity:

$$|| \varphi ||_1^2 = \int_1^2 \nabla \varphi \, dx = \int_1^2 u \, dx \tag{2.101}$$

By substituting the continuity condition ($u(x) = u_1 \frac{A_1}{A(x)}$), an expression for the potential drop is found:

$$|| \varphi ||_1^2 = u_1 \int_1^2 \frac{A_1}{A(x)} \, dx = L_{eq} u_1. \tag{2.102}$$

Here L_{eq} is the *equivalent length*, it is a measure for the amount of mass that is accelerated due to the area change. Linearizing Eq. 2.100 and substituting Eq. 2.102:

$$L_{eq} \frac{\partial u_1'}{\partial t} = -|| \bar{u} u' ||_1^2 - \frac{1}{\bar{\rho}} || p' ||_1^2. \tag{2.103}$$

Or, equivalently:

$$L_{eq}\frac{\partial u_1'}{\partial t} + \bar{u}_1((\frac{A_1}{A_2})^2 - 1)u_1' = -\frac{1}{\bar{\rho}}||\, p'\,||_1^2. \tag{2.104}$$

This equation is valid in one-dimensional, incompressible, isentropic, irrotational flow without external forces, and therefore represents the unsteady compact potential field. Because the acoustic field can be considered the unsteady (velocity) potential field, this equation is suitable to describe smooth, compact area changes. The compactness requirement is fulfilled if the *Helmholtz* number is much smaller than unity: $He = \frac{\omega L}{c} \ll 1$, in which L is a typical length scale associated with the area change. The velocity is the gradient of the potential. Because the gradient may become infinite at discontinuities such as sharp edges, and discontinuities, the velocity may (based on potential theory) become infinite at the discontinuities. In a real fluid, viscosity will always play a significant role if velocity is sufficiently large. Because of viscosity, shear forces near the sharp edges will act on the fluid, resulting in a fluid that is no longer irrotational. Because of this process, part of the acoustic energy will be converted into vorticity. It is very difficult to describe this process in detail. Therefore, a loss coefficient ζ is introduced, such that $||\,\bar{p}\,||_1^2 = \frac{1}{2}\rho\zeta\bar{u}^2$. Thus, a compact area change with viscous loss may be described acoustically as:

$$L_{eq}\frac{\partial u_1'}{\partial t} + \bar{u}_1((\frac{A_1}{A_2})^2 + \zeta - 1)u_1' = -\frac{1}{\bar{\rho}}||\, p'\,||_1^2. \tag{2.105}$$

Note that this relation is entirely described by L_{eq}, ζ, $\frac{A_1}{A_2}$ and the mean flow conditions. It is convenient to introduce the concept of *reduced length*, L_{red}. The reduced length is defined as: $L_{eq} - L_{1,2}$, in which $L_{1,2}$ is the physical distance between position one and two. This expression is very convenient in acoustic network analysis: the area change is then considered a discontinuity in the acoustic field. The reduced length can be considered to represent an amount of mass balancing this discontinuity. For smooth area changes, the reduced length can thus be obtained as: $L_{red} = \int_1^2 \frac{A_1}{A(x)}\,dx - L_{1,2}$. If the area change is not smooth, as is the case for an orifice in a straight tube, this equation may loose validity. Nevertheless, the concept of reduced length may be used. In this case, however, the reduced length could be defined as:

$$L_{red} = \frac{1}{\bar{u}_1}||\,\bar{\varphi}\,||_1^2 - L_{1,2}. \tag{2.106}$$

For practical purposes $\frac{1}{\bar{u}_1}(\bar{\varphi}_2 - \bar{\varphi}_1)$ could be obtained from a (steady-state) calculation of the potential field of the area discontinuity in a straight duct. The location of the axial positions "1" and "2" can be chosen arbitrarily provided these are at a sufficient distance from the discontinuity, in order to ensure a constant potential in the cross section of the duct. The steady-state potential field can be calculated using commercial software packages. It should be noted that for two-dimensional or rotationally symmetric 3-dimensional geometries the potential field is a conformal map of the geometry to the flow field. In this case, analytic methods such as the Schwartz-Christoffel transform or the hodograph method may be used to obtain the steady-state potential field.

2.8 Jump Conditions

Obviously, the area where combustion takes place is of crucial importance in thermoacoustic systems. If this area is small compared to the wavelength, it may be considered a spatial discontinuity, or jump. In this section, the conservation equations across a discontinuity will be derived. First, the static relations will be obtained that describe the mean flow jump condition. In a second step, the acoustic relations across the jump will be obtained. The validity of these equations for the acoustic relations will be demonstrated.
Starting with the equations for continuity, momentum and energy (Eqns. 2.1, 2.2 and 2.3), neglecting time derivatives (static relations), the conservation equations across a discontinuity can be written as:
Continuity

$$\rho_1 (u_1 - S) = \rho_2 (u_2 - S) = \rho_1 S_f \equiv \dot{m} \tag{2.107}$$

In which S_f represent the motion of the discontinuity with respect to the incoming fluid.
Momentum

$$\dot{m} \,||\, u \,||_1^2 + ||\, p \,||_1^2 = 0 \tag{2.108}$$

Energy

$$\dot{m} \,||\, e + \frac{1}{2}u^2 \,||_1^2 + ||\, p\, u \,||_1^2 = Q \tag{2.109}$$

State

$$||\, \frac{\rho\, R T}{p} \,||_1^2 = 0 \tag{2.110}$$

In which $||\cdot||_1^2$ denotes the jump, and $\dot{m}$ is the mass flow seen by a reference frame fixed to the flame front. The flame location is considered to be determined by a balance between flow speed and combustion velocity. Assuming instantaneous combustion of the fuel entering the flame, the heat release in the flame due to the combustion process is given by:

$$Q = \rho_1 S_f y_f h_f, \tag{2.111}$$

In which S_f is the flame speed, y_f the mass fraction of fuel and h_f the specific heat of reaction of the fuel. This representation of the flame as one discontinuity with a closed surface that propagates through the fluid, may not be a very realistic representation of a flame front. Because it is well known that due to auto ignition, recirculation, or turbulent transport, the flame front may not be a closed surface. Nevertheless, the concept of a flame speed may be used. In the case that the flame is not a closed surface at every instant of time, the (equivalent) flame speed is defined as: $S_f = \frac{Q}{\rho_1 y_f h_f}$
In which y_f is the mass fraction of fuel in the mixture, and h_f is the combustion heat per unit mass of fuel. The energy equation can thus be written as:
Energy

$$||\, e + \frac{1}{2}u^2 \,||_1^2 + \frac{1}{\dot{m}} ||\, p\, u \,||_1^2 = y_f h_f \tag{2.112}$$

The flame velocity of a lean premixed natural gas flame is typically two orders of magnitude smaller than the speed of sound. Thus, terms in the equations that depend on the square of

the Mach number will be neglected in this analysis. Note that a similar analysis can be done without the low Mach number assumption [12]. However if the Mach number is included, the resulting equations become very complex, and do not give a good insight to the contribution of the individual quantities. By expressing, $\rho = \frac{\gamma p}{c^2}$ and $e = \frac{p}{\rho(\gamma-1)} = \frac{c^2}{\gamma}\frac{1}{\gamma-1}$ in the conservation equations, it can easily be seen that terms depending on u^2 and on $S\,u$ can be neglected. Now it will be assumed that the velocity of the flame interface is small compared to the mean flow. Thus:

$$\frac{1}{\dot{m}}\,p\,u = \frac{p}{\rho}\frac{u\,(u+s)}{u^2 - S^2} \approx \frac{p}{\rho} + \frac{p}{\rho}\frac{S}{u}. \tag{2.113}$$

Thus, assuming small interface velocity, using the property, $e + \frac{p}{\rho} = c_p\,T$, and neglecting terms of M_a^2 the conservation equations can simply be written as:
Continuity

$$\rho_1\,(u_1 - S) = \rho_2\,(u_2 - S) \tag{2.114}$$

Momentum

$$||\,p\,||_1^2 = 0 \tag{2.115}$$

Energy

$$||\,c_pT\,||_1^2 + S\,||\,\frac{p}{u\,\rho}\,||_1^2 = y_f\,h_f \tag{2.116}$$

Now, small (acoustic) perturbations of the mean flow jump relation will be considered. Each physical quantity $\varphi(t)$ can be represented as the sum of its mean part ($\bar{\varphi}$) and fluctuating part ($\varphi'(t)$). In this analysis, fluctuations of the gas constant (R) and specific heats will be neglected (see [20] for the full analysis). Note that the mean value of the interface velocity (S) equals zero. Then, by linearizing around the mean value, the following relations are found for the fluctuating quantities:
Continuity,

$$\Big|\Big|\,\frac{\rho'}{\bar{\rho}} + \frac{u'}{\bar{u}}\,\Big|\Big|_1^2 = S'\Big|\Big|\,\frac{1}{\bar{u}}\,\Big|\Big|_1^2. \tag{2.117}$$

Momentum,

$$\Big|\Big|\,\frac{p'}{\bar{p}}\,\Big|\Big|_1^2 = 0. \tag{2.118}$$

Energy,

$$||\,c_p\,T'\,||_1^2 + S'\,||\,\frac{\bar{p}}{\bar{\rho}\bar{u}}\,||_1^2 = ||\,c_p\,T'\,||_1^2 = y_f'\,h_f. \tag{2.119}$$

State,

$$\Big|\Big|\,\frac{p'}{\bar{p}} - \frac{\rho'}{\bar{\rho}} - \frac{T'}{\bar{T}}\,\Big|\Big|_1^2 = 0. \tag{2.120}$$

It is remarkable that, although the fluctuations of the flame front are taken into account, this contribution vanishes in the energy equation.
Combining eqns. 2.117, 2.118 and 2.120, the following relation is obtained:

$$\Big|\Big|\,\frac{u'}{\bar{u}}\,\Big|\Big|_1^2 - S'\Big|\Big|\,\frac{1}{\bar{u}}\,\Big|\Big|_1^2 = \Big|\Big|\,\frac{T'}{\bar{T}}\,\Big|\Big|_1^2. \tag{2.121}$$

Using the energy equation and the equation of state, the temperature fluctuations are expressed as:

$$\frac{T_1'}{\bar{T}_1} = \frac{p_1'}{\bar{p}_1} - \frac{\rho_1'}{\bar{\rho}_1} = \frac{\gamma_1 - 1}{\gamma_1}\frac{p_1'}{\bar{p}_1} \tag{2.122}$$

$$\frac{T_2'}{\bar{T}_2} = \frac{y_f'\, h_f}{\bar{T}_2 c_{p_2}} + \frac{c_{p_1}\bar{T}_1}{c_{p_2}\bar{T}_2}\frac{T_1'}{\bar{T}_1} \tag{2.123}$$

$$\tag{2.124}$$

Substituting these expressions for the temperature fluctuations into Eq. 2.121 yields,

$$\left|\left|\frac{u'}{\bar{u}}\right|\right|_1^2 - S'\left|\left|\frac{1}{\bar{u}}\right|\right|_1^2 = \frac{y_f'\, h_f}{T_2 c_{p_2}} + (\frac{c_{p_1}}{c_{p_2}}\frac{T_1}{T_2} - 1)\frac{\gamma_1 - 1}{\gamma_1}\frac{p_1'}{\bar{p}_1} \tag{2.125}$$

The last equation is obtained using the relation $\frac{\rho_1'}{\bar{\rho}_1} = \frac{1}{\gamma_1}\frac{p_1'}{p_1}$, thus assuming that no entropy fluctuations are convected to the flame front from the upstream side. Note that this relation may not be used downstream of the flame, because entropy fluctuations will be present due to flame heat release fluctuations . Finally, by making use of the relation for flame speed fluctuations, $u_1' - S' = S_f'$, and the relation $\frac{R_2}{R_1}\frac{\gamma_1 - 1}{\gamma_1} = \frac{c_{p_2}}{c_{p_1}}\frac{\gamma_2 - 1}{\gamma_2}$, substituting $\bar{u}_2 = \frac{R_2 T_2}{R_1 T_1}\bar{u}_1$ the relation between acoustic velocity, acoustic pressure, heat release fluctuations and flame speed fluctuations yields:

$$u_2' = u_1' + (\frac{R_2 T_2}{R_1 T_1} - 1)S_f' + \bar{u}_1\frac{R_2}{R_1}\frac{h_f}{c_{p_2}T_1}\, y_f' + \frac{\bar{u_1}}{\bar{p}_1}\frac{\gamma_2 - 1}{\gamma_2}\,(1 - \frac{c_{p_2}T_2}{c_{p_1}T_1})\, p_1' \tag{2.126}$$

This result shows that the acoustic velocity jump across the flame front depends on the fluctuations of pressure, mass-fraction, and flame speed.
Very similar equations were derived by B.T. Chu [20]. In his analysis, he starts with the conservation equations for a static (not moving) discontinuity. Later, he allows perturbations of the moving flame front. However, because he starts with:

$$||\, e + \frac{1}{2}u^2\, ||_1^2 = Q_{B.T.Chu}, \tag{2.127}$$

the work performed by the moving discontinuity on the medium is neglected. As shown in the analysis, this is no problem because this term will drop out of the linearized equations for small velocities of the discontinuity. However, it remains to be demonstrated that these relations will also drop out of the non-linear equations for large velocities of the discontinuity as presented in his paper. The heat release $Q_{B.T.Chu}$ is defined as the heat release per unit mass of the medium. Thus, comparing Eq. 2.116 and Eq. 2.127 it is concluded that $Q = S_f\, y_f\, Q_{B.T.Chu}$. Care should be taken not to mix up the different definitions. Thus, these equations may only be used for flames that are stabilized by a balance between burning velocity and medium speed. Moreover, heat release fluctuations that are not caused by fluctuations of composition of the mixture may not be substituted in these equations.

A more convenient expression for Eq. 2.126 can be found by expressing the flame speed fluctuations as: $S'_f = \bar{S}_f \frac{S'_f}{S_f} = \bar{u}_1 \frac{S'_f}{S_f}$ and the influence of mass fraction fluctuations as: $h_f\, y' = (c_{p_2} T_2 - c_{p_1} T_1)\, \frac{h_f\, y'}{h_f\, \bar{y}_f} = (c_{p_2} T_2 - c_{p_1} T_1) \frac{y'}{\bar{y}_f}$. Then, expressing the specific heats in terms of R and γ, the following relation is obtained:

$$\frac{u'_2 - u'_1}{u_1} = \Big(\frac{R_2 T_2}{R_1 T_1} - 1\Big)\frac{S'_f}{\bar{S}_f} + \Big(\frac{R_2 T_2}{R_1 T_1} - \frac{\gamma_1(\gamma_2 - 1)}{\gamma_2(\gamma_1 - 1)}\Big)\frac{y'_f}{\bar{y}_f} + \Big(\frac{\gamma_2 - 1}{\gamma_2} - \frac{\gamma_1 - 1}{\gamma_1}\frac{R_2 T_2}{R_1 T_1}\Big)\frac{p'_1}{\bar{p}_1} \tag{2.128}$$

Thus, this relation together with the momentum equation:

$$p'_2 = p'_1, \tag{2.129}$$

provide the relation between the acoustic quantities on both sides of the flame sheet. As mentioned before, entropy fluctuations will be created by the flame. Because of the flow, these fluctuations will be convected downstream of the discontinuity. The entropy fluctuations are given by: $\frac{s'_2}{c_{p_2}} = \frac{p'_2}{\gamma_2\, p_2} - \frac{\rho'_2}{\rho_2}$. This can be rewritten as:

$$s'_2 = (R_1 \frac{T_1}{T_2} - R_2)\frac{p'_1}{p_1} + \frac{h_f\, y'_f}{T_2}. \tag{2.130}$$

Note that for equimolar combustion (for example combustion of methane) the ratio of gas constants $\frac{R_2}{R_1} = 1$. To close the relations, the mass fraction fluctuations and the flame speed fluctuations have to be related to pressure and velocity fluctuations which will be done in § 4.

2.9 Discussion

In this chapter, relevant acoustic theory has been discussed that provides the basis of the theory in the subsequent chapters. In this work, the thermoacoustic behavior of gas turbine combustion systems is modeled as a network of acoustic elements. By doing so, simplifying assumptions can be made for each of the sub-systems in the network where appropriate. The acoustic wave equation has been derived, and the underlying assumptions are revealed. Heat release fluctuations have been introduced in a second step. The influence of the mean flow on wave propagation has been included via a coordinate transform of the wave equation (in absence of mean flow). This convective wave equation has been used to obtain expressions for wave propagation in annular ducts with mean flow. These relations will prove to be useful when modeling wave propagation in combustion chambers. An energy balance of an acoustic system including heat release, but in absence of mean flow, has been derived. Such an energy balance is very useful because it provides better insight into the dynamic behavior of thermoacoustic systems. In fact, the Rayleigh instability criterium for thermoacoustic systems is directly related to this energy balance. Green's functions can be considered as impulse responses in space and time. It has been demonstrated how Green's functions can be used in combination with a modal expansion to obtain transfer function representations of arbitrary geometries. Making use of the causality of the Green's functions, these equations will be used later in order to obtain state-space representations of acoustic systems. A simplified representation of the burner can be obtained if the acoustic wave length is large compared to the geometrical extent of the burner. The burner can then simply be treated as an area discontinuity. The relations for an area discontinuity have been derived, and approaches to obtain a representation of a burner for practical systems have been discussed. Similary, if the combustion zone is compact, the acoustic relations for the combustion process reduce to a jump condition across the flame. Relations for a moving discontinuity in a reactive medium have been derived. A low Mach number is assumed in the combustion region, which results in continuity of pressure across the flame sheet. It is concluded that the influence of periodic heat addition mainly affects the jump relation of acoustic velocities. In subsequent chapters, closure relations for the flame model will be derived.

Chapter 3

Experimental techniques

3.1 Introduction

Because of a complex interaction between several physical processes, the thermoacoustic dynamics of a swirl stabilized flame can be very difficult to model accurately. Experimentally obtained transfer matrices are crucial to validate acoustic flame models. Besides validation, the measured transfer functions can give more physical insight to the interactions occurring in the flame. A measured transfer function may also be used directly in an acoustic network, treating the flame element as a "black box".

A technique has been developed at ABB Corporate Research [90, 91, 95], to determine frequency responses of flame transfer matrices experimentally. This technique consists of exciting the flow upstream and downstream of an "acoustic element" by loudspeakers. In this case the "acoustic element" would be a burner with flame. However, because of the black box approach, any acoustic element could be measured, provided one dimensional wave propagation can be assumed at inlet and exit. The response to this excitation is then measured using arrays of microphones. Because it is known from the wave equation how acoustic waves propagate through a straight tube, acoustic pressure and velocity just upstream and just downstream of the acoustic element can be calculated from the measured microphone data. This technique is termed the *Multi Microphone Method*.

The transfer matrix linearly relates the acoustic pressure and velocity on both sides of the acoustic element. The frequency response of the transfer matrix is then obtained from the measured acoustic pressures and velocities by solving a system of four equations with four unknowns. Because one test provides only two equations, two independent test states are required to obtain the matrix coefficients. Two independent test states can be obtained by changing the acoustic boundary conditions, or by consecutively forcing upstream and downstream of the acoustic element.

The idea of experimentally determining the coefficients of an acoustic system represented as a black box with two inputs, two outputs and two source terms dates back to the nineteen seventies. Cremer [24] (1970) realized that the two port (four pole) representation of systems as used in communication theory applies equally well to acoustic systems. Acoustic and electrical

network systems can be represented in an analogous way if the electrical voltage (current) is replaced by acoustic pressure (velocity). Explained in his paper is how transfer matrix elements and source terms of a fan can be determined from multiple acoustic measurements using different acoustic boundary conditions. The two microphone method, used to separate the acoustic field in a reflected and incident wave was introduced by Seybert and Ross [123]. In their paper the influence of mean flow on the acoustic propagation was taken into account. A similar method has been presented by Chung and Blaser in 1980 [22]. The transfer matrix measurement technique was then developed using the transient techniques described by To and Doige in 1979 [129]. A good explanation of theory and practice of different transfer function measurement techniques is given in the papers of Bodén, Lavrentjev and Åbom [69, 68, 16, 1]. An error analysis of the two microphone method and the transfer matrix estimate is given in [16]. Very useful is the discussion on the linear independence of the test states as presented in [1].
The idea of using this method to obtain acoustic transfer matrices of combustion processes originates from Paschereit and Polifke [90, 91, 95]. Obviously this technique is much more difficult in presence of combustion than cold flow. The first results suffered from unacceptable levels of measurement errors, and poor reproducibility of the results. Moreover, the experiments where very time consuming. During the course of the work presented here, the technique has been improved. Better cross-correlation techniques are used, leading to better accuracy and shorter measurement times. The process of forcing the system, data acquisition and data processing has been fully automated: all signals are generated, acquired and processed by a program written in *LabView*. The program makes an automatic check of consistency of the measured data and allows visualization of the accuracy. The method has been tested thoroughly, repeatability of the experiment has been checked, and the assumption of linearity of the transfer function has been validated. The independence of the obtained transfer matrix to the acoustic boundaries is demonstrated, an error analysis and sensitivity study have been made and are reported here. The technique has then been used successfully to measure more than a hundred transfer matrices of several types of burners at different operating conditions.

3.2 Test Facility

The combustion facility is shown in Figure 3.1. The atmospheric test rig consists of a plenum chamber upstream of the swirl-inducing burner and a combustion chamber downstream of the burner. The plenum chamber contains perforated plates to reduce the turbulence level of the flow. The circular combustion chamber consists of an air cooled double wall quartz glass tube to provide full visual access to the flame. The exhaust system is an air cooled tube with the same cross-section as the combustion chamber to avoid acoustic reflections at area discontinuities. The length of the exhaust tube is adjustable from $x/D = 6.4$ to $x/D = 14.3$. The acoustic boundary conditions of the exhaust system could be adjusted from almost anechoic (reflection coefficient $|r| < 0.15$) to open end reflection. All the experiments have been performed on a swirl-stabilised premix burner. Natural gas was injected upstream of the swirling air to premix the fuel with the air. The flame was stabilized in a recirculation region near the burner outlet. Controlled excitation of the burner flow was accomplished by a circumferential array of four loudspeakers

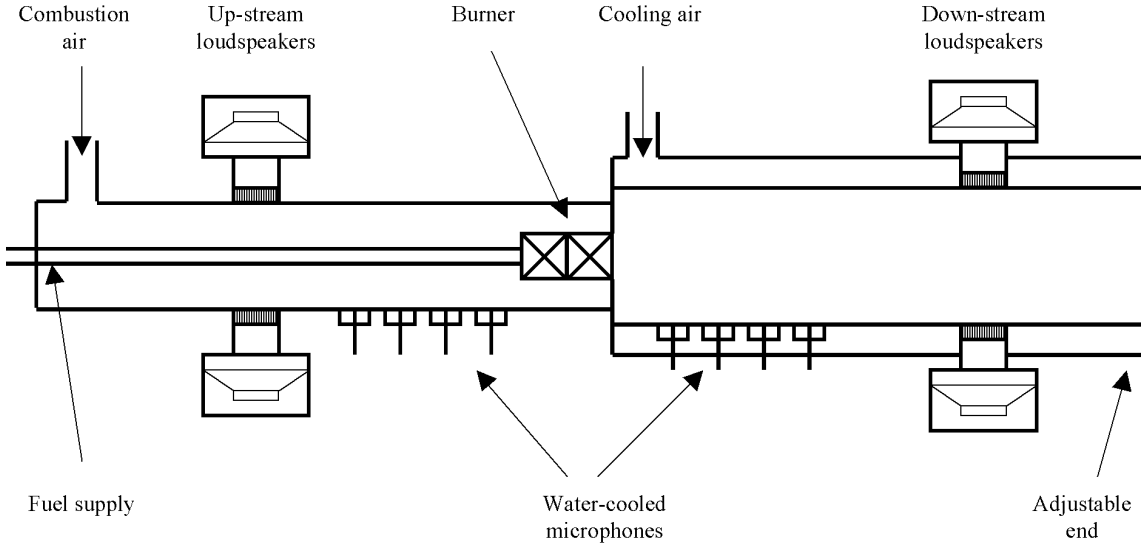

Figure 3.1: The atmospheric combustion test facility, equipped with loudspeakers and water-cooled microphones for acoustic measurement.

equally spaced in polar angle. One set of loudspeakers was placed at a distance of $x/D = 4.2$ upstream of the dump plane and the second set at $x/D = 6.85$ downstream of the dump plane. Pressure fluctuations were measured using water-cooled 1/4" condenser microphones. A detailed explanation and analysis of the properties of the burner used in this work is given in [94]

3.3 Signal Processing

A transfer function relates the output of a system to its input. In this work the term "transfer function" is often used to indicate the frequency response of a transfer function, this is not entirely correct but it will generally be clear from the context what is meant. A linear Single Input Single Output (SISO), system is described in the frequency domain by: $H(s)$ in which the Laplace coefficient $s \equiv i\,\omega + \alpha$ can be considered as a complex frequency. It can be proven that an arbitrary system H is entirely described by either the impulse response $h(t)$ or by the frequency response $H(i\omega)$, provided that the system is linear, time-invariant, and stable [57]. This can be seen from the following relation:

$$H(i\omega + 0) \overset{\mathcal{L}^{-1}_{\alpha=0}}{\Longleftrightarrow} h(t) \overset{\mathcal{L}_{\alpha=\alpha_k}}{\Longleftrightarrow} H(i\omega + \alpha_k), \tag{3.1}$$

for $\alpha_k > 0$. Here, $\mathcal{L}_\alpha$ is the Laplace transform evaluated at α. Thus, even if the transfer function H of a system is only known as a function ω then the dependence of α can be obtained from Eq. 3.1. Consequently, a system can be entirely identified by its steady-state frequency response, provided it is linear, stable and time invariant. Thermoacoustic systems do not necessarily fulfill

these requirements. For small amplitudes the system might be considered linear. However, if the linear system is unstable, amplitudes will grow exponentially until some non-linear effect limits its growth. Under these conditions the system may not be analyzed by a single frequency response.
The transfer function of a system can be obtained experimentally by applying a forcing signal to the input of the system and measuring the response of the system.

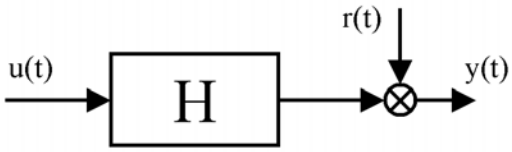

Figure 3.2: System H with forcing signal u at input and noise addition r at output y.

In the absence of external disturbances ($r(t) = 0$ in Fig. 3.2), the ratio of the Fourier transforms of the output and input signal is an estimate of the systems transfer function:

$$\hat{H}(\omega) = \frac{\mathcal{F}\{y(t)\}}{\mathcal{F}\{u(t)\}} \tag{3.2}$$

Generally, experimental data will contain noise, which may lead to substantial error. To reduce these errors the transfer function may be estimated by [131]:

$$\hat{H}(\omega) = \frac{S_{\overline{uy}}}{S_{\overline{uu}}} \tag{3.3}$$

In which $S_{\overline{uy}}$ denotes the "cross spectral density estimate" between signals x and y. The "cross spectral density estimate" is the Fourier transform of the cross correlation vector of the two signals. It can be calculated using for example, Welch's algorithm [59].
In this work a slightly different method is devised. It is more efficient in removing noise contributions since it uses a known, deterministic forcing signal. The method is termed "Pure Tone Method". It consists of exciting the system with a pure sinusoidal signal and calculating the Fourier transform of the input and output signal *exactly* at the forcing frequency. The transfer function can then be estimated using Eq.3.2 the estimation error will decrease with the square root of the number of samples, as will be shown below.

3.3.1 Pure Tone Method

Consider a sinusoidal signal $x(t) = A\cos(\omega t + \phi)$, corrupted by a noisy, stochastic signal $r(t)$ with mean value $\mu_r = 0$ and standard deviation σ_r the resulting signal $y(t)$ is the sum of both contributions:

$$y(t) = A\ \cos(\omega_k\ t) + r(t). \tag{3.4}$$

The aim is to estimate the amplitude (A) and phase (ϕ) of the signal ($x(t)$) from sampled data of y(t).With a sampling interval of T, the samples $y(nT)$ are defined by:

$$y(nT) = A\ cos(\omega_k\ n\ T + \phi) + r(n\ T) \tag{3.5}$$

A discrete Fourier transform of the signal at frequency ω_k will also consist of a deterministic part and a stochastic part. The expected value of the estimation error of A due to the disturbance is $E\{|\hat{r}(\omega_k)|\}$, in which $E\{\ \}$ denotes the expectation of the quantity. The discrete Fourier transform of the signal is given by:

$$\hat{y}(\omega_k) = \frac{2}{N}\sum_{n=1}^{N} y(n\ T)\ e^{i\omega_k n\ T} \tag{3.6}$$

$$= \hat{A} + \frac{2}{N}\sum_{n=1}^{N} r(n\ T)\ e^{i\omega_k n\ T}. \tag{3.7}$$

If $r(t)$ has a normal distribution, then by making use of the linear properties of the expectation operator it is found that:

$$E\{|\hat{r}(\omega_k)|^2\} = \frac{4}{N^2}E\{\sum_{n=1}^{N} r^2(n)\ e^{i2\omega_k dt\ n}\} = \frac{4}{N}\sigma_r^2. \tag{3.8}$$

Use has been made of the property $E\{\sum_{n=1}^{N} x(n)\} = N\sigma_x^2$. Equation 3.8 shows that the error due to the disturbance can be made arbitrarily small if a sufficiently large number of samples (N) is taken. Care has to be taken that the frequency at which the Fourier transform is performed corresponds to the frequency of the sinusoid. The difference between the frequency used for the Fourier transform and the sinusoidal frequency should be well below the value of $\frac{2\pi}{Ndt}$. Thus large values of N could lead to considerable error in case of a frequency mismatch. However, if the forcing sinusoid will be generated on a digital data acquisition board, and the data processing is performed digitally, the frequency is a discrete quantity and a mismatch is avoided. The value of N can therefore be maximized in order to obtain good noise reduction.

3.3.2 Transfer Function Measurement

The response of a linear system to a deterministic sinusoidal input signal will also be deterministic. Introducing the notation $\hat{y}_u(\omega_k)$ for the Fourier transform (Eq. 3.6) of a signal ($y(t)$) evaluated *exactly* at frequency ω_k of a deterministic, sinusoidal signal ($u(t)$), then an estimate of the transfer function of H in Fig. 3.2 is given by:

$$H(\omega_n) = \frac{\hat{y}_u(\omega_k)}{\hat{u}_u(\omega_k)} \tag{3.9}$$

Figure 3.3: Estimate of the amplitude at the forcing signal as a function of the number of samples, calculated with Welch's method and by the Pure Tone method.

Figure 3.4: The variance of the measurement data versus number of samples N.

The error in the estimate of H due to noise contributions will also decrease with the square root of the number of samples. In Fig. 3.3 a comparison is made between Welch's method and the Pure Tone method. The amplitude of the deterministic component of a signal is determined from Welch's method by calculating $\frac{S_{\overline{xy}}}{\sqrt{S_{\overline{xx}}}}$ and from the Pure Tone method, $\hat{y}_u(\omega_k)$. The test signal used was a microphone signal placed in the combustion chamber of the combustion test facility. The forcing was applied by a loudspeaker placed in the air supply. Figure 3.3 makes clear that both methods converge to the same value for a high number of samples, however, the Pure Tone method converges much faster. An additional advantage of the pure tone method is that it is computationally more efficient.

The variance of the measurement data is shown in Fig. 3.4. For numbers of samples larger than 70000, the variance remained below unity. The estimated value of the amplitude has an average

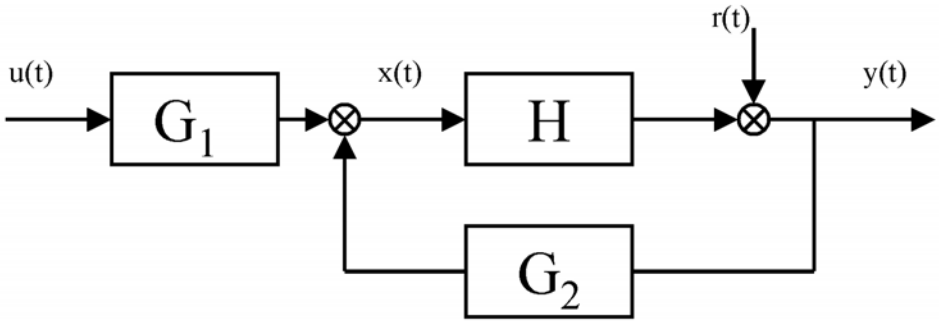

Figure 3.5: Block diagram of H contained in a feedback loop. The transfer functions G_1 and G_2 describe the (unknown) dynamics of the actuator and the feedback system.

of 126.17 (arbitrary units). Thus the measurement error is approximately: 0.8%.
The estimation of a transfer function (H) using the Pure Tone Method can also be used when H is placed in a feedback loop as shown in Fig. 3.5. The measured signals $\hat{y}$ and $\hat{x}$ are given by:

$$\hat{y} = \frac{HG_1}{1-HG_2}\hat{u} + \frac{1}{1-HG_2}\hat{r} \tag{3.10}$$

$$\hat{x} = \frac{G_1}{1-HG_2}\hat{u} + \frac{G_2}{1-HG_2}\hat{r}. \tag{3.11}$$

By applying the Pure Tone Method, the stochastic contribution will vanish for sufficiently long sampling time and the transfer function can thus be estimated from the measured signals x and y.

$$H(\omega) = \frac{\hat{y}_u}{\hat{x}_u} = \frac{\frac{HG_1}{1-HG_2}\hat{u}}{\frac{G_1}{1-HG_2}\hat{u}}. \tag{3.12}$$

Once H is identified, an estimate of the spectrum of the noise contribution (r) can be obtained. An additional set of data is then required, in which no forcing has been applied. All the measured signals are then responses to the noise source in the feedback loop. The spectrum of the noise input is thus recovered by:

$$\hat{y}_{x,nf} - H\hat{x}_{x,nf} = \frac{1}{1-HG_2}\hat{r} - H\frac{G_2}{1-HG_2}\hat{r} = \hat{r} \tag{3.13}$$

In which the notation $\hat{y}_{x,nf} = \frac{S_{xy}}{\sqrt{S_{xx}}}$ is used. Because of this definition, $\hat{y}_{x,nf}$ has the absolute value of $\hat{y}$ and its phase is equal to the phase difference between $\hat{x}$ and $\hat{y}$. This is merely a matter of definition: since $\hat{r}$ is a stochastic quantity, its phase does not carry information in a statistical sense.

3.4 Acoustic Transfer Matrix Measurement

The method described in the previous section deals with determining a one dimensional transfer function (MIMO) from experimental data. Because the one dimensional acoustic field is de-

scribed by two state variables (acoustic pressure and acoustic velocity), the acoustic elements are generally described by a 2x2 transfer *matrix*. The acoustic field can be described by two state variables because isentropicity is assumed. However, as mentioned in § 2.8, the isentropicity assumption is generally not valid in the flow downstream of the flame. Because of acoustic fluctuations in the heat release rate, entropy fluctuations will be present. The acoustic state should thus be described by acoustic pressure, velocity and entropy. The entropy fluctuations convect with mean flow and will, because of diffusion, generally only be important for very low frequencies. They are assumed to be negligeable in the frequency range of interest.
Transfer matrices can be determined using essentially the same method as described in the previous section, which will be demonstrated in this section.
The aim is to experimentally determine the four elements of a transfer matrix (T) defined by:

$$\begin{bmatrix} \hat{p}_d \\ \hat{u}_d \end{bmatrix} = \begin{bmatrix} T_{11} & T_{12} \\ T_{21} & T_{22} \end{bmatrix} \begin{bmatrix} \hat{p}_u \\ \hat{u}_u \end{bmatrix}. \tag{3.14}$$

The subscripts d and u denote quantities on the downstream and upstream side of the burner. Note that the elements of T depend on frequency and have complex values. If the acoustic pressure and velocity, $\hat{p}$ and $\hat{u}$, on both sides of the burner are obtained experimentally, then the four elements of T can be extracted in a similar manner as described in the previous section. However, two problems arise now:

- Equation 3.14 has four unknown elements in two equations: the system is underdetermined. Thus, T can not be obtained from one set of measurement data. Therefore, two linearly independent sets of measurement data are required to solve for T.
- It is practically very difficult to measure acoustic velocity, especially in harsh environments. To overcome this problem, a method is used to obtain the acoustic velocity from 2 or more axially spaced microphones. This method is called Two Microphone Method or Multi Microphone Method.

3.4.1 Multi Microphone Method

The Two Microphone Method (TMM) and Multi Microphone Method (MMM) are methods to obtain the acoustic pressure and velocity in any position of a straight duct from pressure measurements at multiple locations in that duct. Both methods are essentially the same, the difference is that the MMM uses more than two pressure transducers and gives more accurate results in the presence of measurement uncertainty. The acoustic pressure at two axial positions (1 and 2) in a straight duct with uniform and constant cross-section, speed of sound [1] and mean velocity are related to the Riemann invariants f and g at a certain reference position by combining Eqns. 2.34 and 2.36:

$$\begin{bmatrix} \hat{p}_1 \\ \hat{p}_2 \end{bmatrix} = \begin{bmatrix} e^{-i\omega\frac{x_1}{c+u}} & e^{i\omega\frac{x_1}{c-u}} \\ e^{-i\omega\frac{x_2}{c+u}} & e^{i\omega\frac{x_2}{c-u}} \end{bmatrix} \begin{bmatrix} \hat{f} \\ \hat{g} \end{bmatrix}. \tag{3.15}$$

[1] thus neglecting entropy waves.

In which x_1 and x_2 are the axial distances from the microphone to the reference position. The Riemann invariants are thus obtained by:

$$\begin{bmatrix} \hat{f} \\ \hat{g} \end{bmatrix} = \begin{bmatrix} e^{-i\omega\frac{x_1}{c+u}} & e^{i\omega\frac{x_1}{c-u}} \\ e^{-i\omega\frac{x_2}{c+u}} & e^{i\omega\frac{x_2}{c-u}} \end{bmatrix}^{-1} \begin{bmatrix} \hat{p}_1 \\ \hat{p}_2 \end{bmatrix}. \tag{3.16}$$

The acoustic pressure and velocity at the reference position are then obtained by $\hat{p} = \hat{f} + \hat{g}$ and by $\hat{u} = \hat{f} - \hat{g}$. From now on the reference position will be called the "burner location" as this fits better with the subsequent chapter. In the case of N microphones, Eq. 3.16 can be written as:

$$\begin{bmatrix} \hat{p}_1 \\ \vdots \\ \hat{p}_N \end{bmatrix} = \begin{bmatrix} z_1^{\frac{1}{1+M}} & z_1^{\frac{-1}{1-M}} \\ \vdots & \vdots \\ z_N^{\frac{1}{1+M}} & z_N^{\frac{-1}{1-M}} \end{bmatrix} \begin{bmatrix} \hat{f} \\ \hat{g} \end{bmatrix}, \tag{3.17}$$

In which the following notation is used: $z \equiv e^{-i\frac{\omega L}{c}}$ and $z_n \equiv e^{-i\frac{\omega x_n}{c}} = e^{-i\frac{\omega L}{c}\frac{x_n}{L}} = z^{\frac{x_n}{L}}$, in which L is an arbitrary length, introduced to make the exponent non-dimensional.
The system is over-determined now, and the method of least squares can be used to solve the system for f and g:

$$\begin{bmatrix} \hat{f} \\ \hat{g} \end{bmatrix} = \begin{bmatrix} N & \sum_{n=1}^{N} z_n^{\frac{-2}{1-M^2}} \\ \sum_{n=1}^{N} z_n^{\frac{-2}{1-M^2}} & \sum_{n=1}^{N} z_n^{\frac{-4}{1-M^2}} \end{bmatrix}^{-1} \begin{bmatrix} z_1^{\frac{-1}{1+M}} & \cdots & z_N^{\frac{-1}{1+M}} \\ z_1^{\frac{2}{(1+M)(1-M^2)}} & \cdots & z_N^{\frac{2}{(1+M)(1-M^2)}} \end{bmatrix} \begin{bmatrix} \hat{p}_1 \\ \vdots \\ \hat{p}_N \end{bmatrix} \tag{3.18}$$

For ease of notation, the matrix in Eq. 3.17 is denoted as Z, the product of the two matrices in Eq. 3.18 is then written as $Z^{\dagger}$, since this product can be considered as the inverse of Z in the least squares sense (pseudo inverse).
The error in the estimates of f and g will mainly have two contributions. The first contribution is because of noise contributions in the pressure signals σ_p. The second is due to errors in Z. An error in Z depends on errors in the speed of sound, the microphone positions and the Mach number. In addition Z should be applicable (frequency below cut off, no damping, uniform cross sectional area, uniform mean flow, uniform temperature). The first error contribution can be estimated from the variance of the least squares method [106], in this application it is found to be :

$$\sigma_f^2 = \sigma_g^2 = \frac{N}{N^2 - |\sum_{n=1}^{N} z_n^{\frac{1}{1-M^2}}|^2} \sigma_{p_n}^2 \tag{3.19}$$

As expected, the error in f will decease with an increasing number of microphones N. Generally, the Mach number will be small and can be considered zero in this analysis. Equation 3.19 has a singularity if all microphones are spaced at distances $\Delta\, x = m\; c/\omega$, in which m is an integer number. Thus if all the distances between the microphones are multiples of half the wavelength, the error in f will become infinite. Generally a range of frequencies is measured, and thus a

range of wavelengths is covered. When using the Two Microphone Method (N=2) there will always be a frequency at which the distance between the microphones corresponds to half a wavelength. Thus there will always be a frequency at which the error becomes infinitely large. In the Multi Microphone Method this problem is avoided provided that the microphones are not equally spaced. On the other hand, Eq. 3.19 is minimized if the spacing of the microphones is $\Delta\ x = \frac{c}{N\omega}$, thus an equal spacing is not necessarily bad. Equation 3.19 does not only give an error estimate for a given microphone placement, it can also be used to choose an optimal placement prior to the test. The aim is then to minimize Eq. 3.19 for a certain frequency range of interest by adjusting x_n.

3.4.2 Transfer Matrix Determination

As mentioned in the introduction, two independent sets of measurement data are required to extract the transfer matrix from experimental data. One set of data can be obtained by measuring the response to an excitation by an upstream loudspeaker (test state A). The other test is then created by using downstream excitation (test state B). The Fourier transformed microphone signals from two experiments (A and B) with N_u microphones upstream and N_d microphones downstream is grouped in the following two matrices:

$$P_u = \begin{bmatrix} \hat{p}^A_{u,1} & \hat{p}^B_{u,1} \\ \vdots & \vdots \\ \hat{p}^A_{u,N_u} & \hat{p}^B_{u,N_u} \end{bmatrix} \qquad P_d = \begin{bmatrix} \hat{p}^A_{d,1} & \hat{p}^B_{d,1} \\ \vdots & \vdots \\ \hat{p}^A_{d,N_d} & \hat{p}^B_{d,N_d} \end{bmatrix} \tag{3.20}$$

In which superscripts A and B refer to the test state, and subscripts u and d refer to data obtained from microphones place upstream or downstream from the element. Note that all quantities depend on frequency, thus for each frequency measured (for each spectral line), two matrices of data P_u and P_d are obtained. The Multi Microphone Method can now be applied to these matrices to obtain the Riemann invariants:

$$\begin{bmatrix} \hat{f}^A_u & \hat{f}^B_u \\ \hat{g}^A_u & \hat{g}^B_u \end{bmatrix} = Z^{\dagger}_u\ P_u, \tag{3.21}$$

and similarly to obtain the downstream Riemann invariants. The acoustic pressure and velocity at the burner location will then be calculated using Eq. 2.34:

$$\begin{bmatrix} \hat{p}^A_u & \hat{p}^B_u \\ \hat{u}^A_u & \hat{u}^B_u \end{bmatrix} = \begin{bmatrix} 1 & 1 \\ 1 & -1 \end{bmatrix} \begin{bmatrix} \hat{f}^A_u & \hat{f}^B_u \\ \hat{g}^A_u & \hat{g}^B_u \end{bmatrix} \tag{3.22}$$

The error in the estimates of $\hat{p}$ and $\hat{u}$ is found to be: $\sigma^2_p = \sigma^2_u = 2\sigma^2_f$. And, finally, the transfer matrix is obtained:

$$\begin{bmatrix} T_{11} & T_{12} \\ T_{21} & T_{22} \end{bmatrix} = \begin{bmatrix} \hat{p}^A_d & \hat{p}^B_d \\ \hat{u}^A_d & \hat{u}^B_d \end{bmatrix} \begin{bmatrix} \hat{p}^A_u & \hat{p}^B_u \\ \hat{u}^A_u & \hat{u}^B_u \end{bmatrix}^{-1}. \tag{3.23}$$

Obviously, the inverse in Eq. 3.23 should exist in order to determine the transfer matrix. The inverse of a matrix exists if the matrix has maximum possible rank, or equivalently, if its determinant does not equal zero. In order to have maximum possible rank, the vectors

$$\begin{bmatrix} \hat{p}_u^A \\ \hat{u}_u^A \end{bmatrix} \qquad \text{and} \qquad \begin{bmatrix} \hat{p}_u^B \\ \hat{u}_u^B \end{bmatrix} \tag{3.24}$$

should be linearly independent. Which corresponds to the aforementioned requirement that two linearly independent test states are needed to obtain the transfer matrix. The two vectors are independent if:

$$\frac{\hat{p}_u^A}{\hat{u}_u^A} \neq \frac{\hat{p}_u^B}{\hat{u}_u^B}. \tag{3.25}$$

Generally, everything upstream of the burner can be described by an impedance (Z_u)and a source (u_s):

$$\hat{p}_u = Z_u \hat{u}_u + \hat{u}_s. \tag{3.26}$$

The source corresponds to the influence of the loudspeaker. In test state B, the upstream loudspeaker is off, so $u_s^B = 0$, and $\hat{p}_u^B = Z_u \hat{u}_u^B$. In test state A, the upstream loudspeaker is on, thus: $\hat{p}_u^A = Z_u \hat{u}_u^A + \hat{u}_s^A$. Clearly these two test states are linearly independent because:

$$Z_u \neq Z_u + \frac{\hat{u}_s^A}{\hat{u}_u^A} \tag{3.27}$$

for finite values of the impedance Z_u and $\hat{u}_u^A$.
A norm bounded error (e) in $\hat{p}$ and $\hat{u}$ will result in a norm bounded error (t) in T. The norm of t will fulfill the following inequality:

$$\|t\| \leq \|e\| \left(1 + \left\| \begin{array}{cc} T_{11} & T_{12} \\ T_{21} & T_{22} \end{array} \right\| \right) \left\| \begin{bmatrix} \hat{p}_u^A & \hat{p}_u^B \\ \hat{u}_u^A & \hat{u}_u^B \end{bmatrix}^{-1} \right\| \tag{3.28}$$

Thus, the issue of sensitivity to measurement errors is clearly related to the linear independence of the test states. The *transfer matrix* relates the acoustic pressure and velocity on both sides of an element. The relation between the Riemann invariants is given by the *scattering matrix*:

$$\begin{bmatrix} \hat{f}_d \\ \hat{g}_u \end{bmatrix} = \begin{bmatrix} S_{11} & S_{12} \\ S_{21} & S_{22} \end{bmatrix} \begin{bmatrix} \hat{f}_u \\ \hat{g}_d \end{bmatrix}. \tag{3.29}$$

The conversion between transfer matrix and scattering matrix can be done in a straightforward manner.

3.4.3 Source Term Measurement

Not all acoustic elements are passive, i.e, some elements may contain an independent source of sound. In a turbulent flame this source is due to non-steady disturbances of the flow and heat release that propagates into the acoustic far-field. If these disturbances are of turbulent nature, only a small fraction of the energy contained in this field will reach the acoustic far-field. From Eq. 2.90 can be seen that the sources enter the wave equation via the following integral:

$$Source = \int\int\int_V \psi_n(\mathbf{x}_0)\hat{h}(\mathbf{x}_0)dV + \oint_S \psi(\mathbf{x}_s)\hat{f}(\mathbf{x_s})dS. \tag{3.30}$$

If the flame region is small compared to wave length (compactness) then ψ may be considered constant in the flame region. Thus, for compact flames the far field source term is the spatial average of the sources $\hat{h}(\mathbf{x})$. The volume source term ($\hat{h}(\mathbf{x})$) is caused by the non-steady flow and non-steady heat release. Generally these processes can be considered as a superposition of a part that is influenced by the acoustic field and a part that is not influenced by the acoustic field: $\hat{h}(\mathbf{x}) = \hat{h}_d(\mathbf{x}) + \hat{h_i}(\mathbf{x})$. Here the subscript i and d refer to independent and dependent sources respectively. The measured transfer matrix relates the acoustic quantities across the flame in a linear way. All *linearly dependent* sources are absorbed in the transfer function, the *linearly independent* sources that propagate to the far field will be termed *source terms* [2].
The following definition of the source term will be used here: the source term contains all sound produced in the flame region that contributes to the acoustic far-field, but is not affected by the acoustic field itself. The pressure fluctuations in the flame region that do not propagate with speed of sound to the far-field are termed *pseudo sound* [25].
A measure of linear dependence between two signals is the coherence. The source terms as it has been defined previously is often referred to as the *coherent source*. This refers to the fact that the source term has strong spatial coherence (as opposed to the pseudo-sound source).
An additional measurement is required for experimental determination of the source term . The required test-state is obtained by applying no forcing to the loudspeakers. The measured response is thus the response to the source term. The source term can be obtained by making use of the previously measured scattering matrix:

$$\begin{bmatrix} \hat{f}_s \\ \hat{g}_s \end{bmatrix} = \begin{bmatrix} \hat{f}_d \\ \hat{g}_u \end{bmatrix} - \begin{bmatrix} S_{11} & S_{12} \\ S_{21} & S_{22} \end{bmatrix} \begin{bmatrix} \hat{f}_u \\ \hat{g}_d \end{bmatrix}. \tag{3.31}$$

Note the similarity between this expression and Eq. 3.13.

3.4.4 Flame Transfer Matrix

In order to measure a transfer matrix, arrays of microphones have to be placed at both sides of the element. Since a flame is always stabilized by some kind of flame holder (the "burner") it is not possible to measure a flame transfer matrix directly. However, the transfer matrix of the combined burner and flame element (T) can be measured, and also the transfer matrix of

[2] The consequence of this definition is that if the transfer function is not linear, the non-linear processes will contribute to the source term.

the burner only (in absence of combustion) can be measured (B). The desired flame transfer function (F) can then easily be obtained by:

$$F = TB^{-1} \tag{3.32}$$

The underlying assumption is that the transfer matrix (B) does not change due to the combustion process. This is a very dangerous assumption, but this will be validated in the next section.

3.5 Experimental Results

3.5.1 Burner Transfer Function Without Combustion

The transfer function of the burner without combustion has been measured for a range of operating conditions. As mentioned in section 2.7, the burner can be represented as a simple area discontinuity with mean flow. The burner transfer matrix (without combustion) can then be expressed as a function of the reduced length (L_{red}), a loss coefficient (ζ_b), cross sectional area before, in and after the burner (A_u, A_b and A_d), Mach number in the burner (M_b) and angular frequency (ω), similar as in Eq. 2.104:

$$\begin{bmatrix} \hat{p}_d \\ \hat{u}_d \end{bmatrix} = \begin{bmatrix} 1 & M_b \frac{A_b}{A_u}\{1 - \zeta_b(\frac{A_u}{A_b})^2 - (\frac{A_u}{A_d})^2\} - i\frac{\omega}{c} L_{red} \frac{A_b}{A_u} \\ 0 & \frac{A_u}{A_d} \end{bmatrix} \begin{bmatrix} \hat{p}_u \\ \hat{u}_u \end{bmatrix}. \tag{3.33}$$

Note that $\hat{p}_d$ and $\hat{p}_u$ are the acoustic pressures scaled by the characteristic impedance (ρc), thus the unit of these quantities is meters per second.

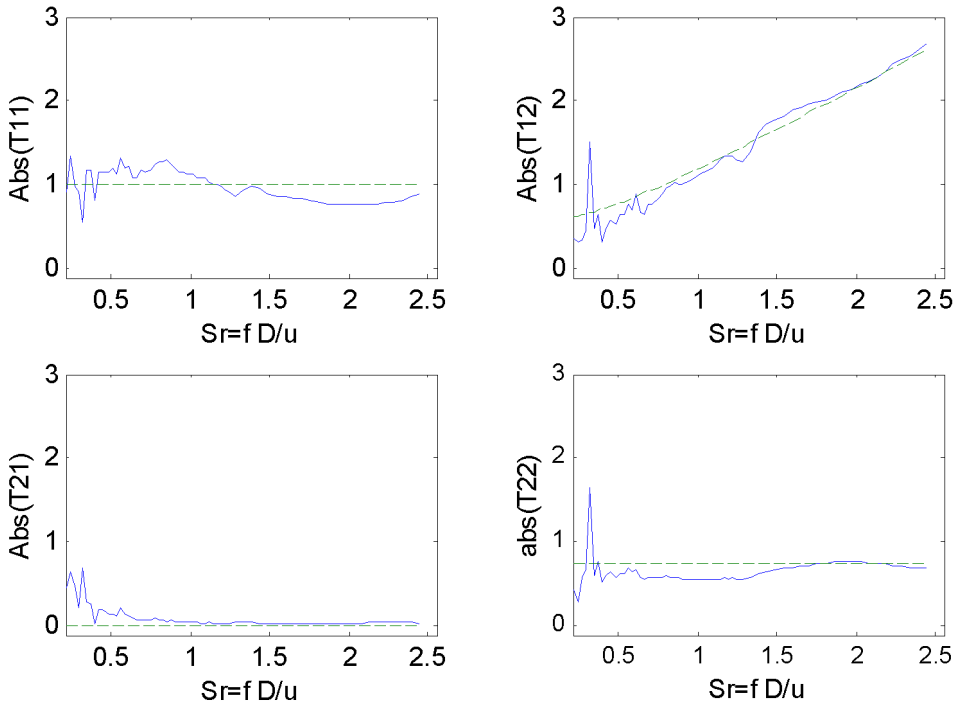

Figure 3.6: Fit of the $L\zeta$-model to the absolute values of the measured burner transfer function.

The values of L_{red} and ζ_b are not known a priori, and have been obtained by a curve fit to the measured transfer function. The frequency range was sufficiently low to ensure one dimensional wave propagation. However, the $L\zeta$ model is a zero dimensional representation, and acts as a discontinuity in the one dimensional acoustic field. The burner has a finite axial extent, thus it

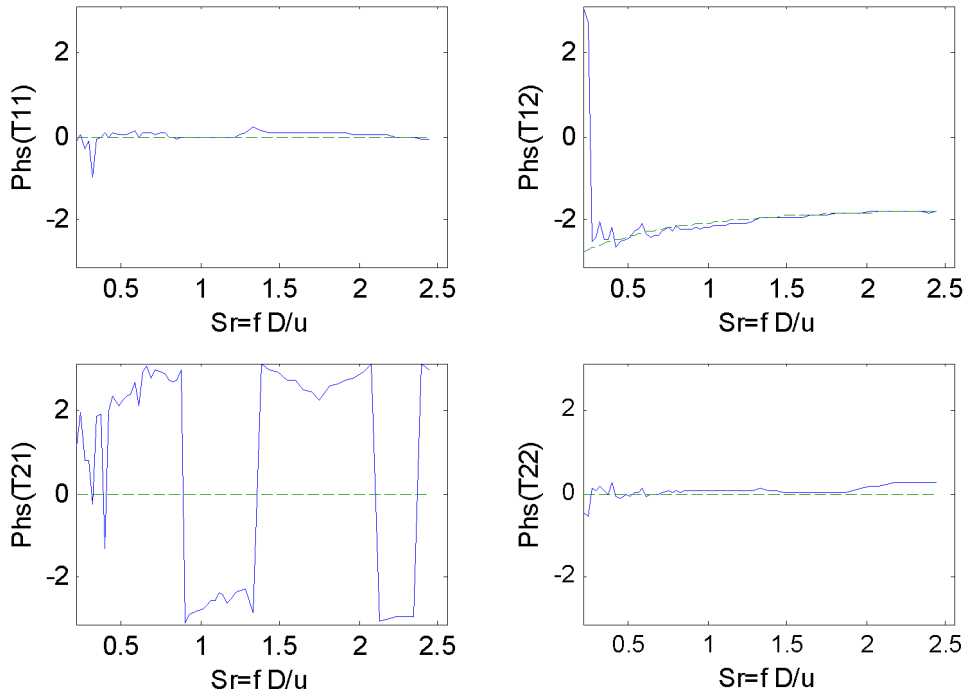

Figure 3.7: Fit of the $L\zeta$-model to the phase values of the measured burner transfer function.

is not obvious at what axial location the discontinuity should be chosen. Or, differently stated, it is not obvious what value should be chosen for the reference position in Eq. 3.17 because the burner has a finite extent. The axial position was then chosen such that the fit to the measured transfer function gave the best result. The results of the curve fits have been displayed in Figs. 3.6 and 3.7. The agreement between the measured transfer matrix and the model is very good for all measured operating conditions. This indicates that the transfer matrix of Eq. 3.33. is appropriate to model the acoustic behavior of the burner (without combustion). However, care should be taken when interpreting the value of L_{red} as an acoustic property of the burner, because this value depends on the cross sectional area of the test rig. An idea of the quality of the measured transfer matrix can be obtained by comparing the values of ζ_b obtained from the measured transfer function to the mean flow loss coefficient. Because the relation for the acoustic loss has been obtained from a linearization of the mean flow loss, both values should be equal. The mean flow loss coefficient has been calculated from the measured mean flow static pressure difference across the burner. In table 3.5.1 the ratio between the acoustic and mean flow loss coefficient is given, together with the value of L_{red} for several values of the mean flow Mach number. The mean flow loss coefficient ($\zeta_{b,static}$) is the loss coefficient calculated from the static pressure difference across the burner. The reduced length is normalised by the burner exit diameter (D).

Based on the analysis in section 2.7 it is expected that the value of ζ_b obtained from the curve

$\frac{M_b}{M_{b,ref}}$	$\frac{L_{red}}{D}$	$\frac{\zeta_b}{\zeta_{b,static}}$
1	1.30	0.98
1.3	1.41	0.84

Table 3.1: The values of L_{red} and the ratio of the acoustic and mean flow loss coefficient for several mean flow Mach numbers.

fit is equal to the mean flow loss coefficient. Indeed, the loss coefficients obtained from curve fits to the measured transfer function and from the static pressured difference are very similar according to table 3.5.1.

3.5.2 Burner Transfer Function With Combustion

Transfer matrices have been measured for a large variety of operating conditions. A detailed analysis of the influence of flame temperature and the mass flow through the burner is given in § 4. Here the influence of burner velocity and flame temperature is shown by comparing three transfer matrices measured at three operating conditions. The "burner velocity", V_b is defined as the total mass flow divided by the cross sectional area of the exit of the burner nozzle. The "flame temperature", T_f, is defined as being the adiabatic flame temperature, the adiabatic flame temperature is calculated using an energy balance, based on measured mass flow of gas and measured mass flow of air. In Fig. 3.8. the absolute values of the four elements of three transfer matrices have been plotted. In Fig. 3.8 the phases of the transfer matrices have been plotted. These plots show that the transfer matrices of the burner with flame have the following properties in common:

- The T_{11} element that relates the pressures across the burner and flame has zero phase for the entire frequency range. This indicates that the dynamics in the flame are not strongly dependent on the pressure.
- The T_{12} element relates the pressures downstream to the velocity upstream of the burner and flame, and is (for high frequencies) characterized by a linear increase of the absolute value with frequency and a phase of $-\pi/2$. This behavior is typical for a confinement in the acoustic field, as demonstrated in the previous section. This effect is due to the burner geometry and flow field in the burner and is not affected strongly by the combustion process. Indeed, this curve is not strongly affected by a change in flame temperature, but does change with changing burner velocity.
- The T_{21} element relates the velocity downstream to the velocity upstream, the absolute value of this element is very small compared to the other elements and is of little importance. The phase of this quantity has a very irregular trend, this is because the absolute value is small. Small noisy contributions result in very large errors of the phase.
- The T_{22} element relates the acoustic velocity across the flame and shows a rather complex dependence on frequency. The phase drops linearly for low frequencies which is charac-

Figure 3.8: Absolute values of transfer matrix measured at reference operating condition(dotted), at V_b=2/3 $V_{b,ref}$ (dashed) and at T_f=$T_{f,ref}$+100K (solid).

teristic for time delays. The behavior of the phase indicates that this element behaves dynamically. This element is strongly affected by both flame temperature and burner velocity. This result shows that the most important characteristic of the burner and flame dynamics depend on the acoustic velocity, because the dynamics of the T_{22} element strongly depend on temperature.

3.5.3 Flame Transfer Matrix

In order to obtain a better insight into the flame dynamics, Eq. 3.32 is used to obtain the flame transfer matrix from the measurements of the transfer matrices of the burner with and without combustion. In Figs.3.10 and 3.11 the transfer matrices of the burner without combustion, the burner with combustion and of the flame only are shown. These results show very clearly the individual contributions of the burner geometry and the combustion process.

- The T_{12} of the flame transfer matrix is nearly zero, while the T_{11} element is constant and has a value close to $\frac{\rho_1 c_1}{\rho_2 c_2}$. Note that the pressure signals have been scaled by the the characteristic impedance (ρc). Thus, the pressure across the flame is continuous.
- The value of T_{21} is very small compared to T_{22}. The absolute value and phase of T_{22} are

Figure 3.9: Phase angles of transfer matrix measured at reference operating condition(dotted), at V_b=2/3 $V_{b,ref}$ (dashed) and at T_f=$T_{f,ref}$+100K (solid).

strongly frequency dependent for low frequencies, indicating a strong dynamic behavior. For higher frequencies T_{22} converges to unity. Apparently the dynamic behavior is damped for higher frequencies, resulting in continuity of acoustic velocity at these frequencies.

The flame transfer matrix clearly shows that all the dynamics of the flame are contained in the T_{22} element of the flame. This is important information when deriving acoustic models of the flame. In some flame models the coupling mechanism between the acoustic field and heat release is assumed to result from fluctuation in the fuel supply system. If this were the case, this would be manifested by a strong dependence of the acoustic velocity on the acoustic pressure. This is clearly not the case here because the T_{12} and T_{21} matrices are nearly zero. Note that these results are specific for this burner. For other types of burners or in a different combustion regime, these results might be different. In other models [104], the instability mechanism is caused because the derivative of the pressure across the burner and flame with respect to mass flow through the burner is negative. Generally this derivative would be positive, however it is argued that this derivative could become negative because of complex interactions in swirl-stabilized flames. This acts as a "negative damping coefficient" in the wave equation, and may cause instability. Because the mass flow is proportional to the velocity, this mechanism would be characterized by a T_{12} element with a positive real part. However, in the burner and flame transfer matrix, T_{12} has negative real part for all frequencies, which corresponds to acoustic dissipation. A detailed

analysis of the T_{22} matrix element is presented in § 4.

Figure 3.10: Absolute values of transfer matrix of the burner with flame (solid), the burner without combustion (dashed) and the transfer matrix of the flame only calculated from Eq. 3.32 (dotted).

3.5.4 Source Terms

The source term has been measured using Eq. 3.31. In figure 3.12 the source term component f_s has been plotted for different values of the burner velocity. Because the source term is caused by turbulent combustion processes, it is expected that the frequency dependency scales with the Strouhal number ($Sr = \frac{f\,D}{u}$).
In figure 3.12 can be seen that this assumption holds for the larger burner velocities. However, for the smaller burner velocity ($U = 2/3\,U_{ref}$) this assumption does not hold.

3.5.5 Sensitivity Analysis

In order to obtain a quantitative estimate of the error in the transfer matrix measurement, a sensitivity analysis is carried out. Two different contributions to the measurement error are considered:

- error in parameters that are used in the MMM such as the error in speed of sound, measured distance between microphones, and mean flow velocity

Figure 3.11: Phases of transfer matrix of the burner with flame (solid), the burner without combustion (dashed) and the transfer matrix of the flame only calculated from Eq. 3.32 (dotted).

- noise in the microphone signals

The sensitivity to a parametric error is estimated by determining the transfer function while applying an offset to some parameters. The result is shown in Fig. 3.13. A disturbance has been applied to the upstream temperature, downstream temperature and on the Mach number. The influence of an error in the microphone distance is not shown here because the sensitivity is the same as for an error in the speed of sound, which depends on the square root of the temperature. A measurement of distance will generally be much more accurate than a measurement of temperature. It is difficult to give an estimate of the probable error in the measurement of temperature and velocity in the test facility, but this error will certainly be much smaller than the disturbances used to generate the results shown in Fig. 3.13, demonstrating that the relative error is small enough to obtain unbiased, reproducable results. The noise contribution in the peak estimate of the microphone signal is estimated (from Fig. 3.2)to be less than 1%. In order to investigate the influence of noise on measurement, the pressure signals have been corrupted artificially with 2% noise. The transfer matrix was then recalculated several times, the result is shown in Fig. 3.14. The error is within 5% for all frequencies, except for the very low frequency regime, where the error becomes considerable. This is important because in many flame transfer functions spikes in the transfer function have been observed at very low frequencies. This analysis indicates that it is dangerous to give a physical interpretation to these spikes, since they

Figure 3.12: Source terms measured for different burner velocities.

may equally well be caused by measurement uncertainty.

3.5.6 Linearity of the Transfer Matrix

Although the thermoacoustic system to be analyzed may be unstable, it is assumed here that the subsystems are stable. This assumption is based on experimental observations: if a (nearly) anechoic end is placed at the exit of the combustion chamber, this always results in low pulsation levels. Or, expressed in control theory terms: if the feedback gain is zero (anechoic end) the system is stable. Because the transfer functions of the subsystems are measured (and not that of the entire closed loop system), the transfer functions to be measured are stable, and the method is valid. Moreover, operation in the linear regime is guaranteed by applying the anechoic end condition. The method for experimental determination of the transfer matrix assumes linearity of the transfer functions. Validity of this assumption can easily be checked by measuring the transfer function and source terms twice, with different amplitudes of the forcing signal. Figures 3.15 and 3.16 show the result for this test. Both measurements yield the same result, the differences between the curves are within measurement accuracy. Note that when using a smaller forcing amplitude the signal to noise ratio decreases, thus a larger error will be introduced. This experiment also provides a measure of reproducibility of the method.

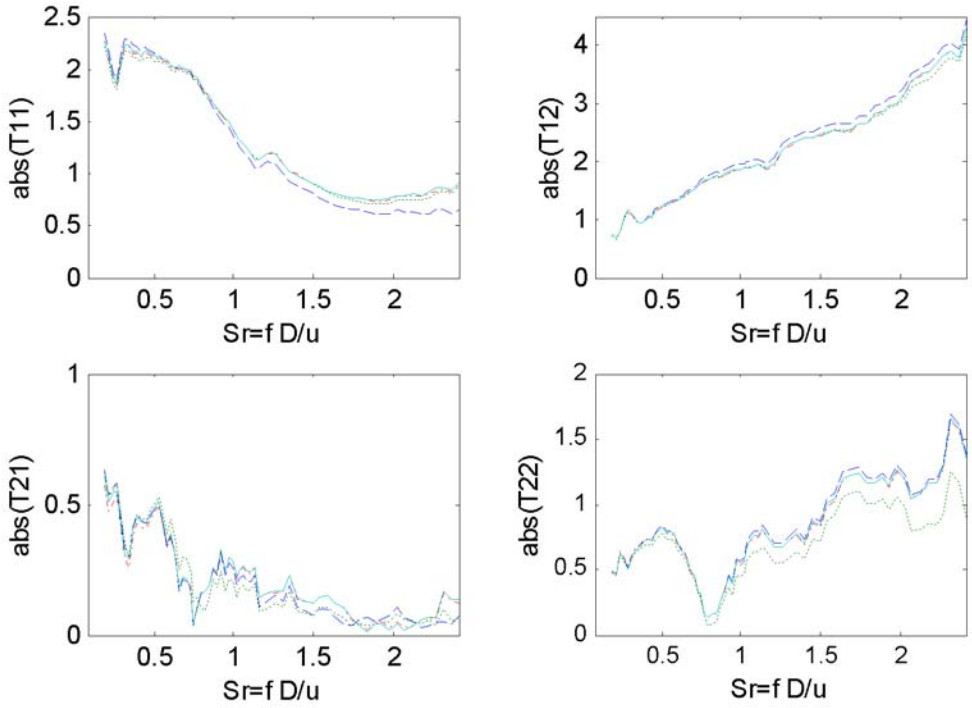

Figure 3.13: Absolute values of the transfer matrix plotted versus Strouhal number: nominal (solid line), 50 K error in upstream temperature (dashed), 100 K error in downstream temperature (dotted), Mach number neglected (dash-dotted).

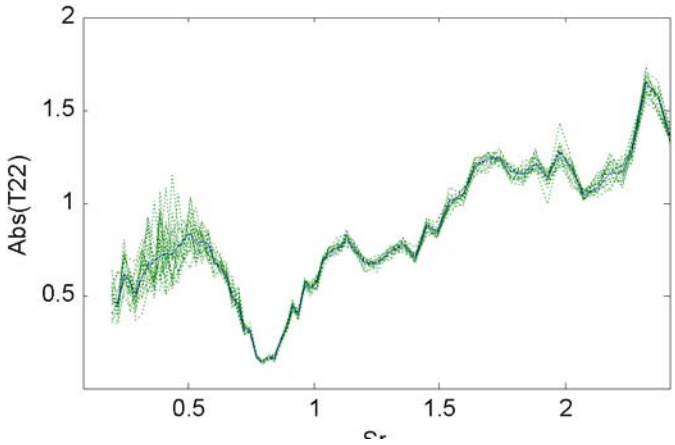

Figure 3.14: The T_{22} element calculated 20 times with two percent random disturbance on the pressure signals.

Figure 3.15: transfer matrix measured with 0.5 Volt forcing (dotted), and 1.0 Volt forcing (solid).

Figure 3.16: Source terms measured with 0.5 Volt forcing (dotted), and 1.0 Volt forcing (solid).

3.6 Validation

The measured transfer matrices proved to be reproducable and linear. As well, they are not strongly affected by measurement noise (except for very low frequencies). The question remains if the measured transfer matrices can be used to predict the acoustic behavior of a combustion system. In order to answer this question an acoustic network model of the test facility has been made. The block diagram of this system is shown in Fig. 3.17. The burner and flame block consists of the measured transfer matrix. Measured source terms are included and measured reflection coefficients have been used to represent the boundary conditions at inlet and exit of the system. The plenum and combustion chamber have been modeled as one dimensional ducts with mean flow. The model is described in the frequency domain and consists mainly of measured transfer matrices. This model was then used to "predict" the frequency spectrum of the pressure in the combustion chamber. The "predicted" spectrum was then compared to the measured spectrum of the pressure. Both spectra were in almost perfect agreement. This is not surprising, since all blocks in the model have been obtained from measured responses.

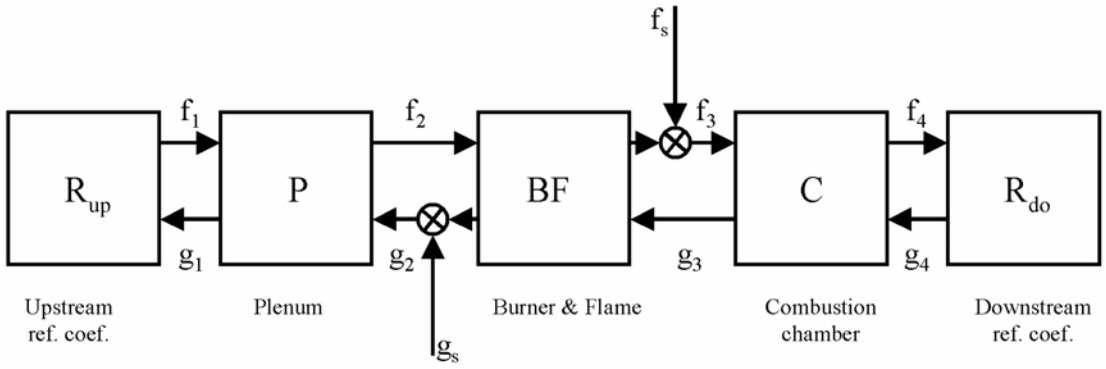

Figure 3.17: Acoustic network representation of test facility.

A better test is to change the acoustic boundary conditions and see if the change of the measured pressure spectrum corresponds to the prediction. The variable geometry of the combustion chambers allowed for changes in the length of the combustor and the reflection coefficient at the end of the combustion chamber. The transfer function of the burner was measured, while having an absorbing boundary condition in the test rig. According to the model, a significant increase of the pressure amplitudes can be expected if the exit condition is changed to fully reflecting. An (almost) fully reflecting exit condition can be created by removing the throttle plate at the exit of the combustion chamber. The absolute value of the reflection coefficient of the exit (with and without throttle plate) has been plotted in Fig. 3.18.
Figure 3.19. shows a comparison between the measured spectra with and without orifice and the spectrum predicted by the network model. The spectrum changes dramatically by changing the acoustic boundary condition. This change is predicted correctly by the model.

Figure 3.18: Comparison of measured reflection coeficients of the exit with throttle plate (dotted) and without throttle plate (solid).

The next test is to investigate the influence of the combustor length on the pressure fluctuations. Simulations with the network model predicted decreasing values of the resonance frequency for increasing combustor length. Figure 3.20 shows the frequency (normalized as a Strouhal number) at which maxima occur in the pressure spectrum as a function of combustor length. The lower frequencies correspond roughly to the quarter wave resonance mode, the higher frequencies to the three-quarter wave mode. This result is not very surprising because the trend of the frequencies can be expected from basic acoustic insight. However, a stability analysis showed

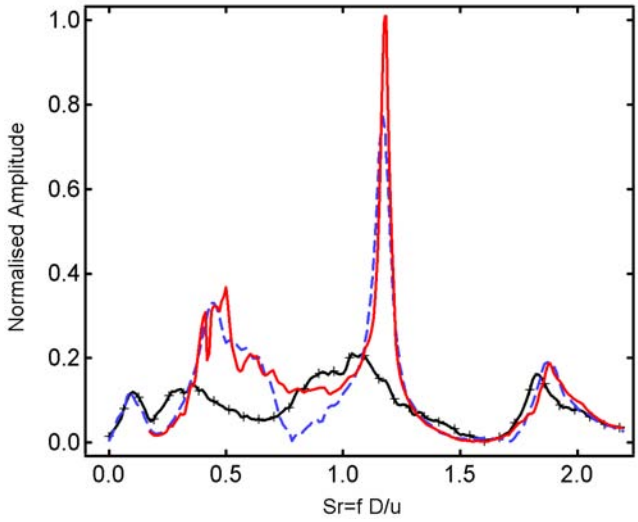

Figure 3.19: Comparison of measured and modeled pressure spectra. Measured pressure spectrum with absorbing exit (dotted), measured spectrum with fully reflecting exit (dashed) and predicted spectrum with fully reflecting exit (solid).

Figure 3.20: The calculated (dashed) and measured (crosses) resonance frequencies (scaled as a Strouhal number) as a function of duct length.

that instability could be expected for small combustor lengths, increasing the length results in more stable combustion followed by an unstable region again.
In order to obtain a quantitative measure for the stability of the system, the *gain margin* of the system has been evaluated. The gain margin (a term commonly used in control theory) is defined as the amount of gain that can be inserted in the (closed loop) network before the system reaches instability. In our analysis, a gain was applied to the downstream reflection coefficient. A stability map has been made of combustor length versus gain. The gain margin obtained in this way is plotted as a function of combustor length in Fig. 3.21 for the first and second resonance mode. In the same plots, the measured pressure amplitudes are plotted as a function of length. A positive gain margin indicates stable combustion, whereas a negative margin indicates unstable combustion. This comparison shows that high pressure amplitudes were measured for these combustor lengths where the system was predicted to be unstable. The actual pressure amplitudes can not be predicted using linear theory if the system is unstable.

3.7 Discussion

In this chapter a method for experimental determination of acoustic transfer matrices has been discussed. The method consists of forcing a test facility with loudspeakers, and measuring the acoustic reponse using arrays of loudspeakers placed on both sides of the element (the burner) to be measured. By forcing downstream and upstream of the element consecutively two independent test states are created. From the arrays of microphones, the acousic velocity and pressure at the burner location is calculated using the relations for one dimensional wave propagation. The transfer matrix relating the acoustic pressure and velocity at both sides of the element is calculated from the experimental data obtained from the two test states. The transfer matrix of the combustion process only is obtained by matrix division of the transfer matrices with combustion and without combustion.

Figure 3.21: The calculated gain margin and measured pulsation amplitudes of the first and second resonance mode. A negative gain margin indicates instability.

The method is restricted is restricted in bandwidth, the upper frequency being limited by the cut-off frequency of the test duct. The method does, however, take into account the effect of a mean flow. Becasue the transfer matrices relate the acoustic quantities in a linear way, this method may only be used to analyse linear systems. However, it is well known that thermoacoustic systems may exhibit limit cycle behavior and are thus non-linear. This problem is avoided by applying a (nearly) anechoic acoustic boundary to the test facility and thus ensuring low amplitude, stable acoustics.
The transfer matrix measurement method is particulary difficult in combustion systems. This is because of the high temperatures, and strong background noise due to turbulent processes in the flame. The method has been improved during the course of this work by applying the "pure tone method" to remove noise contributions that are not correlated to the excitation signal. The measurement procedure has been automated in order to obtain transfer matrices systematically and quickly.
The measurement procedure has been validated theoretically and experimentally. A sensitivity analysis has been performed, and the assumption of linearity of the transfer matrix validated.
A network model of the combustion test facility has been made that consisted of measured transfer matrices only. Comparison of the results obtained with this network model and experimental data, demonstrated that the relevant acoustic dynamics are captured by the measured transfer matrices, source terms and reflection coefficients.
After extensively testing and validating the measurement system, more than one hundred transfer matrices and source terms have been measured of different burners at different firing conditions and with different geometrical modifications. Not all results will be discussed in this work, however in the section "flame model" the dependence of flame temperature and through put will be analyzed in more detail.
The transfer function relates two acoustic quantities at both sides of the element. This provides a valid characterisation if one dimensional plane waves are considered. However, the acoustic field

in a gas turbine is typically two dimensional. The acoustic velocity is then a vector quantity and the assumption of plane wave propagation does not hold any longer. Nevertheless, such a one dimensional representation may be used in a two or three dimensional network representation, provided that the heat release process is not affected by transversal acoustic waves. The influence of the heat release on the transversal waves is correcly taken into account even if the transfer function is one dimensional. This is because the heat release acts as a volume source to the acoustic wave, and by Eq. 2.90 a source in the volume may be represented by an equivalent source on the boundary, provided that the region is compact. There is no experimental result available that demonstrates the influence of transversal waves on the heat release in the flame and, hence, it is recommended as a future research activity. It is assumed here that the influence of transversal waves is small compared to the influence of longitudinal waves because only the longitudinal waves modulate the supply of reactive mixture. This mechanism will be explained in more detail in chapter 4.

Experimental analysis of a non-linear flame transfer function would require an experimental set-up with extremely high acoustic forcing levels. A non-linear analysis of the signals is then required. This is recommended as a future research activity.

Chapter 4

Flame Model

4.1 Introduction

For thermoacoustic simulations, the combustion system may be described as a network of acoustic elements modeling the various components of the system (e.g. air supply, burner, flame, combustor, cooling channels, etc.) [80, 118]. As already discussed in chapter 3, the acoustic elements are modeled as two-ports in which the acoustic field (pressure and velocity) upstream and downstream of the element are coupled linearly via a four-element transfer matrix. The eigenfrequencies of the acoustic network determine the linear stability of the combustion system, stability analysis is discussed in § 5. For most of the acoustic elements, simple analytical models provide an adequate description of their thermoacoustic properties (related only to wave propagation). In contrast, the amplifying behavior of the flame makes it an "active" acoustic two-port whose modeling depends on the characteristics of the combustion process (premix or diffusion flame, flame stabilization mechanism, liquid or gas fuel, etc.).

In this work, lean premixed turbulent combustion is considered. The observed sensitivity of the heat release fluctuations to equivalence ratio fluctuations in the lean regime [61] indicates that, in lean premixed gas turbines, fuel concentration fluctuations cause a strong feedback mechanism. Several models to simulate the coupling between heat release and fuel concentration fluctuations have been proposed, mainly based on the "time-lag" approach in which fuel concentration fluctuations are caused by acoustic fluctuations at the fuel injector location. The fuel concentration fluctuations are then convected to the flame, the convective time lag (i.e. the time between injection and combustion of a fuel particle) depending on the fluid dynamic field between injector and flame [118, 37, 85]. Analytical models have been proposed to account for the flame shape effect on the time-lag distribution in the frequency domain [54, 36].

The area of the flame front is assumed to be constant with respect to time. This assumption is supported by pictures of the OH radiation of the flame. Because the OH-chemiluminescence is a measure of the instantaneous heat release, the pictures give information about the heat release dependence on space and time. The pictures of the flame in an air cooled double walled quartz tube were taken using an intensified CCD camera with an OH-filter. The (false color) plot in Fig. 4.1 shows how the heat release is distributed. By forcing the combustion air with

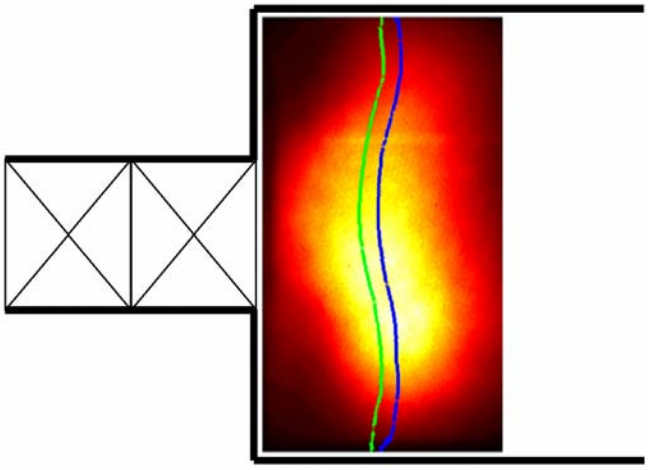

Figure 4.1: False color plot: OH-chemiluminiscence picture of the flame. Left curve: "center of gravity line" at $-90°$ phase angle. Right curve: "center of gravity line" at $+90°$ phase angle.

loudspeakers, and using the forcing signal as a trigger signal for the camera, *phase-locked* images of the flame are obtained. Comparison of the pictures taken at different phase-angles indicated that the axial flame position of the flame varies sinusoidally with time. In Fig. 4.1 the axial "center of gravity" of the flame is plotted in its rightmost and leftmost positions. The "center of gravity" is defined as $g(y) = \frac{\int x\, I(x,y)dx}{\int I(x,y)dx}$, where I is the image intensity and x and y are Cartesian coordinates.

Heat release fluctuations related to flame speed fluctuations are also included. It is difficult to find an analytical expression that correctly relates the turbulent flame speed to the acoustic field. An additional uncertainty is the distribution of time delays. Because of these uncertainties, the dependence of flame speed fluctuations on the acoustic field, and the distribution of the time delays, are obtained by fitting to measured data.

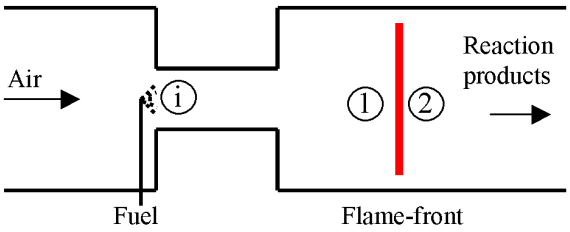

Figure 4.2: Sketch of burner with fuel injection, mixing zone and flame front.

As a basis for the flame model, the jump relations 2.128- 2.130 derived in § 2.8 will be used.

These equations are repeated in Eq. 4.1

$$\begin{aligned} p_2' &= p_1' \\ \frac{u_2'-u_1'}{u_1} &= \Big(\frac{R_2T_2}{R_1T_1}-1\Big)\frac{S_f'}{\bar{S}_f}+\Big(\frac{R_2T_2}{R_1T_1}-\frac{\gamma_1(\gamma_2-1)}{\gamma_2(\gamma_1-1)}\Big)\frac{y_f'}{\bar{y}_f}+\Big(\frac{\gamma_2-1}{\gamma_2}-\frac{\gamma_1-1}{\gamma_1}\frac{R_2T_2}{R_1T_1}\Big)\frac{p_1'}{\bar{p}_1} \\ s_2' &= (R_1\frac{T_1}{T_2}-R_2)\frac{p_1'}{p_1}+\frac{h_f\,y_f'}{T_2} \end{aligned} \tag{4.1}$$

The aim of this chapter is to express the flame speed fluctuations (S_f'), and fuel mass fraction fluctuations (y_f'), as functions of upstream pressure (p_1') and velocity (u_1'). After substitution of these relations in Eq. 4.1, closure of the relations across the flame front is obtained. The flame front can then be represented in frequency domain with the following matrix representation:

$$\begin{bmatrix} \hat{p}_2 \\ \hat{u}_2 \\ \hat{s}_2 \end{bmatrix} = \begin{bmatrix} T_{11} & T_{12} \\ T_{21} & T_{22} \\ T_{31} & T_{32} \end{bmatrix} \begin{bmatrix} \hat{p}_1 \\ \hat{u}_1 \end{bmatrix}, \tag{4.2}$$

in which the matrix elements T_{ij} depend on frequency only.

Equivalence Ratio Fluctuations

Fuel mass fraction fluctuations are considered as a possible coupling mechanism between the acoustic field and the fluctuating heat release [72, 117].
An experiment has been performed to investigate if this is the dominant mechanism. In this experiment, the transfer function of the flame has been measured two times for exactly the same burner. In one experiment the fuel was mixed in the regular way, thus in the burner (premixed operation). In the second experiment, all the fuel was injected far upstream of the burner, in the plenum chamber (pre-premixed operation). This large distance between fuel injection and fuel consumption ensures that the mass fraction waves are dispersed, and can therefore not cause heat release fluctuations. The result is plotted in figure 4.3. This figure makes clear that in absence of the mixture fraction fluctuations the magnitude of the T_{22} matrix element is significantly smaller. This is clear evidence that fluctuations of the mass fraction of fuel are the dominant effect in the thermoacoustic coupling mechanism. Nevertheless, it should be noted that it is not the only mechanism. Because if it where the only mechanism, then the transfer function of the pre-premixed flame would be unity, which is not the case.
A simplified representation of the combustion system is given in Fig. 4.2. The fuel concentration at the injector position is given by: $y_{f,i} = \frac{m_f}{m_f+m_a}$, in which m_f is the mass flow of fuel, and m_a is the mass flow of air at the injector position. Thus, fuel mass fraction fluctuations may either be caused by air fluctuations or fuel supply fluctuations:

$$\frac{y_{f,i}'}{\bar{y}_{f,i}} = \frac{m_f'}{\bar{m}_f} - \frac{\rho'_{a,i}}{\bar{\rho}_{a,i}} - \frac{u_{a,i}'}{\bar{u}_{a,i}}, \tag{4.3}$$

where the condition $m_a \gg m_f$ has been used. In Eq. (4.3), air density fluctuations may be expressed using an isentropic condition. Using the incompressibility hypothesis, the fuel mass

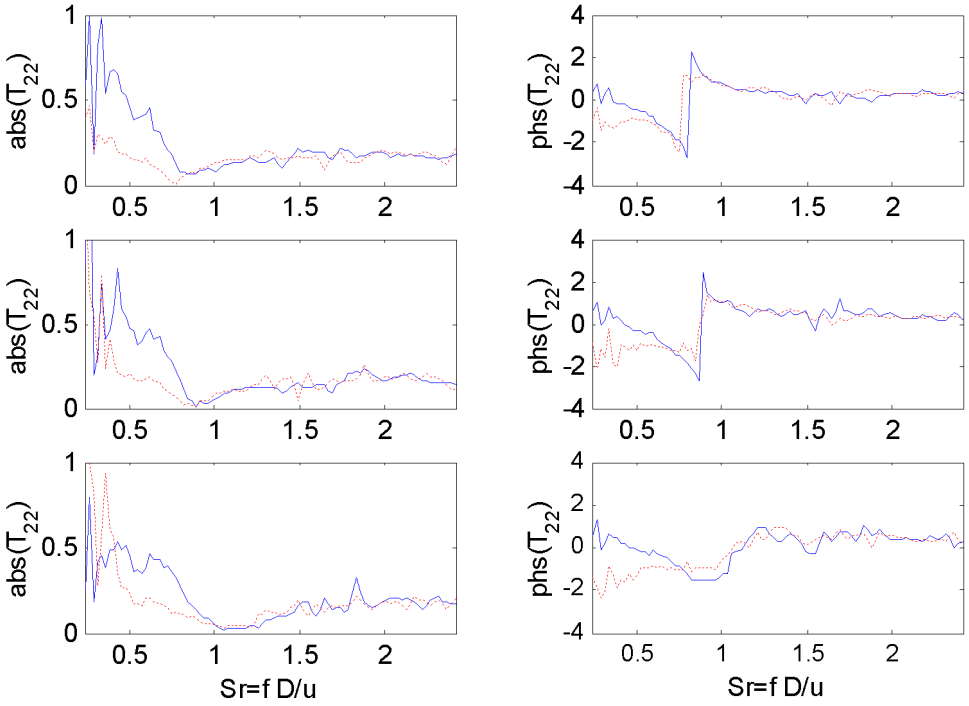

Figure 4.3: The measured T_{22} transfer function element for regular fuel injection (solid) and pre-premixed fuel injection (dotted).

flow rate through the injector is given by:

$$m_f = \sqrt{\frac{\rho_f \bar{p}}{2}} A_i \,, \tag{4.4}$$

and then, from Eq. (4.4):

$$\frac{m'_f}{\bar{m}_f} = -\frac{1}{2}\frac{p'_i}{\bar{p}} \,. \tag{4.5}$$

Eq. (4.5) shows that if $\hat{p}_i/\bar{p} \ll 1$, fuel mass flow rate fluctuations may be neglected in Eq. (4.3). For the combustion systems considered in this work, this approximation is valid.
The equivalence ratio fluctuations at the injector position will be convected to the flame by the mean flow. According to the time-lag model [117], the fuel concentration fluctuations just upstream of the flame at time t are equal to those at the fuel injectors at time $t-\tau$, where τ is the time necessary to convect the equivalence ratio fluctuations to the flame front. It reads

$$y'_{f,1} = y'_{f,i}(t-\tau) \,. \tag{4.6}$$

This representation is correct if:

1. fuel injection takes place at one axial position

2. combustion takes place at on axial position

3. there is no diffusion

For practical combustion systems these assumptions will generally not hold. Although the axial extent of the flame may be considered to be thin with respect to the acoustic wave length ($2\pi c/\omega$), it will generally not be thin with respect to the wavelengths of the equivalence-ratio waves ($2\pi\bar{u}/\omega$). To include the effect of distributed fuel injection, flame shape and diffusion, a model with distributed time delays has been utilized.

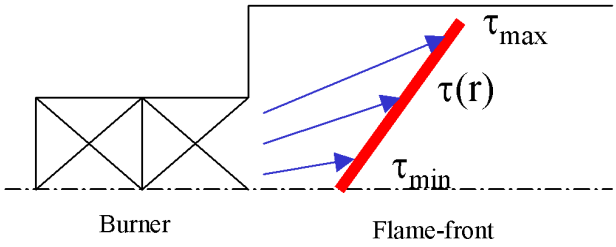

Figure 4.4: Spreading of time delays in a v-shaped flame.

In Fig. 4.4, a graphical representation of the time delay distribution is shown. The value of the time lag is a function of the position on the flame surface. Because the heat release zone is compact with respect to the acoustic wavelength, the "effective" equivalence ratio may be obtained by averaging the time delays associated with each position on the flame surface:

$$y'_{f,1}(t) = \frac{1}{S} \int \int_S y'_{f,i}(t - \tau(\mathbf{x}))d\mathbf{x}, \tag{4.7}$$

in which S denotes the flame surface. The dependence of $\tau(\mathbf{x})$ can be obtained analytically for simple flames [72, 73], for practical flames the probability density function of the time delays can be obtained numerically [37] or from experiment. With the probability density function $\xi(\tau)$ Eq. 4.7 can be written as:

$$y'_{f,1}(t) = \int_{\tau=0}^{\infty} \xi(\tau) y'_{f,i}(t - \tau)d\tau, \tag{4.8}$$

or, in the frequency domain as:

$$\hat{y}_{f,1}(\omega) = \hat{y}_{f,i}(\omega) \int_{\tau=0}^{\infty} \xi(\tau) e^{-i\omega\tau} d\tau. \tag{4.9}$$

Note that the integral in Eq. 4.8 is a convolution integral and the integral in Eq. 4.9 is the Fourier transform (with reversed sign convention). Equation 4.9 can thus be written as:

$$\hat{y}_{f,1}(\omega) = \mathcal{F}^*\{\xi\}\hat{y}_{f,i}(\omega), \tag{4.10}$$

in which $\mathcal{F}^*\{\}$ denotes the complex conjugate of the Fourier transform. The complex conjugate has to be taken because of the sign of ω.

If a Gaussian distribution of the time delays is assumed: $\xi(\tau) = \frac{1}{\sigma_\tau \sqrt{2\,\pi}}\, e^{-\frac{(\tau-\bar{\tau})^2}{2\,\sigma_\tau^2}}$, with $\bar{\tau}$ the mean value, and σ_τ the standard deviation of the time delays, then equation 4.10 reads:

$$\hat{y}_{f,1}(\omega) = \hat{y}_{f,i}(\omega)\, e^{-i\omega\bar{\tau}-\frac{1}{2}\omega^2\sigma_\tau^2}. \tag{4.11}$$

From this representation it is seen that for high frequencies, or large values of σ_τ, the equivalence ratio fluctuations at the flame front decay to zero. In fact, $e^{-i\omega\bar{\tau}}e^{-\frac{1}{2}\omega^2\sigma_\tau^2}$ is a low pass filter[1].

Flame speed fluctuations

The underlying assumption is that the acoustic field does not influence the turbulence field. However, fluctuations of fuel concentration, temperature, and pressure may influence the laminar flame speed. Thus, acoustically induced equivalence ratio fluctuations may influence the turbulent flame speed via a dependence on the laminar flame speed. Several correlations between laminar and turbulent flame speeds have been reported in literature. If the dependence is expressed as a power-law, $S_T = \beta\, S_L^\alpha$, the dependencies vary from, $\alpha = 0$ for sufficiently high turbulence levels (Damköhler, Peters [98]), to $\alpha = 0 - 0.5$ (Williams, [133]), and to $\alpha = 0.6$ (Zimont, [139]). Thus the flame speed fluctuations induced by fuel concentration fluctuation can be expressed as:

$$\frac{S'_f}{\bar{S}_f} = \frac{\alpha}{\bar{S}_L}\Big(\frac{\partial \bar{S}_L}{\partial \bar{y}_f} y'_f + \frac{\partial \bar{S}_L}{\partial \bar{T}_1} T'_1 + \frac{\partial \bar{S}_L}{\partial \bar{p}_1} p'_1\Big) \tag{4.12}$$

For the laminar flame speed in methane, a relation given by Abu-Off and Cant [2] is used:

$$S_L = A\phi^B e^{-C(\phi-D)^2}(\frac{T}{T_R})^2(\frac{p}{p_R})^{-0.5} \tag{4.13}$$

in which $A = 0.6079$ m/s, $B = -2.554$, $C = 7.31$, $D = 1.23$, $P_R = 1$ bar and $T_R = 300K$. With this relation at hand, equation 4.12 can be expressed as:

$$\frac{S'_f}{\bar{S}_f} = \alpha\Big\{(-2C\phi^2 + 2\,C\,D\,\phi + B)\frac{y'_f}{\bar{y}_f} + 2\,\frac{T'_1}{\bar{T}_1} - \frac{1}{2}\frac{p'_1}{p_1}\Big\} \tag{4.14}$$

$$= \alpha\Big\{(-2C\phi^2 + 2\,C\,D\,\phi + B)\frac{y'_f}{\bar{y}_f} + (2\frac{\gamma_1 - 1}{\gamma_1} - \frac{1}{2})\frac{p'_1}{p_1}\Big\} \tag{4.15}$$

4.2 Closure

Substitution of Eqns. 4.10. and 4.14. into Eq. 4.1 provides closure of the jump conditions across the flame front. In order to investigate the influence of the Mach number on the transfer function,

[1] Note that the normal distribution has the unique property that the absolute value of the Fourier transform of the normal distribution is again a normal distribution. The variance of the function in frequency domain having reciprocal dependence on the original variance.

it is convenient to express the transfer function as $T_{22} = 1 - n\,\mathcal{F}^*\{\xi\}$, in which n is referred to as the *interaction index* and does not depend on frequency.
If one assumes that the gas constant and ratios of specific heats are constant across the flame, a very simple expression is found for n:

$$n = (\frac{T_2}{T_1} - 1)(1 + \alpha\,\{-2C\phi^2 + 2\,C\,D\,\phi + B\}) \tag{4.16}$$

In Fig. 4.5 the interaction index is plotted as as a function of the equivalence ratio for several values of α. For large values of α, the interaction index increases when reducing the equivalence ratio from stoichiometric conditions. This is in agreement with results obtained in [72]. For very low equivalence ratios, the interaction index decreases again, unfortunately no results are reported for these values in [72].

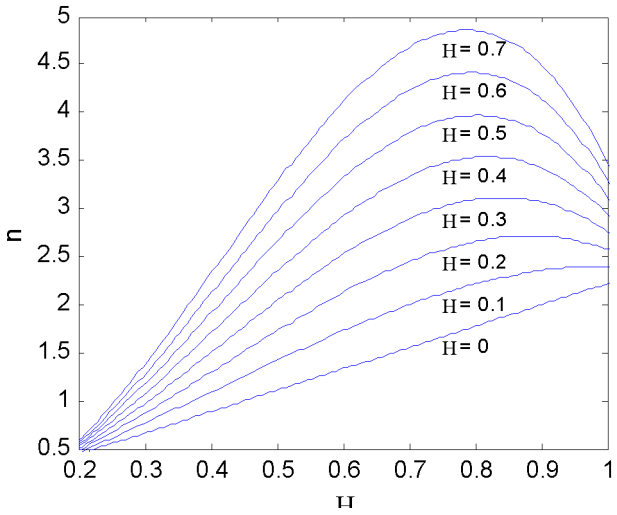

Figure 4.5: The interaction index as a function of equivalence ratio, plotted for several values of the exponent α.

With the expression of the interaction index and with the Fourier transform of a Gaussian distribution of time delays, the T_{22} element of the transfer matrix can be written as:

$$T_{22} = 1 - (\frac{T_2}{T_1} - 1)(1 + \alpha\,\{-2C\phi^2 + 2\,C\,D\,\phi + B\})e^{-i\omega\bar{\tau} - \frac{1}{2}\omega^2\sigma_\tau^2}. \tag{4.17}$$

4.3 Experimental validation

The transfer matrices measured in an atmospheric test facility are compared with the analytic model using different flame speed fluctuation expressions. Transfer function measurements have been performed for a range of operating conditions relevant for premixed gas turbine operation. The mean flow velocity was varied from $\bar{u}_{1,ref}$ to 1.4 $\bar{u}_{1,ref}$, and the mass fraction of fuel was increased in steps of 5%. The distribution of the time lags, $\xi(\tau)$, is not known a-priori. A

Gaussian distribution with mean value $\bar{\tau}$ and a standard deviation σ is assumed. The numerical values of $\bar{\tau}$, σ and α are obtained by fits to the experimental data.

Figure 4.6: Measured (dashed) and modeled (solid), absolute value of the T_{22} element of the flame transfer function versus Strouhal number at $y_{f,ref}$ and $u = 1.4\ u_{ref}$.

Figure 4.7: Measured (dashed) and modeled (solid), phase of the T_{22} element of the flame transfer function versus Strouhal number at $y_{f,ref}$ and $u = 1.4\ u_{ref}$.

In the comparisons, the most important transfer matrix element is T_{22} which links the acoustic velocity upstream and downstream of the flame. In fact, as shown by the experimental data the T_{11} element is approximately constant in amplitude and phase, while T_{12} and T_{21} are approximately zero.

In Figs. 4.6 and 4.7, a comparison between the measured transfer function and the modeled transfer function is shown for $\bar{u}_1 = 1.4\ \bar{u}_{1,ref}$ and mass fraction $y_{f,ref}$. Note that the values of τ, σ are obtained by fitting the model to experimental data.

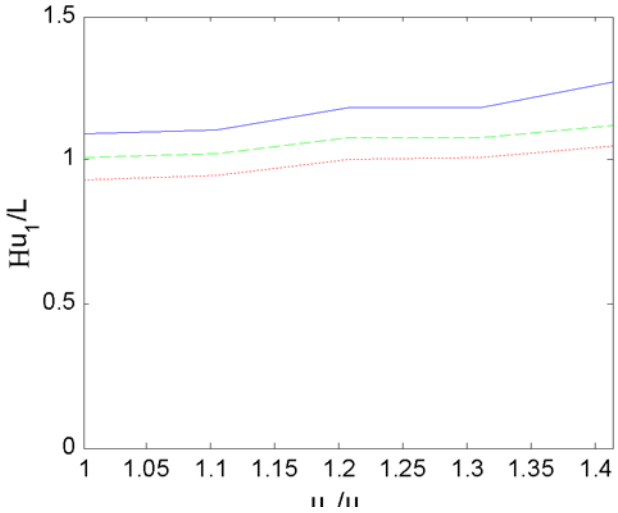

Figure 4.8: The normalized mean values of the time delays, $\bar{\tau}$, plotted against medium velocity for several values of the adiabatic flame temperature - $y_{f,ref}$ (solid), $y_{f,ref}$ + 5% (dashed), $y_{f,ref}$ + 10% (dotted).

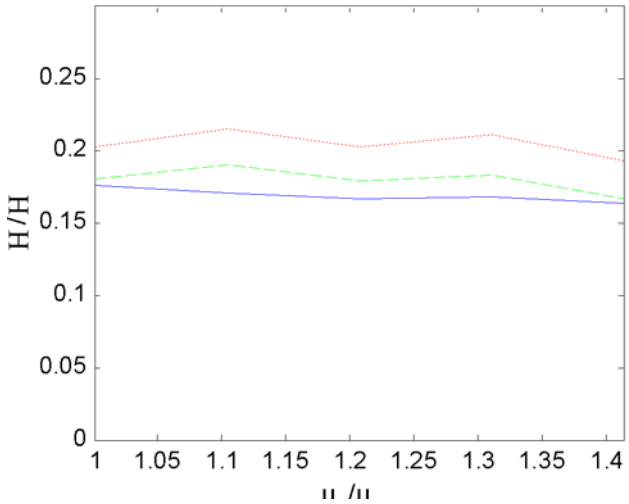

Figure 4.9: The normalised standard deviation of the time delays, σ plotted against medium velocity for several values of the adiabatic flame temperature - $y_{f,ref}$ (solid), $y_{f,ref}$+5% (dashed), $y_{f,ref}$ + 10% (dotted).

In Figs. 4.8-4.10, the values of τ and σ are plotted as a function of velocity at several levels of the fuel mass fraction. From Fig. 4.8, two trends can be observed. First, the average time delay

between fuel injection and fuel consumption, τ, decreases with increasing medium velocity. This is expected because τ is a convective time lag corresponding to: $\tau \sim L/u_1$, in which L is the characteristic length between fuel injection and fuel consumption. Because the time delays are normalised by L/u_1, nearly horizontal lines are obtained in Fig. 4.8. The second observation is that $\bar{\tau}$ decreases with increasing flame temperature. This is in agreement with the experimental observation that the flame stabilizes closer to the burner exit at higher flame temperatures. The standard deviation of the time delays, decrease strongly with increasing velocity, but is not strongly dependent on the temperature, as can be seen in Fig. 4.9. This can be explained by a diffusive effect: the longer the time delays, the more diffusion (the more spread in time delays). However, a detailed analysis of the flow field and the flame structure is required to analyse this effect quantitatively.

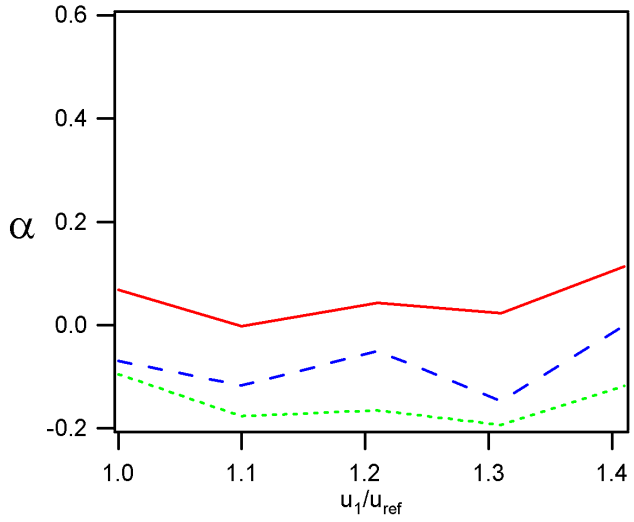

Figure 4.10: The values of the exponent α plotted against medium velocity for several values of the adiabatic flame temperature - $y_{f,ref}$ (solid), $y_{f,ref} + 5\%$ (dashed), $y_{f,ref} + 10\%$ (dotted).

The best fit to the experimental data was obtained with $\alpha = -0.0012$. This means that fluctuations of the laminar flame speed do not affect fluctuations in the turbulent burning velocity. This indicates that the turbulent flame speed in this flow is mostly determined by turbulence, and has only a weak dependence on the laminar flame speed. This is generally true for high Damköhler numbers. In the limit of $\alpha = 0$ fluctuations of the flame speed are de-coupled of the acoustic field. This means that the flame front fluctuations are equal to the acoustic velocity fluctuations. In Fig. 4.11 the absolute value of the T_{22} element of the transfer matrix is shown for different values of α.

A laser measurement technique has been used to obtain time resolved fuel mass fraction measurements. This technique makes use of the property that CH_4 absorbs infrared light. An infrared laser beam was send through the fuel-air mixture, and the intensity of the out coming laser beam was measured. Thus, the absolute value of this intensity has an inverse proportionality with the fuel concentration. The heat release rate has been monitored by means of OH

Figure 4.11: The absolute value of the T_{22} element versus Strouhal number plotted for several values of α.

chemiluminescence measurement. The intensity of light emitted by OH radicals is assumed to have some proportionality with the heat release. The set-up is shown in figure 4.12.

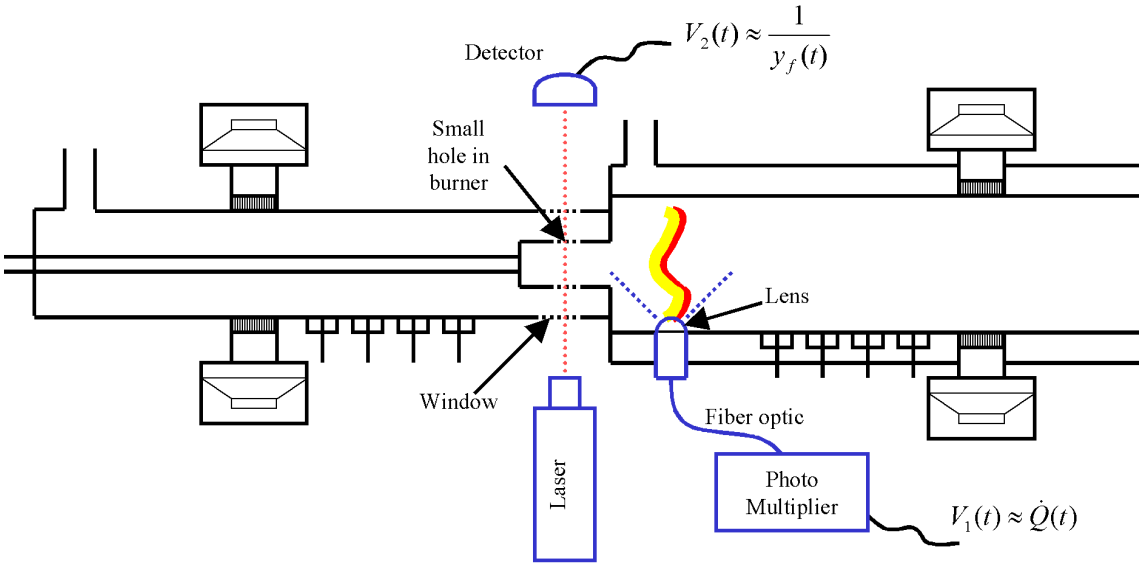

Figure 4.12: Experimental set-up for simultaneous measurement of transfer matrices, equivalence ratio fluctuations and heat release fluctuations.

Transfer matrix measurements have been performed for three different operating conditions. The chemiluminescence measurement and fuel mass fraction measurement have been performed simultaneously with these transfer matrix tests. The response of the mass fraction fluctuation

measurement ($V_1(t)$) and heat release fluctuations ($V_2(t)$) to the pure tone forcing was then evaluated using the method described in chapter 3. In this way an estimate of the transfer function between "heat release" and "fuel concentration fluctuations" was obtained by $H(\omega) = \frac{\hat{V}_2}{-\hat{V}_1} \approx \frac{\hat{Q}}{\hat{y}_f}$. Note, that care should be taken when giving a physical interpretation to the absolute value of the transfer function obtained in this way. This is because the signals only have *some proportionality* to the physical quantity. However, the phase relation between the two quantities should reflect the physical phase difference. Moreover, the signal delivered by the laser did not have a constant intensity in time (fluctuating with a time scale much larger than the forcing frequency). Development of the laser measurement technique was not part of this work, therefore this method will not be explained in detail here. A very similar technique was used by [70, 77], a detailed description of the method can be found in their papers.
By making use of Eq. 2.111 and 4.10 it can be seen that the following relation is found between the heat release, mass fraction fluctuations and the T_{22} matrix element.

$$\angle(\frac{\hat{Q}}{\hat{y}_f}) = \angle(\mathcal{F}^*\{\xi\}) = \angle(1 - T_{22}) \tag{4.18}$$

Thus, if the proposed model is correct, the phase of the measured transfer function $H(\omega)$ should correspond to the phase of $(1-T_{22})$. Note that when a Gaussian time delay distribution is used, $\angle(\mathcal{F}^*\{\xi\}) = -\omega\,\bar{\tau}$. This comparison has been made in figure 4.13, note that only the phases should be compared. The comparison shows that the phase of both quantities is very similar, and has the same trend when varying the flame temperature. Moreover, the phase characteristic is nearly linear which is consistent with the predicted trend of $-\omega\,\bar{\tau}$.

4.4 Approximations

In this section, an approximation of the Fourier transform of the Gaussian distribution will be derived. In order to avoid a convolution integral in the time domain simulations, the function will be approximated by a time delay in series with a second order system.
The $n-\tau$ model with distributed time delays:

$$H = e^{-s\bar{\tau}} e^{\frac{1}{2}s^2\sigma^2}, \tag{4.19}$$

will be approximated by a delay (τ^*) and a second order system with parameters α and β:

$$F = n\ e^{-s\tau^*} \frac{1}{(\alpha s+1)(\beta s+1)}. \tag{4.20}$$

The choice of this equation is based on two considerations:

1. in the original equation a time delay is present. A time delay is of infinite order, so the approximating function should also contain an element of infinite order.

2. the magnitude of the original equation decreases strongly with frequency - a second order system can reproduce the same effect.

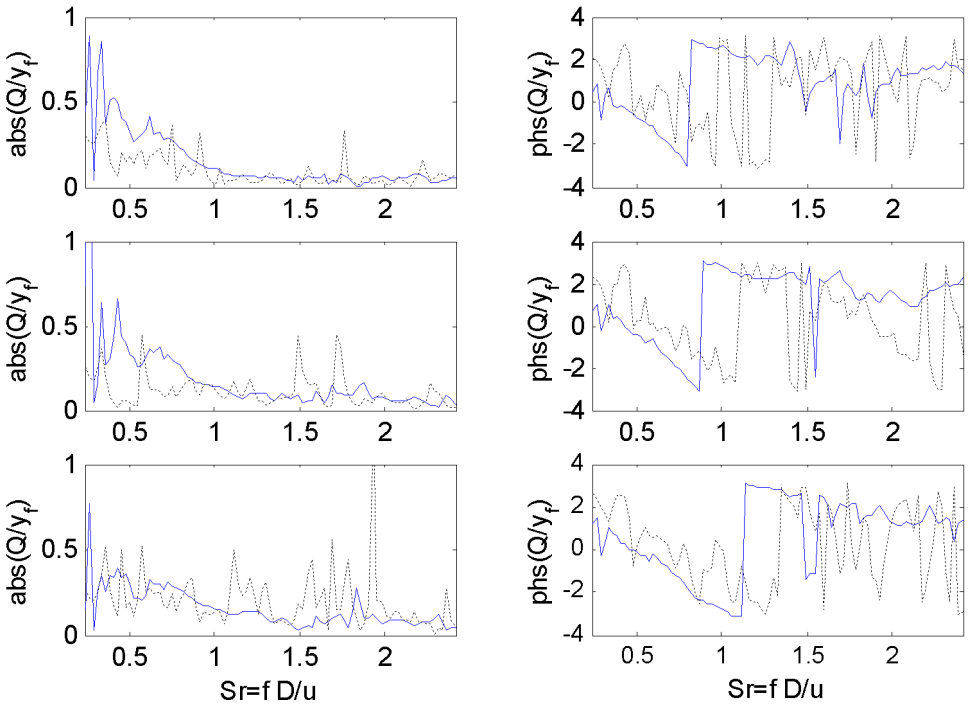

Figure 4.13: The absolute values and phase of $T_{22} - 1$ and of $-H(\omega) = \hat{V_2}/\hat{V_1}$.

A complex exponential can be expanded in series as:

$$e^z = \sum_{n=0}^{\infty} \frac{z^n}{n!}. \tag{4.21}$$

Expanding H up to the second the term, the following relation are found for α and β:

$$\alpha = \frac{(\bar{\tau} - \tau^*) - \sqrt{(\bar{\tau} - \tau^*)^2 + 2\sigma^2}}{2} \tag{4.22}$$

$$\beta = \frac{(\bar{\tau} - \tau^*) + \sqrt{(\bar{\tau} - \tau^*)^2 + 2\sigma^2}}{2} \tag{4.23}$$

$$. \tag{4.24}$$

To ensure that the function is real and stable, the following inequality needs to be fullfilled: $0 < \tau^* < \bar{\tau} - \sqrt{2}\sigma$. It was found that the best approximation was obtained when τ^* is large. Therefore, the maximal value was chosen: $\tau^* = \bar{\tau} - \sqrt{2}\sigma$.
Thus the approximation of the Fourier transform of the Gaussian distribution is found to be:

$$H = \frac{e^{-s(\bar{\tau} - \sqrt{2}\sigma)}}{\frac{1}{2}\sigma^2 s^2 + \sqrt{2}\sigma s + 1} \tag{4.25}$$

The approximated transfer function of the flame model is then simply $1 + n\ H$.

4.5 Non-linearities

The acoustic flame model with distributed time delays is linear. This may be a valid assumption for small amplitudes of oscillation, however, for sufficiently large amplitudes, the linearity assumption will no longer hold. If the linear representation of the combustion system is unstable, this would mean that infinitesimally small disturbances will grow exponentially to infinitely large amplitudes. Because infinite amplitudes do not exist in technical systems, it is clear that there must be some non-linear mechanism that limits the exponential growth. Strictly speaking, a combustion system will never be unstable, because the amplitudes are always finite. In this respect it is important to make a distinction between stability and asymptotic stability. An asymptotically stable acoustic system has an impulse response that decays to zero after sufficient time, while a system is said to be stable if all amplitudes of the system remain bounded, i.e., finite.
The acoustic amplitudes encountered in gas turbine combustion chambers are generally low enough to ensure the validity of the linear acoustic wave equation as far as wave propagation is concerned. Therefore, it is assumed here that the non-linear limiting effect is due to a limitation of the periodic heat release. In the acoustic flame model, the amount of fuel injected is assumed to be constant. Fluctuations in equivalence ratio are then created by fluctuations of the acoustic velocity at the injection location. The heat release is then assumed to be proportional to the equivalence ratio. This last assumption (heat release proportional to equivalence ratio) will not hold for large amplitudes. This can easily be understood by considering the dependence of the mean (steady) heat release as a function of equivalence ratio:

- for very low equivalence ratios the flame will extinguish and the heat release is therefore zero
- for equivalence ratios larger then unity not all fuel will be consumed
- for very large equivalence ratios the flame will also extinguish

Note that the acoustic velocity fluctuations are not necessarily small compared to the mean velocity, thus the equivalence ratio fluctuations are not necessarily small compared to the mean value either. Deriving a thermoacoustic model that describes the non-linear physical processes in the flame accurately will be very difficult, if possible at all. Therefore, an ad hoc systems approach will be used to describe the phenomenon: the flame will simply be assumed to extinguish locally if the equivalence ratio is lower than a certain threshold value. It is important to note that the flame will only extinguish locally, it will not blow off completely.
The flame can therefore be considered to consist of multiple flame models in parallel, each sub-model having it's own time delay (τ) and it's own saturation function (Γ). Expressing the linearized sub-models as an $n-\tau$ model: $u_2' = u_1' + nu_1'(t-\tau)$, the saturated sub-functions are written as: $u_2' = u_1' + n\Gamma^*\{u_1'(t-\tau)\}$. Note that the saturation function (Γ^*) acts here on $u_1'(t-\tau)$ rather than on the heat release. This was done for ease of notation, for the final result this does not matter because the heat release is directly proportional to the velocity fluctuations. This saturation function can be expressed as:

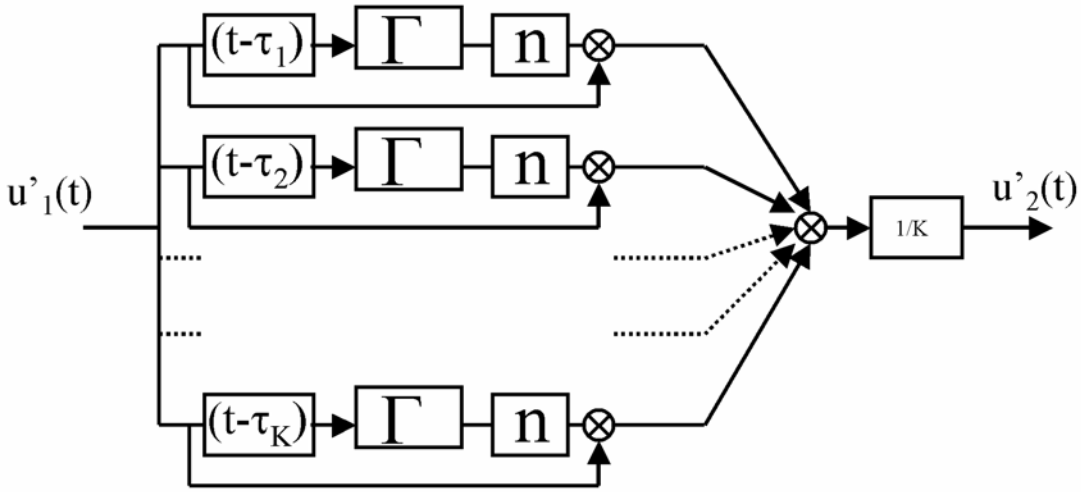

Figure 4.14: System of parallel flames with non-linear saturation.

$$\Gamma^*\{u_1'(t-\tau)\}\begin{cases} u_{lim} & \text{if} \quad u'(t-\tau) < u_{lim} - \bar{u} \\ u_1'(t-\tau) & \text{if} \quad u_{lim} - \bar{u} < u'(t-\tau) < \bar{u} - u_{lim} \\ u_{lim} & \text{if} \quad u'(t-\tau) > \bar{u} - u_{lim} \end{cases}$$

The system of K parallel flames can be represented in a block diagram as shown in Fig. 4.14. In this diagram, $(t-\tau_k)$ represents the k^{th} time delay.
If the saturation functions in this diagram would have been placed before the time delay, the system would have the same input-output relation, because the delay only causes a phase shift. Thus, the saturation function may as well be placed such as to act directly on $u_1'(t)$. This makes clear that the system of Fig. 4.14 can simply be represented by:

$$u_2'(t) = u_1'(t) + n\Gamma\{u_1'(t)\} * \xi(\tau), \tag{4.26}$$

in which $*$ denotes the convolution product between two signals.
Following this line an "effective" equivalence ratio in the presence of the non linear saturation function can be defined in a similar way:

$$\begin{aligned} y'_{f,1}(t) &= \int_{\tau=0}^{\infty} \xi(\tau)\Gamma\{y'_{f,i}(t-\tau)\}d\tau & (4.27) \\ &= \Gamma\{y'_{f,i}(t)\} * \xi(\tau) & (4.28) \end{aligned}$$

4.6 Discussion

An acoustic transfer matrix model for lean-premixed flames is presented. The model accounts for heat release fluctuations due to both fluctuations in fuel concentration and flame speed. A "time-lag" model is employed to model the fuel concentration fluctuations which are produced by air fluctuations at the injector location and thereafter convected to the flame.
Phase-locked images demonstrate that temporal fluctuations of the flame shape are minimal. They are therefore neglected in this analysis. The model accounts for acoustic fluctuations of the flame speed. The flame model has two unknowns: the distribution of the time delays and the dependence of the flame speed on the laminar burning velocity. These a-priori unknown parameters are obtained by fitting the model to measured transfer functions. Starting from the general flame model, influence of flame velocity and distribution of time delays have been validated. The flame transfer function of a swirl stabilized lean premix combustor is obtained experimentally in an atmospheric test facility for a range of operating conditions.
A very good agreement between measured data and the analytical model is found. The values obtained for the time delays show a strong correlation between the ratio of mean flow velocity and estimated distance between fuel injection and consumption. The dependence of the flame velocity on the laminar flame velocity is found to be very weak, which can be expected in combustion processes dominated by turbulence.
A non-linear saturation mechanism has been introduced in the flame transfer function. The description of the (static) non-linearity is not based on physical models but on an ad-hoc systems modeling assumption. A detailed, physical understanding of the non-linear processes in the flame would require transfer function measurements and flame visualization at different (very high) forcing levels. This is recommended as a future research activity.
Although the derived model demonstrated to be in good agreement with experimental results, it should be noted that different mechanism could lead to a similar transfer function. A possible candidate for such a mechanism is based on heat release fluctuations caused by periodic vortex shedding. It is well known that a confinement in a flow may cause periodic vortex shedding. This mechanism of vortices that build up can be triggered by acoustic waves. Because vorticity convects with mean flow as well, they could exhibit a similar time-lag behavior as the aforementioned equivalence ratio mechanism. Recent experimental results demonstrate that when the air and fuel are mixed far upstream of the burner (and thus avoiding equivalence ratio fluctuations near the burner), the magnitude of the transfer function relating the acoustic velocities is decreased by a factor four. This is a strong indication that equivalence ratio fluctuations are of crucial importance in the thermoacoustic interaction mechanism. Nevertheless, even in the case of completely temporal uniform mixture supply, the transfer matrix was not completely passive, and could, in principle, cause thermoacoustic instabilities.

Chapter 5

System Analysis

5.1 Introduction

In this chapter, the representation of thermoacoustic systems as networks of acoustic elements will be discussed. An important issue is the inter-connection with annular ducts – three possible ways for doing this have been investigated. The first method consists of a quasi two-dimensional description of annular ducts. By making use of the symmetry of annular ducts, an annular combustion system can be represented by a one-dimensional network. The advantage of this method is its simplicity. A disadvantage is that only rotationally symmetric systems can be investigated. Furthermore, it is a typical frequency domain approach, making this method less suitable for the design of control systems. Stability analysis of these systems requires a numerical search in the complex plane which is difficult because the equations are discontinuous. This method, which was developed by Polifke et. al. [105] will be referred to as the *1-D Wave Propagation Method* . In order to overcome the limitation to rotationally symetric systems, a new method has been developed that makes use of expansion of the acoustic field in Fourier series. This method proved to be successful for relatively simple systems. However, more complex systems became badly conditioned, and in some cases numerical difficulties were encountered. This method will be referred to as the *Fourier Expansion Method*. Because this model proved to be not suitable for control design and testing, a third method has been developed in this work: the *Modal Expansion Method*. This method can be analyzed in frequency *and* time domains. The stability analysis is straightforward and does not require a numerical search, guaranteeing that all eigenvalues of the system are found in one step. The method is not restricted to rotationally symmetric ducts; in fact, any geometry can be included. Very complex geometries can be included by using input from Finite Element Packages. In this method, a state-space representation of the system is used, thus making the method suitable for control system design.

5.2 System Analysis in the Frequency Domain

In this section, the analysis of relatively simple thermoacoustic systems will be addressed. Thermoacoustic stability will be addressed from three different points of view:

1. energy balance analysis, using impedances and reflection coefficients in the frequency domain as done in "classical" acoustics

2. addressing the Rayleigh criterion

3. using the passivity criterion.

All of these methods are "frequency domain" methods. The aim is to show the similarities between these methods. As well, these simple examples will give good insight as to how different modeling and analysis techniques presented in this work can be combined. In section 5.6 a different stability analysis method is addressed.
Generally it does not matter whether a linear system is analyzed in the time domain or in the frequency domain (both representations carry the same information). It should be noted, however, that the frequency is a complex quantity. Thus the system should be known in the entire complex plane. If it is known a priori that the system under consideration is stable, then it is sufficient to know the system as a function of real valued frequency to get a full description of the system (See § 3.3. for more details). Systems in classical acoustics without mean flow are known to be stable. Therefore, it is sufficient to analyze these systems as a function of real frequency, time domain behavior can then be recovered via an inverse Fourier transform. If interactions with mean flow or heat release occur, then the acoustic system may become linearly unstable. In this case, the system is no longer described by the (real valued) frequency response. Nevertheless, frequency responses can be useful, provided the system is split into sub-systems in an appropriate way. The possibilities and limitations of such an approach will be discussed in this section.
We will start with a very simple but also very generic combustion system: two volumes connected by compact reaction zone. It is assumed here that the acoustic field in the reaction zone is one-dimensional: only axial wave propagation. A sketch of such a system is given in Fig. 5.1.

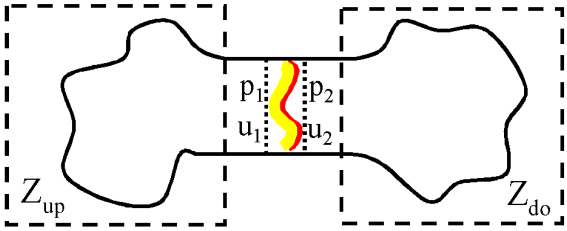

Figure 5.1: Generic thermoacoustic system.

In this system, the upstream geometry is referred to as Z_{up}, the downstream geometry as Z_{do}, because they are entirely described by the acoustic impedances $Z_{up} = \frac{\hat{p}_1}{-\hat{u}_1}$ and $Z_{do} = \frac{\hat{p}_2}{\hat{u}_2}$. The minus sign in the upstream impedance shows up because the impedance is defined based on a velocity pointing out of the surface. Both volumes are interconnected by the combustion zone. From the acoustic jump condition obtained in § 2.8, and from the experimental results in § 3, it is clear that the pressure across the flame can be considered continuous, while the unsteady heat release is mainly caused by the acoustic velocity. The dependence of the acoustic heat release on

the acoustic field will be given here as: $\hat{\dot{Q}} = F\,\hat{u}_1$, in which F is referred to as the heat release transfer function. If the fluctuating heat release is a function of equivalence ratio fluctuations only, then Eq. 4.1 can be written as:

$$\begin{aligned} \hat{u}_2 &= \hat{u}_1 + (\frac{T_2}{T_1} - 1)\bar{u}_1 \frac{\hat{y}_f}{\bar{y}_f} \\ &= \hat{u}_1 + (\frac{T_2}{T_1} - 1)\bar{u}_1 \frac{\hat{\dot{Q}}}{\bar{\dot{Q}}} \\ &= \hat{u}_1 + (\frac{T_2}{T_1} - 1)\frac{\bar{u}_1}{\bar{\dot{Q}}} F\,\hat{u}_1 \end{aligned} \tag{5.1}$$

And thus the heat release transfer function is $F = \frac{\hat{\dot{Q}}}{\hat{u}_1} = -\frac{\bar{\dot{Q}}}{\bar{u}_1} e^{-i\omega\tau} e^{-\frac{1}{2}\omega^2\sigma^2}$. For ease of notation, the transfer function between the acoustic velocities will be defined as: $\hat{u}_2 = H\hat{u}_1$. With these equations, the system is closed, and can be expressed in a block diagram as shown in figure 5.2:

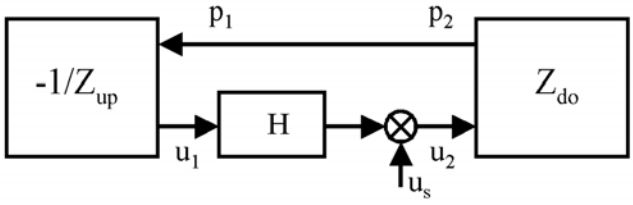

Figure 5.2: Block diagram of generic thermoacoustic system.

Such a representation might seem to be over simplified, but it is not. In fact, the more complex models describing the thermoacoustic behavior in an annular gas turbine combustion chamber can be cast in *exactly* the same block diagram. Therefore, it is worthwhile to analyze this system in greater detail. Note that a source has been added in this block diagram because the system would be trivial if it did not have any input. The response to the input source is then:

$$\hat{p} = \frac{Z_{do}}{1 + Z_{do} Z_{up}^{-1} H}\,\hat{u}_s \tag{5.2}$$

The eigenvalues of this system are the frequencies (complex valued) for which the denominator of Eq. 5.2. equals zero:

$$Z_{do}(\omega) Z_{up}^{-1}(\omega) H(\omega) = -1 \tag{5.3}$$

Note that this is a remarkably simple equation! Especially because the underlying assumptions are not very restrictive. The imaginary part of the eigenvalues (ω_i) determines the stability of the system. If the imaginary part of the eigenvalue (ω) is negative, the system is unstable. The real part of the eigenfrequency (ω_r) determines the instability frequency. However, solving this equation analytically for ω is not that straightforward, but can be done by using a numerical

search, provided of course that Z_{do}, Z_{up} and H are known functions of the (complex valued) frequency. If the system is on a stability *border*, then ω_i equals zero. Thus if the stability border of the system has to be found, $\omega = \omega_r$ may be substituted. In the case without acoustic losses in the two volumes, the real part of the impedances will be zero ($\Re\{Z(\omega_r)\} = 0$), thus the ratio of the two impedances will be real. It is then easily seen from Eq. 5.3 that the imaginary part of the flame transfer function should equal zero ($\Im\{H(\omega_r)\} = 0$). Assuming a flame transfer function as in Eq. 5.1, with $H = 1 - (\frac{T_2}{T_1} - 1)e^{-i\omega\tau}e^{-\frac{1}{2}\omega^2\sigma^2}$, it is readily seen that a stability border is encountered if $\omega\tau = n\pi$, in which n is an integer number. This is again a remarkably simple solution for a very general system, but does not supply much useful information because although the stability borders are known, it is not known at what side of the stability border the system is stable or unstable. It only says that at $\omega\tau = n\pi$ the system will change either from stable to unstable or from unstable to stable. However, if it is known (from experiment, from numerical analysis or by the Rayleigh criterion) that for one specific value of $\omega\tau$ the system is stable (or unstable) then the stability for all values of $\omega\tau$ are known by investigating $\omega\tau = n\pi$. The stability borders of systems with damping can be found by solving equation 5.4 :

$$Z_{do}Z_{up}^{-1}(1 - (\frac{T_2}{T_1} - 1)e^{-i\omega\tau}e^{-\frac{1}{2}\omega^2\sigma^2}) = -1 \tag{5.4}$$

for σ and τ:

$$\tau = \frac{-1}{\omega}\Im\{\ln(1 + \frac{Z_{up}}{Z_{do}}\frac{T_1}{T_2 - T_1}) + 2\,n\,\pi\} \tag{5.5}$$

$$\sigma^2 = \frac{-2}{\omega^2}\Re\{\ln(1 + \frac{Z_{up}}{Z_{do}}\frac{T_1}{T_2 - T_1}) + 2\,n\,\pi\}. \tag{5.6}$$

A parametric plot of $\sigma(\omega)$ versus $\tau(\omega)$ provides the stability borders of the system.
The boundary conditions may equally well be expressed as reflection coefficients. A reflection coefficient is the ratio between the outgoing and incoming wave or Riemann invariant, $R_{up} = \frac{f_1}{g_1}$ and $R_{do} = \frac{g_2}{f_2}$. Thus the reflection coefficients may be obtained from the following transform: $R = \frac{Z-\rho c}{Z+\rho c}$.
The system boundary of the upstream system will be changed such that it includes the combustion area. The upstream impedance that includes the flame will now be denoted by $Z_{up,f} = Z_{up}H^{-1}$. Expressing the two impedances in terms of their reflection coefficients, the dynamics of the system are governed by:

$$\frac{1}{1 - R_{up,f}R_{do}} \tag{5.7}$$

which is equivalent to the dynamics of Eq. 5.2. In this case, the eigenvalues can be found by solving $R_{up,f}(\omega)R_{do}(\omega) = 1$ for ω. Although this expression is equivalent to Eq. 5.3, it is more convenient because the reflection coefficients typically have order of magnitude 1, while the impedances may take values between $-\infty$ and $+\infty$. The stability of the system may be analyzed by making a parametric plot of $-R_{up,f}(\omega_r)R_{do}(\omega_r)$ in the complex plane and using Nyquist's stability criterion. This criterion states that if $R_{up,f}$ and R_{do} themselves are stable, then the entire system is stable if the parametric plot of $-R_{up,f}(\omega_r)R_{do}(\omega_r)$ does not encircle -1 in the clockwise direction. Note that the functions only need to be known as a function of

ω_r, thus one may equally well use measured reflection coefficients using the methods described in section 3. A sufficient condition for stability is thus: $|R_{up,f}R_{do}| < 1$. For slightly damped systems the absolute value of R_{do} will always be smaller than 1. Thus, the sufficiency criteria reduces to $|R_{up,f}| < 1$, which corresponds to $\Re\{Z_{up,f}\} > 0$. Conversely, a necessary condition for instability is $|R_{up,f}| > 1$, the sufficiency criterion then depends on the absolute value and phase of $R_{up,f}R_{do}$.

As mentioned before, both reflection coefficients should be stable in order to perform this analysis. If (one of) the reflection coefficients are (is) unstable (open-loop unstable), then the simplified Nyquist criterion may no longer be used, and the number of unstable open loop eigenvalues of the system should be known in order to analyze the system. The method would then not be useful because determining the number of unstable open loop eigenvalues requires approximately the same computational effort as determing the eigenvalues of the closed loop system directly. Thus it is of interest to investigate the likelihood of the open loop system being unstable. The upstream reflection coefficient, including the flame, is given by:

$$R_{up,f} = \frac{1 - \frac{H}{Z_{up}}}{1 + \frac{H}{Z_{up}}} \tag{5.8}$$

The flame transfer function is stable because H is a Finite Impulse Response system (which is always stable). If it is assumed that Z_{up} has some damping, chosen here to be infinitesimally small (worst case), then all eigenvalues and zeros of Z_{up} are stable, thus the inverse is stable as well. We may now use Nyquist's criterion to determine the stability of $R_{up,f}$, by investigating the stable open-loop system $Z_{up}^{-1}H$. The instability criterion is fulfilled if $|H(\omega)| > |Z_{up}(\omega) + 1|$. In absence of damping, and for $\sigma = 0$, it can easily be seen that a necessary condition for instability of the upstream reflection coefficient is: ($\frac{T_2}{T_1} > 2$). The sufficiency depends on the time delay (τ). Thus, the "simplified" Nyquist criterion may not be used under these conditions. From experimental observations in the test facility described in § 3 it is known that the system will *always* be stable if the downstream reflection coefficient is reduced to sufficiently low levels (even if the temperature ratio is larger than two). This can be explained because in a real test facility, the acoustic losses are considerable, and the spread of time delays in the flame (σ) is considerable. Thus, for this test facility, measured reflection coefficients may be used to analyze the stability. However, in numerical or analytical analysis the losses are often neglected (in order to analyze a worst case scenario) and σ assumed to be zero (time lag model). In these cases, it is incorrect to use the simplified Nyquist criterion if the temperature ratio exceeds two.

Because Z_{up}, Z_{do} and H are all stable transfer functions, the simplified Nyquist criterion *may* be used when plotting $H_o(\omega_r) = Z_{do}(\omega_r)Z_{up}^{-1}(\omega_r)H(\omega_r)$. This is, however, generally not very convenient because the values of the impedances can take extremely large or extremely small values. This disadvantage can be overcome by using appropriate scaling of the absolute value of the transfer function while leaving the phase angle unchanged. The following map proved very useful: $H_o(\omega_r) \rightarrow \arctan(|H_o(\omega_r)|)|H_o(\omega_r)|^{-1}H_o(\omega_r)$. However, such a map may be difficult to interpret, especially when several modes are close to instability.

There is a close link between the analysis presented before, the energy balance derived in §2.5, and the Rayleigh criterion. Consider that the system presented above is zero-dimensional, thus the spatial integral over the energy balance is easily obtained:

$$\frac{d}{dt}\mathcal{E} = (\gamma - 1)\frac{p_1'\dot{Q}'}{\rho c^2} - p_1'u_1' + p_2'u_2' \tag{5.9}$$

The first term on the right hand side can be considered as internal power generation, and the last two terms as external power input. Thus, E can be considered as the amount of energy stored in the system, while the right-hand term of Eq. 5.9 is a "supply rate", or "power flux".
The acoustic velocities may be eliminated by substituting the relation for the impedances. Furthermore, the heat release will be related to the acoustic pressure as: $\hat{\dot{Q}} = F\,\hat{u}_1 = -F\,\frac{1}{Z_{up}}\,\hat{p}_1$. The transfer function F_{Qp} will be defined here as the transfer function between pressure and heat release: $F_{Qp} = \frac{-F}{Z_{up}}$. Assuming periodic oscillations, the energy balance is integrated over one oscillation period ($T = \frac{2\pi}{\omega}$) in order to obtain the average energy gain over one cycle. Because all signals are real, the integral over the product of velocity and pressure is obtained as:

$$\frac{\omega}{2\pi}\int_0^{\frac{2\pi}{\omega}} p'(t)u'(t)dt = \frac{\omega}{2\pi}\int_0^{\frac{2\pi}{\omega}} (\hat{p}e^{i\omega t})^2\, Z^{-1}\, dt = \frac{1}{2}|\hat{p}|^2\Re\{Z^{-1}\}, \tag{5.10}$$

and similarly for the integral over pressure and heat release. The energy balance over one cycle is therefore:

$$\Delta E \;=\; \frac{1}{2}|\hat{p}|^2\frac{\gamma-1}{\rho c^2}\Re\{F_{Qp}\} - \frac{1}{2}|\hat{p}|^2\Re\{Z_{up}^{-1}\} - \frac{1}{2}|\hat{p}|^2\Re\{Z_{do}^{-1}\} \tag{5.11}$$

Thus the system gains energy if the dissipation on the boundaries is smaller than the energy added by the heat release term. If there are no losses in the upstream and downstream volumes, then $\Re\{Z_{up}^{-1}\} = 0$ and the Rayleigh criterion is recovered: the system gains energy if $\Re\{F_{Qp}\} > 0$ (if acoustic pressure and velocity are in phase). However, this does not mean that the system is unstable at every frequency where F_{Qp} has positive real part.
The energy balance and the Rayleigh criterion are closely related to the *passivity* property. A system is passive if the increase of energy storage ($\frac{d}{dt}\mathcal{E}$) is smaller than the supply rate [125, 121]. Thus it can be considered as a system that itself does not "produce" energy. A linear system is passive if and only if it is stable and if its transfer function (evaluated at positive, real frequencies) has a non-negative real part. Thus, the acoustic impedance (in classical acoustics) is an example of a passive system. It can be demonstrated [125, 121] that a negative feedback interconnection of two passive systems is passive as well[1] (and thus stable).
Analyzing, in this light, the system described in the introduction (Fig. 1.2) we may conclude that the transfer function from $\hat{\dot{Q}}$ to $\hat{p}$ is passive. The interconnected system will be *stable* if F_{Qp} is passive, thus if F_{Qp} has a *negative real part*, which corresponds to the result obtained before. Thus, the Rayleigh criterion can be considered as a passivity condition.
The modal expansion provides good insight into the stability of the system. Considering only one mode of (Eq. 2.90) and integrating over the volume yields:

[1] This holds as well for non-linear systems and MIMO systems.

$$\hat{p} = \frac{\psi^2(x_0)}{\lambda\,(\omega^2 - i\,\omega\,\alpha - \omega_n^2)}(1-\gamma)\,i\,\omega\hat{\dot{Q}}, \tag{5.12}$$

after substituting the relation for the heat release, the homogenous equation can be written as:

$$-\omega^2 + i\,\omega\,\alpha + \omega_n^2 = \frac{\psi^2(x_0)}{\lambda}(\gamma-1)\,i\,\omega F_{Qp}. \tag{5.13}$$

Generally, the transfer function, F_{Qp}, depends on the flame transfer function and on the geometry of the combustion system. Nevertheless, in order to investigate the influence of the phase relation between acoustic pressure and velocity, it is useful to assume a time delay model between heat release and pressure fluctuations. The right hand term of Eq. 5.13 can then be written as: $\epsilon\,i\,\omega e^{-i\,\omega\tau}$. In which τ is the time delay, and ϵ is some interaction coefficient. If the interaction coefficient is very small, then the instability frequency will be close to ω_n. An approximate solution of Eq. 5.13 for the eigenvalue (ω) is then found:

$$\omega_{eig} \approx \omega_n + i\,\alpha - i\,\epsilon\,e^{-i\,\omega\tau} \tag{5.14}$$

The system is unstable if the imaginary part of the eigenvalue (ω_{eig}) is smaller than zero. Thus from Eq. 5.14 it is clear that the system is unstable if $\omega\tau = 0$ (heat release in phase with pressure) and $\epsilon > \alpha$ (thermoacoustic amplification larger than damping). The dependence of the eigenvalue ω_n as a function of τ is sketched in figure 5.3.

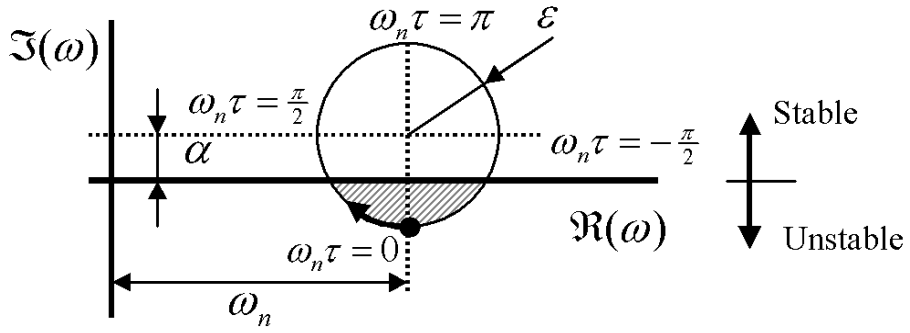

Figure 5.3: Eigenvalues as a function of phase between heat release rate and pressure ($\omega\tau$)

This figure also makes clear that if the phase difference between heat release and pressure is $\pm\frac{\pi}{2}$, then the stability of the system is not affected, but the frequency of instability ($\Re(\omega_{eig})$) changes. This is in accordance with [108].

5.3 Annular Geometries

The *1-D annular method* and *Fourier expansion method* will be mentioned briefly here, more attention will be paid to the *Modal Expansion Method*.

5.3.1 Wave Propagation Method (Quasi 1-D)

Starting from the solution of the wave equation for a thin annular duct (Eq. 2.54), neglecting the radial dependence ($m = 0$), and assuming rotational symmetry: $R_{\pm+} = R_{\pm-}$, using the notation $f = R_{++} = R_{+-}$ and $g = R_{-+} = R_{--}$, then because:

$$e^{-ik_x^{\pm}x - i\frac{2n}{D}y} + e^{-ik_x^{\pm}x + i\frac{2n}{D}y} = 2e^{-ik_x^{\pm}} cos(\frac{2n}{D}y), \tag{5.15}$$

equation Eq. 2.54 can be written as:

$$\frac{\hat{p}(x,y,\omega)}{\rho c} = \sum_{n=0}^{N}(f_n e^{-ik_x^{+}x} + g_n e^{-ik_x^{-}x})\cos(\frac{2n}{D}y), \tag{5.16}$$

$$\hat{u}(x,y,\omega) = \sum_{n=0}^{N}(f_n\kappa^{+} e^{-ik_x^{+}x} + g_n\kappa^{-} e^{-ik_x^{-}x})\cos(\frac{2n}{D}y), \tag{5.17}$$

$$\tag{5.18}$$

with:

$$k_x^{\pm} = \frac{\frac{-\omega}{c}M \pm \sqrt{(M^2-1)((\frac{\pm 2n}{D})^2) + (\frac{\omega}{c})^2}}{1-M^2} \tag{5.19}$$

$$\kappa^{\pm} = \frac{k_x^{\pm}}{k - Mk_x^{\pm}} \tag{5.20}$$

Note that the origin of y can be chosen arbitrarily. The notation $\breve{p}_n(x,\omega)$ will be introduced for the maximum value of the acoustic pressure in the azimuthal direction: $\hat{p}_n(x,y,\omega) = \breve{p}_n(x,\omega)\ \cos(\frac{2n}{D}y)$. Denoting conditions at the inlet of the duct by the subscript u and outlet by subscript d, the following relations are obtained between inlet and outlet for the n^{th} circumferential mode:

$$\begin{bmatrix} \breve{p}_u \\ \breve{u}_u \end{bmatrix} = \begin{bmatrix} 1 & 1 \\ \kappa^{+} & \kappa^{-} \end{bmatrix}\begin{bmatrix} \hat{f}_u \\ \hat{g}_u \end{bmatrix}, \qquad \begin{bmatrix} \breve{p}_d \\ \breve{u}_d \end{bmatrix} = \begin{bmatrix} 1 & 1 \\ \kappa^{+} & \kappa^{-} \end{bmatrix}\begin{bmatrix} \hat{f}_d \\ \hat{g}_d \end{bmatrix}. \tag{5.21}$$

$$\begin{bmatrix} \hat{f}_d \\ \hat{g}_d \end{bmatrix} = \begin{bmatrix} e^{-ik_n^{+}L} & 0 \\ 0 & e^{-ik_n^{-}L} \end{bmatrix}\begin{bmatrix} \hat{f}_u \\ \hat{g}_u \end{bmatrix}. \tag{5.22}$$

The transfer matrix relating the acoustic quantities at the inlet to the outlet can thus be written for one mode as:

$$\begin{aligned} \begin{bmatrix} \breve{p}_d \\ \breve{u}_d \end{bmatrix} &= \begin{bmatrix} 1 & 1 \\ \kappa^{+} & \kappa^{-} \end{bmatrix}\begin{bmatrix} e^{-ik_n^{+}L} & 0 \\ 0 & e^{-ik_n^{-}L} \end{bmatrix}\begin{bmatrix} 1 & 1 \\ \kappa^{+} & \kappa^{-} \end{bmatrix}^{-1}\begin{bmatrix} \breve{p}_u \\ \breve{u}_u \end{bmatrix} \\ &= \frac{1}{\kappa^{+}-\kappa^{-}}\begin{bmatrix} \kappa^{+}e^{-ik_n^{+}L} - \kappa^{-}e^{-ik_n^{-}L} & e^{-ik_n^{+}L} - e^{-ik_n^{-}L} \\ \kappa^{+}\kappa^{-}(e^{-ik_n^{+}L} - e^{-ik_n^{-}L}) & \kappa^{+}e^{-ik_n^{+}L} - \kappa^{-}e^{-ik_n^{-}L} \end{bmatrix}\begin{bmatrix} \breve{p}_u \\ \breve{u}_u \end{bmatrix} \end{aligned} \tag{5.23}$$

Note that if $n = 0$, this corresponds to the transfer function of a simple one-dimensional duct with mean flow. In the case of a one-dimensional duct, the Riemann invariants f and g can be considered as two disturbances (or waves) traveling in opposite directions at the speed of sound. In the case of an annular duct, the Riemann invariants f and g may be interpreted in a similar way because these are disturbances travelling in the axial direction as well. The difference is that in this case, the physical disturbance is generally not traveling in the axial direction, but in any direction. If, for convenience, the Mach number is assumed to be zero, then the wave travelling in the positive axial direction can be written as: $fe^{-ix\sqrt{(\frac{\omega}{c})^2-(\frac{2n}{D})^2}}$. This is the projection on the axial direction of the physical disturbance that propagates at an angle, α, to the x-axis. The propagation angle (α) is given by $\sin(\alpha) = \frac{2cn}{\omega D}$. The propagation speed in the axial direction is $c_x = \{(\frac{1}{c})^2 - (\frac{2n}{\omega D})^2\}^{-\frac{1}{2}}$, thus the propagation velocity in the axial direction is always larger than the speed of sound, except for longitudinal modes ($n = 0$). At the cut-off frequency ($\omega = \frac{2cn}{D}$) the f and g waves propagate in the axial direction with infinite speed! The angle of propagation of the physical disturbance is then $\pm 90°$. At frequencies lower than the cut-off frequency, the magnitude of f *increases* exponentially in the axial direction, while the direction of propagation is reversed. f then travels in the upstream direction (thus in the direction of propagation, the magnitude decreases). It should be clear from this analysis that f and g can still be considered as waves traveling in opposite directions, however, care should be taken with the physical interpretation. Although this is not done here, $k_x^{\pm}$ can be defined in a different way to ensure that f is always traveling in the positive direction and g always in the negative direction, even for frequencies below the cut off frequency. However, for the final result (in terms of pressures and velocities) this does not matter.

If the transfer matrices of the other subsystems (burner, flame, etc.) in the combustion system are known, then all the transfer matrices can be combined in one system of equations:

$$\mathbf{S}(\omega, \mathbf{n})\mathbf{p} = \mathbf{e}, \tag{5.24}$$

in which the matrix $\mathbf{S}$ contains all the transfer functions, the vector $\mathbf{p}$ contains the unknown pressure and velocities at all the interfaces, while the vector $\mathbf{e}$ (the forcing vector) contains the acoustic sources of excitation in the system. The system can be solved for $\mathbf{p}(\omega)$, in order to obtain the frequency response of the system. If a linear system is stable, then the absolute value of this frequency response corresponds to the absolute value of the Fourier transform of the (steady state) time domain signal. However, this is not the case if the system is unstable, simply because an unstable system grows without limitation, and does not have a steady state. The frequency response data can easily be misinterpreted if no information about the stability of the system is available. Note that the *more unstable* a linear system is, the *lower* the peak in the frequency spectrum will be. This is a general property of unstable linear systems, thus no matter what modeling approach is used, the frequency response of a linear system is useless if the system is not guaranteed to be stable.

Stability of the system can be assessed by solving the homogeneous system $\mathbf{S}(\omega, \mathbf{n})\mathbf{p} = \mathbf{0}$. Apart from the trivial solution $\mathbf{p} = \mathbf{0}$, non-trivial solutions exist for those ω where the determinant of $\mathbf{S}(\omega, \mathbf{n})$ equals zero. These values of ω are eigenfrequencies (or poles) of the system and

are generally complex. The system is said to be stable if there are no eigenfrequencies with a negative imaginary part. Solving $|\mathbf{S}(\omega, \mathbf{n})| = 0$ requires a numerical search of complex roots of a complex function, which can be done using standard numeric routines. The acoustic system under consideration has an infinite number of eigenfrequencies, this is because of the time delays in the system which have an infinite order. Strictly speaking, all eigenfrequencies would have to be found numerically to prove stability of the system, which is impossible in finite time. Practically, however, the system model is only valid in a certain frequency range, the search of eigenvalues can then be restricted to this frequency band. Nevertheless, this approach may be dangerous, because there is no proof that all relevant eigenfrequencies have been found in the frequency band.

The function $|\mathbf{S}(\omega, \mathbf{n})|$ is generally not continuous, but will have branch cuts. This can easily be seen from Eq. 5.19: the square root of a complex value is taken, and it is well known that the square root function has a branch cut. This may cause numerical difficulties in root finding, because bracketing methods do not work.

Note that because the azimuthal modes are orthogonal, the system may be evaluated independently for every mode. This property will be used later when deriving active control algorithms for annular combustion systems.

An advantage of the approach described here, is that the mean flow effect is included. In order to investigate the influence of the mean flow on the acoustic waves in an annular duct, the eigenfrequencies have been calculated for a closed-closed annular duct. Thus, the following boundary conditions have been imposed on Eq. 5.23: $\breve{u}_d = 0$ and $\breve{u}_u = 0$. After rearranging the equations and solving the homogenous equation for ω, the eigenfrequencies are found to be:

$$\omega = c\sqrt{(1-M^2)\left\{\left(\frac{2n}{D}\right)^2 + (1-M^2)\left(\frac{w\pi}{L}\right)^2\right\}} \tag{5.25}$$

Expressing the ratio of the diameter (D) and the length (L) of the duct as β, the relative change of the eigenfrequencies due to the mean flow is expressed as:

$$\frac{\omega}{\omega_{M=0}} = \sqrt{\frac{(1-M^2)\{(2n\beta)^2 + (1-M^2)(w\pi)^2\}}{(2n\alpha)^2 + (w\pi)^2}} \tag{5.26}$$

This relative change of the frequency has been plotted as a function of the Mach number in figure 5.4. A separate plot for each value of the azimuthal mode (n) has been made. A diameter to length ratio (β) of 4 has been chosen. This is typical for a gas turbine combustion chamber. In each plot, four curves have been plotted corresponding to axial modes $w = 0, 1, 2, 3$ (except for the trivial combination where $w = 0$ and $n = 0$). In the first plot, ($n = 0$), the four lines coincide, and are thus indistinguishable, which can be directly understood by investigating Eq. 5.26. In the third plot ($n = 2$) the lines do not coincide exactly, but are very close. At first thought, it might be surprising that even for a purely azimuthal mode ($w = 0, n = 1$) there is an influence of the Mach number on the resonance frequency. However, it should be considered that although the wave propagates in a direction orthogonal to the axis, the direction of the wave propagation is not orthogonal to the mean flow direction if a coordinate system is used

that moves with the mean flow. The mean velocity of the flow in a gas turbine combustion chamber is generally smaller than $M = 0.03$. Figure 5.4 shows that for these low mach numbers the influence of the mean flow is negligible. Nevertheless, the influence of the Mach number on the boundaries will generally not be negligible. Note that a closed-closed duct with mean flow is a physical contradiction because the flow has to come in somewhere. However, it is assumed here that for a more realistic configuration, the order of magnitude of the influence will be the same.

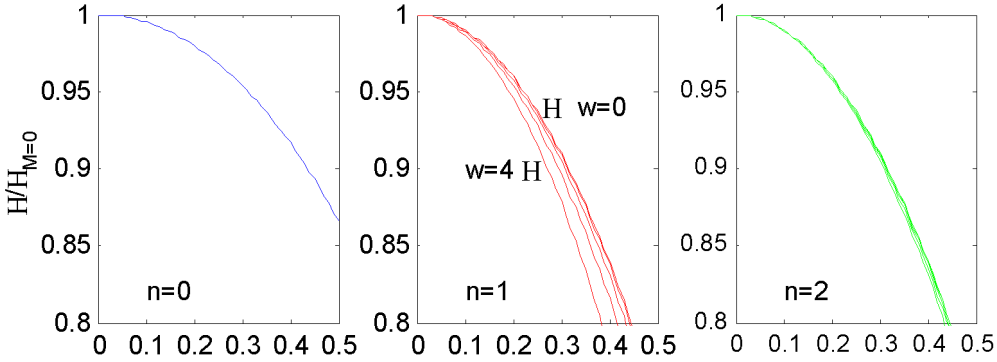

Figure 5.4: Influence of Mach number on the eigenvalues of a closed-closed annular duct for three longitudinal modes (w) and four azimuthal modes (n).

5.3.2 Fourier Expansion Method (Quasi 2-D)

The Fourier expansion method is similar to the previously described method, however, in this case no rotational symmetry is assumed. This method can be used to analyze the three-dimensional wave propagation in combustion systems with multiple burners, where the burners do not need to have the same transfer functions. Within the framework of this approach, it is straightforward to apply impedances at the entrance or exit of the ducts that vary with the azimuthal coordinate. As a starting point, Eqns. 2.57 and 2.58 are used. The idea is to discretise the system in the azimuthal direction and apply boundary conditions at coordinates $(x = 0, y_i)$ and $(x = L, y_i)$, where L is the length of the annular duct. From Eqns. 2.57 and 2.58, it is seen that $2 + 4\,N$ unknowns have to be solved, namely F, G and $r^{(n)}_{\pm\pm}$ with $n = 1 \ldots N$, thus the discretization in the azimuthal direction has to be done such that $2 + 4\,N$ boundary conditions are applied. The value of N should then be chosen such that a sufficient spatial resolution is obtained [2]. In order to avoid lengthy expressions, the following notation is adopted to express Eqns. 2.57 and 2.58:

$$
\begin{aligned}
\frac{p'(x,y)}{\rho c} &= \vec{R} \cdot \vec{H}_p(x,y) \qquad (5.27)\\
u'(x,y) &= \vec{R} \cdot \vec{H}_u(x,y)\\
&\text{with}\\
\vec{H}_p &= [P, -P, H^{n=1}_{++}, H^{n=1}_{+-}, H^{n=1}_{-+}, H^{n=1}_{--} \cdots H^{n=N}_{++}, H^{n=N}_{+-}, H^{n=N}_{-+}, H^{n=N}_{--}]\\
\vec{H}_u &= [P, -P, H^{*,n=1}_{++}, H^{*,n=1}_{+-}, H^{*,n=1}_{-+}, H^{*,n=1}_{--} \cdots H^{*,n=N}_{++}, H^{*,n=N}_{+-}, H^{*,n=N}_{-+}, H^{*,n=N}_{--}]\\
\vec{R} &= [F, G, R^{n=1}_{++}, R^{n=1}_{+-}, R^{n=1}_{-+}, R^{n=1}_{--}, \cdots, R^{n=N}_{++}, R^{n=N}_{+-}, R^{n=N}_{-+}, R^{n=N}_{--}]\\
&\text{and}\\
H^{n}_{\pm\pm} &= e^{-ik^{\pm}_x x - i\frac{\pm 2n}{D} y}\\
H^{*,n}_{\pm\pm} &= \frac{k^{\pm}_x}{k - M k^{\pm}_x} H^{n}_{\pm\pm}
\end{aligned}
$$

As a very simple example, consider an annular duct open on one side, $p'(x = 0, y) = 0$, and closed on the other side, $u'(x = L, y) = 0$, except for $y = 0$ where a source term (ϵ) is applied: $u'(x = L, y = 0) = \epsilon$. In order to obtain the same number of equations as unknowns, the azimuthal direction will be discretised in $1 + 2\,N$ points. The system of equations is then obtained as:

[2] This can be understood by considering that the series are Fourier expansions. By Nyquist's or Shanon's sampling criterion, the spatial resolution can not be smaller than $\frac{\pi D}{N}$.

$$\underbrace{\begin{bmatrix} \vec{H}_p(x=0,y_1) \\ \vdots \\ \vec{H}_p(x=0,y_{1+2\,N}) \\ \vec{H}_u(x=L,y_1) \\ \vdots \\ \vec{H}_u(x=L,y_{1+2\,N}) \end{bmatrix}}_{S} \vec{R}^T = \underbrace{\begin{bmatrix} 0 \\ \vdots \\ 0 \\ \epsilon \\ \vdots \\ 0 \end{bmatrix}}_{e} \tag{5.28}$$

In which the square system matrix (S) has dimensions $2+4\,N$ and the vector e has the same length. The acoustic pressure at any point (x,y) within the boundaries is thus obtained as:

$$\frac{p'(x,y)}{\rho c} = \vec{R}\cdot\vec{H}_p(x,y) = \vec{H}_p(x,y)\,S^{-1}e, \tag{5.29}$$

and similarly for the acoustic velocities.

Using the representation of Eq. 5.28, it is straightforward to extend the method to include (complex valued, frequency dependent) impedances on the boundary. An impedance defined by $Z=\frac{\hat{p}}{\rho c\,\hat{u}}$ at the boundary for $(x=0,y_i)$ can simply be included by writing the i^{th} row of S as: $\vec{H}_p(x=0,y_i) - Z\,\vec{H}_u(x=0,y_i)$.

The same methodology can be used to obtain the transfer matrix of an annular duct. The transfer matrix M is defined here as the matrix relating the K acoustic pressures on one of the boundaries to the K acoustic velocities at the same locations. Denoting these K locations as $y_{I,k}$, with $k=1\ldots K$ (the subscript I denoting that at these locations, external inputs are applied) the system matrix is expressed now as:

$$\underbrace{\begin{bmatrix} \vdots \\ \mathbf{H} \\ \vdots \\ \hline \vec{H}_u(x=L,y_{I,1}) \\ \vdots \\ \vec{H}_u(x=L,y_{I,K}) \end{bmatrix}}_{S} \vec{R}^T = \underbrace{\begin{bmatrix} \vdots \\ 0 \\ \vdots \\ \hline \hat{u}(x=L,y_{I,1}) \\ \vdots \\ \hat{u}(x=L,y_{I,K}) \end{bmatrix}}_{e}. \tag{5.30}$$

In which the upper part of the $(4\,N+2-K)\times K$ matrix $\mathbf{H}$ contains the relations at the boundaries (except for the input locations), as described before.

Similar to the previous example, the acoustic pressures at $y_{I,k}$ are recovered now:

$$\begin{bmatrix} \frac{\hat{p}}{\rho c}(x=L,y_{I,1}) \\ \vdots \\ \frac{\hat{p}}{\rho c}(x=L,y_{I,K}) \end{bmatrix} = \underbrace{\begin{bmatrix} \vec{H}_p(x=L,y_{I,1}) \\ \vdots \\ \vec{H}_p(x=L,y_{I,K}) \end{bmatrix} S^{-1} \begin{bmatrix} \mathbf{0} \\ \hline \mathbf{I} \end{bmatrix}}_{M} \begin{bmatrix} \hat{u}(x=L,y_{I,1}) \\ \vdots \\ \hat{u}(x=L,y_{I,K}) \end{bmatrix} \tag{5.31}$$

In which M is the $K \times K$ transfer matrix that is solved for. This input-output relation of an annular duct with mean flow (with complex impedances specified at the boundaries) can now be used in a network representation of a combustion system, in a similar manner as described in section 5.3.1. However, in this case every node in the network relates K acoustic quantities, and therefore the matrices become accordingly larger. In order to validate the approach to obtain the transfer matrix of a duct, a comparison with the finite element package Sysnoise has been performed. A thin annular duct of 1 meter diameter and 2 meter length is modeled in Sysnoise, a unit velocity source has been applied to the boundary at $(x = 0, y = \pi/2)$. The transfer matrix of such a duct was obtained using the method described before. After applying the correct inputs to the transfer matrix (all input velocities equal zero, except at $\hat{u}(x = 0, y = \pi/2) = 1$), the resulting pressure spectra have been compared. The result is displayed in figure 5.5.

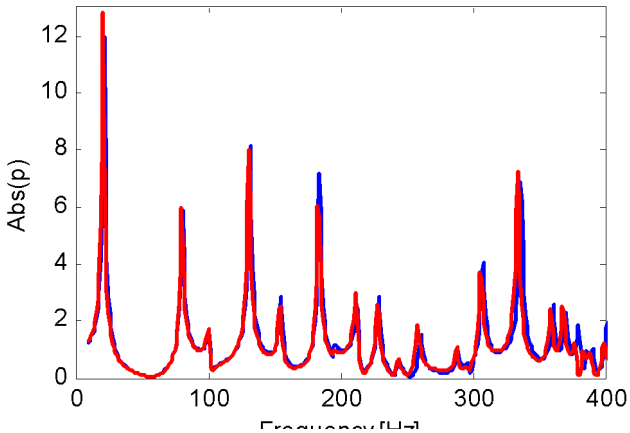

Figure 5.5: Comparison of the fourier expansion method (solid lines) against Sysnoise (dashed lines), both curves nearly coincide.

The acoustic pressure (at a certain frequency) can be calculated at any point within the boundaries. In figure 5.6, the acoustic pressure distribution has been plotted for 131 Hz.
In order to perform a stability analysis of the system, the eigenvalues of the homogenous system have to be solved for. Thus $det[S(\omega)] = 0$ has to be solved for $\omega \in \mathbb{C}$. As discussed in the previous section, a numerical routine can be used to find the eigenvalues. Although good results have been obtained for reasonably simple systems, more complex systems suffered from numerical problems. The reason is that in order to obtain reasonably small spatial resolution, a very large value of N is needed. Because the wave popagation (in absence of mean flow) is defined as: $e^{-ik_x^+ x} = e^{-ix\sqrt{(\frac{\omega}{c})^2-(\frac{2n}{D})^2}}$, large values of N will cause a large positive value of the exponent if the frequency is below the cut-off frequency. Because of this, the matrix in Eq. 5.31 becomes ill conditioned and the inversion causes numerical difficulties. Also, note that the the square root in the exponent has a branch-cut, and is thus discontinuous, this can cause problems for root finding algorithms. The numerical difficulties associated with this method make this approach not useful. This is the reason why a more robust method has been developed, which is the subject of the next section.

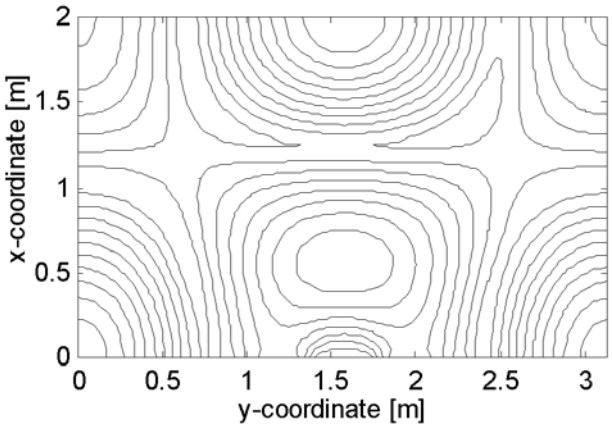

Figure 5.6: Contour lines of the acoustic pressure in the annular duct evaluated for the peak at 131Hz.

5.4 Modal Expansion of Arbitrary Geometries (1-D, 2-D or 3-D)

Equation 2.90 is very useful in obtaining an acoustic transfer function for *any* volume. In this section will be shown how Eq. 2.90 can be used to obtain an acoustic transfer function of a volume. The acoustic transfer function is defined here as the ratio between the acoustic pressure at a certain position ($\mathbf{x}$) in the volume to the acoustic velocity (u_s) acting as an input on an area (A_0) centered on the boundary at $\mathbf{x_0}$. The source of acoustic velocity is defined such that it is positive if the direction of the velocity points into the volume. The pressure as a function of a source of acoustic velocity (u_s) is found by substituting Eq. 2.9 into Eq. 2.90:

$$\hat{p}(\mathbf{x}) = \sum_{n=0}^{\infty} \frac{\psi_n(\mathbf{x})}{\Lambda(k^2 - k_n^2)} \oint_S -i\omega\rho c^2 \hat{u}_s(\mathbf{x_s})\psi(\mathbf{x}_s)dS \tag{5.32}$$

If the distribution of the velocity is uniform and if the area (A_0) is small compared to the wavelength, then Eq. 5.32 can be rewritten to obtain the transfer function ($H(\omega)$) between $\hat{p}(\mathbf{x})$ and $u(\mathbf{x_0})$.

$$H(\omega) = \frac{\hat{p}(\mathbf{x})}{\hat{u}(\mathbf{x_0})} = -i\omega\rho A_0 c^2 \sum_{n=0}^{\infty} \frac{\psi_n(\mathbf{x})\psi_n(\mathbf{x_0})}{\Lambda(\omega^2 - \omega_n^2)} \tag{5.33}$$

More complex systems can be modeled by combining several transfer functions in an acoustic network, also including flame and burner transfer matrices in the case of a network model of a combustion system. Equation 5.33 relates the acoustic pressure at one location to the acoustic velocity at another location. This Single Input Single Output (SISO) representation can easily be extended to the general Multiple Input Multiple Output (MIMO) case. The K velocities at $\vec{\mathbf{x}}_{in}$ are then related to the J pressures at $\vec{\mathbf{x}}_{out}$ by a JxK *transfer matrix* ($\mathbf{H}$):

$$p(\vec{\mathbf{x}}_{out}) = \mathbf{H}\ u(\vec{\mathbf{x}}_{in}), \tag{5.34}$$

in which the elements of $\mathbf{H}$ are given by:

$$\mathbf{H}_{jk} = -i\omega\rho A_k c^2 \sum_{n=0}^{\infty} \frac{\psi_n(\mathbf{x_j})\psi_n(\mathbf{x_k})}{\Lambda(\omega^2 - \omega_n^2)} \tag{5.35}$$

5.5 State-Space Representation

Because all the elements of the transfer matrix, $\mathbf{H}$, have the same system poles (ω_n) the transfer matrix can be expressed more conveniently by a *state-space representation*. An additional advantage of this representation is that it is more numerically robust. One mode of the SISO system of 5.33 can be represented as:

$$\begin{aligned} \dot{x}(t) &= \mathbf{A}\mathbf{x}(\mathbf{t}) + \mathbf{B}u(t) \\ \frac{p(t)}{\rho c} &= \mathbf{C}\mathbf{x}(\mathbf{t}) + \mathbf{D}u(t) \end{aligned} \tag{5.36}$$

$$\begin{aligned}
\mathbf{A}_n &= \begin{bmatrix} -\alpha_n & -\omega_n \\ \omega_n & -\alpha_n \end{bmatrix} \\
\mathbf{B}_{nj} &= \begin{bmatrix} 0 \\ \psi_n(\mathbf{x}_j) \end{bmatrix} \\
\mathbf{C}_{nk} &= \begin{bmatrix} 0 & \frac{cA_k}{\Lambda}\psi_n(\mathbf{x}_k) \end{bmatrix} \\
\mathbf{D} &= [0]
\end{aligned}$$

Note that α, the modal damping, has been introduced here. It is assumed that the value of α is small compared to ω_n. There are many different possible state space representations of a system. The representation chosen here has the advantage that it can easily be extended to the MIMO case. The state of the system is represented by the $2x1$ vector x_n, this notation is chosen to be consistent with notation used in control theory. The first element of this vector can be interpreted as the modal value of the velocity potential, the second element corresponds to the modal value η_n. The validity of this equation can easily be verified in the frequency domain, because $\dot{\hat{x}} = i\omega\hat{x}$, the transfer function, $\mathbf{H}$, is found to be equal to: $\mathbf{C}[\mathbf{i}\omega\mathbf{I} - \mathbf{A}]^{-\mathbf{1}}\mathbf{B} + \mathbf{D}$. The structure of the equations for the general case, having N modes, J inputs and K outputs is the same as for 5.36. However, the matrix $\mathbf{A}$ becomes a 2Nx2N block-diagonal matrix and the matrices $\mathbf{B}$ and $\mathbf{C}$ become 2NxK and Jx2N matrices respectively:

$$\begin{bmatrix} \dot{x}_1 \\ \vdots \\ \dot{x}_{2N} \end{bmatrix} = \begin{bmatrix} A_1 & & \\ & \ddots & \\ & & A_N \end{bmatrix} \begin{bmatrix} x_1 \\ \vdots \\ x_{2N} \end{bmatrix} + \begin{bmatrix} B_{11} & \dots & B_{1J} \\ \vdots & \ddots & \vdots \\ B_{N1} & \dots & B_{NJ} \end{bmatrix} \begin{bmatrix} \dot{u}_1 \\ \vdots \\ \dot{u}_J \end{bmatrix}$$

$$\begin{bmatrix} \dot{p}_1 \\ \vdots \\ \dot{p}_K \end{bmatrix} = \rho c \begin{bmatrix} C_{11} & \dots & C_{1N} \\ \vdots & \ddots & \vdots \\ C_{K1} & \dots & C_{KN} \end{bmatrix} \begin{bmatrix} x_1 \\ \vdots \\ x_{2N} \end{bmatrix} + \begin{bmatrix} 0 & \dots & 0 \\ \vdots & \ddots & \vdots \\ 0 & \dots & 0 \end{bmatrix} \begin{bmatrix} \dot{u}_1 \\ \vdots \\ \dot{u}_J \end{bmatrix}$$

In order to obtain an acoustic transfer function or matrix of some volume, the eigenfrequencies (ω_n), and the eigenvectors (ψ_n) need to be known. For practical (often very complicated) systems the eigenfrequencies and -vectors can be obtained from finite element analysis. Note that only a modal analysis is required in the finite element method. This is computationally very efficient. For more simple geometries, the eigenfrequencies and vectors can be obtained analytically. Two examples that are of practical importance will be presented here: a simple one-dimensional duct, and an annular duct.

5.5.1 One-Dimensional Duct

The longitudinal eigenfrequencies and eigenvectors of a duct of length L and diameter D, closed at both ends are given for mode n by:

$$\begin{aligned}
\omega_n &= \frac{\pi n c}{L} \\
\psi_n &= cos(\frac{\pi n x}{L})
\end{aligned} \tag{5.37}$$

$$\Lambda = \int_0^L cos^2(\frac{\pi n x}{L})dx = \begin{array}{lll} L & if\ n & = & 0 \\ L/2 & if\ n & > & 0 \end{array}$$

or,

$$\Lambda = \frac{L}{2 - \delta_{kron}(n)} \tag{5.38}$$

with δ_{kron} being the Kronecker delta.
Note that $\psi(x = 0) = 1$, thus the transfer function between the acoustic pressure at $x = 0$ and the acoustic velocity at $x = 0$ is found by substituting 5.37 into 5.33:

$$\frac{\hat{p}}{\rho c \hat{u}} = \frac{-i\omega c}{L}\Big\{\frac{1}{\omega^2} + \sum_{n=1}^{N} \frac{1}{\omega^2 - (\frac{\pi n c}{L})^2}\Big\} \tag{5.39}$$

This transfer function can be represented in state-space form:

$$\begin{bmatrix} \dot{x}_1(t) \\ \dot{x}_2(t) \\ \dot{x}_3(t) \\ \dot{x}_4(t) \\ \vdots \\ \dot{x}_{2N-1}(t) \\ \dot{x}_{2N}(t) \end{bmatrix} = \begin{bmatrix} -\alpha_0 & 0 & & & & & \\ 0 & -\alpha_0 & & & & & \\ & & -\alpha_1 & -\frac{\pi c}{L} & & & \\ & & \frac{\pi c}{L} & -\alpha_1 & & & \\ & & & & \ddots & & \\ & & & & & -\alpha_N & \frac{-\pi c N}{L} \\ & & & & & \frac{\pi c N}{L} & -\alpha_N \end{bmatrix} \begin{bmatrix} x_1(t) \\ x_2(t) \\ x_3(t) \\ x_4(t) \\ \vdots \\ x_{2N-1}(t) \\ x_{2N}(t) \end{bmatrix} + \begin{bmatrix} 0 \\ 1 \\ 0 \\ 1 \\ \vdots \\ 0 \\ 1 \end{bmatrix} u'(t)$$

$$p'(t) = \rho c^2 \begin{bmatrix} 0 & \frac{1}{L} & 0 & \frac{2}{L} & \dots & 0 & \frac{2}{L} \end{bmatrix} \begin{bmatrix} x_1(t) \\ x_2(t) \\ x_3(t) \\ x_4(t) \\ \vdots \\ x_{2N-1}(t) \\ x_{2N}(t) \end{bmatrix} \tag{5.40}$$

Note that α_n equals zero for ducts without acoustic attenuation, and will have a small positive value for practical systems.

5.5.2 Annular Duct

A combustion chamber of a gas turbine can be represented as an annular duct with K input and output ports (fig. 5.7), K being the number of burners.
The input-output relation is given by a transfer matrix relating K inputs to K outputs.

$$\begin{aligned} \omega_n &= \sqrt{(\frac{2cm}{D})^2 + (\frac{\pi c n}{L})^2} \\ \psi_{n,m} &= cos(\frac{\pi n x}{L}) \begin{cases} cos(\frac{2my}{D}) \\ sin(\frac{2my}{D}) \end{cases} \end{aligned} \tag{5.41}$$

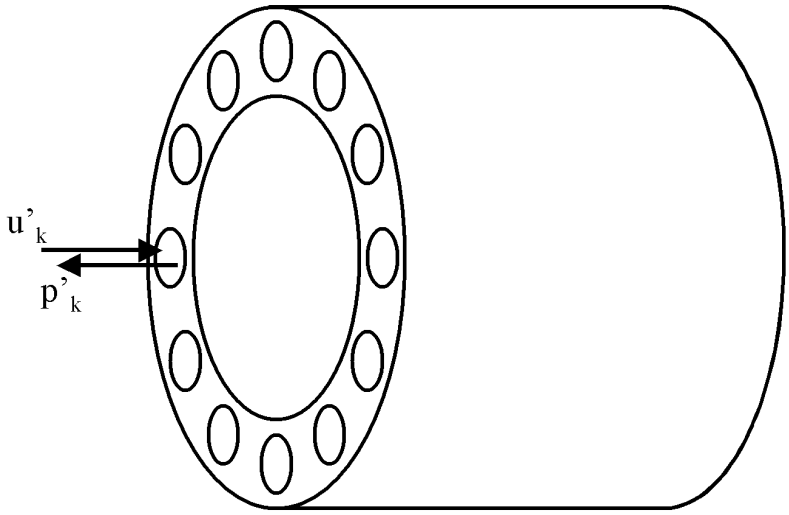

Figure 5.7: Annular duct with 12 input/output ports located at $x = 0$.

$$\Lambda_{n,m} = \begin{cases} \int_0^L \int_0^{\pi D} \{cos(\frac{\pi n x}{L}) cos(\frac{2my}{D})\}^2 dy\ dx = \frac{LD\pi h}{(2-\delta_{kron}(n))(2-\delta_{kron}(m))} \\ \int_0^L \int_0^{\pi D} \{cos(\frac{\pi n x}{L}) sin(\frac{2my}{D})\}^2 dy\ dx = \frac{LD\pi h}{2(1+\delta_{kron}(n))\delta_{kron}(m)} \end{cases}$$

Thus, the transfer function between the pressure at location y and the velocity at location x (at $x = 0$) is given by:

$$\frac{\hat{p}(y)}{\rho c \hat{u}(y_0)} = -i\omega c \frac{\pi D h}{K} \sum_{n=0}^{N} \sum_{m=0}^{M} \left\{ \frac{cos(\frac{2my}{D}) cos(\frac{2my_0}{D})}{\Lambda(\omega^2 - \omega_{n,m}^2)} + \frac{sin(\frac{2my}{D}) sin(\frac{2my_0}{D})}{\Lambda(\omega^2 - \omega_{n,m}^2)} \right\} \tag{5.42}$$

It has been assumed here that $A_k = \frac{\pi D}{K}$, this implies that each burner "communicates" via a "surface" that equals the total cross sectional area divided by the number of burners. Note that "surface" (A_k) is one-dimensional here, this is a consequence of the fact that the annulus has been considered to be thin i.e., the height of the annulus is assumed to be negligible. Because $\cos(a)\cos(b) + \sin(a)\sin(b) = \cos(a - b)$, Eq. 5.42 can be simplified to:

$$\frac{\hat{p}(y)}{\rho c \hat{u}(y_0)} = -i\omega c \frac{\pi D h}{K} \sum_{n=0}^{N} \sum_{m=0}^{M} \frac{cos(\frac{2m(y-y_0)}{D})}{\Lambda(\omega^2 - \omega_{n,m}^2)}. \tag{5.43}$$

This last step is due to the rotational symmetry of the annulus: the transfer function depends on the azimuthal distance between input and output location and is thus *independent* of the choice of the origin of y. In order to relate all K inputs to all K outputs, a KxK transfer matrix is required in which every element is given by Eq. 5.43. This can equivalently be expressed by a state-space realization.

$$
\begin{aligned}
A_{n,m} &= \begin{bmatrix}
-\alpha & -\sqrt{(\frac{2cm}{D})^2+(\frac{\pi cn}{L})^2} & & \\
\sqrt{(\frac{2cm}{D})^2+(\frac{\pi cn}{L})^2} & -\alpha & & \\
 & & -\alpha & -\sqrt{(\frac{2cm}{D})^2+(\frac{\pi cn}{L})^2} \\
 & & \sqrt{(\frac{2cm}{D})^2+(\frac{\pi cn}{L})^2} & -\alpha
\end{bmatrix} \\
B_{n,m} &= \begin{bmatrix}
0 & \dots & 0 & \dots & 0 \\
cos(\frac{2\pi m1}{K}) & \dots & cos(\frac{2\pi mk}{K}) & \dots & cos(\frac{2\pi mK}{K}) \\
0 & \dots & 0 & \dots & 0 \\
sin(\frac{2\pi m1}{K}) & \dots & sin(\frac{2\pi mk}{K}) & \dots & sin(\frac{2\pi mK}{K})
\end{bmatrix} \\
C_{n,m} &= \frac{(2-\delta_{kron}(n))(2-\delta_{kron}(m))}{KL}
\begin{bmatrix}
0 & cos(\frac{2\pi m1}{K}) & 0 & sin(\frac{2\pi m1}{K}) \\
\vdots & \vdots & \vdots & \vdots \\
0 & cos(\frac{2\pi mk}{K}) & 0 & sin(\frac{2\pi mk}{K}) \\
\vdots & \vdots & \vdots & \vdots \\
0 & cos(\frac{2\pi mK}{K}) & 0 & sin(\frac{2\pi mK}{K})
\end{bmatrix}.
\end{aligned}
\tag{5.44}
$$

The burner's azimuthal positions are given by: $y = k\frac{\pi D}{K}$ in which the integer k is the burner number.

Validation

In order to validate the approach described in this section, a benchmark between this method and a commercial acoustic finite element package has been made. The geometry consists of a rigid walled annular duct as shown in fig. 5.7. The mean diameter of the annular duct is 0.44 meters, the length 0.35 meters and the height 0.12 meters. As an input, an acoustic velocity $\hat{u} = 1m/s$ has been applied to one of the "holes" or "burners" of the duct. The holes have a diameter of 0.03 meters and are equally spaced around the circumference and centered at the average radius of the annular duct. The speed of sound is 340 m/s and the density is 1.225 kg/m^3. The pressure in the centers of the "holes" was calculated in three different ways:

- numerically, using the commercial package Sysnoise
- modal expansion, using analytically obtained eigenvectors and eigenfrequencies. In this analysis longitudinal modes 0 and 1 and azimuthal modes 0 to 4 have been included.
- modal expansion, using eigenvectors and frequencies obtained from Finite Element Analysis

Figure 5.8 shows the comparison between the results of the three methods. Care has to be taken when using modal analysis data obtained from finite element codes because some of these codes won't give the 0 Hz mode as an output. Indeed the 0 Hz is generally not of interest in acoustics, however every closed volume will have an eigenfrequency at zero Hertz. Omitting this mode in

the modal expansion will result in erroneous results in the low frequency range, the phase of the pressure up to the first (non zero) resonance frequency will be especially strongly affected. In Sysnoise, the zero Hertz mode is not calculated because it causes numerical difficulties [56]. As a consequence of this, the frequency response calculated by Sysnoise is incorrect for the very low frequency regime. This "resonance at zero Hertz" might be somewhat surprising when considering the physical interpretation of this acoustic effect. The reason is that these very low frequencies are generally not considered to be acoustic. Note, however, that this phenomenon is present in any rigid walled enclosure. A good example is the impedance of a one dimensional duct of length L, which can be derived using the equations 2.34 and 2.36: $Z(\omega) = \frac{p}{u} = \frac{1}{i\rho c \tan(\omega \frac{L}{c})}$, which has infinite response at $\omega = 0$. The physical explanation is that in the limit case of the frequency approaching zero, an "acoustic" velocity source acts as a constant (time invariant) addition of mass. When continuously adding mass to a fixed volume the density (and accordingly the pressure) will continuously increase. Another explanation is found when considering that if the frequency becomes very low, the wavelength becomes very large, and thus gradients can be neglected if the wavelength is much larger than the geometrical extent of the volume. Indeed, the "mode-shape" corresponding to the eigenvalue at $\omega = 0$ is uniform in space. From a systems point of view, an eigenvalue in the origin corresponds to an "integrator", the step response of an integrator is a ramp function in time. This expresses the phenomenon that mass is accumulated in a closed vessel with continuously increasing density as a result. Note that a duct closed at one side, and open at the other side has an impedance $Z(\omega) = \frac{p}{u} = i\rho c \tan(\omega \frac{L}{c})$, which is zero at $\omega = 0$ thus if one side is open, no pressure can build up in the tube. Note also that if the acoustic response due to a unit boundary displacement would have been applied (instead of an acoustic velocity boundary), the peak at zero Hertz would be absent. This can be understood by the relation between acoustic velocity $\hat{u}$ and boundary displacement $\hat{x}$ given by: $\hat{x} = \frac{\hat{u}}{i\,\omega}$. Thus, a unit acoustic velocity source in the frequency domain implies an infinite boundary displacement at zero Hertz.
Note that it is important to know how the the eigenvectors are scaled, the scaling in Sysnoise is such that $\psi_{sysnoise} = \sqrt{\frac{\rho c^2}{\Lambda}}\psi$ in which ψ has unit amplitude.

5.5.3 Two Sided Duct

The two previous examples give a relation between the acoustic velocity and pressure at one side of a duct, thus implying that the other side of the duct is a solid wall. Often times it is required that a duct be connected to other systems on *both* sides. The state-space representation can easily be extended to the more general case with inputs and outputs on both sides of the duct (at $x = 0$ and $x = L$). When doing so, it is helpful to apply the following partitioning of the B,C and D matrices:

$$\begin{aligned} \dot{\mathbf{x}} &= \mathbf{A}\mathbf{x} + \mathbf{B_l}\mathbf{u_l} + \mathbf{B_r}\mathbf{u_r} \\ \frac{\mathbf{p_l}}{\rho c} &= \mathbf{C_l}\mathbf{x} + \mathbf{D_{ll}}\mathbf{u_l} + \mathbf{D_{lr}}\mathbf{u_r} \\ \frac{\mathbf{p_r}}{\rho c} &= \mathbf{C_r}\mathbf{x} + \mathbf{D_{rl}}\mathbf{u_l} + \mathbf{D_{rr}}\mathbf{u_r} \end{aligned} \tag{5.45}$$

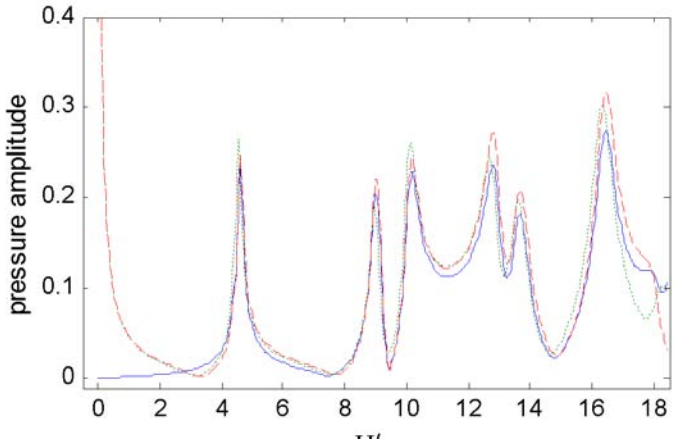

Figure 5.8: Frequency response of annular duct, calculated with Sysnoise (solid), analytic solution(dotted), and modal expansion (dashed).

In which l and r refer to the left or right hand side inputs and outputs. The matrix $\mathbf{A}$ is the same as for the single-sided duct. The matrices $\mathbf{B_l}$ and $\mathbf{C_l}$ contain the values of the eigenvector on the left side of the duct and are identical to the matrices $\mathbf{B}$ and $\mathbf{C}$ in Eq. 5.44. The matrices $\mathbf{B_r}$ and $\mathbf{C_r}$ contain the values of the eigenvectors at $x = L$. Because $\cos(\frac{\pi n x}{L}) = (-1)^n$ if $x = L$ the following expressions are obtained for $\mathbf{B_r}$ and $\mathbf{C_r}$ in annular ducts:

$$\begin{aligned} \mathbf{B_r}_{n,m} &= (-1)^n \mathbf{B_l}_{n,m} \\ \mathbf{C_r}_{n,m} &= (-1)^n \mathbf{C_l}_{n,m} \end{aligned}$$

Although the $\mathbf{D}$ matrices are empty again, they are shown here in order to be more consistent with a more general notation of partitioned state-space systems:

$$H = \begin{bmatrix} H_{11} & H_{12} \\ H_{21} & H_{22} \end{bmatrix} = \left[\begin{array}{c|cc} A & B_l & B_r \\ \hline C_l & D_{ll} & D_{lr} \\ C_r & D_{rl} & D_{rr} \end{array}\right]$$

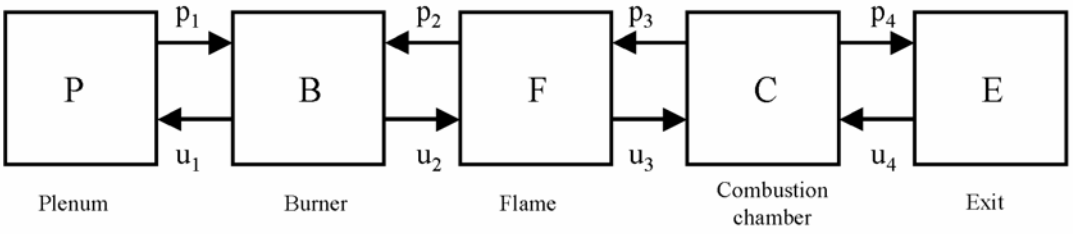

Figure 5.9: Interconnection of two MIMO systems H and G, using the Redheffer star product. Note that all arrows represents *vectors* of input or output signals.

5.6 Network Interconnections

In order to obtain a model of the acoustic behavior of a gas turbine combustion system, acoustic transfer functions can be combined in a network of acoustic elements. The approach is similar to the frequency-domain approach described in chapter 3. However, in order to make physical sense, a time domain model has to be interconnected in a proper, causal way.
The lumped element representation of the annular combustion system of figure 5.9 can be represented by the block diagram of Fig. 5.9.
All submodules relate N pressure and N velocity signals on both the upstream and downstream side. The entire system can now be modeled by interconnecting all the outputs of the subsystems to the inputs of their "neighbours". To do so, every subsystem will be represented as a state-space system having the shape of 5.36 or 5.46. These subsystems can be inter-connected in a very convenient way by making use of the *Redheffer star product*. The Redheffer Star Product is a matrix operation based on a *linear fractional transform* [137]. It is often used in control theory to model uncertainty in systems, but can be used to interconnect any network of state-space systems. The interconnection of two ducts (or any other systems) H and G is then simply given by: $H \star G$ in which $\star$ denotes the Redheffer star product, and is defined by:

$$H \star G = \begin{bmatrix} \mathcal{F}_l(H, G_{11}) & H_{12}(I - G_{11}H_{22})^{-1}G_{12} \\ G_{21}(I - H_{22}G_{11})^{-1}H_{21} & F_u(G, H_{22}) \end{bmatrix},$$

in which $\mathcal{F}_u()$ and $\mathcal{F}_l()$ denote the upper and lower linear fractional transform, defined as: $\mathcal{F}_l(M, g) := M_{11} + M_{12}g(I - M_{22}g)^{-1}M_{21}$. The interconnection is illustrated in Fig.5.10.
Thus the system of Fig. 5.9 can easily be represented by the matrix $\mathbf{S} = P \star \mathbf{B} \star \mathbf{F} \star \mathbf{C} \star E$. This system has no inputs or outputs, these could of course be added, but are not required for a stability analysis. Stability requirement of the system is then satisfied if the real parts of all eigenvalues of S are negative. The eigenfrequencies or poles of the system are the complex

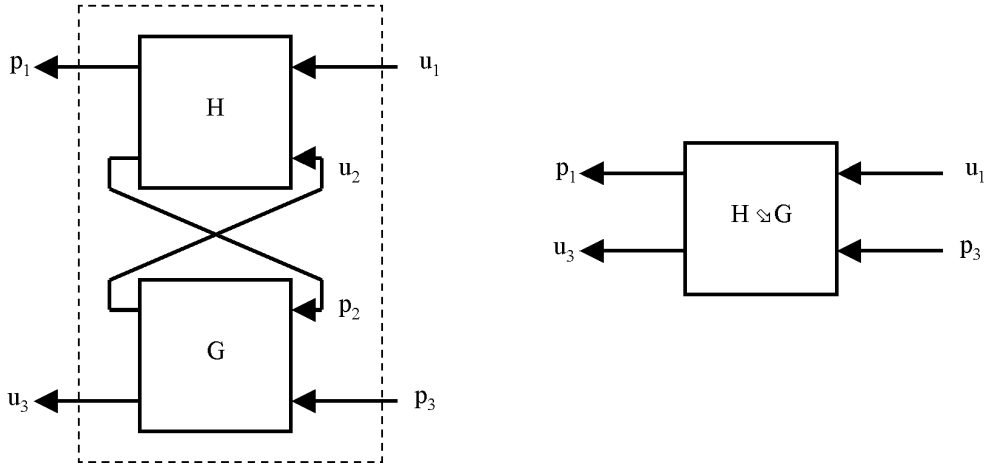

Figure 5.10: Interconnection of two MIMO systems H and G, using the Redheffer star product. Note that all arrows represents *vectors* of input or output signals.

eigenvalues of the matrix $\mathbf{S}$. Note that $\mathbf{S} \in \mathbb{R}$, is time invariant and does not depend on ω. Computing the eigenvalues can be done using standard methods available in linear algebra.

Validation

The use of the Redheffer star product can be illustrated by applying end conditions to a one-dimensional duct. With E being the boundary condition of the duct described by a partitioned state space matrix, H. The transfer function (or impedance) of the duct plus this exit condition is then simply given by: $H \star E$. The complex frequency dependent admittance E is set to: $E = \frac{u}{p} = \frac{c}{-i\omega\frac{1}{2}-200}$ and then represented in state-space. This admittance corresponds to strong acoustic absorption for low frequencies and almost full reflection at higher frequencies, as shown by the reflection coefficient plotted in Fig. 5.11. The frequency response of $H \star E$ is plotted in the right part of Fig. 5.11, together with the analytic result.

As a second example, the one-dimensional thermoacoustic system described in [65] will be analyzed. This system consists of a straight duct, closed on one side, open on the other side, with a flame stabilized in the middle of the duct. The pressure drop across the flame sheet is assumed to be negligible. The acoustic velocity jump is modeled by the so-called $n - \tau$ model: $u_2(t) = u_1(t) + n\, u_1(t - \tau)$. The impedance of the open end is simply: $Z_3 = 0$. A sketch of the system and its lumped element block diagram is given in Fig. 5.12. Note that the $n - \tau$ model contains a delay and is thus of infinite order. In order to avoid systems of infinite order, the time delay is approximated by a *Padé approximation*, a technique commonly used in control theory. The upsteam duct can be represented by the transfer function of Eq. 5.33, represented

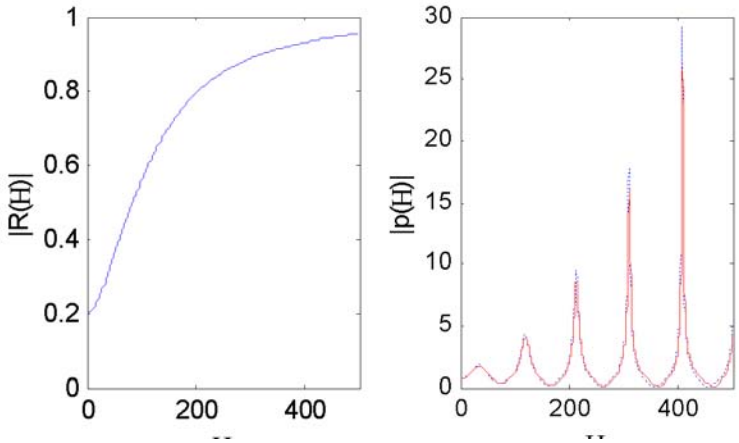

Figure 5.11: Absolute value of the reflection coefficient used for the validation model, left. Absolute value of pressure response as a function of frequency, right. Analytic solution (dotted line), modal expansion (solid line).

in state-space. However, in this case p is an input and u an output, thus the inverse of Eq. 5.33 has to be used to represent the duct, P. Because Eq. 5.33 is a minimum-phase transfer function with 1 more pole than zeros, the inverse was taken after adding an "artificial" zero . Using the Redheffer star product, the system can be represented as: $\mathbf{S} = P \star \mathbf{F} \star \mathbf{C} \star Z$. An analytic solution for the eigenvalues is not given in [65], however the eigenvalues of the system

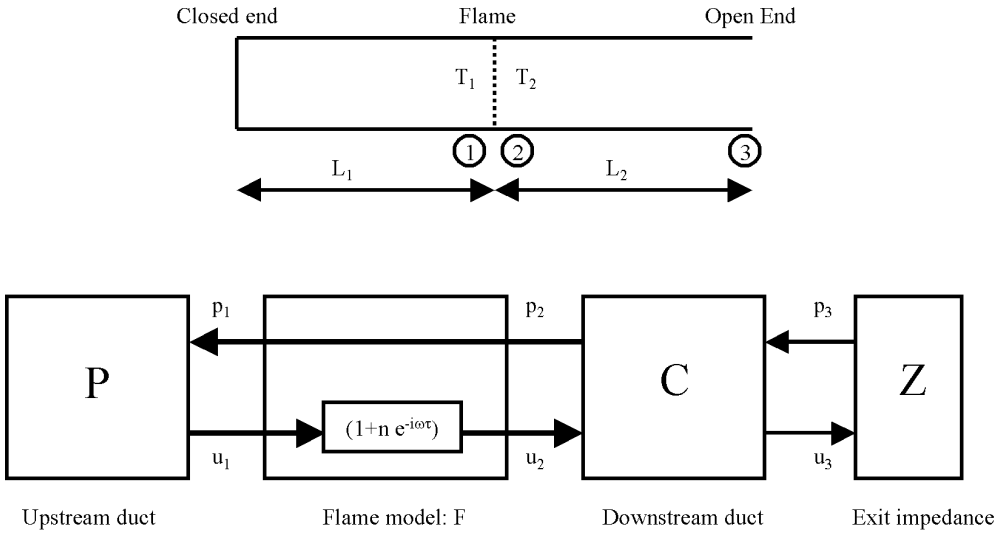

Figure 5.12: Sketch of a one-dimensional combustion system, and block-diagram representation.

are shown to be the roots of:

$$\cos(2\frac{\omega L}{c}) - \sin^2(\frac{\omega L}{c})\, n\, e^{-i\omega\tau} = 0, \tag{5.46}$$

which requires a numerical search. Both the results obtained via modal expansion and the roots of Eq. 5.46 are plotted in Fig. 5.13, in which ω_0 is the resonance frequency in the case $n = 0$. For large values of $\omega_0\tau$ both curves deviate, this is because the order of the Padé approximation was relatively low (six), however a perfect match can be obtained by increasing the order of the Padé approximation.

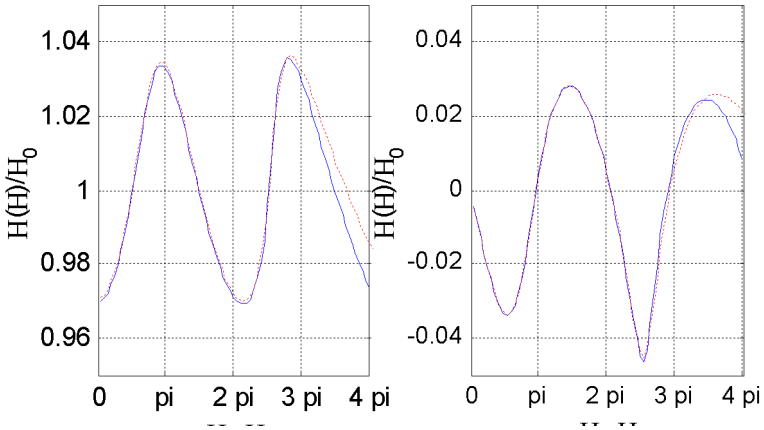

Figure 5.13: Eigenfrequencies of the Rijke tube as a function of normalized time delay, τ. Real part of frequency (left), imaginary part (right), analytic solution (solid line), modal expansion (dotted line).

In order to validate the interconnection of MIMO systems, a very simple geometry is chosen as the bench mark: 2 annular ducts coupled by 24 short ducts. This represents, in essence, a gas turbine combustion chamber geometry [35]: the first annular duct corresponds to the plenum chamber (diameter D_{up}, length L_{up}, annulus height h_{up}), the smaller ducts (length l, diameter d) represent "burners" and the second annular duct (diameter D_{do}, length L_{do}, annulus height h_{do}) represents the combustion chamber. The dimensions are tabulated in table 5.6. A sketch of the geometry is given in Fig. 5.14. A length correction was given to the small ducts, in accordance with [111].

$\frac{L_{up}}{c_{do}}$	$\frac{L_{do}}{c_{do}}$	$\frac{l}{c_{do}}$	$\frac{D_{up}}{c_{do}}$	$\frac{D_{do}}{c_{do}}$	$\frac{d}{c_{do}}$	$\frac{h}{c_{do}} = \frac{h}{c_{do}}$
$0.70\ 10^{-3}$	$0.95\ 10^{-3}$	$0.06\ 10^{-3}$	$3.07\ 10^{-3}$	$3.07\ 10^{-3}$	$0.19\ 10^{-3}$	$0.40\ 10^{-3}$

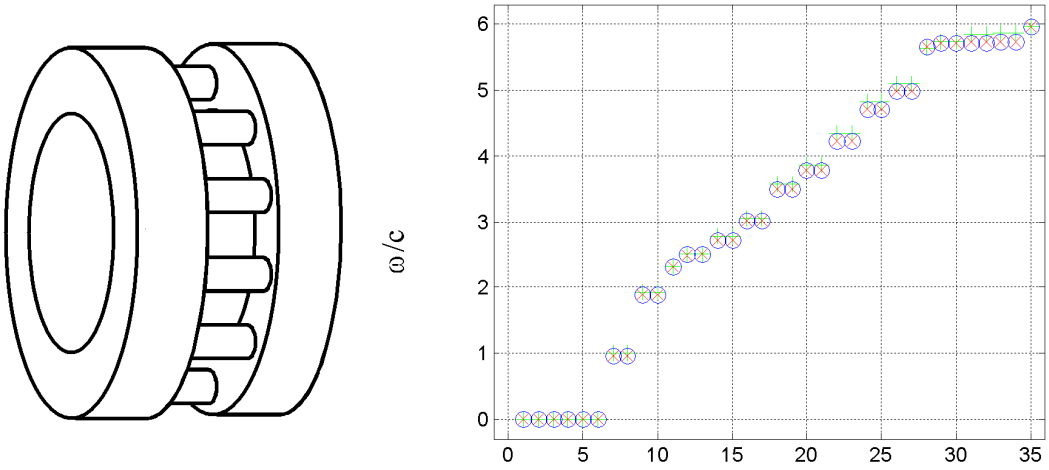

Figure 5.14: Eigenfrequencies of the coupled duct with temperature jump obtained directly by Sysnoise (o) compared to the modal expansion method based on numerically obtained eigenvalues and vectors(x) and the analytic solution (+).

5.7 Test Rig Model

In this section, the network modeling approach will be used to obtain an acoustic model of an atmospheric combustion test facility. The acoustic pressure spectra of this test rig have been recorded systematically for a wide range of operating conditions. This set of experimental data is used here to validate the network modeling and the stability analysis. The test rig is described in section 3.2. A sketch of the test facility together with a network representation is given in Fig. 5.15. The model has been split up into five sub-systems. The Inlet block describes the acoustics of everything upstream of the burner. It contains the wave propagation through the plenum chamber and the air supply system (including air pre-heater and measurement orifices-plates). The geometry of this system is rather complex, and therefore this sub-system is represented by a measured impedance. This impedance is obtained as: $Z_{in}(\omega) = -\frac{\hat{p}(\omega)}{\hat{u}(\omega)}$, in which $\hat{p}(\omega)$ and $\hat{u}(\omega)$ have been obtained using the Multi Microphone Method (described in section 3.). A state-space system representation of this measured frequency response is obtained using a built-in routine in Matlab®, special care should be taken to ensure that this system is a minimal realization (no pole-zero cancellation), and that the system is causal and stable.

The Burner block has two pressure signals as inputs and two velocity signals as outputs, its transfer matrix will be represented by the symbol **B**, the dynamics are described by the $L-\zeta$ model as desribed in sections 2.7 and 3.33. The causal representation of this sub-model is given in the diagram of Fig. 5.16, in which:

$$L\zeta(s) = \frac{1}{-\frac{L_{red}}{c}s + M(1-\zeta-(\frac{A_0}{A_1})^2)}. \tag{5.47}$$

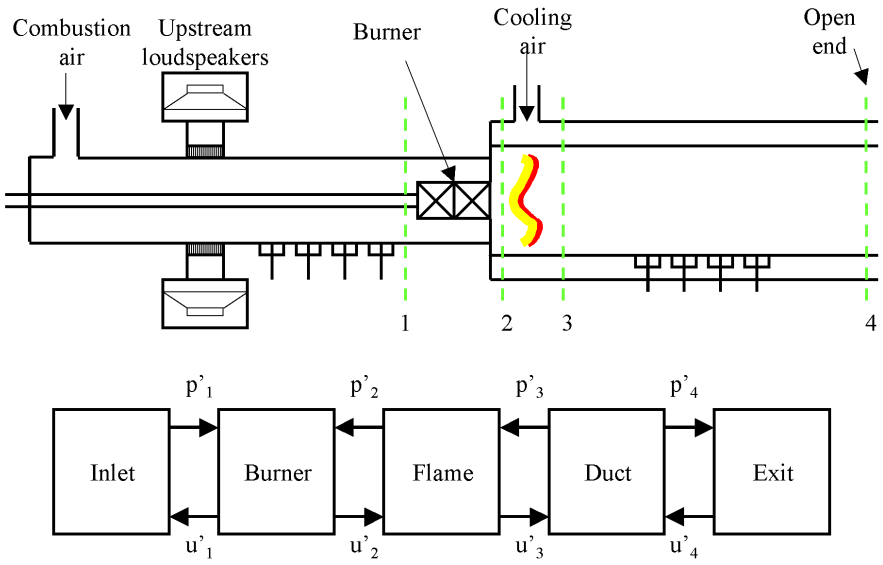

Figure 5.15: Sketch of the atmospheric combustion facility and the corresponding network blocks

The values of L_{red} and ζ are obtained from a fit to measured transfer functions, as described in section 3.33.

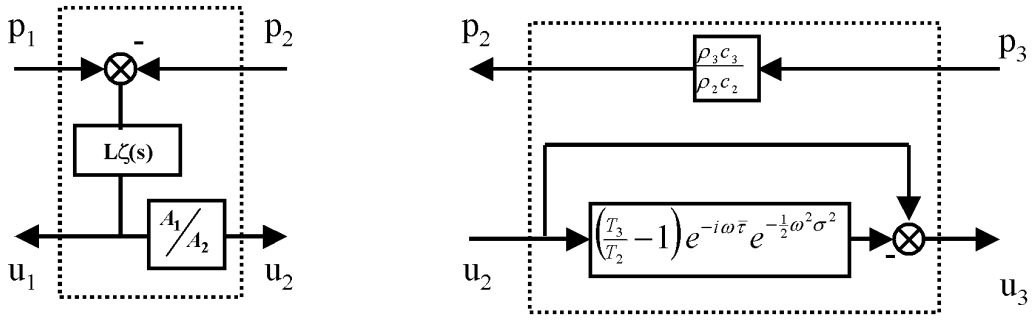

Figure 5.16: Block diagrams of the burner model (left), and the flame model (right).

The Flame module (**F**) consists of a dynamic relation between the two acoustic velocities $u_1(t)$ and $u_2(t)$ and a static relation between $p_2(t)$ and $p_1(t)$. These relations have been discussed in detail in chapter 4. The causal representation of **F** is given in Fig. 5.16. In this model the following relation is used between the acoustic velocities on both sides of the flame sheet: $\hat{u}_3 = \hat{u}_2 + (\frac{T_2}{T_1} - 1)\, e^{-i\omega\tau} e^{-\frac{1}{2}\omega^2\sigma^2}\, \hat{u}_2$. This model will be referred to as the $\tau\sigma$-model because the values of the mean time delay τ and the standard deviation σ of the delays have been obtained by fitting to experimentally obtained transfer functions. Alternatively, a model $\hat{u}_3 = k\,\hat{u}_2 + n\, e^{-i\omega\tau} e^{-\frac{1}{2}\omega^2\sigma^2}\, \hat{u}_2$ can be used where two additional parameters (n and k) are introduced. Because in this case

additional degrees of freedoms are introduced in the curve fit, a better match between model and experiment is obtained. This model will be referred to as the $n\tau\sigma k$-model.
The Duct module represents a one-dimensional duct with up- and down- stream velocity inputs and pressure outputs. The state-space representation of this system, $\mathbf{D}$, is given by Eq. 5.40.
In the Exit system, A_{exit} represents the impedance of a duct with an open end. Because of acoustic radiation, considerable losses will occur in this element. Such a radiative element has been described by Levine and Swinger [71] it is characterized by an impedance having a real part (resistance) that increases with the square of frequency: the imaginary part (reactance) is similar to the imaginary part of the $L-\zeta$ model and consists of an end correction or virtual length L_{cor} and thus increases linearly with frequency. The exit impedance of a duct of diameter r with an un-flanged end is given for low frequencies as: $Z_{exit} = i\,\omega\,\frac{L_{cor}}{c_4} + (\frac{r\omega}{2c_a})^2\frac{\rho_a c_a}{\rho_4 c_4}$, with $L_{cor} = 0.61r$ and the subscript a denoting ambient conditions. The geometry of the exit condition of the test rig is not that of a perfect un-flanged open end. In reality, the exit geometry is somewhat more complicated, therefore a correction factor (α) has been introduced for the real part of this impedance. The correction factor and the reduced length L_{cor} have been fit to a measured impedance of the test rig exit. For reasons of causality, the reciprocal of the impedance (the admittance) will be used in the network interconnection:

$$A_{exit} = \frac{\hat{u}_4}{\hat{p}_4} = \frac{-1}{s^2\frac{r^2\rho_a}{4c_a\rho_4 c_4}\alpha - s\,\frac{L_{cor}}{c_4}} \tag{5.48}$$

The impedance of the combustion chamber at the flame location is then given by the star-product of the exit admittance and the duct transfer function. This impedance has been measured in the test-rig as well using the Multi Microphone Method. The modeled and measured impedances have been plotted together in Fig. 5.17.

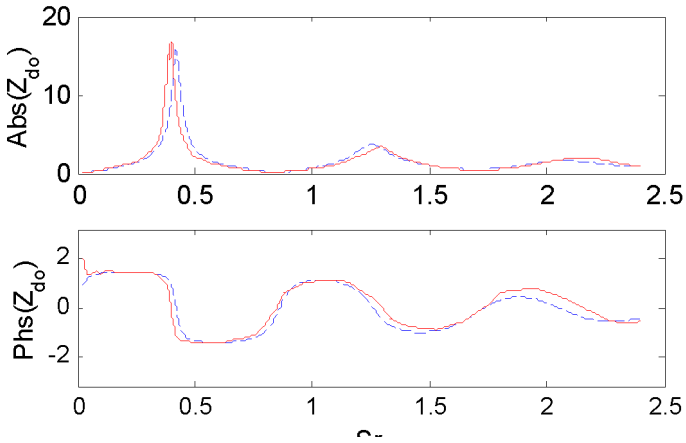

Figure 5.17: Comparison of measured (solid) and modeled (dashed) exit impedance of the combustion chamber, $Z_{do} = \mathbf{D} \star A_{exit}$, as a function of frequency.

Because the transfer functions of every subsystem have been defined, the final interconnection is easily obtained by making use of the star products, provided that all systems are represented as

state-space realizations. Note that no source terms have been introduced in this model. These could of course easily be added, but are not necessary for a stability analysis. The dynamics of the system are governed by the eigenvalues (poles) of: $S = Z_{in} \star \mathbf{B} \star \mathbf{F} \star \mathbf{E} \star A_{exit}$. The system is said to be unstable if one ore more eigenvalues has a positive real part. The real part of the eigenvalues can be considered as a growth rate. In Fig. 5.18 the maximum value of the Fourier transform of the measured pressure signal in the combustion chamber has been plotted.

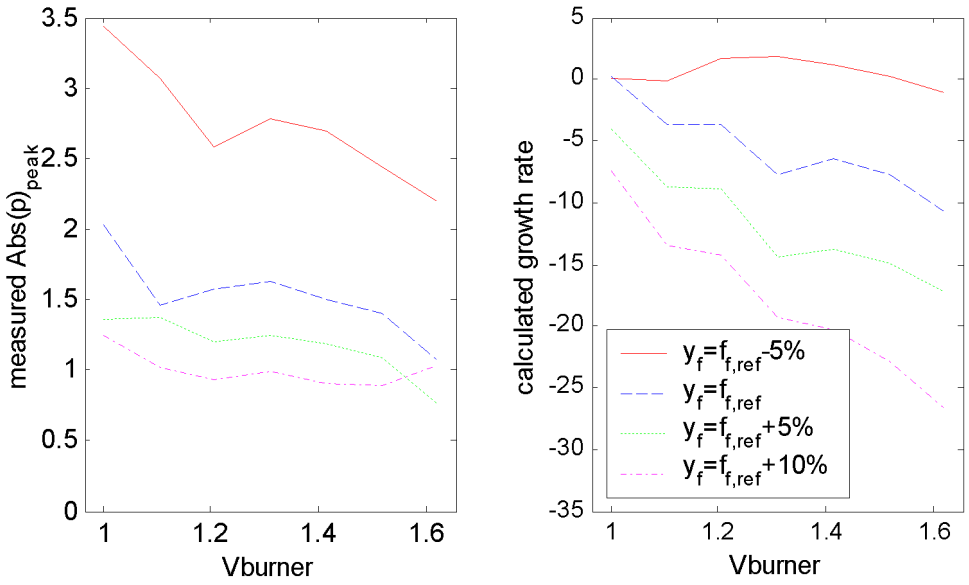

Figure 5.18: Comparison of measured pulsation amplitudes (left plot) and predicted growth rates (right plot) of the atmospheric test facility.

The largest growth rates $\max(\Re\{eig(S)\})$ have been plotted in the same figure for several values of the adiabatic flame temperature (mass fraction of fuel) and throughput (velocities). The imaginary part of these eigenvalues correspond to the frequency of oscillation associated with these eigenvalues. In Fig. 5.19, the frequency at which the highest peak occurred in the Fourier transform of the pressure pulsations is plotted together with the imaginary part of the eigenvalue. The frequency has been scaled as a Strouhal number. The measured and modeled instability frequencies have very good agreement. The measured pulsation amplitudes and modeled growth rates can not be compared directly, nevertheless they show similar trends. Instability is predicted for the lowest fuel mass fraction (lowest flame temperature). The measured amplitudes are indeed highest for the lowest flame temperature.

The real parts of the eigenvalues clearly have some relation with the pulsation amplitudes. However, in order to obtain a quantitative estimate of the pulsation amplitudes, a time-domain simulation has to be performed in which the non-linearity in the flame transfer function needs to be taken into account. As stated before, no detailed physical or empirical model is available for the non-linear processes in the flame. The non-linear process is simulated here by assuming a saturation process on the heat release as discussed in section 4. The value of the saturation function has been adjusted such as to match the experiments. A comparison between the time-

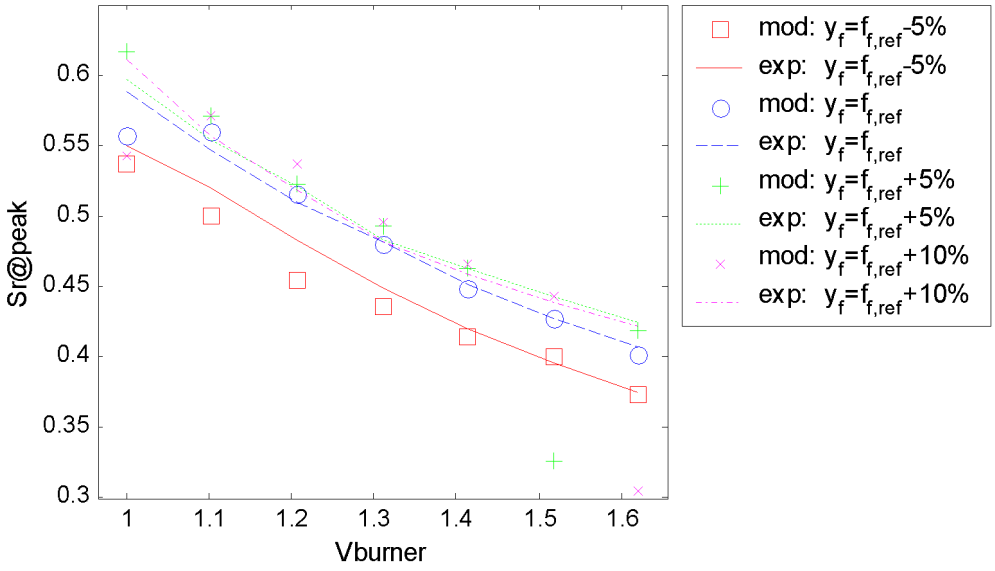

Figure 5.19: Comparison of measured (markers) and predicted (lines) peak pulsation frequencies of the atmospheric test facility.

domain simulation and the measured frequency response is given in Figs. 5.20 and 5.21.

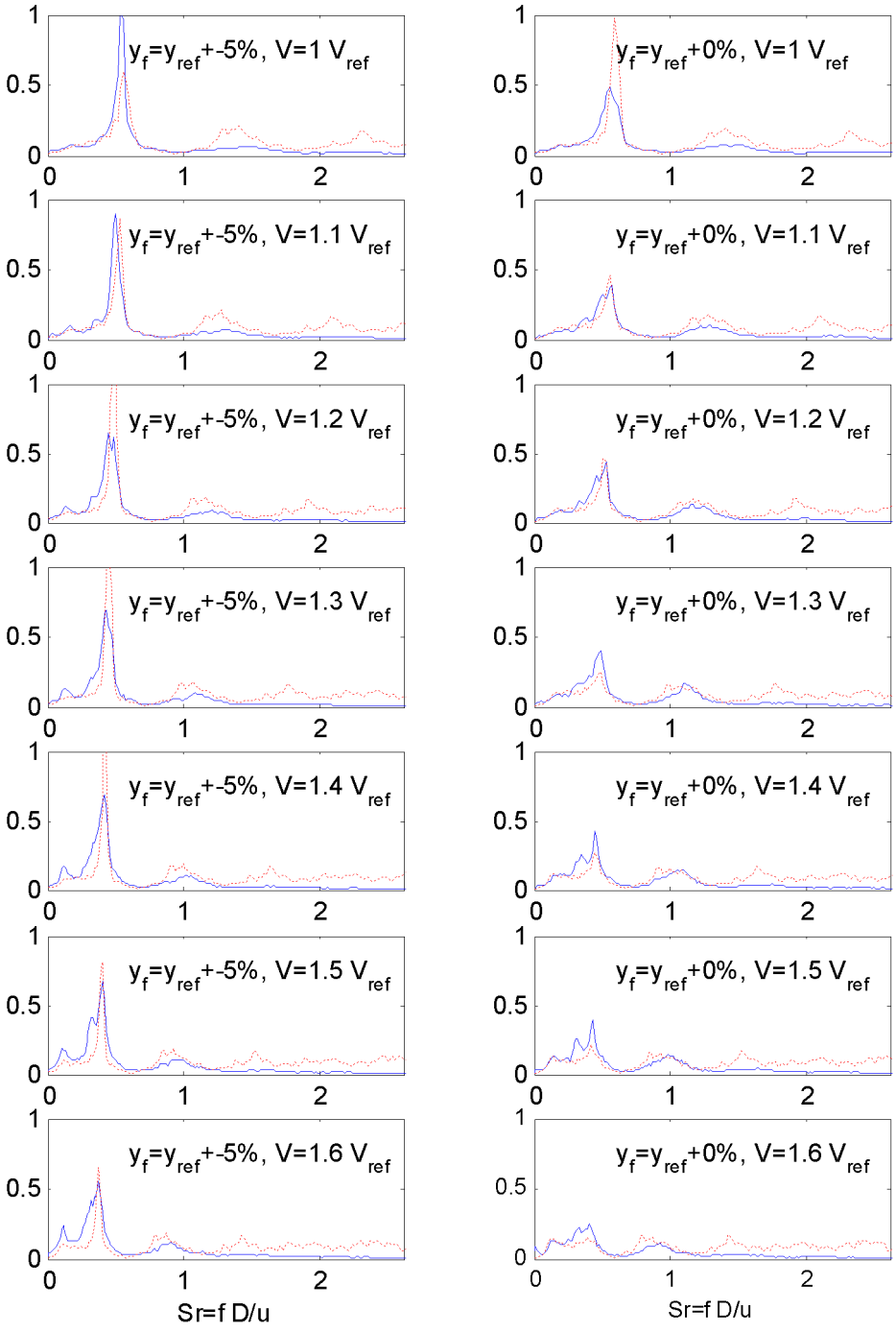

Figure 5.20: Comparison of measured (solid) and predicted (dotted) pulsation spectra of the atmospheric test facility.

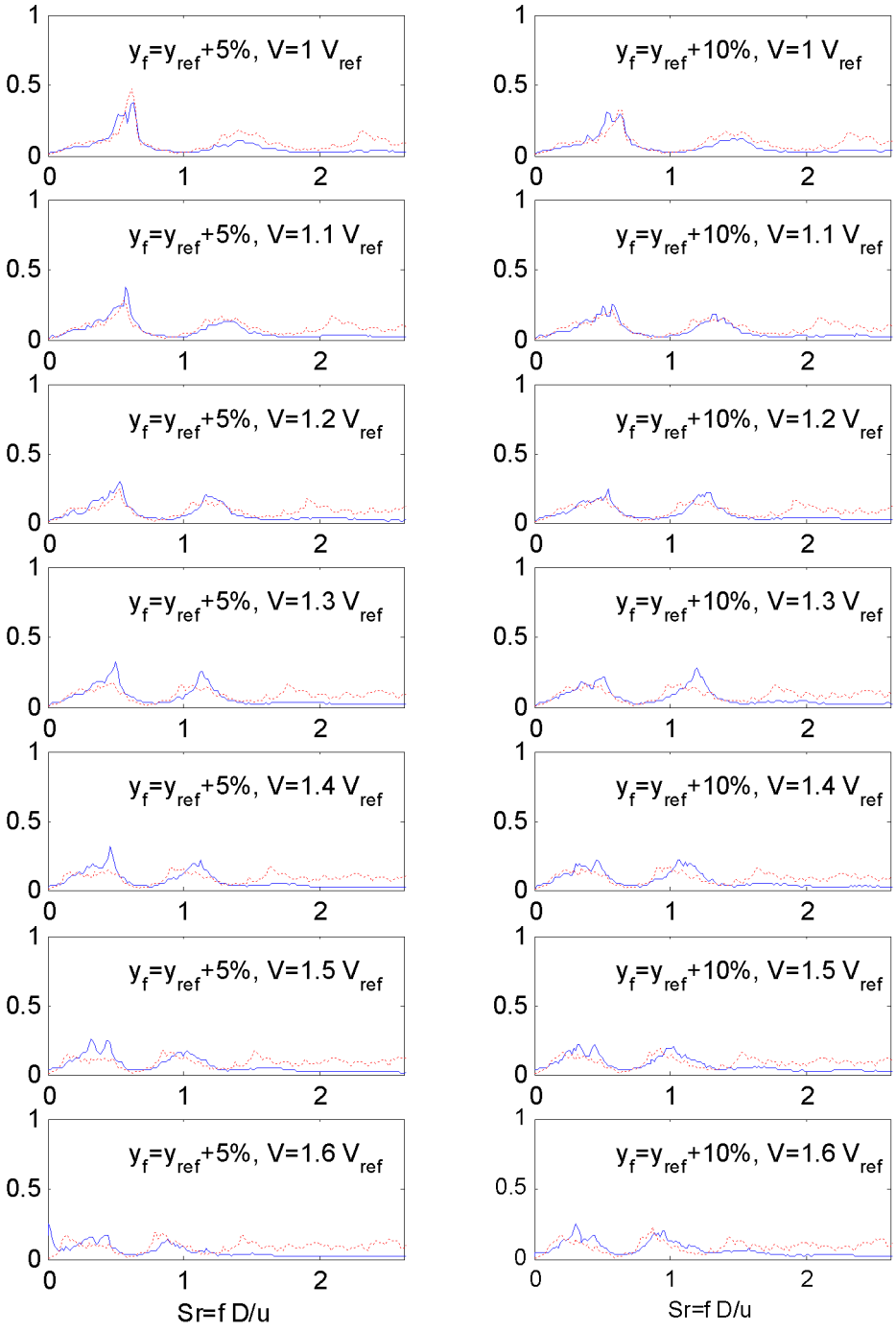

Figure 5.21: Comparison of measured (solid) and predicted (dotted) pulsation spectra of the atmospheric test facility.

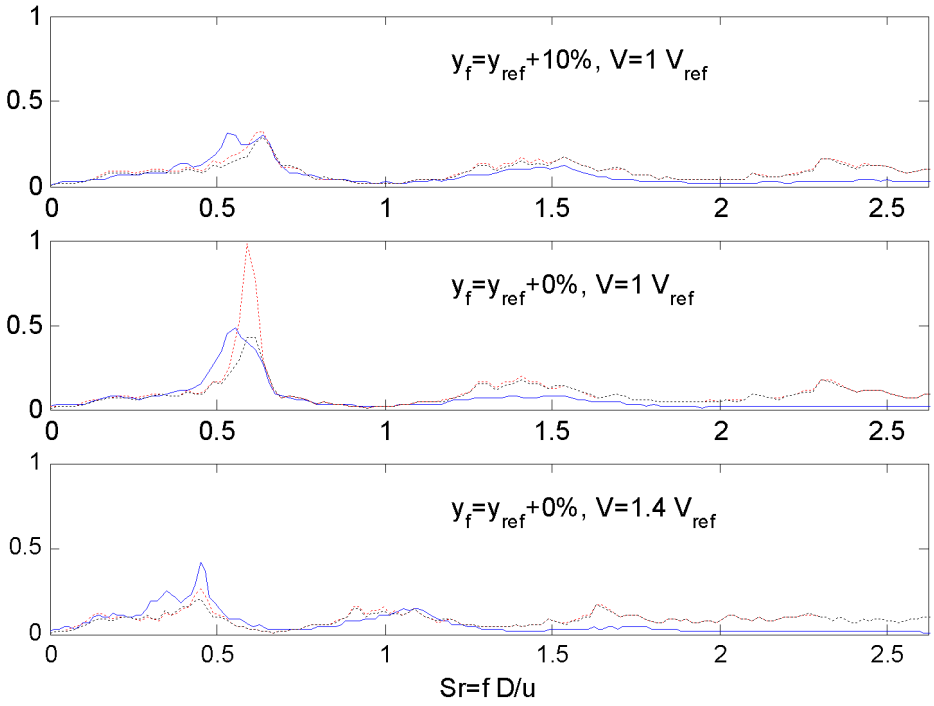

Figure 5.22: Comparison of measured (solid) and predicted pulsation spectra of the atmospheric test facility for two different flame models, the n$\tau\sigma$k-model (solid) and the $\tau\sigma$-model (dashed).

5.8 Annular Combustion System

Having validated the coupled annular duct problem and the model interconnection of the test facility, the step to a model of a (gas turbine) combustion system with an annular combustion system is straightforward. For a combustion system with J burners, the upstream system (plenum) and the combustion chamber will be modeled as annular ducts with J inputs and outputs. The burner and flame modules are essentially the same, however, in this case these modules will consists of J parallel burner and flame modules. Thus the transfer matrix of $\mathbf{B}$ is a block diagonal matrix: $\mathbf{B} = diag[B_1, B_2, \cdots B_J]$. Note that if geometrically different burners are used, the elements B_j will be different. Because of the high Mach number exit of the combustion chamber, the relation for sonic nozzles is used: $E = \frac{\hat{u}}{\hat{p}} = \frac{\gamma-1}{2}M$.
With the plenum chamber represented by annular duct $\mathbf{P}$, the burner by $\mathbf{B}$, the flame by $\mathbf{F}$, the combustion chamber by $\mathbf{C}$ and the high Mach number exit by $\mathbf{E}$, all the sub-modules can be combined as: $\mathbf{S} = \mathbf{P} \star \mathbf{B} \star \mathbf{F} \star \mathbf{C} \star \mathbf{E}$. The eigenvalues of S are plotted in Fig. 5.23. Note that the eigenfrequencies with negative real parts are not plotted, note also that the eigenfrequencies with very large positive real part are not plotted. The eigenvalues with negative imaginary parts are unstable. This system has one unstable pair of eigenvalues.

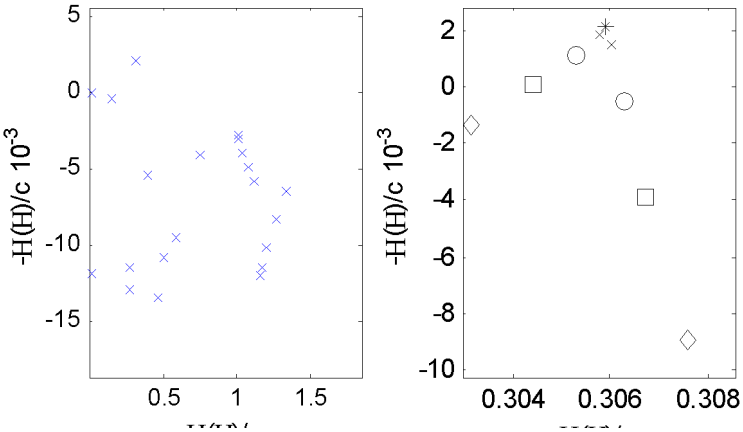

Figure 5.23: Eigenvalues of the annular combustion system (left plot). A negative imaginary part indicates instability. Change of most unstable eigenvalue due to non-uniform distribution of convective time-delays (right plot). Uniform distribution (stars), +/- 20% deviation of time delays (diamonds).

The eigenvalues appear in degenerate pairs because of rotational symmetry of the system. If a non-uniform distribution of the parameters in the y direction is chosen, the previously degenerate eigenvalue pairs separate. This has been investigated by applying a circumferential distribution of the mean values of the time delays in the $n - \tau$ model. A sinusoidal distribution was chosen $\bar{\tau}(\phi) = \bar{\tau}_0(1+\gamma\sin(\phi))$ in which γ is set to values ranging from zero (uniform distribution) to 0.2. The most unstable eigenvalue pair has been plotted for different values of γ in Fig. 5.23. From this figure can be seen that when γ is non-zero, the pole pairs split. This figure also shows that

the previously unstable system can be stabilized by modifying the circumferential distribution of time delays. The order of the system is very high: 254 eigenvalues. However, this does not cause any numerical problems. Moreover, by using the Matlab package, convenient methods for model reduction are available. The order can be reduced considerably if rotational symmetry of the system may be assumed, however this is not done in this work.

Time Domain Simulation

The systems can be analyzed in the time domain by applying an additional input for source terms in the flame module. The frequency spectra of the independent source terms have been determined experimentally. A transfer function (H_s) was then fitted to the magnitude of the frequency spectra. A time domain source signal can then be obtained by filtering white noise with the transfer function (H_s). The source terms are defined as acoustic far-field turbulent combustion noise. The mechanism of noise generation is independent of the acoustic field. Note that this last statement is merely a matter of definition: in the transfer function measurement technique, acoustic quantities that are linearly dependent of an external excitation signal are attributed to the transfer function of the flame. The source term consists of signals that are linearly independent of external excitation. In a multi-burner configuration, all source terms should be linearly independent. This is obtained by generating different white noise sequences for each burner. The model was then simulated in the Matlab/Simulink environment, using a 5th order integration scheme. Two models have been compared: one in which the value of $\bar{\tau}$ was chosen such that the system was stable, and another model that was made slightly unstable. To avoid unbounded growth of the unstable model, a saturation function has been applied to the output velocity of the flame model. The resulting time trace of the unstable model at one burner location has been plotted in Fig. 5.24. The exponential growth and non-linear saturation can be

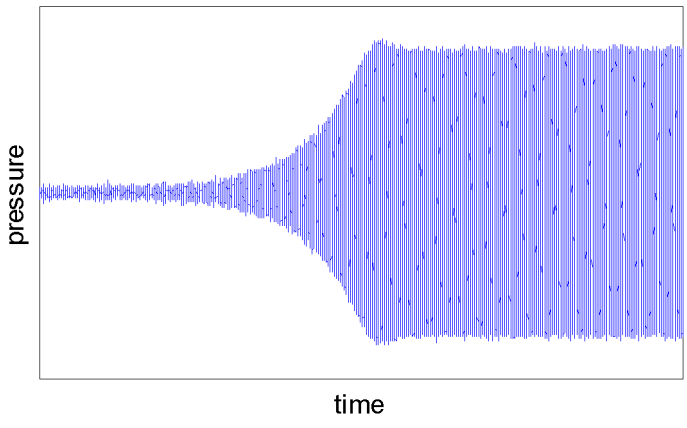

Figure 5.24: Time trace of the pressure signal at one burner location, during transition from exponential growth to non-linear saturation.

observed in this plot. The spatial distribution of the pressure amplitudes at the peak frequency

has been calculated from the time traces in a similar manner as described by [64]. This is done by calculating the transfer function estimate ($T_{r,k}$) between the pressure signal at every burner location (p_k) and the pressure trace at a reference position (p_r):

$$T_{r,k}(\omega) = \frac{S_{\overline{p_r p_k}}(\omega)}{S_{\overline{p_k p_k}}(\omega)} \tag{5.49}$$

The absolute value and phase of $T_{r,k}$ at the peak frequency has been plotted for every burner position in Figs. 5.25 and 5.26 for the stable case and for the unstable case. The stable case shows a typical standing wave pattern (sinusoidal distributed absolute values, ±180 degree phase jump). The unstable case is characterized by a travelling wave (uniform amplitude distribution, linear phase drop). The plots have a striking similarity with the experimental results obtained by [64].

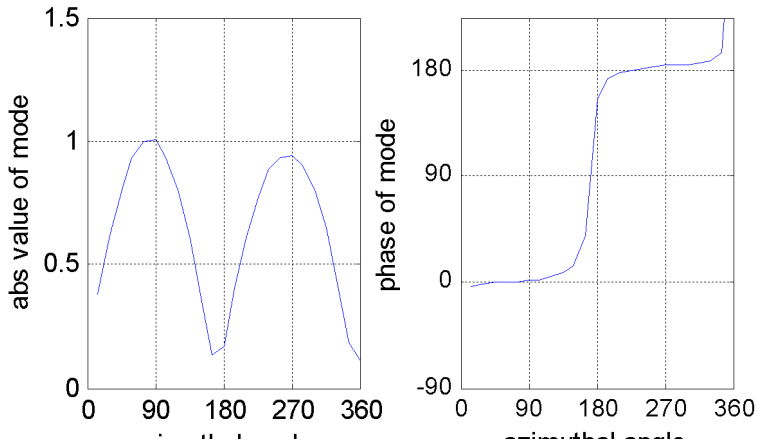

Figure 5.25: Standing wave pattern.

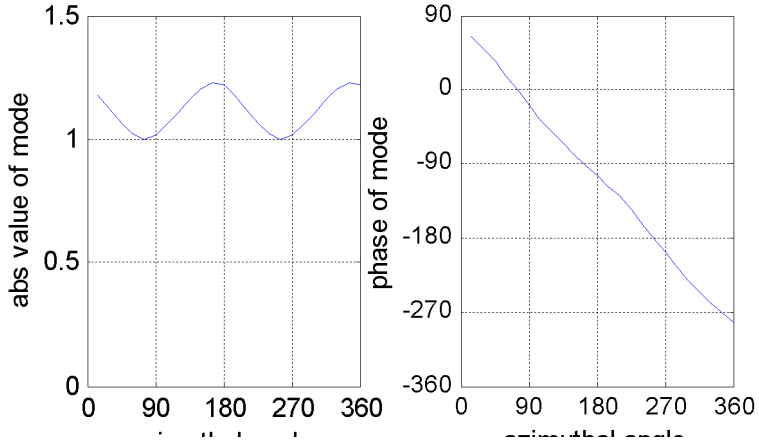

Figure 5.26: Travelling wave pattern.

In this case, the system under consideration is completely rotationally symmetric, the orientation of rotation of the traveling wave is determined by the random sequences that are used as an input to the system. When using a rotationally symmetric excitation, a standing wave pattern is observed, even for the unstable case. However, it was observed that after a very long simulation time a rotating wave pattern is obtained again. This phenomenon is not observed when the non-linear saturation function is removed. The hypothesis is that the non-linear dynamic system has two types of solutions (fixed points): a center point and a saddle point. The center point corresponds to the traveling wave, the saddle point solution corresponds to standing wave. Thus the standing wave type solution exists, but the smallest (possibly numerical) disturbance will cause the solution to drift to the rotating mode type solution. This hypothesis will be proved in the next section.

5.9 Non-linear Analysis: Rotating Modes

5.9.1 Analysis

During the time domain simulation of the model of the annular combustion system with non-linear heat release limitation, the following has been observed:

- If the linear system has slightly damped eigenvalues, then forcing of the system with white noise results in standing wave patterns. The location of nodes and anti-nodes in the azimuthal direction changes slowly, depending on the forcing signal.
- If the linear system has unstable eigenvalues, then forcing of the system with white noise results in exponentially growing standing wave patterns. The location of nodes and anti-nodes in azimuthal direction does not change. If the amplitudes become larger than the threshold in the saturation, then after some time a limit cycle takes place. During the transition from exponential growth to limit cycle behavior, the wave shape transforms from a standing wave pattern to a traveling wave. The traveling wave has a phase speed of approximately the speed of sound.

Questions arise now:

- why does the wave shape transform from a standing wave to a traveling wave?
- what determines if it is a clockwise or counter clockwise rotation?
- is it a numerical artifact, or is there experimental evidence that this behavior occurs in real gasturbines?

The answer to the last question is: yes, there is evidence that this phenomenon occurs in gasturbines. Measurement of instantenous heat release in Alstom gas turbines, showed that the amplitude of heat release intensity in the azimuthal direction was uniform, but the phase of the heat release fluctuations changed linearly with azimuthal position [44]. Acoustic measurement in a gas turbine with twelve pressure transducers in circumferential positions show the same result [64], (in fact figures 5.25 and 5.26 are almost identical to the results presented in [64]). In order to give an answer to the remaining questions, a simplified version of the annular combustion model will be analysed. This reduced non-linear model has to be as simple as possible while retaining the typical wave pattern switching behavior.
Starting from the wave equation with damping coefficient α and spatially distributed heat addition Q:

$$\nabla^2 p - \alpha \frac{\partial p}{\partial t} - \frac{1}{c^2}\frac{\partial^2 p}{\partial t^2} = -\frac{\gamma - 1}{c^2}\frac{\partial Q}{\partial t}. \tag{5.50}$$

After modal expansion:

$$\frac{\partial^2 \eta_m}{\partial t^2} + \alpha \frac{\partial \eta_m}{\partial t} + \omega_m^2 \eta_m = \frac{\gamma - 1}{\bar{p}\Lambda} \int_V \frac{\partial Q}{\partial t} \psi_m dv. \tag{5.51}$$

The eigenfrequencies and modes of a one-dimensional annulus are given by:

$$\omega_m = \frac{2cm}{D} \tag{5.52}$$

$$\psi_m = \begin{cases} \cos(\theta m) \\ \sin(\theta m) \end{cases}$$

$$\Lambda = \pi \tag{5.53}$$

The heat release in this equation remains to be coupled to the acoustic field. For reasons of simplicity, the heat release will be assumed to be proportional to the acoustic pressure: $-\frac{\gamma-1}{\bar{p}\Lambda}Q = \beta p$ for small amplitudes. If the amplitude of p exceeds a certain threshold value, the heat release is not proportional any more, but is limited to a fixed constant value. Introducing Γ as the non-linear saturation function, Eq. 5.51. can be written as:

$$\frac{\partial^2 \eta_m}{\partial t^2} + \alpha \frac{\partial \eta_m}{\partial t} + \omega_m^2 \eta_m = \beta \int_V \frac{\partial \Gamma(p)}{\partial t} \psi_m dv. \tag{5.54}$$

If the spatial heat release distribution is not assumed to be continuous, but discrete, with N points of heat addition equally distributed around the circumference, Eq. 5.51 can be represented by the feedback diagram of Fig. 5.27. Note that this representation is very similar to the representation of the combustion chamber with N burners.

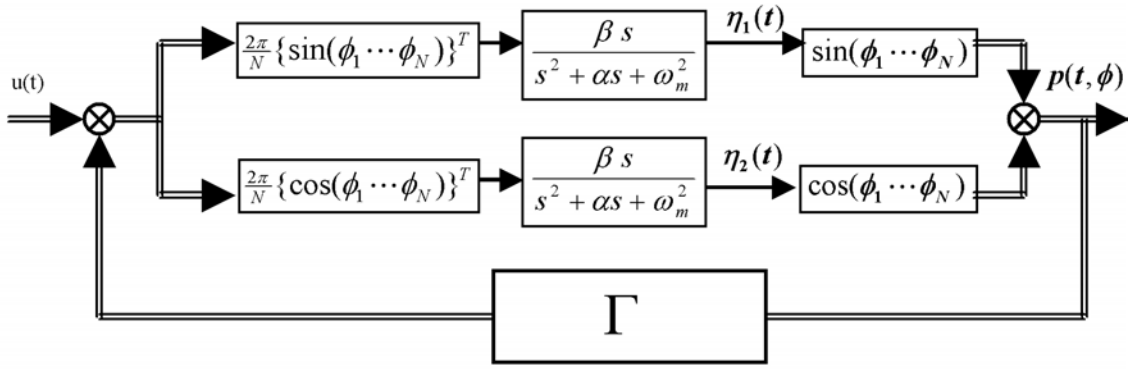

Figure 5.27: Simplified non-linear feedback representation of one mode of the combustion system.

In this figure, the two second order transfer functions represent the dynamics of the two orthogonal modes. The input to the system is represented by $u(t)$. One mode is represented by η_r with eigenvector $\psi_r(\phi) = \sin(m\phi)$, the other by $\psi_i(\phi) = \cos(m\phi)$. Here, ϕ represents the azimuthal angle of every burner position, and m represents the azimuthal mode number. The acoustic pressure in the azimuthal direction is then given by: $\sum_{m=1}^{\infty}\{\eta_{r,m}\psi_{r,m} + \eta_{i,m}\psi_{i,m}\}$. In this example the first azimuthal mode will be considered (m=1). In the diagram, single lines represent scalar signals, double lines represent vectors (as a function of time). The dimension of the vector signals is equal to the number of burners. The non-linear saturation simply passes through the signal if the magnitude of the signal is below a certain threshold value, L. If the absolute value of

the signal $p(t, \phi_k)$ is larger than L, then the k^{th} ouput is given by: $\Sigma(p(t, \phi_k)) = sign(p(t, \phi_k))L$. The saturation acts on all elements of the vector $p(\phi)$ independently.
Note that one mode is described by two identical pairs of eigenvalues with orthogonal eigenvectors (degenerate pole pairs). Thus the acoustic field can be considered as the sum of two orthogonal modes having the same eigenfrequency. Equation 5.42 shows that one mode has a sinusoidal distribution and the other a cosinuoidal distribution in the azimuthal direction. In the linear system these two modes are not coupled. However, in the non-linear system these modes will be coupled because the saturation takes place on the *sum of the two modes*. Note that a similar representation can be found in terms of a clockwise and counter clockwise pair of Riemann invariants, these can also be considered as two orthogonal eigenmodes of the system.
It is of interest now to see if the dynamic system represented by Fig. 5.27, has the same "mode-switching" behavior as the original system. The distinction between standing wave and travelling wave behavior can be made by analysing the time traces of the phase and absolute value of $\eta_c(t)$:

- A standing wave is characterised by a constant value of the argument of $\eta_c(t)$ in time (apart from $\pm\pi$ jumps). The absolute value of $\eta_c(t)$ changes periodically from zero to its maximal value. Thus, in the complex plane $\eta_c(t)$ moves with time along a straight line through the origin.

- A traveling wave is characterised by a constant absolute value of $\eta_c(t)$, while the phase changes proportionally with time. In the complex plane this is represented by a circle centered at the origin.

The two complex Riemann invariants can be optained from $\eta(t)$ in a very elegant way using the Fourier transform of a complex signal. With $\eta(t) = |\eta|e^{i\phi(t)}$ the pressure distribution in the azimuthal direction can be written as:

$$p(\theta, t) = |\eta(t)| \sin(\theta m + \phi(t)) = \eta(t)e^{i\theta m} + c.c. \,, \tag{5.55}$$

in which $c.c.$ denotes that the complex conjugate of the quantity is added. The acoustic field can also be expressed in terms of Riemann invariants traveling in opposite directions:

$$p(y, t) = f(t - \frac{y}{c}) + g(t + \frac{y}{c}) = \hat{F}(\omega)e^{+i\omega(t-\frac{y}{c})} + \hat{G}(\omega)e^{+i\omega(t+\frac{y}{c})} + c.c. \tag{5.56}$$

Upon substitution of $e^{i\omega\frac{y}{c}} = e^{im\theta}$, this can be written as:

$$\begin{aligned} p(\theta, t) &= \hat{F}(\omega)e^{+i\omega t}e^{-im\theta} + \hat{G}(\omega)e^{+i\omega t}e^{+im\theta} + \hat{F}(-\omega)e^{-i\omega t}e^{+im\theta} + \hat{G}(-\omega)e^{-i\omega t}e^{-im\theta} \\ &= \{\hat{F}(-\omega)e^{-i\omega t} + \hat{G}(\omega)e^{i\omega t}\}e^{im\theta} + c.c. \end{aligned} \tag{5.57}$$

This has the same shape as 5.55 and thus $\eta(t) = \{\hat{F}(-\omega)e^{-i\omega t} + \hat{G}(\omega)e^{i\omega t}\}$. Therefore, the spectra $\hat{F}(-\omega) = \hat{\eta}(-\omega)$ corresponds to the component of the signal rotating counter clockwise and $\hat{G}(\omega) = \hat{\eta}(+\omega)$, corresponds to signals rotating clockwise. Because $f(t) = \hat{F}(-\omega)e^{-i\omega t} + \hat{F}(\omega)e^{i\omega t}$, the Fourier transform of the modal value $\hat{\eta}(\omega)$ corresponds to the Fourier transform of g for positive values of omega and vice versa for f.

The time domain representation of f and g can then be obtained by an inverse Fourier transform of the positive and negative spectra of η respectively.

$$\begin{aligned} g(t) &= \mathcal{F}^{-1}\{\mathcal{H}(\omega)\mathcal{F}\{\eta(t)\}\} + c.c. \\ f(t) &= \mathcal{F}^{-1}\{\mathcal{H}(-\omega)\mathcal{F}\{\eta(t)\}\} + c.c. \end{aligned} \tag{5.58}$$

The simplified system is simulated in the time domain, the parameters in the system are chosen such that the linear system is unstable: $\omega_n = 200\pi, \beta = \frac{40}{\pi}, \alpha = 4\pi, L = 5$. As an initial condition, $\eta_c(t = 0) = 1 + i$ was chosen, thus ensuring that both η_1 and η_2 have initially equal amplitudes and are in phase. During the simulation, standing wave behavior is observed. The amplitudes grow exponentially until they are limited by the saturation function. After being saturated, the wave pattern is still that of a standing wave. However, when running the simulation long enough, the wave pattern changes from a standing wave to a traveling wave. The hypothesis is that because the system is completely symmetric, there is initially nothing driving the system in one direction or the other. After a suffciently long simulation time, numerical errors due to finite word length will accumulate in the time integration and cause asymmetry in the system. If this is what really happens, then deliberately introducing a small asymmetry in the system should cause a similar (but stronger) effect if the asymmetry is large compared to the floating point error. Moreover, by reversing the asymmetry, the direction of the traveling wave should be reversed. In order to see if the system indeed behaves like this, a small gain (value 1.001) was added in the feedback loop. In a first simulation this gain was made such that it only acted on the real part of η_c (on η_r). In a second simulation the same gain was added, but now only acting on the imaginary part of η_c (on η_i). The simulation result correspond exactly to what is predicted. The system starts as a diagonal line in the η_c plane, η_r and η_i having equal values at each instant of time. Then, when the saturation starts to affect the system, the line slowly evolves to an elipse, and finally to a circle. Depending on the asymmetry applied, the circle rotates clockwise or counter clockwise. In Fig. 5.28, the timetraces of $p(t)$, $v(t)$, $f(t)$ and $g(t)$ are plotted in the complex plane. These quantities are defined here as:

$$\begin{aligned} p(t) &= \eta(t) \\ f(t) &= \mathcal{F}^{-1}\{\mathcal{H}(\omega)\mathcal{F}\{\eta(t)\}\} \\ g(t) &= \mathcal{F}^{-1}\{\mathcal{H}(-\omega)\mathcal{F}(\eta(t))\} \\ v(t) &= f(t) - g(t), \end{aligned} \tag{5.59}$$

and are obtained from $\eta(t)$ in a post processing step. Note that the complex conjugate part has been neglected, thus the signals are complex valued and can be considred as Hilbert transforms of the real valued signals. Figure 5.28 makes clear that, in the final state, one of the Riemann invariants vanishes. If the initial value is perturbed with reversed asymmetry, the same, but mirrored plot is obtained.

The system was evaluated several times with a random perturbation on the initial conditions. The absolute values of $g(t)$ were then plotted against $f(t)$, the result is shown in Fig. 5.29. From this plot it is clear that depending on the initial condition, the solution will be a left running wave or a right running wave.

5.9.2 Analytic Solution

The analysis in the previous section makes clear that there are two types of solutions to the problem of the annular duct with saturated heat release: the first solution is a traveling wave, the second a standing wave. The second solution does not seem to be stable. In this subsection the wave equation for a one-dimensional annulus with saturated heat addition will be derived. An analytic solution of the system will be obtained, demonstrating the existence of the two types of solutions. The stability of both solutions is investigated and the standing wave solution is found to be unstable.
The analysis continues here from Eq. 5.54. Combining the two orthogonal modes in the complex plane:

$$\frac{\partial^2 \eta_{r,m}}{\partial t^2} + \alpha \frac{\partial \eta_{r,m}}{\partial t} + \omega_m^2 \eta_{r,m} + i\frac{\partial^2 \eta_{i,m}}{\partial t^2} + i\alpha \frac{\partial \eta_{i,m}}{\partial t} + i\omega_m^2 \eta_{i,m} = -\frac{\gamma - 1}{\bar{p}\Lambda} \int_V \frac{\partial \dot{Q}}{\partial t} (\psi_{r,m} + i\psi_{i,m}) dv, \tag{5.60}$$

in which $\eta_{r,m}$ is the modal value corresponding to $\psi_{r,m} = \sin(\theta m)$, and $\eta_{i,m}$ corresponds to $\psi_{i,m} = \cos(\theta m)$. Defining the complex modal values and modes as: $\eta_m = \eta_{r,m} + i\eta_{i,m}$ and $\psi_m = \psi_{r,m} + i\psi_{i,m}$, the wave equation can be expressed as:

$$\frac{\partial^2 \eta_m}{\partial t^2} + \alpha \frac{\partial \eta_m}{\partial t} + \omega_m^2 \eta_m = \frac{\gamma - 1}{\bar{p}\Lambda} \int_0^{2\pi} \frac{\partial \dot{Q}}{\partial t} e^{i\theta m} d\theta. \tag{5.61}$$

$$\frac{\partial^2 \eta_m}{\partial t^2} + \alpha \frac{\partial \eta_m}{\partial t} + \omega_m^2 \eta_m = \beta \int_0^{2\pi} \frac{\partial \Gamma(p)}{\partial t} e^{i\theta m} d\theta, \tag{5.62}$$

with the saturation function defined as:

$$\Gamma(p) = \{\mathcal{H}(|p| - L)\frac{L}{|p|} + \mathcal{H}(L - |p|)\}p, \tag{5.63}$$

in which $\mathcal{H}$ is the Heaviside function.
Expressing $p(\theta, t) = \sum_{k=0}^{\infty} \eta_k e^{i\theta k}$, retaining only the mode $k = m$ and substituting this in the right part of Eq. 5.62:

$$\beta \int_0^{2\pi} \frac{\partial \Gamma(\eta_m e^{i\theta m})}{\partial t} e^{i\theta m} d\theta \tag{5.64}$$

Carrying out the integration piecewice from $\theta = 0$ to $\theta = \arcsin(\frac{L}{\eta_m})$, and from $\theta = \arcsin(\frac{L}{\eta_m})$ to $\pi/2$, equation 5.62 can be written as the scalar complex differential equation:

$$\frac{\partial^2 \eta_m}{\partial t^2} + \alpha \frac{\partial \eta_m}{\partial t} + \omega_m^2 \eta_m = \pi\, \beta \frac{\partial}{\partial t} \Gamma_2(|\eta_m|) e^{i\phi}, \tag{5.65}$$

with the non-linear function Γ_2 defined as:

$$\begin{array}{rcll} \Gamma_2(|\eta|) & = & |\eta| & \text{if} \quad |\eta| < L \\ \Gamma_2(|\eta|) & = & \frac{2}{\pi}|\eta| \arcsin(\frac{L}{|\eta|}) + \frac{2}{\pi} L \sqrt{1 - (\frac{L}{|\eta|})^2} & \text{if} \quad |\eta| > L \end{array} \tag{5.66}$$

and $\eta \equiv |\eta| e^{i\phi} \equiv \eta_r + i\,\eta_i$.
By separating the real and the imaginary part of Eq. 5.65, the complex differential equation can be expressed as two real, second order differential equations:

$$\frac{\partial^2 \eta_r}{\partial t^2} + \alpha \frac{\partial \eta_r}{\partial t} + \omega_m^2 \eta_r = \pi\,\beta \frac{\partial}{\partial t} \frac{\Gamma_2(|\eta|)}{|\eta|} \eta_r, \tag{5.67}$$

$$\frac{\partial^2 \eta_i}{\partial t^2} + \alpha \frac{\partial \eta_i}{\partial t} + \omega_m^2 \eta_i = \pi\,\beta \frac{\partial}{\partial t} \frac{\Gamma_2(|\eta|)}{|\eta|} \eta_i, \tag{5.68}$$

If $|\eta| > L$ the two equations are nonlinearly coupled by $\Gamma_2(|\eta|) = \Gamma_2(\sqrt{\eta_r^2 + \eta_i^2})$. For small values of η, the two equations are de-coupled, because $\frac{\Gamma_2(|\eta|)}{|\eta|} = 1$ if $|\eta| < L$ and the system is linear. It is easily seen that for small amplitudes (in the linear regime) the eigenvalues of the system are: $s = (\pi\,\beta - \alpha) \pm i\,\omega_n$. Thus, for small amplitudes the system is locally unstable if $\pi\,\beta > \alpha$. If both η_r and η_i have non-zero intial conditions, they will both evolve as sinusoidal functions with same frequency (ω_m) and an amplitude that increases exponentially in time. The phase between the two sinusoids and the ratio of their absolute values depends on the intial conditions only. If the initial conditions are such that both η_r and η_i are in phase, then this is observed spatially as a standing wave with growing amplitude. If their amplitudes are equal and the phase difference is 90 degrees, this corresponds to a traveling wave.
If the amplitude of oscillation $|\eta|$ exceeds the limit value (L), then the two waves (η_r and η_i) may not be considered separate anymore: both their amplitudes and phases are inter-dependent.
Solving Eq. 5.67 is a difficult task, therefore an approximate analysis will be made. The method used here is a variant of the "describing function method" [125], which is based on the principle of equivalent or harmonic linearization [114]. The underlying idea is to do a spectral decomposition and to consider only the frequency of the limit cycle. The effect of the nonlinearity (the ratio between "input" and "output") at this frequency is expressed as a quasi static "gain". This gain is only allowed to change very slowly in time; it is considered to be constant during one period of oscillation. This gain is obtained as the ratio between the Fourier transform of the output (evaluated at the frequency of the limit cycle) and the amplitude of the input. Because it desribes a non linear function, the value of the gain depends on the amplitude of the incoming signal. The problem can be solved by evaluating at what value of the gain (and hence the amplitude) a solution is obtained.
This specific case is somewhat more complicated, because the system contains two parallel second order systems. In order to extend the harmonic linearization method to two coupled systems, solutions of the type $\eta = A\,\cos(\omega_n\,t) + i\,B\,\sin(\omega_n\,t)$ will be considered. It is assumed that $A(t)$ and $B(t)$ are functions that vary slowly in time; their time scales being much larger than $1/\omega_n$. It might, at a first glance, be surprising that the phase difference between η_r and η_i is chosen to be 90 degrees. However, considering that the system is completely symmetric in ϕ, this type of solution is general, because a coordinate transform in ϕ is allowed. The "output" of the nonlinear function is assumed to be of a similar form:

$$\frac{\Gamma_2(|\eta|)}{|\eta|} \eta_r \approx A^*\,\cos(\omega_n t), \tag{5.69}$$

In which A^* is the slowly varying component of the nonlinear function's "output". An estimate of A^* can be obtained by means of the Fourier transform:

$$A^* = \frac{1}{\pi}\int_{\omega\, t=0}^{2\pi} \frac{\Gamma_2(|\eta|)}{|\eta|}\eta_r \cos(\omega_n t) d(\omega_n t) \tag{5.70}$$

Because both A and A^* vary slowly in time, their ratio can be considered as a quasi static gain: $K_r = \frac{A^*}{A}$, and similar for the imaginary component: $K_i = \frac{B^*}{B}$:

$$K_r = \frac{1}{\pi}\int_{\omega\, t=0}^{2\pi} \frac{\Gamma_2(\sqrt{A^2\cos^2(wt) + B^2\sin^2(wt)})}{\sqrt{A^2\cos^2(wt) + B^2\sin^2(wt)}} \cos^2(\omega_n t)\, d(\omega_n t) \tag{5.71}$$

$$K_i = \frac{1}{\pi}\int_{\omega\, t=0}^{2\pi} \frac{\Gamma_2(\sqrt{A^2\cos^2(wt) + B^2\sin^2(wt)})}{\sqrt{A^2\cos^2(wt) + B^2\sin^2(wt)}} \sin^2(\omega_n t)\, d(\omega_n t) \tag{5.72}$$

This doesn't seem to make the expressions much simpler but this will change for well-chosen combinations of A and B. Using the expression for K_r, the differential equation governing the real part is written as:

$$\frac{\partial^2\eta_r}{\partial t^2} + \alpha\frac{\partial\eta_r}{\partial t} + \omega_m^2\eta_r = \pi\,\beta\,K_r\,\eta_r, \tag{5.73}$$

and similar for the differential equation of the imaginary part. The solution is now readily seen, a limit cycle will occur if $K(A,B) = \frac{\alpha}{\beta\,\pi}$.
In order to obtain $K_r(A,B)$ and $K_i(A,B)$, Eq. 5.71 can be integrated piecewise, in a similar manner as in Eq. 5.64. However, in order to keep the analysis simple, the saturation function will be approximated by an analytic function that has similar properties as Eq. 5.66. A good approximation is obtained with:

$$\Gamma_2 = \frac{8\,L}{\pi^2}\arctan(\frac{|\eta|\,\pi^2}{8\,L}). \tag{5.74}$$

Two types of solutions will be considered now: the standing wave solution characterised by $B = 0$ (or by $A = 0$), and the rotating or traveling wave, characterised by $A = B$. It will first be investigated if these two wave types are indeed solutions to the problem under consideration. In a second step, the stability of both solutions will be investigated.

Solution 1. Standing wave
Substituting $B = 0$ and Eq. 5.74 into Eq. 5.71 and carrying out the integration yields:

$$\begin{aligned} K_r &= \frac{4}{\pi}\int_0^{\frac{\pi}{2}} \frac{\Gamma_2(\sqrt{A^2\cos^2(\omega\, t)})}{\sqrt{A^2\cos^2(\omega\, t)}} \cos^2(\omega\, t)\, d(\omega\, t) \\ &= \frac{4}{\pi}\int_0^{\frac{\pi}{2}} \frac{\Gamma_2(A\cos(\omega t))}{A} \cos(\omega\, t)\, d(\omega\, t) \\ &= \frac{16\,L}{8\,L + \sqrt{64\,L^2 + A^2\,\pi^4}} \end{aligned} \tag{5.75}$$

A solution is obtained for $\alpha = \pi\,\beta K_r$, and thus, solving for A yields:

$$A_{sol\,1} = \frac{16\,L\sqrt{\pi\,\beta^2 - \alpha\,\beta}}{\pi^{\frac{3}{2}}\,\alpha} \tag{5.76}$$

The entire system has been simulated in Simulink with values: $\omega_n = 200\pi, \beta = \frac{40}{\pi}, \alpha = 4\pi, L = 5$ with symmetric initial conditions, the resulting standing wave stabilised at an amplitude, $A_{sim} = 21.3674$. Substituting the values of β , α and L into Eq. 5.76 results in the same value: $A_{sol\,1} = 21.3674$.
In order to investigate the stability of this solution, a small perturbation $B \neq 0$ is considered. The gain K_i is evaluated for very small values of B and with $A = A_{sol\,1}$. The resulting expression is rather lengthy, evaluating the numerical result yields: $K_i = 0.583$. The dynamic relation for the imaginary component of the modal value is unstable, because $\alpha < \pi\,\beta K_i$. The implication is that if the initial conditions are such that $B(t = 0) = 0$ then the limit cycle is given by: $\eta_r = A_{sol\,1}\,\sin(\omega\,t)$. However, the slightest perturbation of $B(t)$ will grow exponentially, and as a result, the solution will drift away from $(A = A_{sol\,1}, B = 0)$.

Solution 2. Traveling wave
Substituting $B = A$ and Eq. 5.74 into Eq. 5.71 and carrying out the integration yields:

$$\begin{aligned} K_r &= \frac{4}{\pi}\int_0^{\frac{\pi}{2}} \frac{\Gamma_2(\sqrt{A^2\cos^2(wt) + B^2\sin^2(wt)})}{\sqrt{A^2\cos^2(\omega\,t) + B^2\sin^2(\omega\,t)}}\,\cos^2(\omega\,t)\,d(\omega\,t) \\ &= \frac{4}{\pi}\int_0^{\frac{\pi}{2}} \frac{\Gamma_2(A)}{A}\,\cos^2(\omega\,t)\,d(\omega\,t) \\ &= \frac{8\,L\,\arctan(\frac{A\,\pi^2}{8\,L})}{A\,\pi^2}, \end{aligned} \tag{5.77}$$

and $K_r = K_i$.
Thus the solution is given by:

$$\alpha - \pi\,\beta\frac{8\,L\,\arctan(\frac{A\,\pi^2}{8\,L})}{A\,\pi^2} = 0 \tag{5.78}$$

Solving for A yields: $A_{sol\,2} = B_{sol\,2} = 17.2947$, while the result obtained from simulation is $A_{sim} = B_{sim} = 17.2947$ as well. The stability of this solution can be directly seen by observation of Eq. 5.77. Any positive perturbation will make the gains K_r and K_i smaller, while any negative perturbation will make the gains larger. And thus the final solution will always be driven back to $A_{sol\,2} = B_{sol\,2}$.
It has been demonstrated analytically that only the rotating mode is a stable solution of the nonlinear system. The physical interpretation can be understood as follows. If the system is unstable, and the mode shape would be that of a standing wave around the circumference (sinusoidal distribution), then, the burners that are located where the standing wave has its maximum will be most affected by the saturation. The burners that are close to an anti-node of the standing wave (where the pulsation amplitudes are minimal) will not directly be affected

by the saturation mechanism. If, in addition to this sinusoidal pattern, there would be a much smaller component with a cosinusoidal distribution, then this second distribution has a maxima where the original distribution has a minima. Thus, the maxima of the cosine distribution will not be affected by the saturation. From this point of view, it is obvious that the cosine distribution is "less saturated" and will therefore grow in time, until it will be limited as strongly as the sine distribution. The sum of these cosine and sine distributions correspond to a sine wave, but with a spatial phase shift that increases linearly in time. Such a solution is observed as a rotating mode.

5.10 Discussion

This chapter started with an explanation of different system analysis techniques for thermoacoustic systems. Although the mechanisms involved are rather complex, relatively simple techniques can be used to analyze the stability of the systems. The relation between Nyquist's stability criterion, Rayleigh's stability criterion, the acoustic energy balance and the concept of passivity has been demonstrated. It was concluded that Nyquist's simplified stability criterion (for stable open-loop systems only) may not always be used, and its application should be avoided if no information is available about the location of the open-loop eigenvalues. Rayleigh's criterion gives good insight into the mechanism that leads to thermoacoustic instability. However, this criterion is based on the phase relation between acoustic pressure and acoustic heat release, whereas the characteristic behavior of lean premix flames is dominated by the phase relation between acoustic velocity and heat release. Nevertheless, Rayleigh's criterion can be applied, but in order to predict stability of the system, the response of the entire system needs to be evaluated. A disadvantage of frequency domain system analysis techniques of unstable systems is that the more unstable the system is, the smaller its frequency response close to the instability frequency.

Because of the importance of annular geometries in modern gas turbine combustion systems, three different approaches to model wave propagation in annular geometries have been discussed. The first approach is quasi one-dimensional: the three-dimensional acoustic waves are considered as an infinite sum (over all azimuthal mode numbers) of waves propagating in the axial direction. The azimuthal dependence of these axial waves is fixed, and depends on the azimuthal wave number only. This method is valid if the system is completely rotationally symmetric (the boundaries do not depend on the azimuthal coordinate). A network interconnection of an annular combustion system can be made including such a representation of the annular ducts. Because the entire system is considered to be quasi one-dimensional, the final system matrix is relatively small. Nevertheless, solving for the eigenvalues is not that trivial because it requires a numerical search in the complex field. This approach includes mean flow, and because of its low order it is computationally efficient.

This method has been extended in order to model three-dimensional annular ducts in a quasi two-dimensional manner. The underlying idea is to recognize that equations expressing the wave propagation can be considered as two-dimensional spatial Fourier series. By applying as many boundary conditions in the azimuthal direction as the number of unknown Fourier coefficients, the system can be solved for the unknown Fourier coefficients. Using this approach, a method has been developed to obtain transfer matrices of three-dimensional ducts. These transfer matrices can be combined in a network interconnection including the burner and flame transfer matrices, in which no rotational symmetry is assumed. Because the system matrices are larger than the previously mentioned approach, the method is less computational efficient. Nevertheless, the frequency response of a typical gas turbine configuration could be calculated in approximately 0.3 seconds per frequency. However, when it comes to finding all the eigenvalues of the system, the numerical search becomes very lengthy. Moreover, numerical difficulties can occur when the root finding algorithm is searching for a value close to a discontinuity of the function caused by

branch cuts.
The disadvantage of the aforementioned methods could be largely overcome by using the Green's function approach in combination with a modal expansion. A transfer function of an annular duct (or any other geometry) can then be expressed in terms of the eigenvalues and eigenmodes of the geometry with solid walls. These eigenvalues and modes can be obtained analytically for relatively simple geometries or can be obtained from a finite element package for geometries of arbitrary complexity. The resulting transfer matrix is represented in state-space. By representing all other elements in the network as state-space systems, the final system interconnection can be performed in an elegant way using linear fractional transforms. The stability analysis of the interconnected system reduces now to calculate the eigenvalues of a real valued frequency independent matrix, which can then be performed in a very straightforward manner using commonly available techniques in linear algebra. The advantage of a state-space representation of the network is that time domain simulations of the system can easily be performed (this is in strong contrast with the methods mentioned before) using a time marching procedure. In the time domain, inclusion of non-linearities is straightforward. Moreover, the method is very computationally efficient: within seconds all the eigenvalues of the (linear) system can be obtained, whereas in the wave propagation method this would take many hours (without a guarantee that all eigenvalues have been found). This approach has been validated by comparison against results found in literature, against analytic solutions and by comparing to experimental data from a single burner atmospheric test facility. The comparison was very good for all test cases. No numerical difficulties have been observed, not even when using unrealistically high order of the modal expansion. However, it should be noted that in this method the influence of the mean flow was neglected. The influence of mean flow could, in principle, be introduced, but is recommended here as a topic of future research. Nevertheless, the approach is very useful because the influence of the mean flow was investigated in practical systems, and concluded to be negligible.
When analyzing the network interconnection of a gas turbine combustion system a somewhat unexpected behavior of the system was observed when a non-linear saturation function was introduced into the system. The impulse response of the (unstable) system resulted (as expected) in a standing wave behavior in azimuthal direction. However, after sufficient simulation time the mode started rotating (which was unexpected), as the system was completely symmetric. Because there is experimental evidence for similar behavior in gas turbines, this mechanism has been investigated in more detail. The conclusion was that due to the saturation function, the standing wave behavior is unstable: infinitesimally small perturbations will cause the standing wave pattern to change to a rotating wave behavior.

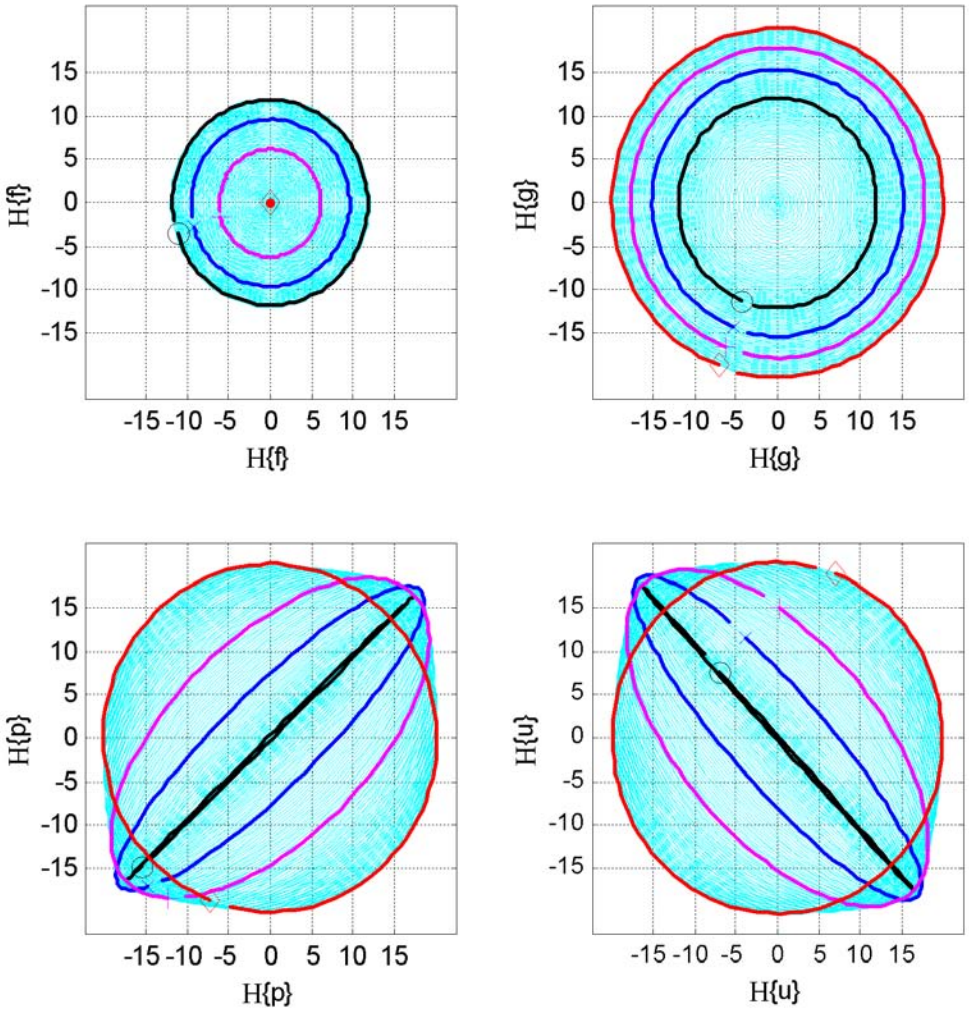

Figure 5.28: f(t), g(t), p(t) and v(t). Evolution from a standing wave pattern to a traveling wave due to non-linear coupling. Time traces of the signal during (almost) one period have been plotted with thick lines, at the begin of the simulation (marked by circles), halfway the simulation (crosses) and at the end (diamonds).

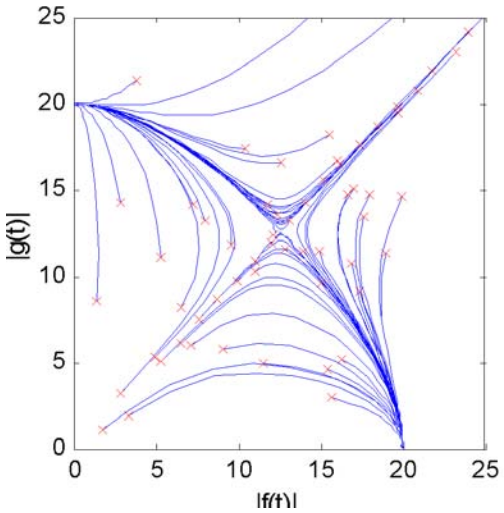

Figure 5.29: The absolute values of the Riemann invariants plotted against each other for several runs with randomly perturbed initial conditions. The crosses indicate starting points.

Chapter 6

Active Control

This chapter starts with an overview of active combustion control strategies and a literature review. Major advantages and disadvantages of several controller algorithms, actuating devices, and sensors will be discussed. The second section describes the test facility and experimental equipment used at Alstom for active control experiments. In the same section, a system identification technique is described that has been developed to obtain a dynamic model of the acoustic behaviour of the combustion test facility. Section 6.3 describes how model based controllers have been obtained based on the identified dynamic model. The control performance was first assessed in a numerical analysis. In a second step, the controllers have been tested on the combustion test facility. The experimental results at different operating conditions for different controllers are reported. A self-tuning controller, based on an evolution strategy (or genetic algorithm), has been developed in the course of this work. The algorithm and test results are reported in section 6.4. Section 6.5 deals with a control method that has been developed for multi-burner annular combustion chambers. Results of numerical simulations are shown in this section. Section 6.6 gives a comparison between the different control approaches and the conclusions for this chapter.

6.1 Active Control Strategies

Active control of combustion instabilities can be defined as: *control and suppression of combustion instabilities by actively and continuously perturbing certain combustion parameters in order to interrupt the growth and persistence of resonant oscillations* [75]. As opposed to passive control, active control techniques include control systems whose operation depends on a dynamic or time-varying hardware component (e.g. a loudspeaker, or fast response fuel flow actuator). A distinction can be made between open loop and closed loop control. Closed loop control uses a time-varying input from the combustion system (e.g., from an acoustic pressure transducer or instantaneous heat release sensor) to determine the control action (feedback control). As opposed to open loop control, where the actuation signal is an external, independent input [75]. The control action in closed loop control can be in the same dynamic range as the combustion instability (fast response feedback), or on a much larger time scale (trim-adjust controllers). In

this work only fast response closed loop controllers will be considered. A further distinction can be made between adaptive, self-tuning, and fixed-parameter controllers. An adaptive controller uses an internal algorithm that adjusts its (time varying) parameters automatically in order to achieve the control performance. A self-tuning controller is similar to an adaptive controller, but the time-scale at which the controller parameters change is much larger. The transfer function of a fixed parameter controller is time independent. Fixed parameter controllers can either be manually tuned to achieve a desired control objective, or the transfer function of the controller can be obtained based on a dynamic model of the thermoacoustic system. The model of the controller can either be obtained from physical knowledge of the system (*physics based*) or be obtained by an empirical method (*system identification*).

6.1.1 Sensors

The sensors for feedback control should be able to capture a dynamic combustion parameter related to the instability phenomenon in the frequency range of interest. Transducers for acoustic pressure (such as microphones or piezo transducers) have the advantage that they do not need to be placed close to the heat release zone, because acoustic waves will propagate through the entire combustion chamber and air supply system. Generally, it is the objective of the control system to minimize the acoustic pulsations in the system. Because the acoustic waves will be present as standing waves, and thus have a pattern of alternating minima (nodes) and maxima (anti-nodes), the intensity of a microphone signal will strongly depend on the location where it is placed in the combustion chamber. Even if the pressure transducer would be placed strategically close to an anti-node, there is a danger that because of the control action, a mode will be excited that has a node close to the sensor position, and can therefore not be measured [1].
Ideally, multiple microphones would have to be installed, from which the acoustic intensity in the entire combustion system can be obtained, but this is not a very practical solution. Generally the frequencies of interest are low (long wavelength) and therefore it is often assumed that one transducer represents the acoustic intensity in the combustion chamber. This is a dangerous assumption that should be handled with care, particularly at high frequencies. In annular gas turbines, multiple sensors are even more important, as they are required to capture the azimuthal distribution of the modes. The required number of sensors depends on the order of the modes present in the system. In [48], 12 piezo pressure transducers are used in the plenum chamber of an annular gas turbine with 24 burners. Making use of the symmetry of the system, these 12 transducers give an estimate of the acoustic pressure at the 24 burner locations. Note that even less transducers are required by making use of modal decomposition techniques (section 6.5).
Because fluctuating heat release is the driver for acoustic instabilities it is natural to monitor this heat release. Photo multipliers are used to measure the light intensity emitted from the flame. This intensity has some proportionality with the heat release in the flame. Using optical filters in front of the photo multiplier enables one to filter out the spectral bands that are related to certain reaction progress chemical components (OH, C_2, CH) in the combustion zone . The advantage of this method is that it is independent of changes in modal shapes of the acoustic

[1] In control theory, this phenomenon is related to the "observability" of a system's state.

field. A disadvantage is that visual access is required to the reaction zone (this can be solved by making use of fiber optics). These signals tend to be more "noisy" than pressure signals, which is unwanted in feedback applications. An additional disadvantage is that these devices have a limited optical scope. Thus if the flame position changes out of the line of sight of the sensor, the sensor signal intensity will decrease. This is of course dangerous in active control applications: the flame may change position due to the control action, the cost function based on the intensity signal then reduces, and the controller achieves its goal (reducing the cost function), without changing the pulsation behavior. Both types of sensors have advantages and disadvantages, in table 6.1.3 the sensor types used by different researchers are listed.

6.1.2 Actuators

The actuator should be capable of interacting with the dynamics of the thermoacoustic system in the same time scale as the acoustic perturbations. The frequencies reported by most authors are typically in a range between 50 and 500Hz. The performance of the actuators is always limited in the high frequency range because of actuator inertia considerations. Loudspeakers placed in the air supply (or in the exhaust, if cooled) can be used to apply acoustic forcing to the system. The advantage of loudspeakers is that they are cheap and have good response up to high frequencies. Loudspeakers are less suitable for industrial applications because of their short lifetime in harsh environments and because of limited actuation power. Loudspeakers are, of course, not an option in industrial gas turbines.

Modulation of the fuel supply has the advantage that, because of the chemical enthalpy of the fuel, small modulations may have a strong impact on the entire system. The fuel flow can be modulated by placing loudspeakers in the fuel supply [99]. However, for industrial applications a fast-response fuel valve is more suitable. Solenoid type fuel valves, as used for fuel injection in automotive engines, have fast response but have the disadvantage that they are of the open/close type, and thus not linear. This poses serious limitations to control design and implementation. Valves driven by a linear motor as used in [48] do not have this disadvantage. Magneto strictive materials and piezo stacks have very high frequency response but only a limited stroke (typically 100 microns). A valve that uses a magneto strictive material (Terfenol-D) was used in [83]. Note however, that magneto strictive materials have highly non-linear dynamics, which may cause problem in control design [23].

A disadvantage of actuation valves is that a pressure drop across the valve is required to have good actuation power. If the pressure drop is larger than the critical pressure drop (thus creating sonic conditions in the valve orifice), nearly linear response of the mass flow with respect to opening area off the valve is obtained. In industrial applications, especially under pressurized conditions, such a large pressure drop over the actuation valve is unwanted. Thus, a good actuation valve should create high amplitude flow modulation while ensuring a low pressure drop across the burner. From basic fluid dynamic insight, it is understood that this means that the stroke of the valve should be large. However, a large stroke causes high inertial forces that are difficult to realize technically.

The fuel flow actuators can generally not be placed arbitrarily close to the reaction zone, and

some piping is required between the actuator and the fuel injection position. This will cause a delay time between the actuation signal and the heat release associated with it, which will invariably deteriorate the controller performance. An additional complication is that acoustic standing waves will be present in the tubing connecting the actuator to the burner. Because of acoustic resonance, actuation power will be strongly frequency dependent. Proper choice of the length of the tubing enables one to tune this resonance frequency to be close to the frequency encountered in the combustor, thus ensuring high gain at the frequency of interest. However, if the frequency of the combustion instability changes, the gain at this new frequency may not be sufficient.
A different actuation technique is based on local acoustic excitation at the burner exit enabling interference with the formation of spanwise vortices. The presence of these vortices have a strong effect on the flame shape and position. A periodic heat release can be achieved by periodic excitation of the shear layer. Although shear layer excitation is mostly reported as a technique for open loop control, it has also been applied in closed loop [42].

6.1.3 Controllers

Active instability control (AIC) in combustion systems dates back to the early 1950's [130], where active control of liquid-fueled rockets is proposed. However, no references mentioning any experimental results in this early stage have been found. This is probably due to hardware limitations of the electronic components at that time. The first experimental results of AIC are reported in the early 1980's for so called *Rijke Tubes* [31, 46].
In a later stage AIC, has been applied to combustion systems [107, 99, 14, 67]. All the controllers used at this stage where manually tuned, fixed parameter controllers, generally some variant of the "band-pass phase-shift" type. These controllers are effective if only one acoustic mode is dominant. They rely on the principle that the effect of the actuator on the acoustic field is opposite to the acoustic field present in the combustion system, provided that the phase at the instability frequency is well chosen. The control loop consists of a sensor, amplifier, and a "phase shifting device". The sensor signal is often passed through a bandpass, lowpass or highpass filter in order to remove unwanted spectral components. The phase shift can be realized in several ways. One way is to use a simple time delay line, the phase of the delay line is a function of frequency: $\phi = -\omega\ \tau$, in which τ is the delay time. Another method to generate the desired phase is to make use of a phase lock technique: a zero crossing of the input signals triggers the generation of a sine wave of the right frequency and phase. A third possibility is to make use of a lag/lead compensator. The desired phase is then created by a transfer function $(\tau s + 1)$, because this function is not proper, it can be realized as: $H = \frac{\tau s+1}{s^2+\omega_0^2}$. The denominator of this function acts as a very narrow bandpass filter. This is similar to the approach used by [42] where the cut-off frequencies of low pass and high pass Butterworth filters are adjusted such as to create the desired phase at a certain frequency in the passband. Although simple in nature, these controllers have proven to be effective in many experimental and theoretical investigations [124, 74, 92, 42, 58, 83], even in heavy duty industrial size gas turbine applications [48, 122].
The settings of the gain, phase shift, and filter coefficients can be tuned manually to achieve

optimal pulsation suppression. A different possibility is to make use of measured transfer functions and to choose the right settings based on classical control design techniques such as Bode plots, or Nyquist diagrams [40]. However, a drawback of this type of control is that instabilities at other frequencies than the original instability frequency may be excited. In some cases this limitation may be partially overcome by choosing the right settings of the bandpass filter. The frequency of secondary peaks are often close to the frequency of a (previously stable) higher harmonic of the original frequency, but can also be close to the original frequency [67, 124, 74]. If more than one resonance peak has to be suppressed, the same methodology can be used but with the use of two or more parallel control circuits. Each control circuit has a bandpass filter, gain and phase shift adjusted to one of the resonance peaks [122].
A different approach is used by [58, 83]: an online frequency and phase observer algorithm is used to detect the most dominant resonance frequency and the phase of the signal at that frequency. The algorithm consists of an online Fourier transform, of a short sample of the time trace of the signal at one or more frequencies. The frequencies at which the Fourier transforms are performed are adapted such as to maximise the calculated Fourier coefficients. The controller then creates the right phase shift for each resonant mode. Thus, if secondary peaks are created by the control action, they will be detected by the observer and the controller will adapt to the new frequencies.
The performance limitations due to occurrence of secondary peaks and problems encountered with multiple resonance peaks has led to the use of more advanced control strategies. Modern control hardware such as digital signal processing boards (DSP), with very fast CPU's, A/D and D/A converters made it possible to easily implement high-order controllers based on classical loop shaping design methods or on modern control theory. These approaches need a dynamic model of the system. These models can be obtained from physical knowledge of the system or on some experimental technique (time-domain or frequency domain system identification). These models will generally have considerable modeling errors, especially for the high frequency range. Thus the model-based controller should not act on the very high frequency range, because of the uncertainties in this range, resulting in small robustness. On the other hand, the controllers should not act on the very low frequency range because the controllers should reject the acoustic pulsations without interfering with the mean flow variables. Thus, the shape of the open loop system ($K\ P$) should be such that it has low gain in the low and high frequency range and high gain in the passband. This is referred to as loop-shaping, the open loop is shaped in order to meet tradeoffs between performance and robustness. The controller requirements in the passband are: stability and noise rejection. Note that this is different from the more conventional requirements encountered in robust control of, for example, positioning systems or level controllers, where command tracking is required, and thus high gain in the low frequency range.
If a linear model of the system is available, then the controllability of the system can be directly assessed from a state-space representation of the system using straightforward linear algebra techniques. If the system is controllable, and if all states of the system can be accessed (observable), a controller can be found that stabilizes the closed loop system, and has an arbitrarily fast response. However, it is assumed here that the system is linear, but a practical system will never be linear. Actuator response will be especially limited by some physical constraints that often

appear as a saturation mechanism. Therefore, a controller should not only be able to control the linear system, but should also make sure that the desired actuator response is within its physical limits. In addition, there will be requirements on the transient response of the system. The LQR (Linear Quadratic Regulator) control approach deals with this problem as follows: a cost function is formulated that consists of a weighted quadratic sum of the state of the system, and the time integral of the state and the output signal. A controller can be found that minimizes this cost function by solving an algebraic Ricati equation. However, this approach requires that all states of the system can be measured. In thermoacoustic systems this will likely never be the case. The order of these systems is generally high, while often only one sensor is available. Moreover, the states of the system do not always have a direct physical meaning. For example, thermoacoustic systems have considerable time-delays. Time delays have infinite order and will be explicitly (Padé approximation) or implicitly (fit to measured data) approximated by lower order dynamic systems. These states can clearly not be measured, thus a state observer has to be used. The observer obtains the measured signals as an input and gives estimates of the states as an output (Luenberg observer, Kalman-Bucy filter). These states can now be used as an input to the LQR controller. The combination of a Kalman Bucy filter with an LTR controller to achieve robust control is named an LQG-LTR control (Linear Quadratic Gaussian-Loop Transfer Recovery). Both classical loop shaping techniques and LQG-LTR design techniques where used by [51, 113, 135, 8, 6, 45, 7] based on physical or experimental models.

LQR control minimises a quadratic cost term, this means that the root mean square (RMS) of the signals is minimised (the H_2-norm). An alternative is to minimise the peak values in the frequency spectra of the signals (the H_∞-norm). H_∞ control is based on the same philosophy as the LQR control problem. An H_∞ controller will keep the H_∞ norm of a transfer function below a certain value. This transfer function can be the closed loop transfer function of the controlled system, but will generally be augmented with additional transfer functions that apply (frequency dependent) penalty weights on the actuator signal, output signal, and disturbance inputs. In order to address robustness issues, the H_∞ methodology can be used in combination with classical loop shaping techniques (H_∞-loop shaping). The open loop is then shaped such as to obtain desired performance/robust stability tradeoffs. H_∞ optimisation is then used to stabilise the closed loop system and ensure robust stability at all frequencies. AIC controllers based on H_∞ optimisation have been investigated and applied by [21, 7, 128, 50, 4].

The techniques mentioned above, rely on a model of the system at one operating point. If the operating point changes due to for example, a change in load or ambient conditions, the model will not be valid anymore. If the controller is robust enough, it will be able to control the system in some neighbourhood of the design operating point. However, if the deviation from the design point is large, the controller will fail. To overcome this problem, controllers have to be designed for every operating point that may be encountered. Gain scheduling methods, or some interpolation technique can then be used to choose the right controller for every set point. A similar approach was used in [42], the controller consisted of a bandpass, gain and time delay. The operating point could be changed by choosing a different value of the equivalence ratio. A series of tests were then done to obtain the optimal setting of the time delay for every operating point. The values of the equivalence ratios and time delays were then used as a training data

set for a neural network. During the test, the neural network would then choose the optimal setting of the time delay for a given operating condition. In this case only one variable of the operating condition could be changed (the equivalence ratio) and one control parameter (the delay). This method could, in principle, be extended to set more control parameters dependent on more variables of the operating condition. However, this would require extensive amounts of experimental data to train the neural network (or any other response function or interpolation technique).

An adaptive control strategy does not need a-priori knowledge of the system and can adjust automatically to changes in operating conditions, or any other changes in the system. This motivated several researchers to design adaptive control systems for instability control. Adaptive control strategies have been used for noise cancellation (ANC, Active Noise Control) since the beginning of the 1980's. The problem of AIC is different from ANC for two reasons. First, ANC generally deals with cancellation of an *external* noise source. If the external noise source can be measured in some sense, feed-forward control techniques can be used in order to cancel this noise. Second, the original system under consideration in ANC will always be stable. Nevertheless, the problem of AIC is closely related to ANC, thus ANC controllers have been modified for use in combustion systems [55, 13, 62]. These controllers use a Least Mean Squares algorithm (LMS) to minimize the power of an error signal by adjusting the coefficients of a Finite Impulse Response (FIR) or Infinite Impulse Response (IIR) filter. In the approach used by [62], a FIR model of the plant is obtained in an online system identification step, this model is then used to define the control action, done in a second step. Thus, this is actually a model-based type of control. The approach used by [13] directly minimizes the cost function of a pressure signal. A FIR filter is a digital filter that gives a linear combination of its delayed input signal as an output. The order of the filter determines how many delays have been used. An IIR filter gives a linear combination of its delayed inputs plus delayed outputs as an output. Note that any continuous time system can be represented by an equivalent IIR filter of the same order, thus the controller structure is very general.

Generally, an adaptive method is more likely to be effective if it has a small number of variables to be adapted. If the general structure of the dynamics of a plant is known (without knowing the exact values of the model coefficients), a general structure of the controller can be obtained. Thus the plant is not seen as a black box, but could be seen as a "grey box". With this approach, a controller with less coefficients can be obtained. This approach is used in [34, 86], here the time delays in the actuation path are explicitly taken into account by a modified Smith[2] predictor technique. Lyapunov's direct method is used as an adaptive law.

[2]A Smith predictor is a time delay compensation technique, it requires a model of the system and the delay.

Ref	Author	Approach	Controller	Actuator	Sensor	Validation
[7]	MIT 00	PhysB	LQG/H_∞	speaker	p'	num/exp
[112]	MIT 98	PhysB	LQG†	speaker	p'	num
	† Adresses applicability linear controllers in limit cycles.					
[113, 6]	MIT 97	PhysB	LQG	speaker	p'	num/exp
[8, 45]	MIT 95	PhysB	LQG	speaker	p'	num
[40]	GEC 92	ManT	BP&phase	speaker	p'	num/exp
[38, 39]	PenState 91	PhysB	PI	fuel‡	p'	num
[135]	PenState 90	PhysB	LQ†	fuel‡	p'	num
[50]	PenState	PhysB	H_∞	fuel‡	p'	num
	†Uses Luenberger observer for state feedback. ‡Spatially distributed actuation.					
[67]	Cam 90	EmpB†	time lag	fuel	p'	exp
	†Fit to frequency response data					
[14]	Cam 88	ManT	BP&phase	fuel	p'/C_2	exp
[124]	Imp. Col. 92	ManT	BP&phase	fuel/speak	p'	exp
[75]	PsiCorp	ManT	PWD†&phase	fuel	OH'	exp
	†Uses Pulse Width Modulation (PWD) and online amplitude detection					
[47, 122]	Siemens 98	ManT	BP&phase	fuel†	p'†	exp
	†Application to full scale gas turbine, multiple sensors, actuators.					
[48]	Siemens 97	ManT	BP&phase	fuel†	p'/OH'	exp
	†Liquid fuel, piezo actuators					
[99]	CNRS 87	ManT	BP&phase	speaker	p'/OH'	exp
[110]	USDE	ManT	open-loop	fuel		exp
[92]	Alstom 98	ManT	BP&phase	speaker	p'/OH'	exp
[93]	Alstom 99	ManT	open-loop	speaker/fuel	p'/OH'	exp
[41]	NWC 91	AM†	Proportional†	shear‡	C_2	exp
	†Prop. control of Amplitude Modulation (AM) of carrier frequency.					
[42, 116]	NWC 91	ManT	BP&phase†	fuel/shear‡	p'/CH'	exp
	†Also: open loop control. ‡ Shear layer excitation.					
[107]	Yale 87	ManT	BP&phase	speaker/fuel	p'/OH'	exp
[55, 13]	CNRS 93	Adapt	LMS	fuel	p'/OH'	exp/num
[62]	PenState 96	Adapt	LMS	fuel	p'	exp
[43]	NWC 93	Neural†	BP&phase	fuel	p'/CH'	exp
	†Uses neural network to set time delay.					
[21]	Cam 98	PhysB	H_∞	fuel	p'	num
[4]	LSU 01	ExpB†	H_∞	fuel	p'	exp/num
	†Uses fit to measured frequency response data.					
[128]	CalTech 92	ExpB†	H_∞	speaker	p'	num
	†Uses fit to measured frequency response data of a Rijke tube.					
[58, 83]	GeoTech 96	ManT	BP&phase†	fuel	p'	exp
	†Uses online frequency, amplitude observer					
[50]	PenState 00	PhysB	H_∞	fuel	p'	num

Ref	Author	Approach	Controller	Actuator	Sensor	Validation
[87]	Stanf 95	Adapt	DS†	shear	CH'	exp
	†Downhill Simplex algorithm with search for optimal initial values.					
[51]	GE 91	ExpB†	LQG	speaker	p'	num
	†Uses fit to measured frequency response, closed loop system identification.					
[34]	Cam/MIT 00	Adapt	†	fuel	p'	num
[86]	MIT 00	Adapt†	†	fuel	p'	num
	†Uses generalised model, Smith predictor, Lyapunov functions					
[81]	MIT 03	ExpB†	LQG	fuel	p'	num
	†Time domain, non-linear system ID					

Table 6.1: Active control literature overview

Approach			*Controller*	
PhysB	Based on physical model		LQG	Linear Quadratic Gaussian
ManT	Manually Tuned parameters		H_∞	H_∞ optimal control
Adapt	Adaptive Control		BP&Phase	Bandpassed and phase shift control
ExpB	Based on Emperical Model		PI	Proportional Integral Control
			LQ	Linear Quadratic control
			LMS	Least Mean Squares Algorithm
Sensor			*Validation*	
p'	pressure transducer		num	numerical simulation
CH'	CH chemiluminescence		exp	tested in experiment
OH'	OH chemiluminescence			
C_2'	C_2 chemiluminescence			

Table 6.2: Abreviations in literature table

6.1.4 Control Objectives and General Considerations

The purpose of active instability control in combustion systems is to reduce acoustic pulsation levels in combustion chambers. In addition, it is required that the overall combustion properties such as emission levels, flame blow out behavior, and flashback properties are not deteriorated. The acoustic behavior of a combustion system will change with operating conditions or ambient conditions. In addition, aging of the combustion system or measurement equipment may cause changes. Thus, the controller should either be robust enough to deal with these changes in the system, or the controller should adapt itself to the changing conditions. For commercial applications, cost limitations and safety considerations will be important as well, but will not be discussed here in detail. The amount of fuel required for actuation is not considered here as a limitation as long as it does not require valves that are so large that the costs of application are seriously affected.
Based on the discussion in the previous section, the following issues are considered crucial for any active control system development and application:

- In practical applications the actuation power is limited, and the controller should thus be able to reduce the pulsation levels with this limited control authority.
- Considerable time delays will always be present with any actuation system.
- The sensors will always be affected by noise. The high turbulence levels in practical combustion systems will cause an especially poor signal to noise ratio.
- The amount, type and location of measurable dynamic quantities is limited.

In addition, it should be noted that the most challenging task is not to reduce very high amplitude pulsations with only very little spectral components, but that the real difficult control problem is that of a system that is characterized by relatively low, but broad-spectrum pulsation peaks. This class of systems is especially difficult to control if relatively large time delays are present.
A time delay can be compensated for in a certain frequency bandwidth[3]. It is obvious that a time delay can never be compensated (inverted) for over the entire frequency range, because it would violate the general physical constraint of causality. Because of reasons of causality, a system's transfer function has a phase that generally decreases with frequency. A transfer function can be shaped such that it has a local increase in phase. However, the phase of any transfer function depends on the absolute value, as can be understood from Bode's gain-phase relation [137]. This means that the absolute value and phase of a transfer function can not be shaped "at will". Specifically, a region of increase of phase is followed by a region of increase in gain. Thus if it is desired to have an increase of phase in a certain frequency range (in order to compensate for a time delay), then the maximum gain of the controller will be just outside of this region (where the phase relation is not correct). It is obvious that the combination of a high gain and amplifying phase easily results in "secondary peaks", or even instability.

[3]Note that the bandwidth does not necessarily start at zero frequency!

This simple analysis explains why it is much more difficult to control broad band pulsation behavior than narrow band pulsations: the decrease of the phase with frequency can only be compensated for in a narrow frequency range.

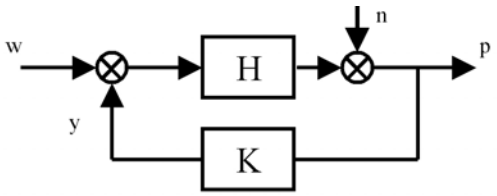

Figure 6.1: Essential block diagram of a control system, with plant H, controller K, disturbance inputs w and n, control output y and measured output p.

Secondary Peaks

The phenomenon of secondary peak generation can be understood by investigating the sensitivity function of the closed loop control system to an external disturbance n as defined in figure 6.1:

$$S(s) = \frac{\hat{p}}{\hat{n}} = \frac{1}{1 + H(s)\,K(s)} = \frac{1}{1 + \frac{Z_H}{P_H}\frac{Z_K}{P_K}} = \frac{P_H\,P_K}{P_H\,P_K + Z_H\,Z_K}, \tag{6.1}$$

In which $P_H = \Pi_n^N(s - p_n)$ where p_n is the n^{th} pole of H and similar for the zeros z_n. Clearly, the poles of the original system become zeros of the closed loop system. Because the dominant poles are close to the imaginary axis, the frequency response will have minima at the location of the original peaks. This corresponds to the intuitive idea that the feedback signal "cancels" the acoustic field. However, the poles of the system determine if the closed loop system is stable. Stability of the closed loop can be ensured by choosing the right phase of the controller close to the open loop resonance peaks (e.g., by means of Nyquist or Bode stability criterion). The phase of a time delay is linear with frequency. Thus, if a time delay is used to create the desired phase shift at, say, the first resonance frequency, then the phase at the harmonic frequencies will generally not be optimal, and may create unstable poles at other frequencies. This problem can be overcome by applying a bandpass filter that ensures only a certain frequency band has high gain. Thus making the gain of the feedback path very low at harmonic frequencies. This method has the disadvantage that a strong phase roll-off will be introduced in the passband. The phase in the passband will drop by $\frac{\pi N}{2}$ in which N is the order of the filter. If the phase introduces a phase drop of π within a frequency range where the open loop gain is larger than unity, the system will become unstable. This simple analysis explains the phenomena observed by several researchers that by increasing the gain of the bandpass phase-shift controllers, the peak of the original instability decreases, but peaks very close to the main instability appear and increase.

Even if a more sophisticated controller would be used that has a transfer function shaped to stabilize the system over a wide frequency range, similar effects may be present. This is easily seen from Bode's sensitivity integral [137]. Let, in this case, $p_1, p_2, ..., p_m$ be the right half plane

poles of $K\ H$. Bode's sensitivity integral states:

$$\int_0^\infty \ln|S(j\omega)|d\omega = \pi \sum_{i=1}^{m} \Re(p_i) \tag{6.2}$$

if the open loop transfer function has at least two more poles then zeros. This relation states that no matter what controller is used, if the controller reduces the sensitivity in a certain frequency range it will *always* increase the sensitivity in an other frequency range. The capability of the controller to shift the sensitivity from one frequency range to an other can be used to ensure that the sensitivity is low in a frequency band where the disturbance (the source term) is large. But, vise versa, the frequency at which the sensitivity increases should be shifted to the frequency range were the disturbance is small.

Active Control Performance Index

The controllers are judged according to their capability to reduce pressure pulsations (or noise in general) inside of the chamber. The best criterion to judge the effectiveness of the controllers would be the reduction of the *total acoustic energy* in the combustion chamber. This is, however, no practical measure, because it can not be measured with one microphone at one location. Because the instability *frequencies* do not change very much, the signal of one microphone, strategically placed close to an anti-node of the corresponding mode, provides a good measure. So, the following two indices are used to measure the controller performance: NRR (Noise Reduction Ratio) and PA (Peak Attenuation)

$$NRR = 10 \cdot \log_{10}\left[\frac{Pressure\ power_{on}}{Pressure\ power_{off}}\right]\ \mathrm{d}B \tag{6.3}$$

$$PA = 20 \cdot \log_{10}\left[\frac{\max\limits_{\omega} \hat{p}_{on}(\omega)}{\max\limits_{\omega} \hat{p}_{off}(\omega)}\right]\ \mathrm{d}B \tag{6.4}$$

where ω represents frequency, $\hat{p}(\cdot)$ Fourier Transform of the pressure measurement $p'(t)$, the sub indexes $\cdot_{on}$ and $\cdot_{off}$ test with controller on and off respectively, and

$$Pressure\ power_{(\cdot)} = \frac{1}{N}\sum_{\omega} |\hat{p}_{(\cdot)}(\omega)|^2 = \frac{1}{N}\sum_{t} |\hat{p}_{(\cdot)}(t)|^2$$

with N number of samples for evaluation. The *Pressure power* should not be confused with acoustic power. Note that the Peak Attenuation, is a measure for the reduction of the H_∞-norm due to the controller action.

6.2 Model for Active Control

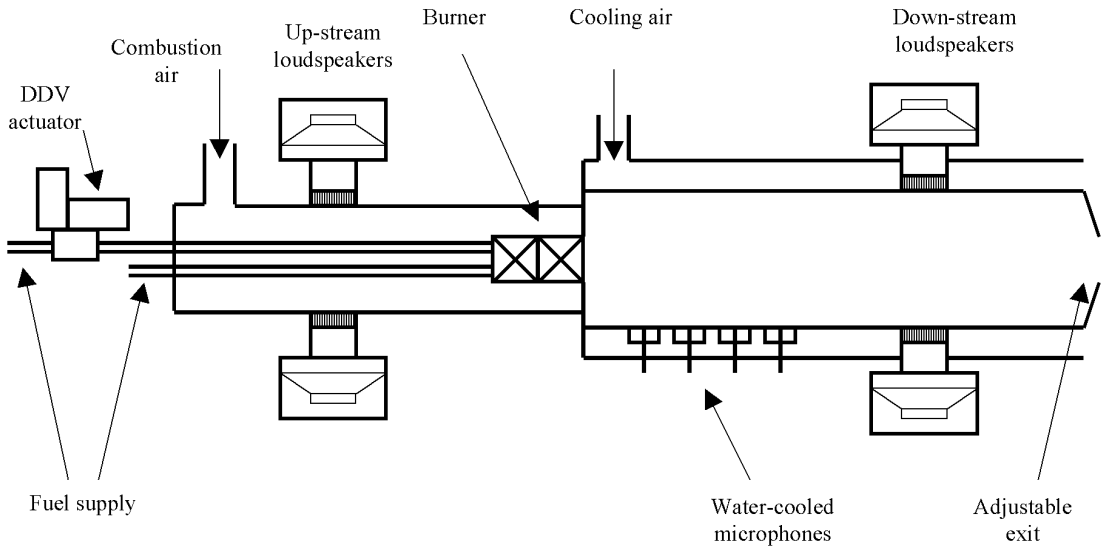

Figure 6.2: The atmospheric combustion test facility, equipped with a Direct Drive Valve (DDV) for fuel flow modulation.

6.2.1 Experimental set-up

The set-up for active control is essentially the same as the set-up described in chapter 3 and in section 5.7. The only difference is that an actuator has been placed in the fuel supply. A schematic representation is given in Fig. 6.3. The actuator is a MOOG D633-Series Direct Drive Servo-Proportional Valve (DDV-valve) [53] and is designed for high dynamic response requirements.

The control strategies were implemented in the test-rig using a dSpace system 'DS1103' [52], which contains a Digital Signal Processing board (DSP) with 20 analog inputs and 10 outputs. This system has a direct interface with MATLAB/Simulink which facilitates the implementation of controllers using SIMULINK block diagrams. The sampling rate was specified at 12 kHz, high enough to capture all system dynamics. The controller parameters can be adjusted online, via an interface. Adjustment of parameters can be done "on the fly", manually or from the MATLAB environment running on a PC.

The loudspeakers are used for system identification purposes only. They are not used for the active control applications.

6.2.2 Block Diagram Representation

The block diagram of the combustion system as discussed in section 5.7 can be extended to include the actuator and controller. This representation is given in Fig. 6.3. In this representation, the output of the "valve" (the fuel flow actuator) acts as a volume source in the combustion chamber. Physically, this representation is not entirely correct because the valve acts as a source on the fuel flow. However, the fuel will burn in the flame, and the associated heat release will, finally, result in a volume expansion of the reaction zone in the combustion chamber. Thus, in this representation, the "valve" also includes part of the flame dynamics (it is just a matter of choice of the system boundaries of the sub-systems). The pressure signal that is sent to the controller is taken in this diagram at the flame location. In real applications, this signal is taken somewhat downstream of the flame, however, this has not been shown in order to simplify the diagram . The flame source signal is again represented as "filtered white noise", w being the white noise signal.

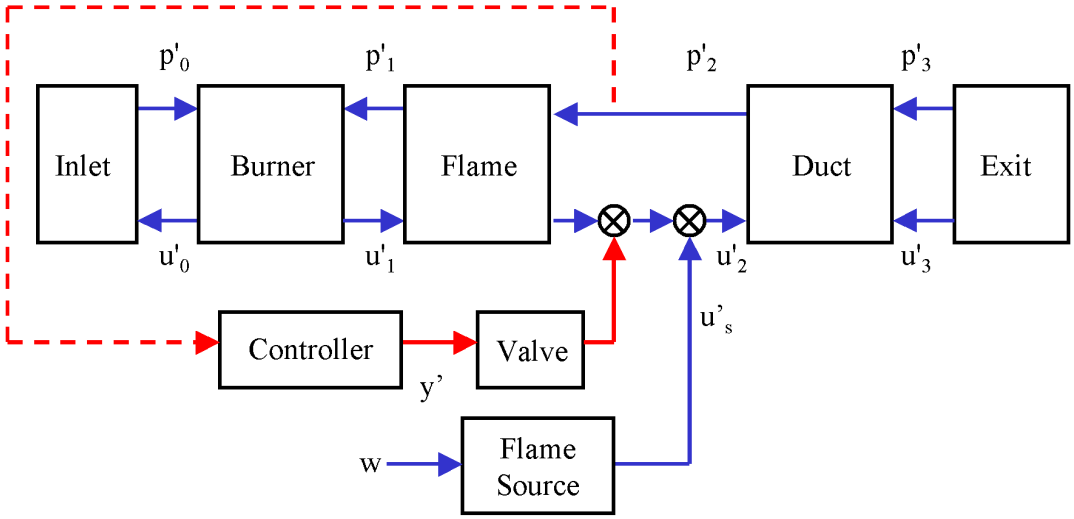

Figure 6.3: Block diagram of combustion facility with fuel flow actuators and closed loop control loop.

The blocks of the *Inlet*, *Burner* and *Flame* may be combined into one subsystem Z_{up}^{-1} and the blocks *Duct* and *Exit* may be combined in a block Z_{down} to get a representation similar to that of Fig. 5.2. The system is then represented in terms of impedances, acoustic pressures and velocities, but can equally well be expressed in terms of Riemann invariants and reflection coefficients via the following transformation: $R(\omega) = \frac{Z(\omega)-1}{Z(\omega)+1}$. In this case the representation of Fig. 6.5 is obtained, which will be used for the empirical system identification.

No matter what internal representation is used, the entire combustion system can be considered as one system (G) having two inputs (the flame noise input u'_s and the control signal input y') and one output (the microphone signal p').

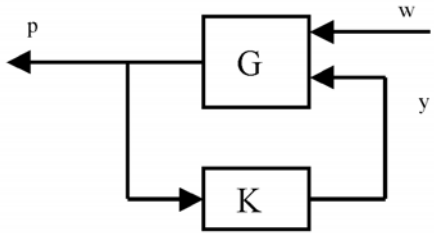

Figure 6.4: Representation of combustion system G with controller K

6.2.3 Empirical Model

In this section, a brief description of the methodology used to obtain an empirical model of acoustic interactions in a single-burner acoustic test rig is given. This model is identified using the same frequency domain system identification methods as described in chapter 3. A problem with this kind of system is that it is not known a-priori whether the system is asymptotically stable or not. The actual, non-linear system is (strictly speaking) always stable. However, this system is not always asymptotically stable as in the case of limit cycle behaviour [4]. Often, limit-cycle behaviour can be recognised by investigating the frequency response: well-distinguished higher harmonics may indicate limit cycle behavior. In practice, it is hard to distinguish between a system that is asymptotically stable and a system that is in a limit-cycle. This is because the open loop system generally acts as a low-pass filter, thereby suppressing higher harmonics. The high turbulence levels and the associated noise make the secondary peaks difficult to distinguish. In this section the terms "stable" and "unstable" will refer to low amplitude pulsation behavior and high amplitude pulsation behavior, respectively.

The system identification technique uses sequential excitation with pure frequency tones. For this purpose, pressure and fuel modulation is applied in sequence. The forcing acoustic signal is driven by water-cooled loudspeakers situated downstream of the burner, and the fuel is modulated by the actuator valve. The use of the described frequency domain system identification methods is only valid if the system is linear. Generally this assumption will not hold in the case when high amplitude acoustic waves are present, or when the system is in a limit cycle. Because it is not clear if the system under consideration is asymptotically stable or not, an identification method has been developed that can be used for systems that are not necessarily asymptotically stable. This is done by regarding the system as different sub-models. Each sub-model was then identified separately. During the identification step of each subsystem, a modification in either geometry or operating condition of another subsystem was applied (without changing the sub-model that has to be identified). These changes were done such that the system had very low

[4] A system is said to be stable if a finite intial disturbance of the states results in a finite output (for all times, including infinity); asymptotically stable if its state decays to zero; unstable if it is not stable.

pulsation amplitudes, ensuring stability of the system.
The identification of all sub-models is done in consecutive steps. It is assumed that the sub-models are all stable, and that possible instabilities are caused by the feedback loop. So, if H_{down} in the block diagram of Fig. 6.5 has to be identified, then the "gain" of H_{up} has to be reduced temporarily to ensure low pulsation amplitudes. And, conversely, during the identification of H_{up} , the "gain" of H_{down} has to be reduced. All identified sub-models can be combined now in the feedback system, which is a representation of the system linearized around its mean operating point.
Clearly such a model does not include the non-linear system dynamics. However as can be understood from *Lyapunov's Indirect Method* [125], a controller that stabilizes the linearized system will also make the non linear system asymptotically stable, provided the system is continuously differentiable around the mean operating point[5].

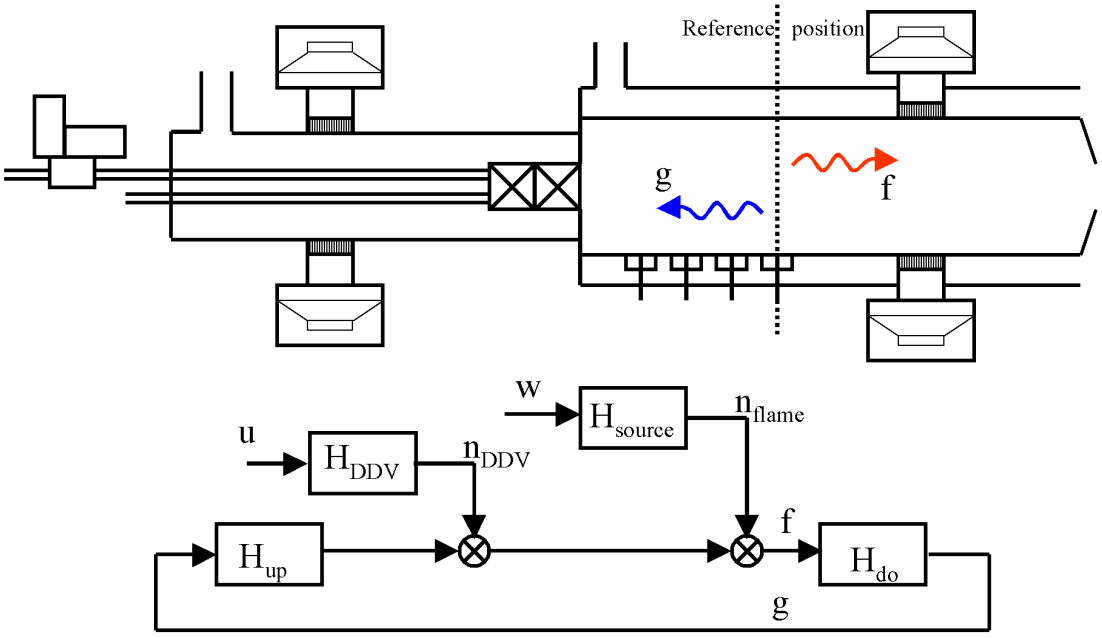

Figure 6.5: The atmospheric combustion test facility, equipped with loudspeakers and water-cooled microphones for acoustic measurement.

This experimental investigation of the combustion chamber is mainly based on acoustic properties. At every identification step the system is excited by some forcing signal (speakers, DDV-valve or flame noise). The response is measured using an array of microphones. The Riemann invariants f and g are obtained using the Multi Microphone Method (chapter 3). The sub blocks are then obtained from the Riemann invariants.
The following 4 blocks are identified as essential parts of the combustor model:

[5]Thus, strictly speaking, only local stability is ensured.

- Upstream (H_{up}). The upstream dynamics include the wave propagation from the reference position to the burner exit, and acoustic properties of the combustion process, burner, and plenum chamber.
- Downstream (H_{down}). The downstream dynamics include wave propagation from the reference postion to the exit of the combustion chamber, and the reflection properties of the exit.
- DDV Actuator (H_{DDV}). This block not only contains the response of the actuator, but also its influence on the combustion process and wave propagation from the flame location to the reference position.
- Source term (H_{source}). The source sub-model describes the acoustic sound source produced by turbulence in the flame. Note that this H_{source} does not contain the thermoacoustic interaction. The interaction is included in H_{up}.

The "gain" of H_{up} could be tuned by choosing an operating condition that is stable. The "gain" of H_{do} could be tuned by mounting a throttle plate at the exit.
These blocks are identified in the following manner:

1. Downstream Model (H_{down}) Figure 6.6.
   - No throttle plate mounted, "stable" operating condition is chosen.
   - No external forcing is applied, sound is generated by the flame. The only input to the system is n_f.
   - Riemann invariants $\hat{f}$ and $\hat{g}$ are obtained using the Multi Microphone Method. Note that in this case the Riemann invariants are defined as: $\hat{f} = S_{\overline{pf}}/\sqrt{S_{\overline{pp}}}$, as discussed in chapter 3.
   - The transfer function describing the downstream interaction is obtained from $H_{down} = \hat{g}/\hat{f}$.

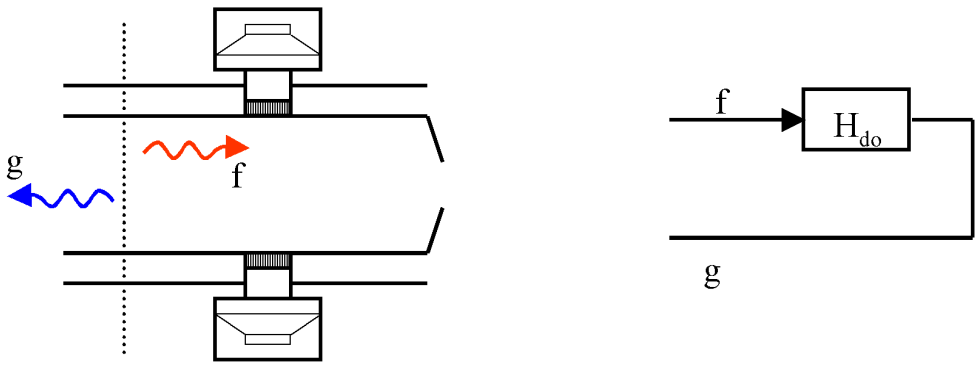

Figure 6.6: Downstream interaction and modeling

2. Upstream Model H_{up}, Figure 6.7

   - Throttle plate mounted, reference operating condition is chosen.
   - The pressure field is modulated with pure tones by downstream loudspeakers.
   - Riemann Invariants $\hat{f}$ and $\hat{g}$ are obtained for each forcing frequency, using the Pure Tone Method and the Multi Microphone Method. Thus, as discussed in chapter 3, $\hat{f}$ and $\hat{g}$ do not contain any contribution of the source term, provided enough samples were taken.
   - The upstream model is obtained from $H_{up} = \hat{f}/\hat{g}$.

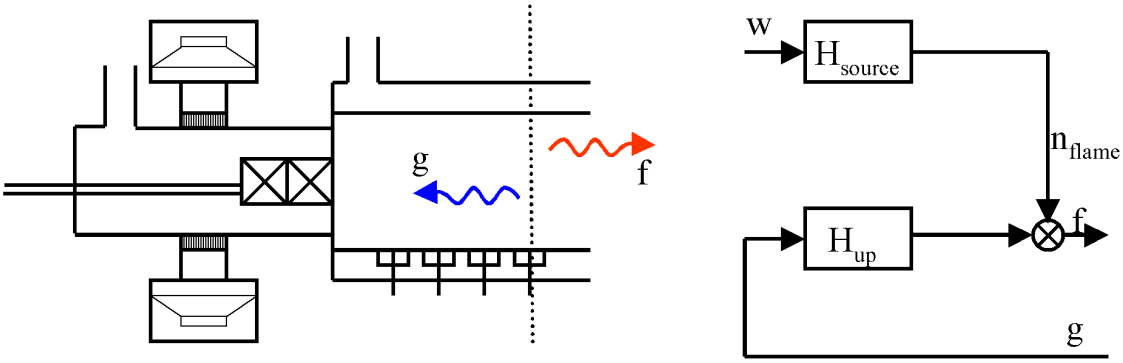

Figure 6.7: Upstream interaction and modeling

3. Response to Direct Driven Valve, H_{DDV}, Figure 6.8

   - Throttle plate mounted, reference operating condition is chosen.
   - Fuel flow is modulated with pure tones by the DDV actuator.
   - Riemann Invariants $\hat{f}$ and $\hat{g}$ are obtained for each forcing frequency, using the Pure Tone Method and the Multi Microphone Method.
   - The following relation is used $\hat{n}_{DDV} = \hat{f} - H_{up}\hat{g}$. Note that H_{up} is obtained from the previous identification step.
   - The forcing signal to the DDV actuator ($\hat{u}$) is known, therefore the actuator response model is given by $H_{DDV} = \hat{n}_{DDV}/\hat{u}$. Note that H_{DDV} is not the transfer function of the DDV actuator only, it also contains the reponse of the combustion system to the fuel modulations.

4. Combustion noise model (H_{source}), Figure 6.7,

   - Throttle plate mounted, reference operating condition is chosen.
   - No external forcing is applied, sound is generated by the flame. The only input to the system is n_f.

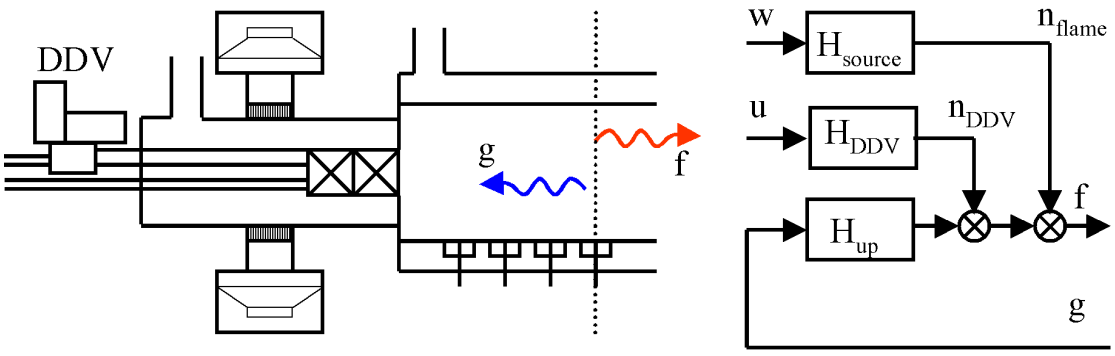

Figure 6.8: Upstream interaction with DDV valve and corresponding block diagram.

- Riemann invariants $\hat{f}$ and $\hat{g}$ are obtained using the Multi Microphone Method. Note that in this case the Riemann invariants are defined as: $\hat{f} = S_{\overline{pf}}/\sqrt{S_{\overline{pp}}}$.
- Use the following relation $\hat{n}_{flame} = \hat{f} - H_{up}\hat{g}$.
- The flame noise is assumed to be "coloured" white noise. Thus the "colouring" transfer function is obtained as $H_{source} = \hat{n}_{source}/\hat{w} = \hat{n}_{source}$. Note that because of this definition, H_{source} will have a phase. However, in this block only the absolute value of the transfer function is relevant.

Note that the upstream interaction is quite complex because it consists of 3 blocks (see Figure 6.8). Thus, it is necessary to follow the procedure in the correct sequence to obtain the correct overall model. Moreover, it is intended to control the combustor using fuel flow modulation, so of particular interest is to obtain the right description for the *DDV* actuator. The contribution of the *DDV* actuator and the flame source enter in the model at the reference position. In the real system these contributions enter in the flame region. Nevertheless, the model is correct. Because of the superposition principle any input to the system can be interchanged by an equivalent input at an other location.
Finally, using the following relation between the Riemann-invariant waves f and g, and the pressure fluctuations

$$p'(t) = \rho c(f + g)$$

the model describing all the interaction processes in the combustion system from the input control voltage of the *DDV* valves to the microphone measurements is given in Figure 6.10. Note that the voltage signal to the *DDV* valves can not be arbitrarily large, so a saturation block has been added.

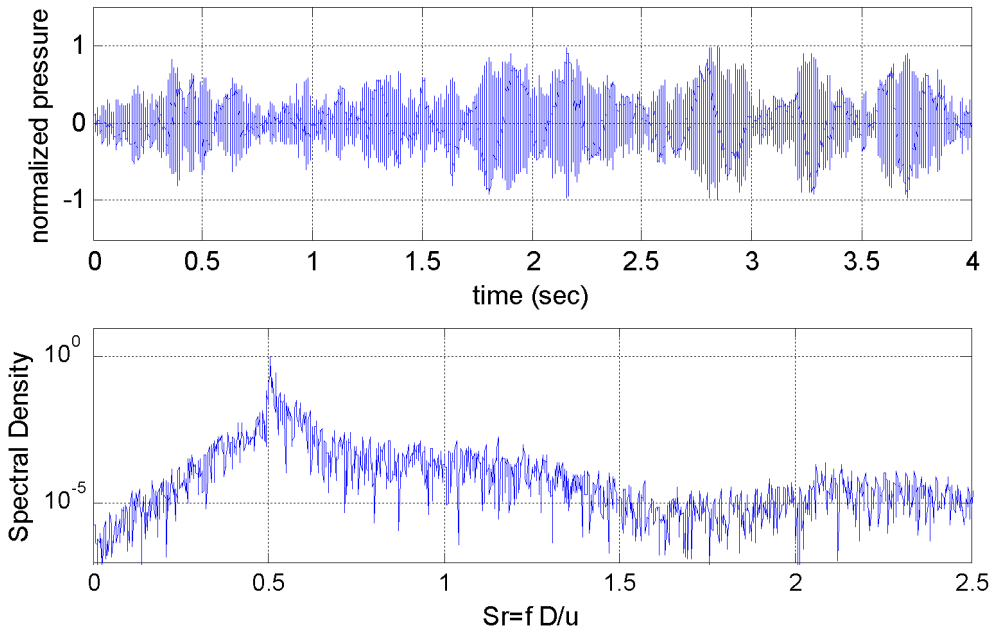

Figure 6.9: Time domain simulation and frequency spectrum of the uncontrolled model.

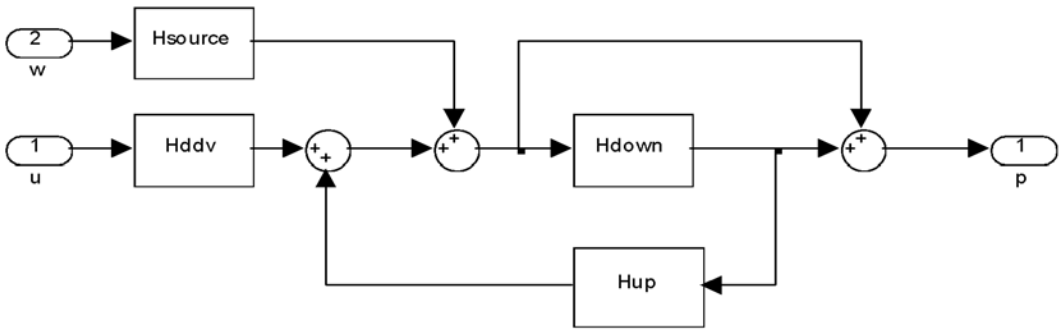

Figure 6.10: Block diagram of empirical combustor model.

6.3 H_∞ Optimal Control

6.3.1 Introduction

In this section, the design, simulation, and experimental validation of H_∞ optimal controllers will be discussed. Two types of controllers have been used: H_∞ *Disturbance Rejection Control* and H_∞ *Loop Shaping Control*. H_∞ design was chosen as a control strategy because this technique has a desired frequency domain interpretation: minimizing the peak amplitude in the frequency response. A disturbance rejection controller attempts to:

1. stabilize the system
2. minimize the response due to the disturbance

In this case the disturbance is the source term. This design philosophy does not explicitly take into account issues of robustness against modeling errors. Thus, modeling errors might significantly reduce the performance of such a controller. This is in contrast to H_∞ Loop Shaping Controllers. In this method, the desired shape of the open-loop (i.e the controller transfer matrix times the plant matrix) is prescribed. H_∞ optimization then makes sure that the closed loop is robustly stable against exogenous disturbances and internal modeling errors of the plant. Both methods will be explained below in greater detail. The theory and application of H_∞ optimal control is discussed extensively in literature. A very clear and yet profound reference is [137].
A major advantage of H_∞ techniques is that issues like robust performance of MIMO systems can be formally proven in a very elegant manner using theorems from linear algebra. A disadvantage, however, is that because of this formalism the link to the underlying physical behavior of the controlled system is not always that obvious. Proofs of the theorems concerning H_∞ control are not given here, instead, an attempt is made to reveal the connection with the physical behavior of the system.
The H_∞ design methodology has been used to obtain controllers for the empirical model of the test facility and for the analytic gas turbine model. The controllers for the test facility have been tested in experiment. This part of the development has been done in close cooperation with Daniel U. Campos-Delgado and has been published in [18].

6.3.2 H_∞ Disturbance Rejection Control

H_∞ control thanks its name to the fact that it minimizes[6] the H_∞-norm of a linear transfer matrix. The H_∞-norm of a transfer function is a measure for the peak value of its frequency response. For example, if a controller K is placed between the pressure signal p, and the DDV input u in Fig. 6.10, then the entire system (including the controller) can be considered to have one input (w) and one output (p) as shown in Fig. 6.4. The transfer function between p and w will be refered to as T. By using the methodology of H_∞-control, a controller (K) is

[6]Because of other control objectives, the goal is generally not to minimize the norm but to achieve a norm smaller than a certain value.

obtained that minimizes the H_∞-norm of T, which results in minimal peak amplitudes of the Fourier transform of the pressure signal $p(\omega)$. Generally, reduction of the peak amplitudes of the system is not the only control objective. In this case, for example, the actuation valve has limited actuation power, especially at high frequency. Thus, a controller should be found that controls the system without exceeding a certain amplitude of the actuation signal. Thus the control objective is two-fold: minimizing pulsation amplitudes while maintaining the control signal below a certain amplitude. Because H_∞ control is not restricted to SISO systems, more outputs can be added to T. If the second output of T corresponds to the (weighted) actuator signal then a minimal H_∞-norm of T corresponds to a low pulsation peak while maintaining a small actuation signal. Generally, a weighting function (or penalty) will also be applied to the pressure signal. Depending on the choice of penalty functions, a trade off can be made between reducing pressure peaks, and actuation amplitude.
In order to be consistent with most literature on optimal control, the model of the test rig and active controller will be represented in this section by the block diagram of Fig. 6.11. In this diagram, G represents the test rig and the weighting functions as shown in Fig. 6.12. K represents the controller. The inputs to the test rig model, w and u are the same as in Fig. 6.5. Output y corresponds to the microphone signal. Output z contains z_1 and z_2 from Fig. 6.12, they represent the frequency weighted control signal and the weighted output signal respectively. Note that the transfer function T_{zw} represents the closed loop plant from disturbances to weighted output signals, and can easily be obtained with the LFT interconnection discussed in chapter 5.

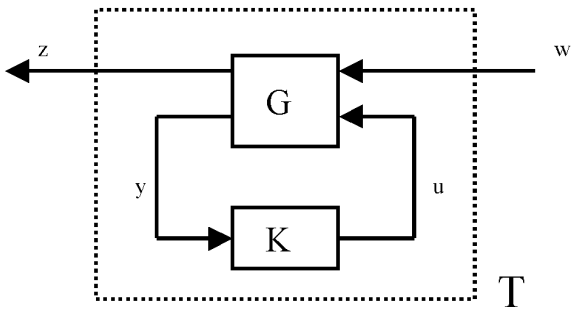

Figure 6.11: Linear Fractional Transform standard diagram.

The goal of the H_∞ optimal control is to obtain a controller $K(s)$ such that

$$\min_K \|T_{zw}\|_\infty$$

The main steps to design an H_∞ controller are summarized as follows

1. Identify control objective: Performance or Robust stability.
2. Select weighting functions
3. Obtain LFT representation of the system

4. Compute optimal controller

5. If necessary, apply model reduction to the resulting controller.

The computation of H_∞ optimal controllers is easily achieved using MATLAB (μ-Analysis and Synthesis Toolbox [9]). Thus, the computation process is completely automated because the LFT representation of the optimal controller can be obtained using just one command. The control design is thus merely a matter of selecting appropriate weighting functions.

Convergence Towards Unstable Controllers

During the control synthesis of the H_∞ controllers, it was found that the resulting controller could be unstable. This is neither an error during the controller computation or a numerical error. Because the H_∞ theory only guarantees that the closed-loop will be stable but there is no restriction on the controller stability. Obviously, these kind of controllers are useless, due mainly to the high sensitivity and lack of robustness[7]. Robustness will especially be an issue because the actuator acts as a saturation function; thus, for high amplitudes it might be that the loop gain is not sufficiently high to stabilize the closed loop system.
During the MATLAB optimization, the closed-loop H_∞ norm is minimized iteratively. For this, MATLAB uses the *bisection algorithm* . So, if exist $\gamma_1 > 0$ such that a controller K makes the closed loop H_∞ norm $< \gamma_1$ and stabilizes the system, then a new γ_2 is checked such that $\gamma_2 < \gamma_1$ and exists a controller that satisfies the former requirements. The iterations end if the closed loop H_∞ norm can no longer be reduced. In this way, it was noticed that during the optimization process the pole of the resulting controller was moving continuously to the RHP after each iteration. Therefore, there was a limiting $\gamma_{stable} > 0$ such that the closed-loop H_∞ norm $< \gamma_{stable}$ and the corresponding controller K is still stable. So, there is a limitation in the performance that can be achieved if a stable controller is required. In addition, it was also noticed that this limiting value $\gamma_{stable} > 0$ could be moved according with the weighting functions W_z and W_u.
There is no result known so far that explains how to obtain a stable controller from the H_∞ optimization. This is an important problem that should be solved, because better understanding may lead to better control.
The frequency response for the resulting optimal controller and a comparison of open loop and closed loop responses is shown in Figure 6.14.

6.3.3 H_∞ Loop Shaping Technique

This design technique incorporates the classical loop-shaping methods to obtain performance/robust stability tradeoffs, and a particular H_∞ optimization problem to guarantee closed loop stability and a level of robustness at all frequencies. The design methodology uses only basic concepts of loop-shaping methods, commonly used in classical frequency based designs like lead-lag con-

[7]Thus in this case, the plant is actually stabilizing the controller!

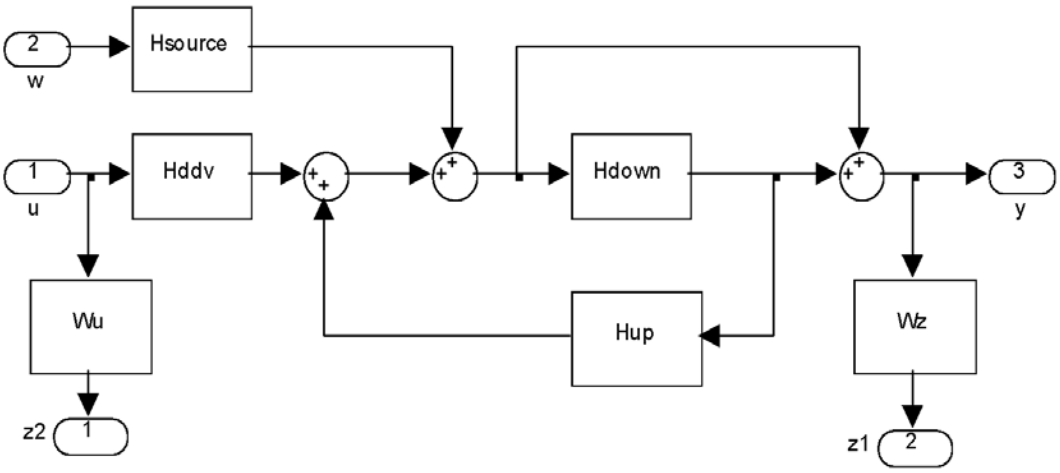

Figure 6.12: Set up for H_∞ optimisation.

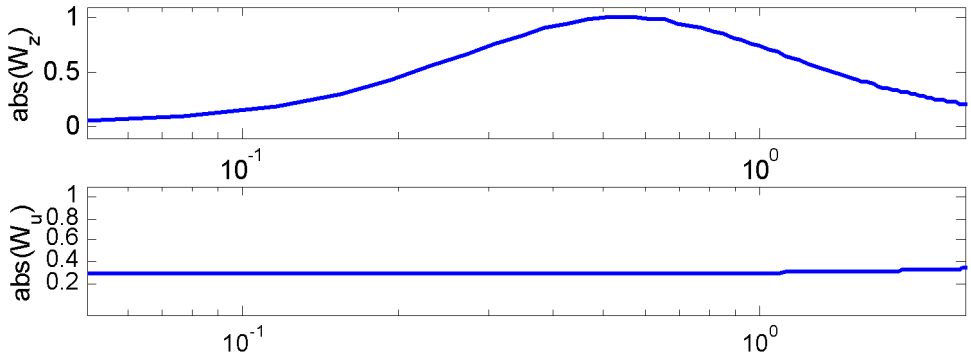

Figure 6.13: Weighting Functions for H_∞ Optimization: (Top) W_z (Bottom) W_u

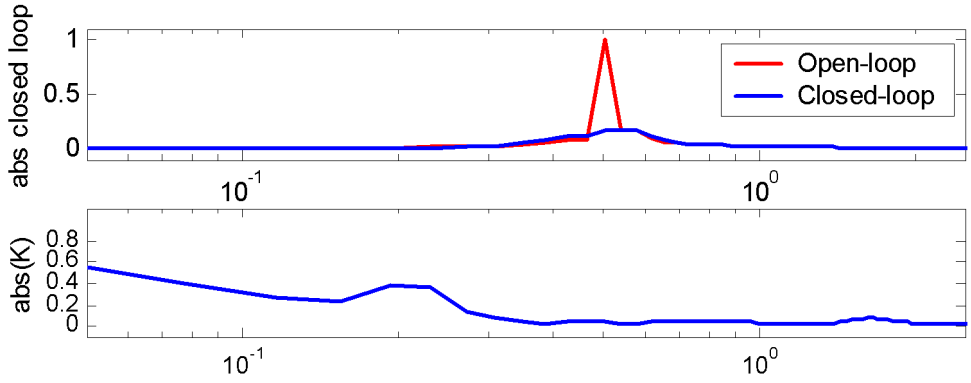

Figure 6.14: (Top) Frequency Response for Closed-Loop with H_∞ controller, (Bottom) H_∞ Optimal Controller Frequency Response

trollers. A robust stabilization controller for a *normalized coprime factor perturbed* [8] system is used to construct the final controller.
It is important to mention that this approach, in contrast to the classical loop-shaping method, is done without explicit regard for the plant's phase information. Thus, when shaping the loop, one does not need to worry about stability of the closed loop system. The closed loop stability will be guaranteed in a next step, using H_∞ optimization. Therefore, the design procedure is both simple and systematic and only assumes knowledge of elementary loop-shaping principles on the part of the designer.
The basic assumption of this procedure is that the open loop plant is a *coprime factor* perturbed plant ([137]), under this assumption the robust stability problem is stated as:

$$\min_K \left\| \begin{bmatrix} K \\ I \end{bmatrix} (I + PK)^{-1} \begin{bmatrix} I & P \end{bmatrix} \right\|_\infty \tag{6.5}$$

by the Small-Gain Theorem. From this representation it is not easily understood how robustness issues are addressed explicitly by this equation. The underlying theory is very elegant but rather involved. However, the physical understanding can easily be understood by analyzing the SISO case. Robustness can be considered as a degree of insensitivity to modeling errors and external perturbations of the closed loop system. If a SISO transfer function, represented as a coprime factorization: $P = \frac{N}{D}$ (with denominator transfer function (D) and numerator transfer function (N)) has additive error on the denominator (Δ_D) and numerator (Δ_N), then it is said to be coprime perturbed: $\tilde{P} = (N+\Delta_N)(D+\Delta_D)^{-1}$. The $\tilde{(\cdot)}$ indicating a perturbed transfer function. Thus if the perturbed plant $(\tilde{P})$ is controlled by a controller (K), the diagram of Fig. 6.15 is obtained after making use of: $(P+\Delta_N^*)(1+\Delta_D^*)^{-1}$ with $\Delta_D^* = \frac{\Delta_D}{D}$. In this diagram, exogenous perturbation signals w_1 and w_2 are perturbing the input and output of the plant, and the modeling errors Δ_D^* and Δ_N^* are perturbing the plant's denominator and numerator transfer functions. The aim of H_∞ loop shaping is to minimize the effect of the external perturbations (source terms) and internal perturbations (modeling errors).

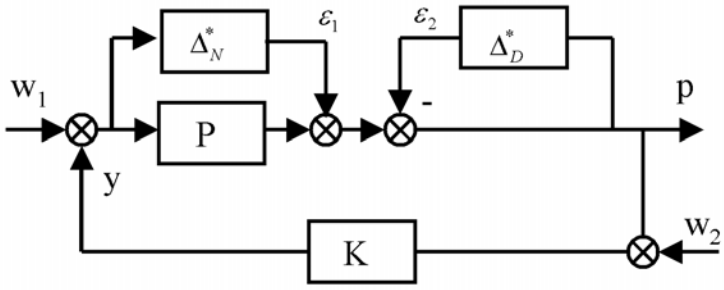

Figure 6.15: SISO coprime perturbed plant

The influence of the external perturbations are minimized if the transfer functions from w_1 and w_2 to p and y are minimized, thus if the norms of $\frac{P}{1-KP}$, $\frac{KP}{1-KP}$ and $\frac{K}{1-KP}$ are minimized.

[8] Can be considered as systems with modeling uncertainty in the "numerator" and "denominator" transfer functions.

The influence of the modeling error Δ_D^* is minimized if the transfer function from ϵ_2 to p is minimized. Using this later transfer function, denoted as $M = \frac{1}{1-KP}$, it easily seen[9] that the modeling error can not render the system unstable as long as $|M|\,|\Delta_D^*| < 1$ for all frequencies, provided that M and Δ_D^* are stable. A similar reasoning holds for the perturbation of the numerator Δ_N^* here the objective is to minimize $\frac{P}{1-KP}$. Combining these objectives in one matrix, it is seen that this corresponds to Eq. 6.5 written for the SISO case:

$$\min_K \left\| \frac{1}{1-PK} \begin{bmatrix} K & KP \\ 1 & P \end{bmatrix} \right\|_\infty , \tag{6.6}$$

and thus minimizing the influence of perturbations. Use has been made of the property that the influence of both the modeling error Δ_N^* and the source term w_1 are minimized by minimizing $\frac{P}{1-KP}$. Note that in the interconnection of Fig. 6.15, the disturbance w_1 corresponds to the flame source term of the combustion system. Thus, this explains the statement made before that the source term model is not taken explicitly into account in this control design method. The disturbance input is thus considered a "worst case" input.
After defining the parameter $b_{P,K}$ as the inverse of the minimum value achieved of $\|\cdot\|_\infty$ after the optimization procedure, i.e.

$$b_{P,K} = \left(\left\| \begin{bmatrix} K_\infty \\ I \end{bmatrix} (I + PK_\infty)^{-1} \begin{bmatrix} I & P \end{bmatrix} \right\|_\infty \right)^{-1} ,$$

the design procedure for the SISO case can be summarized as follows:

1. Loop-shaping: the frequency response of the open loop plant is shaped using a compensator ($W(s)$) to give the desired open loop shape. The nominal plant (P) and the shaping compensator (W) are combined to form the shaped plant (P_s), where $P_s = PW$. It is assumed that there is no pole-zero cancellation of unstable modes of P.

2. Synthesize a stabilizing controller (K_∞) for P_s, through solving (6.5) and compute $b_{P,K}$.

3. Check the resulting parameter $b_{P,K}$, if $b_{P,K} \ll 1$ then return to (1) and adjust W.

4. The final feedback controller (K) is then constructed by combining the H_∞ controller (K_∞) and the shaping compensator (W), such that

$$K = K_\infty W$$

5. If necessary, apply model reduction to the resulting controller (K).

For a more detailed description of this design technique and justification for H_∞ Loop Shaping refer to [137].
The philosophy behind the H_∞ Loop Shaping technique cannot handle direct constraints and disturbance descriptions as in the previous formulation. This means that the model for the

[9] By the Small Gain Theorem or by Nyquist's stability criterion

noise coming from the flame is not actually used in the design stage and the control signal restriction has to be checked individually after the design is complete. From the experimental representation the equivalent open loop plant is given by:

$$P = H_{DDV} \frac{1 + H_{down}}{1 - H_{up} H_{down}}$$

Now, the idea is to shape the open loop in a certain way such that the objectives can be satisfied. Generally, in order to have a good frequency peak attenuation, the controller must have enough control authority at that frequency. On the other hand, there is a hard limitation coming from the control saturation. So, the gain at the dominant frequency has to be limited to a certain value. In addition to this, the actuator has a limited working frequency range. All these specifications were translated in the compensators (W) in Figure 6.16. The corresponding controller was obtained and a comparison between the closed and open loop frequency response is shown is Figure 6.17.

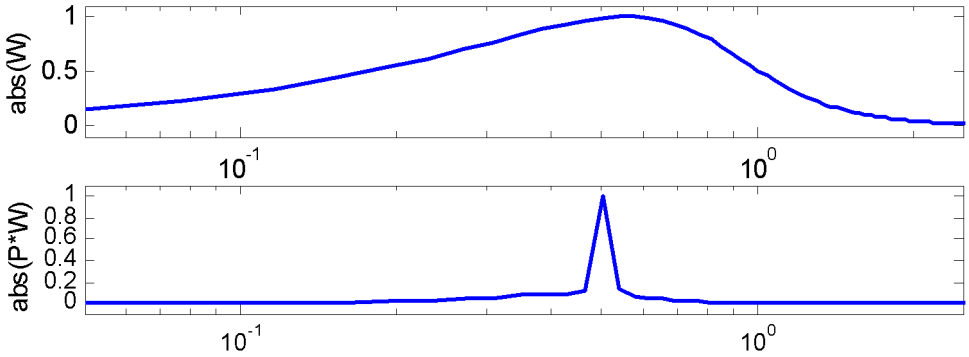

Figure 6.16: (Top) Shaping Compensator, (Bottom) Resulting Open-loop shape.

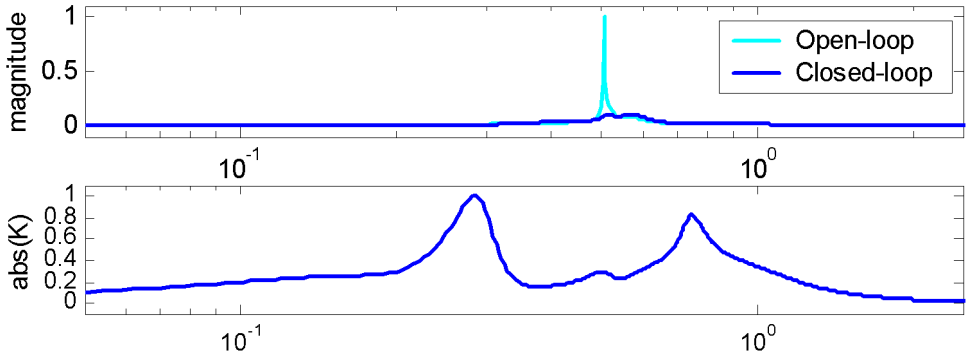

Figure 6.17: (Top) Frequency Response for Closed-Loop with H_∞ Loop shaping controller, (Bottom) Loop shaping H_∞ Controller Frequency Response

6.3.4 Simulation

In order to obtain an estimation of the controller performance in the real combustor, the $H_\infty-$ and $H_\infty-$Loop Shaping controllers have been tested in a simulation. The time-domain simulations were performed in Simulink, using a 5^{th} order numeric integration scheme. The time increment for numeric integration was about fifty times smaller than the period of oscillation at the resonance frequency of the system. The system was simulated without control (open loop) and with control (closed loop). In addition, a simulation was carried out in which the controller was switched on after 2.4 seconds. This enables one to study the transient behavior when control is switched on. The results are plotted in Figs. 6.18 and 6.19. The pressure spectra are calculated using Welsh's algorithm. The reduction of pulsation levels for both controllers is summarized in Table 6.3.

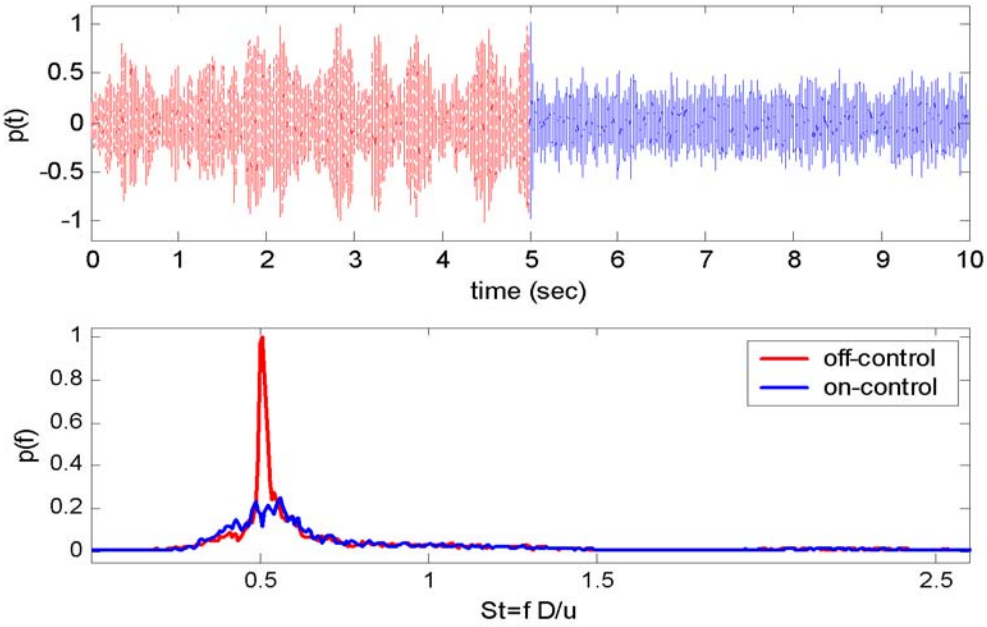

Figure 6.18: H_∞ control simulation. (Top) Time trace of pressure, control switched on after 5 seconds. (Bottom) Pressure spectra with and without control.

	H_∞	H_∞ Loop-Shaping
NRR	-6.08 dB	-5.12 dB
PA	-16.15 dB	-13.95 dB

Table 6.3: Simulation results

These results show that both the H_∞ and H_∞ Loop Shaping controllers perform very well in simulation. Thus, if the model describes the dynamic behavior of the system accurately, then these controllers should also perform well on the real plant. Because both controllers have

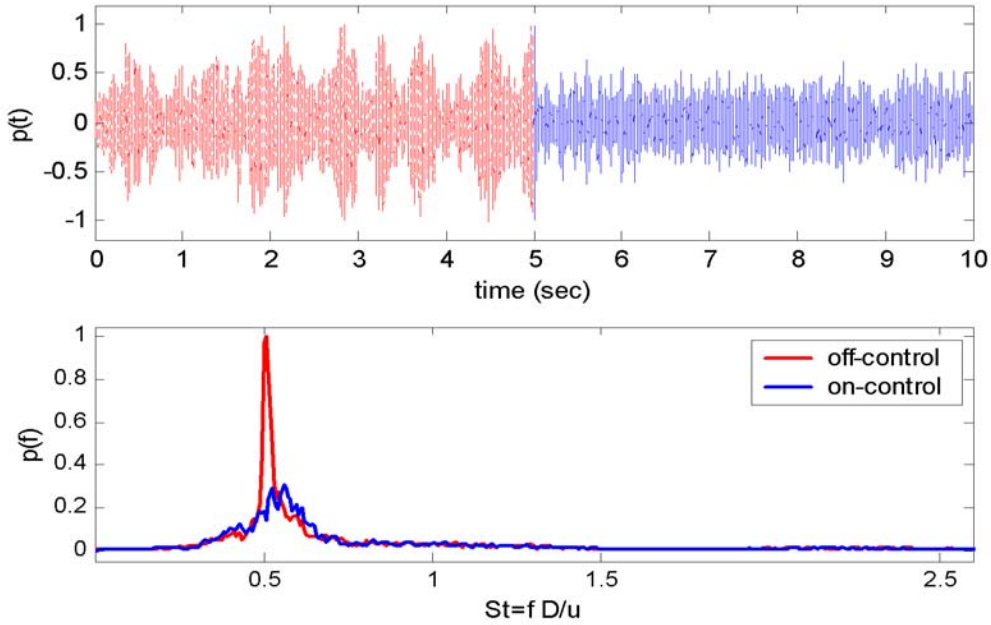

Figure 6.19: H_∞ Loop Shaping control simulation. (Top) Time trace of pressure, control switched on after 5 seconds. (Bottom) Pressure spectra with and without control.

comparable performance, they have both been tested on the atmospheric test facility.

6.3.5 Experimental Results

During the first tests, the same operating condition as for the system identification were chosen. The test results at these conditions are plotted in Figures 6.20 and 6.21. These test confirm the observation made during simulation: both controllers have similar performance, and are capable of reducing the acoustic pulsation levels significantly.
In order to investigate the robustness of the controllers, the operating conditions of the test rig were changed while using the same controllers. The changes in equivalence ratio, burner velocity and temperature are listed in Table 6.4. The results of this experiment are summarized in Table 6.5.
For different operating conditions, the peak frequency does not change significantly. This explains why the H_∞ loop-shaping controller was able to perform that well for a wide range of operating conditions. At these different operating points, the basic dynamics did not change that much, only the intensity levels. Thus, the H_∞ loop-shaping controller was able to adjust to these small changes, because some degree of robustness is inherited from the design procedure.
It was noticed that even though good attenuation of pressure pulsations can be achieved for different conditions, the pollutant levels could rise, especially the levels of UHC and CO. Meanwhile, the NOx level was almost always below the open loop level. The rise of UHC levels suggests that incomplete combustion is taking place inside of the chamber. On the other hand,

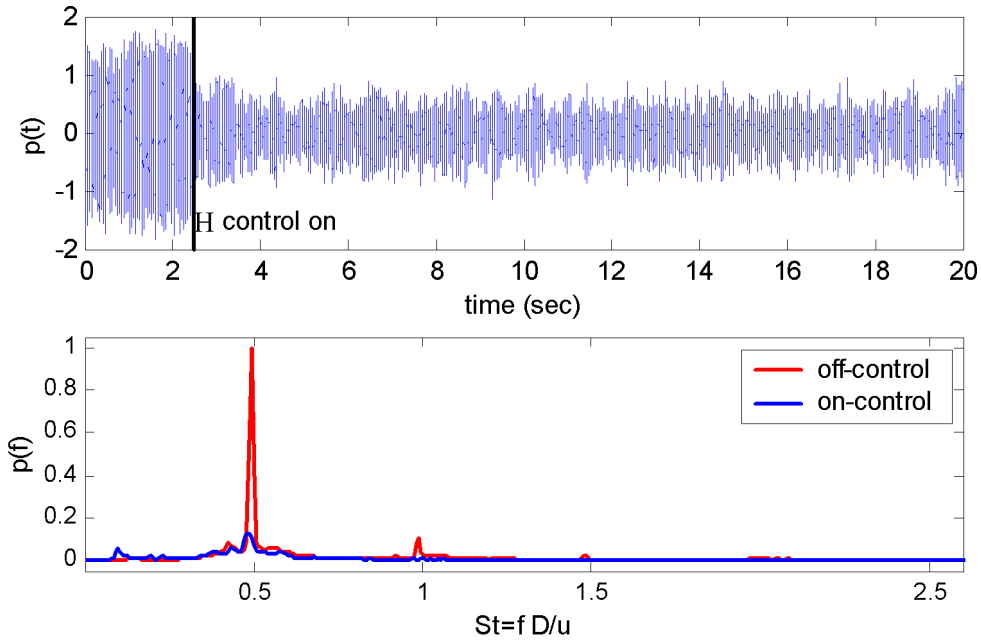

Figure 6.20: H_∞ control test. (Top) Time trace of pressure, the arrow indicates the time the controller has been switched on. (Bottom) Pressure spectra with and without control.

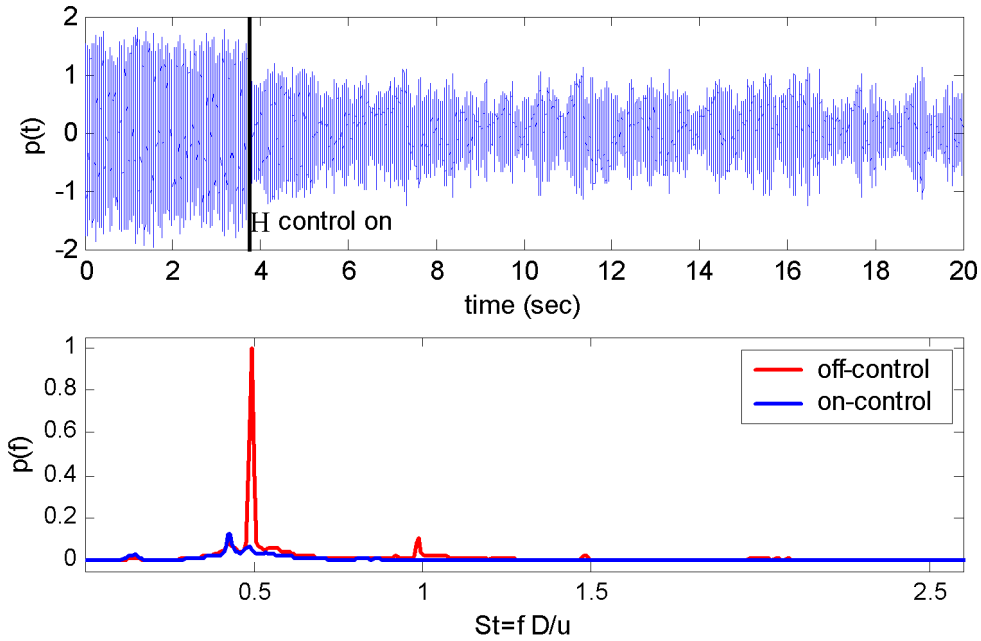

Figure 6.21: H_∞ Loop Shaping control test. (Top) (Top) Time trace of pressure, the arrow indicates the time the controller has been switched on. (Bottom) Pressure spectra with and without control.

Type	ϕ [-]	v_b [-]	T_a [-]	**Peak freq.** S_r	**Peak ampl.** $dB - dB_{ref}$
H_∞ cond.I	1.00	0.91	1.02	0.38	0
H_∞ cond.II	0.78	1.16	1.03	0.42	20.6
H_∞ cond.III	0.84	1.01	1.03	0.49	39.7
H_∞ cond.IV	0.81	1.08	1.02	0.49	41.9
H_∞ loop-shaping cond.I	0.80	1.07	1.03	0.49	43.5
H_∞ loop-shaping cond.II	1.00	1.30	1.01	0.60	11.9
H_∞ loop-shaping cond.III	0.81	1.04	1.00	0.49	36.4
H_∞ loop-shaping cond.IV	0.79	1.35	1.07	0.50	38.1
H_∞ loop-shaping cond.V	0.81	1.18	1.06	0.50	44.7
H_∞ loop-shaping cond.VI	0.88	1.05	1.03	0.50	38.6

Table 6.4: Operating conditions optimal control

Type	**NRR** (dB)	**PA** (dB)	**Closed-Loop Peak freq.** (normalized)
H_∞ cond.I	0.8	1.0	0.35
H_∞ cond.II	-4.7	-7.8	0.07
H_∞ cond.III	-10.5	-24.2	0.49
H_∞ cond.IV	-12.7	-25.1	0.41
H_∞ loop-shaping cond.I	-11.0	-21.4	0.12
H_∞ loop-shaping cond.II	-0.4	-1.7	0.62
H_∞ loop-shaping cond.III	-5.9	-6.5	0.43
H_∞ loop-shaping cond.IV	-15.8	-25.4	0.49
H_∞ loop-shaping cond.V	-13.5	-26.1	0.49
H_∞ loop-shaping cond.VI	-14.1	-24.3	0.50

Table 6.5: Test results optimal controllers.

it was not possible to identify a trend, or pattern, for this problem. A relation between the operating condition and the pollutants level could not be found either. Clearly, this stands as the main drawback of the H_∞ formulation because in order to incorporate this parameter, a model describing the behavior of the pollutants must be derived, which is a very complicated task.

In order to validate the effectiveness of the H_∞ controllers, a comparison with some very simple control structures has been performed. Two different strategies have been tested: a gain-delay controller, and a gain-delay-lead compensator. Both controllers where implemented using the same controller hardware as for the H_∞ tests. The gain gain-delay controller consists of a gain (k) and a delay (τ): $K(s) = k\,e^{-s\tau}$, the gain-delay-lead compensator has the same structure but now a lead compensator is added: $K(s) = k\,e^{-s\tau}\,\frac{1}{s/\omega_c+1}$. The latter structure was believed to have better phase characteristics close to the instability frequency. The values of k, τ and

ω_c have been adjusted manually such as to minimize the peak amplitude. In Table 6.6 the operating conditions of the tests are listed, Table 6.7 summarizes the results. It was observed that for some operating conditions the simple controller strategies had comparable performance to more complicated H_∞ and H_∞-Loop Shaping controllers.

Type	ϕ [-]	v_b [-]	T_a [-]	**Peak freq.** (S_r)	**Peak ampl.** ($dB - dB_{ref}$)
Gain-Delay	0.87	1.07	1.02	0.50	40.80
Lead Comp.+Delay	0.87	1.07	1.02	0.50	41.10
H_∞ loop-shaping	0.90	1.03	1.03	0.50	38.00
H_∞ loop-shaping+lead comp.	0.90	1.03	1.03	0.50	38.00
Gain-Delay	0.90	1.03	1.03	0.50	38.00
H_∞	0.91	1.06	1.02	0.50	36.20
Lead Comp.+Delay	0.91	1.06	1.02	0.50	35.80

Table 6.6: Operating conditions for comparison against low-order controllers.

Type	**NRR** (dB)	**PA** (dB)	**Closed-Loop Peak freq.** (Sr)
Gain-Delay	-9.40	-17.10	0.51
Lead Comp.+Delay	-4.40	-8.80	0.50
H_∞ loop-shaping	-10.20	-19.40	0.43
H_∞ loop-shaping+lead comp.	-9.70	-20.00	0.42
Gain-Delay	-2.70	-2.20	0.49
H_∞	-12.70	-20.20	0.50
Lead Comp.+Delay	-10.50	-21.20	0.57

Table 6.7: Test results comparison optimal controllers versus low order controllers.

Considering the underlying H_∞ theory, this is a rather surprising result, because H_∞ optimization should lead to optimal controllers. However, the comparison is not really a fair one because the parameters of the simple controllers have been tuned manually, whereas the H_∞ controllers had fixed parameters. Therefore, an additional test has been performed in which some tuning of the H_∞-Loop Shaping controller was allowed. This was done by connecting a lead compensator in series with the Loop Shaping controller, thus allowing tuning of the controller's phase. By doing so, it was observed that a slight improvement of the performance of the H_∞-Loop Shaping controller could be obtained. The result of this test is shown in Table 6.7 as well.

6.3.6 Discussion

Based on an empirical model of a single burner combustion system, both H_∞ disturbance rejection and H_∞ loop shaping controllers have been derived. The controllers have both been tested

in simulation as well as in experiment. The tests prove that these control techniques provide an adequate means of attenuating acoustic instabillities.
Although the H_∞ controllers proved to be superior to the simple controller architectures, its superiority is only marginal if the effort to obtain these controllers is considered. Although the method of obtaining the model of the system, as explained in section 6.2.3 is straightforward, it is rather time consuming. The advantage of the H_∞ controller is that no tuning or adjustment is required during implementation.

6.4 Self Tuning Control

The previous section demonstrated that relatively simple controller structures could achieve performance comparable to that of more complex optimal controllers. However, these simple controller structures need to be tuned online. This motivated the idea of testing somewhat less simple control structures and tuning all the parameters in such a controller, hoping for better suppression of the oscillations. Consequently, the tuning becomes a more complex task which can not be done manually by trial-and-error. If a closed interval of variation is provided for each parameter, the space of search would be largely reduced. An optimization algorithm could then be used to tune the controller parameters. For this purpose, a control set-up as shown in Fig. 6.22 was used. The controller was implemented on the same DSP hardware as the previous tests. The parameters of the controller could be adjusted from the computer program MATLAB, running on a PC. The idea was now to make an optimization algorithm in MATLAB that would adjust the parameters of the controller in order to reduce pulsations.

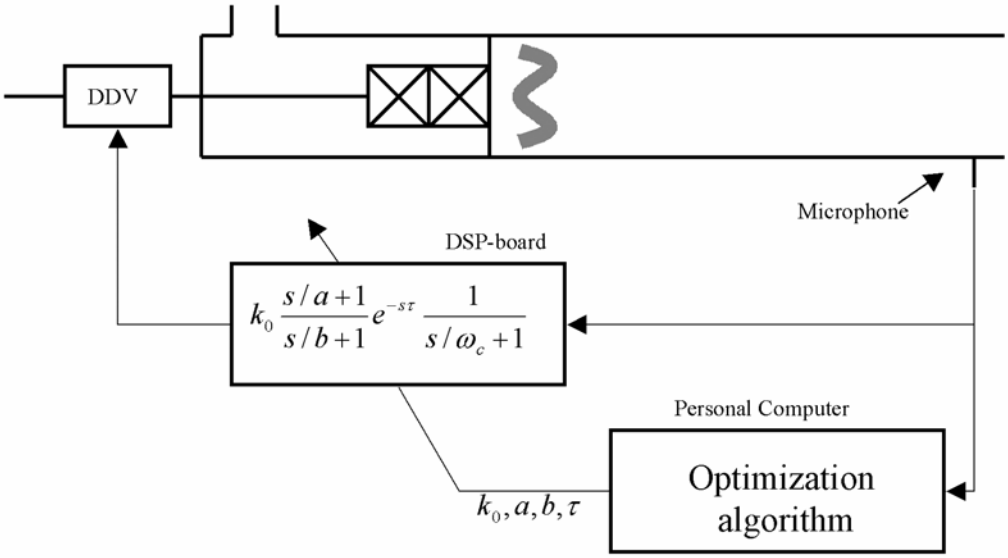

Figure 6.22: experimental set-up for self-tuning active control.

To have some flexibility in the control strategy, several controller structures were implemented on the DSP-board.

$$\begin{aligned} K(s) &= k_0\, e^{-s\tau}\, \tfrac{1}{s/\omega_c+1} \\ K(s) &= k_0\, \tfrac{s/a_1+1}{s/b_1+1}\, \tfrac{1}{s/\omega_c+1} \\ K(s) &= k_0\, \tfrac{s/a_1+1}{s/b_1+1}\, e^{-s\tau}\, \tfrac{1}{s/\omega_c+1} \\ K(s) &= k_0\, \tfrac{s/a_1+1}{s/b_1+1}\, \tfrac{s/a_2+1}{s/b_2+1}\, \tfrac{1}{s/\omega_c+1} \\ K(s) &= k_0\, \tfrac{s/a_1+1}{s/b_1+1}\, \tfrac{s/a_2+1}{s/b_2+1}\, e^{-s\tau}\, \tfrac{1}{s/\omega_c+1} \end{aligned} \tag{6.7}$$

where $(k_0, \tau, a_1, b_1, a_2, b_2)$ defines the overall set of parameters. The parameter ω_c was always set to a fixed value during the optimization process. Therefore, a 2 to 6 parameter optimization

scheme could be chosen depending on the controller prototype. The choice of the number of parameters to be used will generally be a trade-off between increased performance and increased convergence time for the controller.
A performance index is chosen that reflects the pressure changes over some given time. A measure of "power" of the signal over a given period of time is chosen:

$$P.I. = \frac{1}{T}\int_{t-T}^{t} p'(t)^2 dt \tag{6.8}$$

where $p'(\cdot)$ is the pressure fluctuation measurement coming from the microphone, and T is the evaluation time. In order to reduce measurement uncertainty, and to have a consistent and repeatable cost function, a large value of T should be chosen. Some operating conditions needed long evaluation times to obtain an acceptable level of cost function variance. A compromise between reasonable evaluation time and acceptable variance was found for values of T between 5 and 10 seconds. The stochastic behavior of the system poses serious limitations on the optimization strategy to be used. An optimization strategy is required that can deal with a stochastic cost function and that has a reasonable convergence speed. Moreover, no (or as little as possible) a-priori information of the system under consideration should be required.
Methods like the *steepest descent algorithm* or *Lagrangian interpolation* are likely to fail, because they cannot deal with a stochastic cost function. Moreover, the "function" to optimize is not necessarily concave, thus it is likely that these methods get "trapped" in a local minimum. Nevertheless, these methods have been tested both in simulation and in experiment. The tests demonstrated that these methods can not deal with randomness in the system. The algorithms diverged unless extremely long evaluation times (T) were used.
In order to avoid these problems, the use of an evolution strategy (or genetic algorithm) was considered. The key advantage in this application is that in every iteration step of an evolution strategy, not one, but several evaluations of the function are used. Thus, in the algorithm the static properties of several evaluations are combined, this reduces the sensitivity to stochastic processes. In addition, evolution strategies can easily be altered to incorporate additional features, as will be discussed later.

6.4.1 Evolution Algorithm

Genetic algorithms and *evolution strategies* mimic some of the processes observed in natural evolution [30]. Evolution has been responsible for developing optimal (or at least very good) structures in nature. *Evolution* must be considered as a sequential process that exploits the information from preceding successes and failures in order to follow a trajectory in an n-dimensional parameter space[120]. The task of mimicking biological structures and processes with the object of solving technical problems is as old as engineering itself. The widespread use of computers in the past decades made it possible to encode these processes as algorithms.
Evolution as an optimization strategy has intrigued researchers since the 50's and 60's, proof of this is early work by Box [17], Pask [96] and Schumer [119]. However, one of the main contributions came later by Rechenberg. In his book [109], he examines the analogy between natural evolution and technical optimization and presented a scheme for multi-membered evolution.

An evolution algorithm can be explained as follows. Consider a function that has to be optimized with m inputs and one output. The output of this function is referred to as its *fitness*. The idea is now to adjust the input parameters in order to find an optimum in the *fitness*. One combination of m input parameters is called an *individual*. A group of n individuals is a *population*. The idea is to start with a randomly selected initial *population* and to evaluate its fitness. In the next iteration, some random variance is applied to the population (*mutation*), creating a group of *children* out of their *parents*. The fitness of the children is now evaluated and compared with their parents' fitness, and the best of both are selected to be the next generation of parents. This procedure will go on until an optimum is found, or an other termination criterion is fulfilled. Following these ideas the next evolution algorithm was adopted in the optimization process:

1. Initialize parameters of the evolution algorithm, such as: max number of iterations, step size etc.
2. Select the initial population, (this can be a random selection, a guess or the result of a previous experiment).
3. Check if the algorithm termination conditions are satisfied: optimality, max. # of calls or no-progress
   - **Y**ES : Set the best values obtained during the optimization process.
   - **N**O : Continue with evolution algorithm.
4. Adjust step depending on progress achieved.
5. Create children from parents set.
   (a) Check mutation factor.
   (b) Determine new step.
   (c) Generate child adding a random perturbation of variance 'step' to parent.
   (d) Check that child satisfies the parameter's bounds.
   (e) Go back to a) until the population is completed.
6. Evaluate fitness of children.
7. Compare children and parents fitness, keep the best of both.
8. Compute progress velocity according with # of children better that parents.
9. Select the best solutions to judge optimality.
10. Go back to 3.

The algorithm has successfully been used at ALSTOM for other optimization problems, and was slightly adapted here for the optimization problem under consideration.

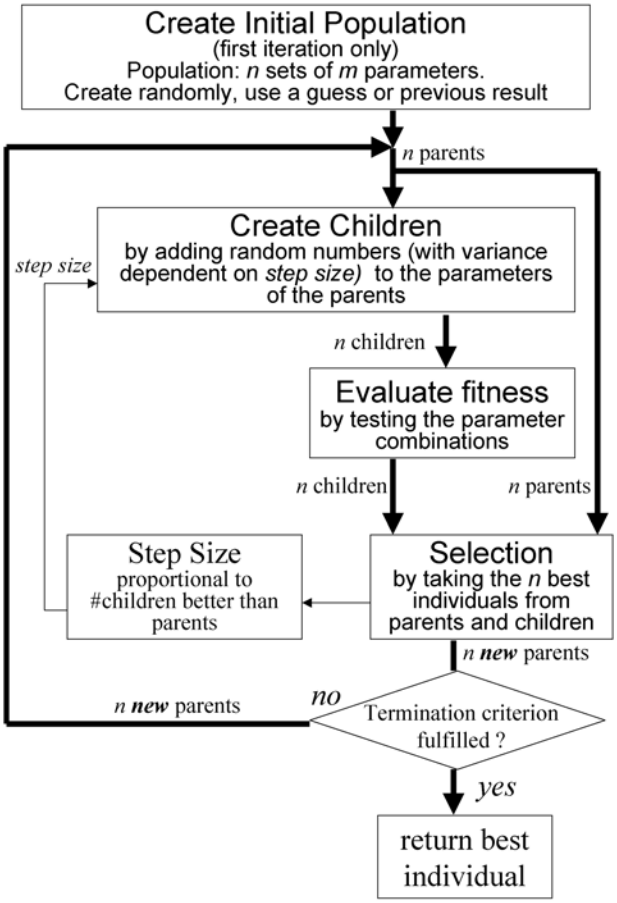

Figure 6.23: Visual representation of the evolution algorithm. Note that this representation is strongly simplified.

In Fig. 6.23, a graphical representation of the algorithm is given. Note that this representation is strongly simplified, and that some (less important) aspects have been omitted because of space limitation.
Tests of this algorithm on well-defined functions, corrupted by noise, showed that the algorithm was able to find the global minimum of the function without getting "trapped" in local minima. However, note that no (finite duration) algorithm can *guarantee* to find a global minimum without a-priori knowledge of the function. A comparison of the evolution strategy with other optimization techniques was carried out on the Simulink model of the combustion chamber. This comparison showed that the evolution strategy was far superior to the other approaches used. This encouraged a lab-test of the evolution self-tuning control.

6.4.2 Optimization of Controller Parameters by Evolution

The evolution algorithm was used to tune the parameters of Eq. 6.7 online. The algorithm was coded as an m-file in MATLAB and it was in charge of running the evolution strategy and

establishing the communication directly with a DSP board on which the controller was running online. Thus, the controller parameters were updated from MATLAB by direct access to the DSP.

Flexibility of the evolution strategy enables one to add some additional features to increase convergence speed, or to obtain other desired effects. During the optimization, parameter combinations might be proposed that *increase* pulsations. This is of course unfavorable in practical applications. Therefore, an intermediate evaluation of the cost function was introduced. The underlying idea is that it is more important to have high accuracy during the evaluation of good parameter combinations than of bad parameter combinations. The cost function is therefore evaluated twice: if the evaluation over a short period of time indicates pulsations higher than a certain threshold, evaluation is stopped and a penalty on the fitness is returned. If the first evaluation indicates pulsations lower than the threshold, the evaluation continues, and the total performance index is returned as the fitness. This approach has the additional advantage that it results in increased convergence time of the algorithm.

Generally the pulsation levels are not the only parameters to be monitored. It might well be that a certain combination of parameters that yields very low pulsation would increase emissions of NO_x or CO, which is undesired. The flexibility of the genetic algorithm also allowed specification of emission level bounds. If the emissions are higher than a certain threshold, a penalty is given to the fitness.

6.4.3 Experimental Results

The evolution strategy as a controller optimization technique was tested in the atmospheric test facility. The evolution algorithm was fixed to stop after a determined number of iterations if an optimal solution was not found before. If the optimum was not reached, the best solution was returned at the end of the iterations. Parameter combinations that gave significant reduction in the cost function were re-evaluated in order to ensure repeatability of these solutions. In order to avoid influence of transients, and to ensure low noise levels, the evaluation time for the cost function (Eq. 6.8) was set to 7.5 sec. and the maximum allowable number of iterations was 200.

The first test was performed using 2-parameter control. A comparison of the pressure signals with and without control is made in Fig. 6.24. The controller with the optimal parameter setting was switched on after 11 seconds, reducing the pulsations levels strongly: a factor 8 reduction in peak amplitude level, and more than a factor 2 reduction of the pressure power of the signal.

Encouraged by these results, controllers with more than two parameters were tested under the same conditions. The results are gathered in Table 6.8. Although the 4-parameter optimization did not seem to reduce pulsations much better than the 2-paramter optimization, the resulting controller from the 6-parameter optimization gave an excellent attenuation factor. In Figure 6.25, the response of the 6-parameters controller is plotted.

It is interesting to note that the emissions of NO_x and CO where also reduced by applying the five and six parameter controllers. Some of the lower order controllers would increase emission levels. As mentioned before, it is easy to incorporate the emission levels in the cost function during optimization. This was not done in these tests, because of the positive results with the

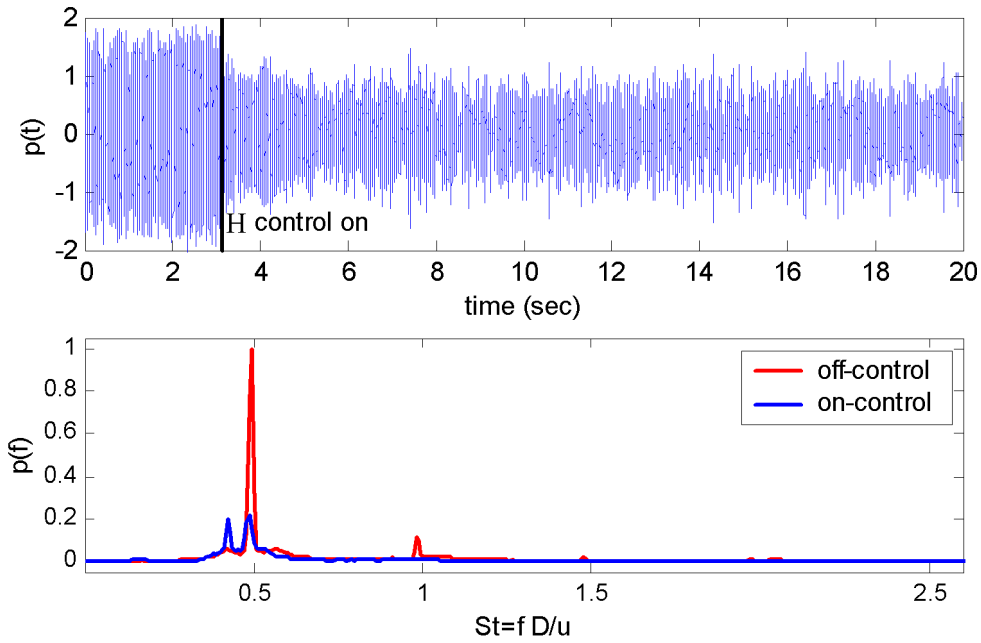

Figure 6.24: (Top) Evolution Optimization 2 param, the arrow indicates the time the best controller has been switched on. (Bottom) Spectral Density for pressure signal

Type	**NRR** (dB)	**PA** (dB)	**CO** (-)	**NO_x** (-)
Gain-Delay	-2.7	-2.2	2	1.3
Evol. 2 param.	-6.9	-18.0	2.6	0.5
Evol. 4 param.	-6.8	-18.7	1.3	0.5
Evol. 5 param.	-13.4	-26.2	0.6	0.4
Evol. 6 param.	-13.0	-26.7	0.6	0.2

Table 6.8: Comparison of controllers, the emission values are relative to the open-loop emission data.

higher order controllers.
The performance of the 6-parameter controller was tested while varying operating conditions. The comparison of the performances is listed in Table 6.10, together with results of the 2 and 4 parameter optimization. The operating conditions are listed in Table 6.9, they are related to the reference operating condition.

6.4.4 Discussion

A relatively simple controller structure with tunable parameters was used for active control. The free parameters of the controller are tuned by an optimization algorithm. The optimization algorithm attempts to set the free variables in such a way that pulsations in the combustion

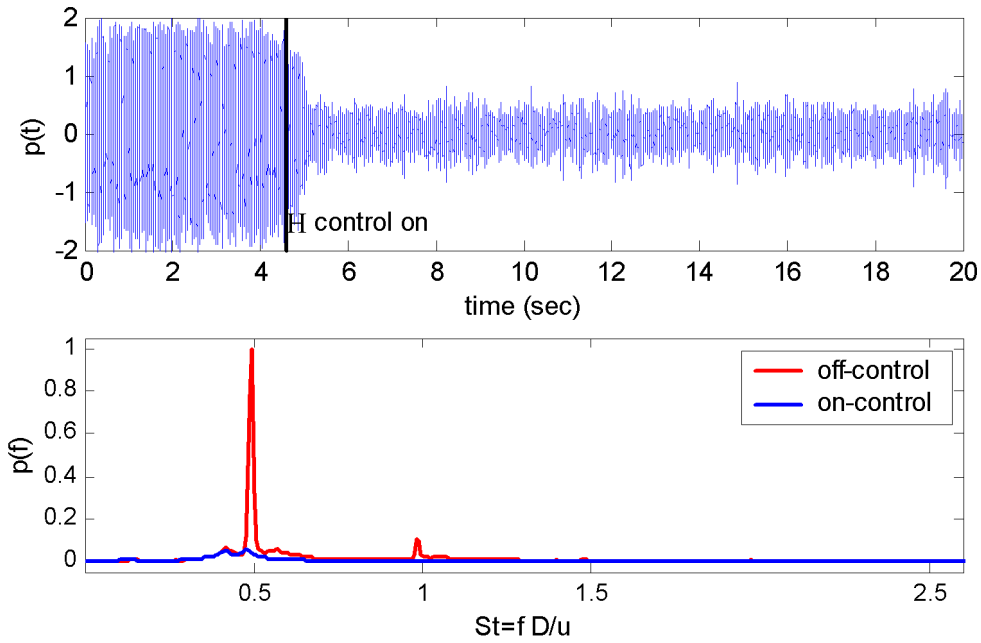

Figure 6.25: (Top) Evolution Optimization 6 param, the arrow indicates the time the best controller has been switched on. (Bottom) Spectral Density for pressure signal

Type	ϕ [-]	v_b [-]	T_a [-]	**Peak freq.** (S_r)	**Peak ampl.** ($dB - dB_{ref}$)
Evolution 2 param.	0.85	1.01	1.02	0.49	40.00
Evolution 4 param.	0.94	0.98	1.02	0.49	40.80
Evolution 6 param. cond.I	0.94	1.17	1.02	0.50	37.10
Evolution 6 param. cond.II	0.90	1.22	1.03	0.50	41.80
Evolution 6 param. cond.III	0.88	1.24	1.03	0.49	41.80

Table 6.9: Operating conditions optimal control

chamber are minimized. Because of its ability to deal with noisy cost functions, an evolution strategy is used for optimization. An additional advantage of an evolution algorithm is that because of its flexible nature, additional features can easily be added. The final controller consisted of a gain and delay plus a rational transfer function of order two, with two free variables in the numerator and denominator. Because the controller has no a-priori knowledge of the system to be controlled, parameter combinations may be suggested that *increase* pulsations. This is not really a problem in a test rig. However, this might be undesired in a practical application. This problem was overcome by applying double evaluation of the cost function, if a specific combination proves to be bad, evaluation is aborted early. This also has the advantage of increased convergence speed. The algorithm converged to an optimum in 15 to 25 minutes. This is very slow for practical applications. If this algorithm would directly be applied to a gas

Type	**NRR** (dB)	**PA** (dB)	**Closed-Loop Peak freq.** (Sr)
Evolution 2 param.	-6.10	-12.60	0.42
Evolution 4 param.	-13.50	-27.50	0.54
Evolution 6 param. cond.I	-12.70	-26.20	0.58
Evolution 6 param. cond.II	-13.70	-26.40	0.50
Evolution 6 param. cond.III	-13.90	-26.30	0.43

Table 6.10: Test results optimal controllers.

turbine, it would mean that that the machine would have to run 15 to 25 minutes at unacceptable pulsation levels after a change of operating condition. Nevertheless, this approach can be used if good initial values are given for the algorithm. This can be done by keeping the optimal values for different operating conditions in a database. If the operating condition changes, the algorithm would have to start with values suggested by the database. Tests demonstrated a reduction of the pressure amplitudes of more than 26 dB for various operating conditions. Emissions of NO_x and CO were reduced as well.

6.5 Modal Control of Multi-Burner Combustion Systems

6.5.1 Introduction

An active control method has been developed for multi-burner combustor configurations. The state-space representation of such models has been discussed in chapter 5.4. One advantage of the H_∞ controller design techniques is that they can deal with MIMO systems. Thus, in principle, the controller design methodologies discussed in section 6.3 could be used for combustion systems with more than one burner. The number of actuators and sensors does not necessarily have to be the same as the number of burners.

Although the transfer matrices of the annular ducts are of a relatively low order ($N \approx 10$), the total system is of a very high order ($N > 300$), this is mainly because J parallel transfer functions of the burners and flames are present. Designing a controller for such a system is not that straightforward, not even when using methods for order reduction (i.e., no sensible result can be obtained by using commercially avalaible tools for H_∞ optimization).

The power of the H_∞ methods is that they guarantee robust stability of the controlled system, and that the design methodology is very systematic. The disadvantage, however, is that physical understanding of the active control mechanism gets somewhat lost in the mathematics. This is especially true for MIMO systems.

The method presented here combines physical insight into the problem with H_∞ optimization. This is done by considering that the acoustic fields can be expanded in modes. In a similar way, the S sensor signals can be expanded in "spatial" orthogonal modes as well. Generally, there is only a small number of dominant modes, thus it is more efficient to control the dominant modes only. Thus the controller acts on the modal amplitudes rather than on the individual signals. The outputs of the controller are then the modal amplitudes of the control signals. Thus the signals that need to be sent to the actuators can be obtained by *modal recombination.*

The controllers for the individual modes are obtained here using H_∞-Loop Shaping. Note, however, that any control design strategy could have been used, including adaptive techniques.

6.5.2 Modal Decomposition

The pressure sensor signals p'_s at location ϕ_s can be expressed in a modal expansion:

$$p'_s(t, \phi_s) = \sum_{m=0}^{M} \breve{p}_m(t)\psi_m(\phi_s) \tag{6.9}$$

Where $\breve{p}_m(t)$ is the modal amplitude of the m^{th} mode. A similar expression can be given for the Y actuation signals ($y(t)$). In practical situations, only a very low number of modes is needed in the expansion (M typically being two or three). This property is used to reduce the amount of control variables: instead of having S sensor signals as inputs and Y actuator signal as outputs, only M modal amplitudes need to be controlled. If an $M \times S$ matrix $\mathbf{\Psi}$ is formed with elements: $\mathbf{\Psi_s}_{(m,s)} = \psi_m(\phi_s)$ and a vector $\mathbf{p'_s}$ of length S containing all the sensor signals, then the modal expansion of $\mathbf{p'_s}$ is:

$$\mathbf{p}'_s(t) = \mathbf{\Psi_s}\breve{\mathbf{p}}_s(t) \tag{6.10}$$

The modal amplitudes can be obtained by making use of the Moore-Penrose pseudo inverese (denoted here by the superscript †):

$$\breve{\mathbf{p}}_s(t) = \mathbf{\Psi_s}^{\dagger} \mathbf{p}'_s(t). \tag{6.11}$$

In which $\mathbf{\Psi}^{\dagger} = (\mathbf{\Psi}^T \mathbf{\Psi})^{-1} \mathbf{\Psi}^T$. For an annular system in which all S sensors are located in the same axial plane, but at different azimuthal angles (ϕ_s), the values of the modes at sensor locations are given by $\psi(m, \phi_s) = e^{im\phi_s}$. Thus, all columns of $\mathbf{\Psi}$ are orthogonal, and therefore it can be demonstrated that the expression for the pseudo inverse reduces, in this case, to: $\mathbf{\Psi}^{\dagger} = \frac{1}{S} \mathbf{\Psi}^T$. If all controller transfer matrices (K_m) are combined in one block diagonal matrix ($\mathbf{K}$), the controller of Fig. 6.26 can simply be expressed as: $\mathbf{y}(s) = \mathbf{\Psi_a}\, \mathbf{K}(s)\, \frac{1}{S}\, \mathbf{\Psi_s}^T\, \mathbf{p}(s)$. In which $\mathbf{\Psi_a}$ is the matrix containing the values of the eigenfunctions at the actuator location. The set-up of such a controller is given in Fig. 6.26. In which T represents the multi burner combustor configuration, H_{source} the source transfer function, w the white noise input, p the measured pressure transducer signals and y the actuator signals. In this example, two controller transfer functions are used: K_1 and K_2 (thus: $M = 2$). Note that the number of actuators does not have to be equal to the number of sensors or burners. The transfer function W is a loop shaping compensator, as discussed in section 6.3.3.

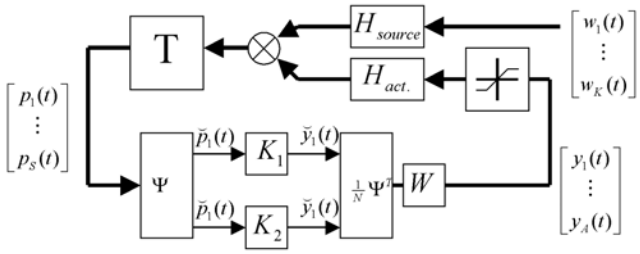

Figure 6.26: Control set up for multi burner system.

If the transfer functions of each burner and flame can be considered the same, and if the combustion chamber and plenum geometries are axially symmetric, then the azimuthal modes are decoupled. If the azimuthal modes are decoupled (independent), then controllers may be derived for each azimuthal mode individually, and recombined later as in Fig. 6.26. The dynamics of one azimuthal mode can be described by a network model that relates the modal amplitudes of the signals rather than the signals themselves, similar to [32]. Thus the structure of the block diagram of Fig.5.9 remains the same, the only difference being that signals are no longer $J \times 1$ vector quantities, but scalars. Thus, the elements representing the burners and flames are no longer represented by J parallel transfer functions, but by just one. The annular duct transfer matrices become SISO instead of MIMO. The matrix elements for the $(n, m)^{th}$ mode of the annular duct then reduce to:

$$
\begin{aligned}
A_{n,m} &= \begin{bmatrix} -\alpha & \omega_{n,m} \\ \omega_{n,m} & -\alpha \end{bmatrix}, \\
B_{n,m} &= \begin{bmatrix} 0 \\ 1 \end{bmatrix}, \\
C_{n,m} &= \frac{4 - 2\delta_{kron}(n)}{J\,L} B_{n,m}^T.
\end{aligned}
\tag{6.12}
$$

The eigenvalues of the network system relating the M modal amplitudes have been compared to those of the original network that relates J signals. As can be seen in Fig. 6.27 both methods yield exactly the same results. Note that if the system is not rotationally symetric (e.g., because different burner geometries have been used), this simplified modeling approach may not be used (but modal decompostion may still be applied). The entire linear system (for the m^{th} mode) between control signal y and sensor p_s will be denoted by $\breve{P}_m(s) = \breve{T}_m\, H_{act.}$.

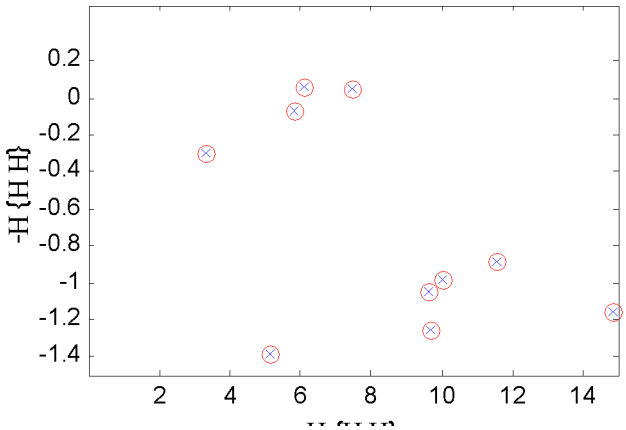

Figure 6.27: Real and imaginary values of the (most dominant) eigenfrequencies of the system, MIMO approach (crosses) and SISO approach (circles).

H_∞ controllers have been designed for the M controller modes using exactly the same procedure as outlined in Section 6.3. Figure 6.27 shows that two azimuthal modes are unstable (m=1, and m=2). Therefore, controllers have been derived that only control these two modes. Note that the mode vectors used for modal decomposition $e^{i\phi_j}$ and $e^{i2\phi_j}$ are complex valued. In order to avoid designing controllers described by complex differential equations, the real and imaginary part of the mode are controlled separately. Which is convenient, because these two (real) controllers are identical. The modal controllers are then combined in one control matrix: $\mathbf{K} = diag(K_1, K_1, K_2, K_2)$. Finally, the controller relating the actuator signals to the sensor signals is obtained: $\mathbf{\Psi_a}\,\mathbf{K}_\infty(s)\,\mathbf{W}(s)\,\frac{1}{S}\,\mathbf{\Psi_s}^T$.

6.5.3 Results

The loop shaping controller has been tested in a time domain simulation. Although the controllers were derived based on the models describing the individual modes, the simulation was performed on the model with full annular ducts and 24 parallel burners. The time domain model is not linear because of the saturation functions on the velocity and thereby heat release. Results of the simulation are plotted in Figs. 6.28. and 6.29. Figure 6.28. shows one of the 24 pressure signals obtained by the sensors, the controller for mode 1 was switched on after two seconds. One second later, the controller for mode two was switched on. In Fig. 6.29, the time traces of the modal amplitudes $\breve{p}_0$, $\breve{p}_1$, $\breve{p}_2$ and $\breve{p}_3$ are plotted. It is interesting to see that if only the most dominant mode is controlled, the second dominant mode increases. When both modes are controlled, a very good suppression is obtained. In Fig. 6.30 the square root of the sum of the power spectra of the J pressure signals has been plotted. This plot shows, again, that a minimum of two modes need to be controlled in order to obtain good suppression. Note that this behavior corresponds qualitatively to active control engine tests reported in [49].

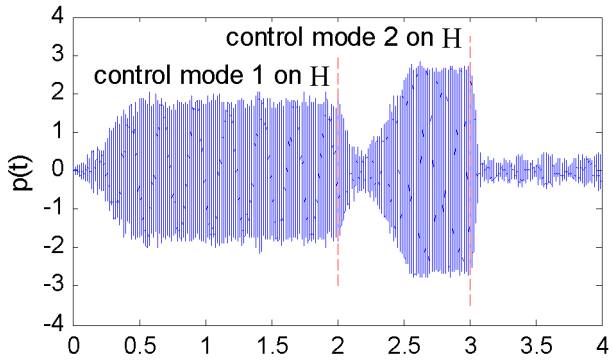

Figure 6.28: Time trace of one pressure signal, at $t = 2$ only the controller for mode 1 is switched on. At $t = 3$ the controller for mode 2 is switched on as well.

6.5.4 Discussion

The state-space representation of acoustic systems via modal expansions, provides a straightforward, fast, efficient way to model complex (thermoacoustic) systems. Generally, the state-space representation is a perfect basis for active control design, however the order of the systems under consideration is very high. This causes difficulties when designing active controllers. A H_∞-loop shaping controller has been derived based on the state space model. In order to reduce control effort, a modal decomposition method is applied. Using H_∞, machinery controllers for the individual modes have been derived. The controllers were then combined using modal recombination. This approach has been tested on a model of a hypothetical gas turbine. The model included all important features relevant for control:

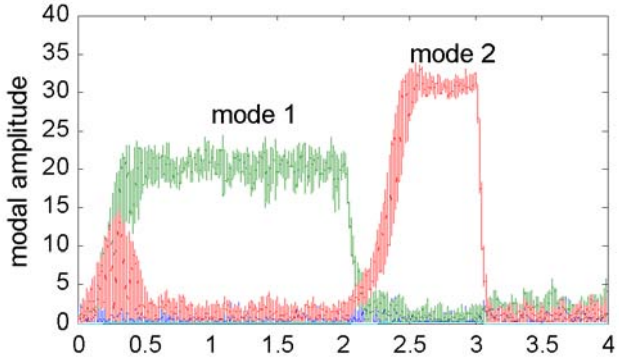

Figure 6.29: Time trace of the absolute values of the modal amplitudes.

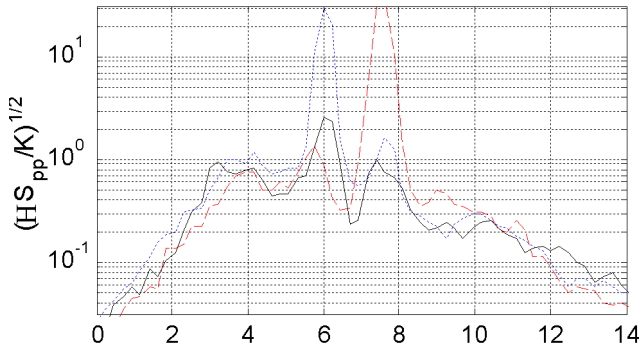

Figure 6.30: Spectra of pulsations without control (dotted), with only the first mode controlled (dashed) and with both modes controlled (solid).

- annular multi burner configuration (modeled using the Finite Element Method package, Sysnoise®)
- actuator models (obtained experimentally using frequency domain system identification)
- source term models (obtained experimentally)
- non-linear saturation of internal dynamics
- non-linear actuator saturation.

The controllers proved to be very effective and capable of suppressing multiple modes.

6.6 Discussion

Active control of combustion instabilities provides an efficient means of reducing acoustic amplitude levels in combustion systems. Using a modulation of the fuel flow, the required actuation power is negligible. An active instability control system can easily be adapted to different combustion systems or to changes in the operating regime.
Because there are many techniques available for active control, an overview of different approaches reported in literature has been given. Two different approaches have been developed and tested in this work. One approach is model-based, the other does not need any a-priori knowledge of the system.
Two different approaches have been used to obtain a model of the combustion system, one approach is based on a physical model of the system. The other is based on an empirical model. The empirical model was obtained using a frequency domain system identification method, similar to the approach described in chapter 3.
Based on the empirical model, H_∞ controllers have been derived. Both H_∞ disturbance rejection control and H_∞ loop shaping control have been tested in simulation as well as in experiment on a full scale gas turbine burner.
An evolution algorithm has been used to tune controller parameters of relatively simple controller structures. The advantage of this method is that no a-priori knowledge of the system is required. The disadvantage is that a considerable amount of time is required to converge to an appropriate solution.
Both the self-tuning and the optimal controllers had similar performance. This is an important result, considering the simplicity of the controller structures that have been used. In Fig. 6.31, the controller transfer functions of the H_∞ controllers and the low order controllers have been plotted (obtained by evolutionary optimization). In Table 6.11 a comparison of the performance of these controllers has been made.
All the controllers have nearly the same phase close to the instability frequency. This result is obvious, because all controllers where able to reduce the peak amplitude significantly. This can only be the case if the phase is correct at the frequency of instability.
The H_∞ disturbance rejection controller has a large gain for low frequencies, whereas the H_∞ loop shaping controller has a low gain in the low frequency region. This is inherent to the underlying control methodology: in the design of the disturbance rejection controller, robustness issues are not addressed. The empirical model has considerable modeling errors for the very low frequency regime (it is an acoustic model). Therefore, the shape of the loop shaping controller was chosen such that it has a low gain for the very low and very high frequency regimes. This explains why the disturbance rejection controller excited very low frequencies during some of the tests.
The H_∞ controllers have a phase characteristic that has a "kink" at the instability frequency. Apparently, the H_∞ controllers try to locally invert the open loop characteristic. The lower order controllers have a much smoother phase characteristic. This is essentially due to the chosen controller structures: all controllers tested are characterized by real-valued poles and zeros. It is possible that controller structures with complex poles and zeros would be able to

reproduce similar phase characteristic as the H_∞ controllers and have even better performance.

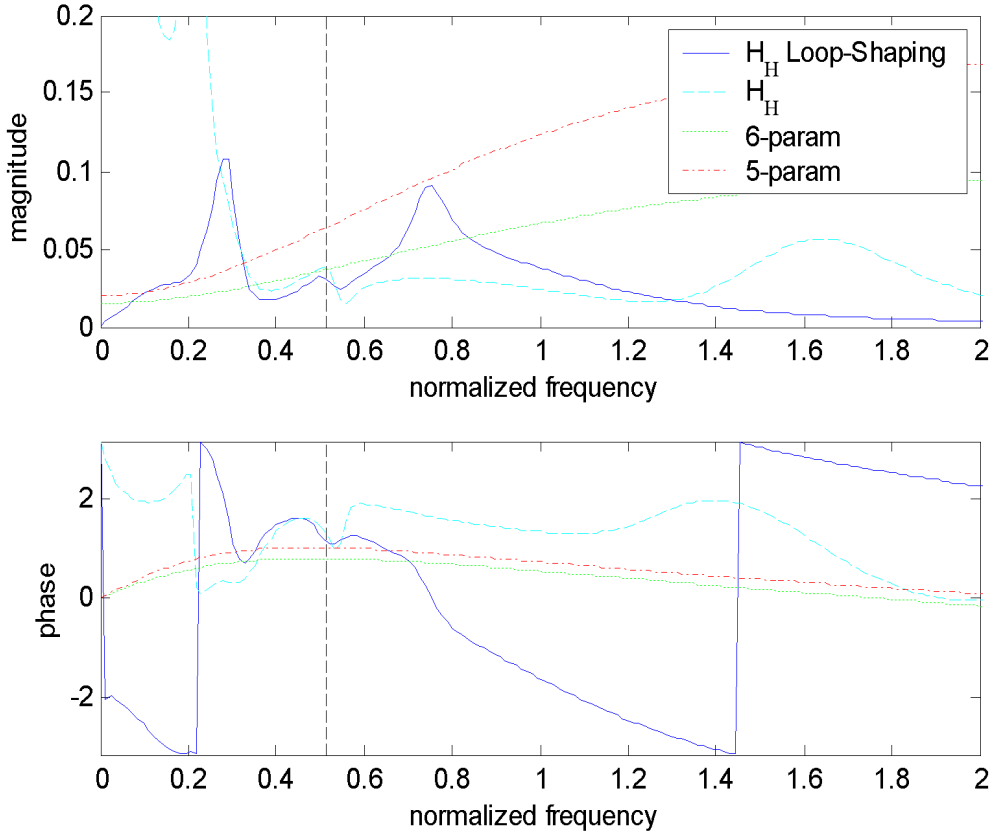

Figure 6.31: Comparison of different controllers H_∞ (solid), $H_\infty - LoopShaping$ (dashed) and the low order controllers obtained by the evolution algorithm with six parameters (dotted) and five parameters (dash-dotted). The vertical dashed line indicates the instability frequency of the open loop.

The model of the annular combustion system described in chapter 5 has been used to derive controllers for multi-burner combustion systems. The method uses a modal decomposition technique. The modal amplitudes are then controlled (rather than the pressure amplitudes themselves). The signals sent to the actuators are obtained using a modal recombination technique. Any type of controller can be used in combination with the modal de-composition technique. However, in this case a loop shaping controller has been tested in simulation.

	Open loop freq. Sr	**Closed Loop freq.** Sr	**NRR** dB	**PA** dB
H_∞ loop-shaping	0.50	0.43	-10.2	-19.4
H_∞	0.50	0.10	-8.4	-19.8
H_∞ loop-shaping+lead net.	0.50	0.42	-9.7	-20
Gain-Delay	0.50	0.49	-2.7	-2.2
Evolution 2 param.	0.50	0.37	-6.9	-18
Evolution 4 param.	0.50	0.41	-6.8	-18.7
Evolution 5 param.	0.50	0.40	-13.4	-26.2
Evolution 6 param.	0.50	0.48	-13	-26.7

Table 6.11: Comparison of controllers, all tested at the same operating condition.

Chapter 7

Conclusions

The thermoacoustic dynamics of gas turbine combustion systems have been analyzed and modeled in detail. Based on these models, active control strategies have been developed and tested. Representation of the combustion system as a network of acoustic elements allowed the combination of several modeling techniques.

The transfer function measurement technique has been validated for a wide range of operating conditions. The measurement technique proved to be repeatable. The validation and error analysis of this method demonstrated its usefulness. The linearity of the burner and flame transfer matrix has been investigated by measuring the transfer functions at different forcing levels. Doubling the forcing level did not affect the transfer matrix.

The network modeling approach reproduced the dynamics of the system correctly. The change in pulsation behavior due to changing acoustic boundaries was correctly predicted by the network model.

Transfer matrices of a burner with regular fuel injection (mixing of air and fuel in the burner) have been compared to those of the same burner, but with fuel injected far upstream of the burner (and thus avoiding temporal mixture fracture fluctuations). Comparison of the experimental results demonstrated that fluctuations of the fuel concentration are the main (but not the only) cause of the interaction between heat release and the acoustic field. Time-resolved laser diagnostics of the fuel concentration supported this observation.

A novel acoustic modeling approach has been developed in which three-dimensional geometries are modeled as causal multi-input multi-output systems. The method uses a modal expansion technique, where the modes required can either be obtained analytically (for relatively simple geometries) or numerically (for systems of any complexity). Because the system is represented in state-space, interconnection with other systems, or application of impedances on the boundaries, is done in a straightforward, efficient way by making use of linear fractional transforms. This method has been successfully validated against analytic solutions and numerical methods (finite element codes).

A thermoacoustic flame model has been derived based on the relations of a discontinuity propagating in a reactive medium. In the model, the heat release fluctuations are assumed to be caused by equivalence ratio and flame velocity fluctuations. The flame shape is assumed con-

stant in time and fluctuating in the axial direction around a mean position. This assumption is consistent with phase-locked chemiluminescence pictures of the combustion process.
A network model of an atmospheric combustion test facility with full-scale gas turbine burner proved to be in excellent agreement with experimental results for a wide range of operating conditions.
The model of an annular gas turbine reproduced the experimentally observed phenomenon that the acoustic field is rotating for high amplitude oscillations. The non-linear dynamics responsible for this behavior has been solved analytically. This analysis proved that a non-linear saturation of the linearly unstable thermoacoustic feedback mechanism makes the standing wave limit cycle solution unstable while the rotating wave limit cycle solution is stable.
A system identification method has been developed to obtain empirical acoustic models of gas turbine combustion systems. Using this model, H_∞ controllers have been developed. The controllers obtained in this way have been tested on a single burner atmospheric test facility with a full-scale gas turbine burner. Experiments demonstrated that these controllers are capable of reducing acoustic peak pulsation levels up to 25 dB, without significantly increasing (and generally even reducing) emission levels of pollutants.
However, it has been demonstrated that even very simple controller structures had comparable performance. This motivated the idea of developing a self-tuning controller. The parameters of the controller transfer function were adjusted online by an evolution strategy such as to minimize the acoustic pulsation levels. Reductions of pulsation levels up to 25 dB have been achieved. This approach has the advantage that no a-priori knowledge of the system is required. The convergence time of the algorithm was less than 30 minutes.
A novel method for active control of multi-burner combustion systems has been developed. The method makes use of on-line modal decomposition and recombination. Using this method the modal amplitudes are controlled rather than the acoustic pressure itself. This method can be used in combination with any control synthesis method. However, in this work an H_∞ loop shaping technique has been used. The advantage of this method is that the controller explicitly treats the system as a distributed parameter system while using low order control schemes. The method has been tested in simulation, and demonstrated the capability of suppressing multiple unstable modes. The time-model used for the simulation included all important features relevant for control:

- annular multi burner configuration modeled in a modal expansion (using modes obtained from a finite element calculation)
- actuator models (obtained experimentally using frequency domain system identification)
- source term models (obtained experimentally)
- non linear saturation of internal dynamics
- non linear actuator saturation

Bibliography

[1] M. Åbom. A note on the experimental determination of acoustic two port matrices. *Journal of Sound and Vibration, 155(1), 185-188.*, 1992.

[2] G.M. Abu-Off and R.S. Cant. Reaction rate modeling for premixed turbulent methane-air flames. *Joint Meeting of Spanish, Portuguese, Swedish and British Sections of the Combustion Institute, Madeira*, 1996.

[3] S. Akamatsu and A.P. Dowling. Three dimensional thermoacoustic oscillation in a premix combustor. *ASME 2001-GT-0034, Proc. ASME Turbo Expo 2001, New Orleans, June 4-7.*, 2001.

[4] D. Allgood, D.U. Campos-Delgado, S. Acharaya, and K. Zhou. Acoustic control of thermoacoustic instabilities using experoimental model-based controllers. *ASME 2001-GT-0518, Proc. ASME Turbo Expo 2001, New Orleans, June 4-7.*, 2001.

[5] A.M. Annaswamy, M. Fleifil, Z. Ghoniem, and A.F. Ghoniem. Feedback model of thermoacoustic instability in combustion processes. *Report No. 9502, May.*, 1995.

[6] A.M Annaswamy, M. Fleifil, J.W. Rumsey, J.P. Hathout, and A.F. Ghoniem. An input-output model of thermoacoustic instability and active control design. *Report No. 9705, MIT, Cambridge, MA 02139.*, 1997.

[7] A.M Annaswamy, M. Fleifil, J.W. Rumsey, R. Prasanth, J.P. Hathout, and A.F. Ghoniem. Thermoacoustic instability: Modelbased optimal control design and experimental validation. *IEEE Transactions Control Systems Technology, vol 8,no 6.*, 2000.

[8] Fleifil Annaswamy, Ghoniem M., and A.F. Active control in combustion systems. *transactions IEEE Control Systems, vol 15, no 6.*, 1995.

[9] G. J. Balas, J. C. Doyle, K. Glover, A. Packard, and R. Smith. μ-analysis and synthesis toolbox: User's guide. *The MathWorks Inc.*, 1998.

[10] A. Banaszuk, R.L. Behnken, C. Candel, F.E.C. Culick, S. Ducruix, D. Durox, J. Hermann, C.A. Jacobson, R. M. Murray, A. Orthmann, J.D. Paduano, K.C. Schadow, D. Veynante, Y. Yang Wang, Yeung V., Yu S., and K.H. Active control of engine dynamics. *RTO-EN-020, ISBN 92-837-1081-9, November.*, 2002.

[11] R. Becker and R. Günter. The transfer function of premixed turbulent jet flames. *13th Symp. (Intl.) on Combustion*, 1971.

[12] V. Bellucci, B. Schuermans, O. Paschereit, and P. Flohr. Thermoacoustic simulation of lean premixed flames using an enhanced time-lag model. *31st AIAA Fluid Dynamics Conference 11-14 June, Anaheim, CA.*, 2001.

[13] G. Billoud, M.A. Galland, C. Huyn Huu, and S. Candel. Adaptive active control of combustion instabilities. *Combust. Sci. and Tech., Vol. 81, pp. 257-283.*, 1992.

[14] G.J. Bloxsidge, A.P. Dowling, N. Hooper, and P.J. Langhorne. Active control of reheat buzz. *AIAA Journal, vol 26, no 7.*, 1988.

[15] G.J. Bloxsidge, A.P. Dowling, and P.J. Langhorne. Reheat buzz: an acoustically coupled combustion instability. part 2. theory. *J. Fluid. Mech. vol. 193, pp. 445-473.*, 1988.

[16] H. Bodèn and M. Åbom. Influence of errors on the two microphone method for measuring acoustic properties in ducts. *J. Acoust. Soc. Am., Vol. 79(2).*, 1986.

[17] G.E.P. Box. Evolutionary operation- a method for increasing industrial productivity. *Appl. Stat 6, pp. 81-101.*, 1957.

[18] D.U. Campos-Delgado, B.B.H. Schuermans, K. Zhou, C.O. Paschereit, E. Gallestey, and Poncet A. Thermoacoustic instabilities: Modeling and control. *Accepted for publication in IEEE Transactions on Control Systems Technology*, 2001.

[19] S. Candel. Combustor dynamics: Analysis and control-modeling. *Active Control of Engine Dynamics, Von Karman Institute for Fluid Dynamics, Rhode-Saint-Genese,Belgium, RTO-EN-20, May.*, 2002.

[20] B.T. Chu. On the generation of pressure waves at a plane flame front. *Fourth Symposium (International) on Combustion, The Combustion Institute, pp. 603-612.*, 1953.

[21] Y.C. Chu, A.P. Dowling, and K. Clover. Robust control of combustion oscillations. *Proc. 1998 IEEE Int. Conf. on Control Apllications, Trieste, Italy, 1-4 September.*, 1998.

[22] J.Y. Chung and D.A. Blaser. Transfer function method of measuring induct acoustic properties. i.theory, ii. experiment. *J. Acoust. Soc. Am., Vol. 68, 907-921.*, 1980.

[23] L. Clark, W.R. Saunders, and G.P. Gibbs. Adaptive structures, dynamics and control. *John Wiley.*, 1998.

[24] L. Cremer. The treatment of fans as black boxes. *Journal of Sound and Vibration, 16(1), 1-15.*, 1971.

[25] D.G. Crighton, A.P. Dowling, J.E. Ffowcs Williams, M. Heckl, and F.G. Leppington. Modern methods analythical in acoustics. *Springer-Verlag.*, 1994.

[26] L. Crocco. Research on combustion instabilities in liquid propellant rockets. *12th Symp. (Intl.) on Combustion*, 1969.

[27] F.E.C. Culick. Nonlinear behavior of acoustic waves in combustion chambers. *Acta Astronautica. Vol. 3, pp. 735-757, March.*, 1976.

[28] F.E.C. Culick. Some recent results for nonlinear acoustics in combustion chambers. *Paper 90-3927,AIAA 13th Aeroacoustics Conference, Tallahassee.*, 1990.

[29] F.E.C. Culick. Combustor dynamics: Fundamentals, acoustics and control. *Active Control of Engine Dynamics, Von Karman Institute for Fluid Dynamics, Rhode-Saint-Genese,Belgium, RTO-EN-20, May.*, 2001.

[30] L. Davis. Handbook of genetic algorithms. *Van Nostrand Reinhold*, 1991.

[31] P. J. Dine. Active control of flame noises. *Ph.D. Thesis, Cambridge University, Cambridge, England.*, 1983.

[32] A.P. Dowling. The calculation of thermoacoustic oscillations. *Journal of Sound and Vibration, 180(4), 557-581.*, 1991.

[33] A.P. Dowling. Nonlinear self-excited oscillations of a ducted flame. *J. Fluid. Mech. vol. 346, pp. 271-290.*, 1997.

[34] S. Evesque, A.P. Dowling, and A.M. Annaswamy. Adaptive algorithms for control of combustion. *Proc. RTO Symposium, Braunschweig, Germany, May.*, 2000.

[35] S. Evesque and W. Polifke. Low-order acoustic modelling for annular combustors: Validation and inclusion of modal coupling. *Paper GT-2002-30064, Proceedings of ASME TURBO EXPO 2002, June 3-6,Amsterdam, The Netherlands.*, 2002.

[36] M. Fleifil, A.M. Annaswamy, Z. Ghoniem, and A.F. Ghoniem. Response of a laminar premixed flame to flow oscillations: A kinematic model and thermoacoustic instability results. *Combustion and Flame 106: 487-510.*, 1996.

[37] P. Flohr, C.O. Paschereit, B. Van Roon, , and B.B.H. Schuermans. Using cfd for time-delay modeling of premixed flames. *ASME 2001-GT-0376, New Orleans, LA, June 8-11.*, 2001.

[38] Y.T. Fung, V. Yang, and A. Sinha. Active control of combustion instabillities with distributed actuators. *Combustion Science Technology, vol 78, pp 217-245.*, 1991.

[39] Y.T. Fung, V. Yang, and A. Sinha. Active control of nonlinear pressure oscillations in combustion chambers. *J. Propulsion Power, vol 8, no 6.*, 1992.

[40] A. Gulat and R. Mani. Active control of unsteady combustion-induced oscillations. *Journal of Propulsion Power, vol. 8, no 5.*, 1992.

[41] E. Gutmark, T.P. Parr, D.M. Hanson-Parr, and K.C. Schadow. Closed-loop amplitude modulation control of reacting premixed turbulent jet. *AIAA journal, vol. 29, no. 12, December.*, 1991.

[42] E. Gutmark, T.P. Parr, D.M. Hanson-Parr, and K.C. Schadow. Structure of a controlled ducted flame. *Combust. Sci. and Tech., vol. 87, pp. 217-239.*, 1992.

[43] E. Gutmark, K.J. Wilson, K.C. Schadow, B.E. Parker, R.L. Barron, and G.C. Smith. Dump combustor control using polynomial neural network. *AIAA 93-0117, 31th Aerospace Sciences Meeting and Exhibit, January 11-14.*, 1993.

[44] K. Haffner. Personal communication ken haffner, alstom (switzerland) ltd.

[45] J.P. Hathout, Ghoniem Annaswamy, and A.F. A model-based active control design for thermoacoustic instability. *Combustion Science Technology, vol 132, pp 99-138.*, 1998.

[46] M. A. Heckl. Active control of the noise from a rijke tube. *IUTAM Symposium on Aero- and Hydro-Acoustics, Lyon 1985, Springer-Verlag, pp. 211-216.*, 1986.

[47] J. Hermann, Vortmeyer Gleis, and N. Active instability control (aic) of spray combustors by modulation of the liquid fuel flow rate. *Combust. Sci. Tech., vol 118., pp. 1-25.*, 1996.

[48] J. Hermann, C.C. Hantschk, P. Zangl, S. Gleis, D. Vortmeyer, A. Orthmann, J.R. Seume, N. Vortmeyer, and W. Krause. Aktive instabilitatskontrolle an einer 170mw gasturbine. *VDI Berichte Nr. 1313, August.*, 1997.

[49] J. Hermann and A. Orthmann. Combustion dynamics: Application of active instability control to heavy duty gas turbines. *Active Control of Engine Dynamics, Von Karman Institute for Fluid Dynamics, Rhode-Saint-Genese,Belgium, RTO-EN-20*, 2001.

[50] B.S. Hong, V. Yang, and A. Ray. Robust feedback control of combustion instability with modelling uncertainty. *Combustion and Flame 120:91-106.*, 2000.

[51] P.K. Houpt and G.C. Goodman. Active feedback stabilization of combustion for gasturbine engines. *????.*, 1991.

[52] http://www.dspaceinc.com.

[53] http://www.moog.com.

[54] S. Hubbard and A.P. Dowling. Acoustic resonance of an industrial gas turbine combustion system. *ASME 2000-GT-0094, Proc. ASME Turbo Expo 2000, Munich, Germany, May 8-11.*, 2000.

[55] C. Huynh-huu, T. Poinsot, and S. Candel. Adaptive control of combustion instabilities. *Transient Phenomena in non Premix Combustors, subtask 2.1.E, E.M2.C, CNRS, Ecole Centrale Paris.*, 1993.

[56] LMS International. Sysnoise revision 5.4 documentation version 1.0. *(May) LMS Intrenational, Leuven, Belgium*, 1999.

[57] L. B. Jackson. Signals, systems and transforms. *Addison Wesley*, 1991.

[58] C.E. Johnson, Y. Neumeier, M. Neumeaier, and B.T. Zinn. Demonstration of active control of combustion instabilities on a full-scale gasturbine combustor. *ASME 2001-GT-0519, Proc. ASME Turbo Expo 2001, New Orleans, June 4-7.*, 2001.

[59] K.D. Kammeyer and K. Kroschel. Digitale signalverarbeitung. *B.G. Teubner Stuttgart.*, 1996.

[60] J.J. Keller. Thermally induced low-frequency oscillations. *Journal of Applied Mathematics and Physiscs (ZAMP) Vol. 36, March.*, 1985.

[61] J.J. Keller. Thermoacoustic oscillations in combustion chambers of gas turbines. *AIAA Journal, Vol. 33, No. 12, December.*, 1995.

[62] S. Koshigoe, T. Komatsuzaki, and V. Yang. Active control of combustion instability with on-line system identification. *AIAA 96-0759, 34th Aerospace Sciences Meeting and Exhibit, January 15-18.*, 1996.

[63] W. Krebs, S. Hoffmann, B. Prade, M. Lohrmann, and H. B"uchner. Thermoacoustic flame response of swirl flames. *Paper GT-2002-30065, Proceedings of ASME TURBO EXPO 2002, June 3-6, Amsterdam, The Netherlands.*, 2002.

[64] W. Krebs, G. Walz, P. Flohr, and S. Hoffmann. Modal ananalysis of annular combustors: Effect of burner impedance. *Paper 200-GT-0042, Proc. ASME Turbo Expo 2001, Louisiana, June 4-7.*, 2001.

[65] W. Lang, T. Poinsot, and S. Claudel. Active control of combustion instability. *Combustion and Flame 70: 281-289.*, 1987.

[66] P.J. Langhorne. Reheat buzz: an acoustically coupled combustion instability. part 1. experiment. *J. Fluid. Mech. vol. 193, pp. 417-443.*, 1988.

[67] P.J. Langhorne, A.P. Dowling, and N. Hooper. Practical active control system for combustion oscillations. *J.Propulsion, vol 6, no 2.*, 1990.

[68] J. Lavrentjev and M. Åbom. Characterization of fluid machines as acoustic multi-port sources. *197(1), 1-16.*, 1996.

[69] J. Lavrentjev, M. Åbom, and H. Bodèn. A measurement method for determining the source data of acoustic two-port sources. *Journal of Sound and Vibration, 183(3), 517-531.*, 1995.

[70] D.S. Lee and T.J. Anderson. Measurements of fuel/air-acoustic coupling in lean premixed combustion systems. *AIAA 99-0450, Reno, January 11-14*, 1999.

[71] H. Levine, Schwinger, and J. On the radiation of sound of an unflanged circular pipe. *Physical Review, 73:383-406.*, 1948.

[72] T.C. Lieuwen. Investigation of combustion instability mechansims in premixed gasturbines. *PhD thesis, Georgia Institute of Technology, August.*, 1999.

[73] T.C. Lieuwen and B.T. Zinn. Theoretical investigation of combustion instability mechanisms in lean premixed gas turbines. *AIAA 98-0641, Reno, NV, January 12-15.*, 1998.

[74] K.R. McManus, J.C. Magill, and M.F. Miller. Control of unstable combustion oscillations in liquid-fuelled gas turbines. *Proc. 1998 IEEE Internal Conference Control Apllications, Trieste, Italy 1-4 September.*, 1998.

[75] K.R. McManus, T. Poinsot, and S.M. Candel. A review of active control of combustion instabilities. *Prog. Energy Combust. Sci. Vol. 19, pp. 1-29.*, 1993.

[76] H.J. Merk. An analysis of unstable combustion of premixed gases. *Sixth Symposium on Combustion 500-512*, 1956.

[77] R. Mongia, R. Dibble, and J. Lovett. Measurements of air-fuel ratio fluctuations caused by combustor driven oscillations. *ASME 98-GT-304, Stockholm, Sweden*, 1998.

[78] P.M. Morse and H. Feshbach. Methods of theoretical physics: Part i. *MC Graw-Hill.*, 1953.

[79] P.M. Morse and K.U. Ingard. Theoretical acoustics. *MC Graw-Hill.*, 1968.

[80] M.L. Munjal. Acoustics of ducts and mufflers. *John Wiley & Sons.*, 1986.

[81] S. Murugappan, S. Park, A.M. Annaswamy, A.F. Ghoniem, S. Acharya, and D.C. Allgood. Optimal control of a swirl stabilized spray combustor using system identification approach. *Combustion Science and Technology , vol.175, pp.55-81.*, 2003.

[82] H.N. Najm and A.F. Ghoniem. Coupling between vorticity and pressure oscillations in combustion instability. *Journal of Prpulsion and Power, Vol. 10, No. 6.*, 1994.

[83] Y. Neumeier and B.T. Zinn. Active control of combustion instabilities with real time observation of unstable combustor modes. *AIAA 96-0758, 34th Aerospace Sciences Meeting and Exhibit, Reno, January 15-18.*, 1996.

[84] A. Ni and B. Goel. Stability of a deflagration front in compressible media. *Journal of Applied Mathematics and Physiscs (ZAMP) Vol. 46, March.*, 1995.

[85] A. Ni, W. Polifke, and F. Joos. Ignition delay time modulation as a contribution to thermoacoustic instability in sequential combustion. *ASME 2000-GT-0103 Munich, Germany, May 8-11.*, 2000.

[86] S.I. Niculescu and A.M. Annaswamy. A simple adaptive controller for positive-real systems with time-delay. *Proc. American Control Conference, Chicago, Ililinois, June.*, 2000.

[87] K.T. Padmanabhan, C.T. Bowman, and J.D. Powell. An adaptive optimal combustion control strategy. *Combustion and Flame 100:101-110.*, 1995.

[88] C. Pankiewitz and T. Sattelmayer. Time domain simulation of combustion instabilities in annular combustors. *Paper GT-2002-30063, Proceedings of ASME TURBO EXPO 2002, June 3-6, Amsterdam, The Netherlands.*, 2002.

[89] P. Papas, P.A. Monkewitz, and A.G. Tomboulides. New instability modes of a diffusion flames near extinction. *Physics of Fluids, Vol.11, no 10*, 1999.

[90] C. O. Paschereit and W. Polifke. Characterisation of lean premixe3d gas turbine burners as acoustic multiports. *Bulletin of the american Physical Society/ Division of Fluid Dynamics, Annual Meeting, San Francisco, California, USA.*, 1997.

[91] C. O. Paschereit and W. Polifke. Investigation of thermoacoustic characteristic of lean premix gas turbine burner. *ASME 98-GT-0582, ASME Turbo Expo 1998, Stockholm, June 2-5.*, 1998.

[92] C.O. Paschereit, E. Gutmark, and W. Weisenstein. Structure and control of thermoacoustic instabilities in a gasturbine combustor. *Combust. Sci and Tech., vol. 138, pp. 213-232.*, 1998.

[93] C.O. Paschereit, E. Gutmark, and W. Weisenstein. Control of thermoacoustic instabilities in a premixed combustor by fuel modulation. *37th AIAA Aerospace Sciences Meeting and Exhibit, AIAA 99-0711, January 11-14.*, 1999.

[94] C.O. Paschereit, E. Gutmark, and W. Weisenstein. Flow-acoustic interactions as a driving mechanism for thermoacoustic instability. *Physics of Fluids Vol. 11, No. 9, pp. 2667-2678, Sept.*, 1999.

[95] C.O. Paschereit, B.B.H. Schuermans, W. Polifke, and O. and Mattson. Measurement of transfer matrices and source terms of premixed flames. *ASME 99-GT-0133, Proc. ASME Turbo Expo 1999, Indianapolis, June 7-10.*, 1999.

[96] G. Pask. Physical and linguistic evolution in self-organizing systems. *Proceedings of the 1st. IFAC Symposium on Optimization and Adaptive Control. April pp. 199-227.*, 1962.

[97] A.A. Peracchio and W.M. Proscia. Non linear heat-release/acoustic model for thermoacoustic instability in lean premixed combustors. *Journal of Engineering for Gas Turbines and Power, Vol. 121, July.*, 1999.

[98] N. Peters. Fifteen lectures on laminar and turbulent combustion. *Aachen, September.*, 1992.

[99] T. Poinsot, F. Bourienne, S. Candel, E. Espositio, and W. Lang. Suppression of combustion instabillities by active control. *J. Propulsion, vol, 5, no. 1.*, 1987.

[100] T. J. Poinsot, A. C. Trouve, D. P. Veynante, S. M. Claudel, and E. J. Esposito. Vortex-driven acoustically coupled combustion instabilities. *J. Fluid. Mech., vol. 177, pp. 265-292.*, 1987.

[101] W. Polifke, A. Fischer, and T. Sattelmayer. Instability of a premixed burner with non-monotonic pressure drop characteristic. *Paper GT-2001-0035, Proceedings of ASME TURBO EXPO 2001, June 4-7, New Orleans.*, 2001.

[102] W. Polifke, C. Hirsch, A. Fischer, and T. Sattelmayer. Instabilität eines vormischbrenners mit nicht-monotoner druckverlust-kennlinie. *VDI-Berichte, Nr. 1629.*, 2001.

[103] W. Polifke, J. Kopitz, and A. Serbanovic. Impact of the fuel time lag distribution in elliptical premix nozzles on combustion stability. *7th AIAA/CEAS Aeroacoustics Conference May 28-30, Maastricht, The Netherlands.*, 2001.

[104] W. Polifke, C. O. Paschereit, and Th. Sattelmayer. Stability analysis for complex thermoacoustic systems. *Technical Report ABB CHCRC 97-29, ABB Corporate Research Ltd., Baden-Dättwil, Switzerland.*, 1997.

[105] W. Polifke, J. Van der Hoek, and B. Verhaar. Basic equations and numerical tools for linear acoustics in gas turbines. *CHCRC 97-16, ABB Corporate Research Ltd., Baden-Dättwil, Switzerland.*, 1997.

[106] W. H. Press, B.P. Flannery, S.A. Teukolsky, and W.T. Vetterling. Numerical recipes. *Cambridge University Press*, 1986.

[107] S. Raghu. Control of combustion and acoustically coupled fluid dynamic instabilities. *PhD Thesis, Yale University.*, 1987.

[108] J.W.S. Rayleigh. The theory of sound. *Volumes 1 and 2. Dover Publications, New York.*, 1945.

[109] I. Rechenberg. Evolutionsstrategie. *Stuttgart.*, 1973.

[110] G.A. Richards, M.J. Yip, and E. Robey. Combustion oscillation control by cyclic fuel injection. *ASME, Int. Gasturbine and Aeroengine Congress and Exhibition, Houston, June 5-8.*, 1995.

[111] S.W. Rienstra and A. Hirschberg. An introduction to acoustics. *Report IWDE99-02, TU Eindhoven.*, 1999.

[112] J.W. Rumsey, M. Fleifil, A.M Annaswamy, and A.F. Ghoniem. Low-order nonlinear models of thermoacoustic instabilities and linear model-based control. *Report No. 9801, MIT, Cambridge, MA 02139.*, 1998.

[113] J.W. Rumsey, M. Fleifil, A.M Annaswamy, J.P. Hathout, and A.F. Ghoniem. The role of active control in suppressing thermoacoustic instability. *Proc. American Control Conference, Albuquerque, New Mexico, June.*, 1997.

[114] T.L. Saaty and J. Bram. Nonlinear mathematics. *Dover*, 1964.

[115] T. Sattelmayer. Influence of the combustor aerodynamics on combustion instabilities from equivalence ratio fluctuations. *ASME 2000-GT-0082, Proc. ASME Turbo Expo 2000, Munich, Germany, May 8-11.*, 2000.

[116] K.C. Schadow, E. Gutmark, and K.J. Wilson. Active combustion control in a coaxial dump combustor. *Combust. Sci. and Tech., Vol. 81, pp. 285-300.*, 1992.

[117] B.B.H. Schuermans, W. Polifke, and C.O. Paschereit. Modeling transfer matrices of premixed flames and comparison with experimental results. *ASME (1999-GT-0132), Indianapolis, USA, June 7-10*, 1999.

[118] B.B.H. Schuermans, W. Polifke, C.O. Paschereit, and J.H. van der Linden. Prediction of acoustic pressure spectra in combustion systems using swirl stabilized gas turbine burners. *ASME 2000-GT-0105 Munich, Germany, May 8-11.*, 2000.

[119] M.A. Schumer and K. Steiglitz. Adaptive step size random search. *IEEE Trans. AC-13, pp. 270-276.*, 1968.

[120] Hans-Paul Schwefel. Evolution and optimum seeking. *John Wiley & Sons, Inc.*, 1995.

[121] R. Sepulchre, M. Jankovic, and P. Kokotovic. Constructive nonlinear control. *Springer.*, 1996.

[122] J.R. Seume, Krause Vortmeyer, D. W., J. Hermann, C.C. Hantschk, P. Zangl, S. Gleis, D. Vortmeyer, and A. Orthmann. Application of active combustion instability control to a heavy duty gas turbine. *ASME J. Eng. Gas Turbines and Power, vol 120, pp. 721-726.*, 1998.

[123] A.F. Seybert and D.F. Ross. Experimental determination of acoustic properties using a two-microphone random-excitation technique. *J. Acoust. Soc. Am., Vol. 61, No. 5, May.*, 1977.

[124] S. Sivasegaram and J.H. Whitelaw. Active control of oscillations in combustors with several frequency modes. *ASME Winter Annula Meeting, Active Control of Noise and Vibration.*, 1992.

[125] J. J. E. Slotine and W. Li. Applied nonlinear control. *Prentice Hall.*, 1991.

[126] S.R. Stow and A.P. Dowling. Thermoacoustic oscillations in an annular combustor. *ASME 2001-GT-0037, Proc. ASME Turbo Expo 2001, New Orleans, June 4-7.*, 2001.

[127] S. Tempkin. Elements of acoustics. *John Wiley & Sons.*, 1981.

[128] J.E. Tierno and J.C. Doyle. Multi mode active stabilization of a rijke tube. *ASME Winter Annual Meeting, DSC-Vol. 38.*, 1992.

[129] C.W.S. To and A.G. Doige. A transient testing technique for the determination of matrix parameters of acoustic systems, i: Theory and principles. *Journal of Sound and Vibration, 62(2), 207-222.*, 1979.

[130] H.S. Tsien. Servo stabilization of combustion in rockets motors. *Journal of the American Rocket Society, pp. 256-268, Sept.-Oct.*, 1952.

[131] T. Van Lunteren. Systemen, signalen, stochastiek. *report wb2300, June, TU delft, The Netherlands.*, 1990.

[132] G. Walz, W. Krebs, S. Hoffmann, and Judith H. Detailed analysis of the acoustic mode shapes of an annular combustor. *Paper GT-99-0113, Proc. ASME Turbo Expo 1999, Indianapolis, June 7-10.*, 1999.

[133] F.A. Williams. Combustion theory. *Addison-Wesley Publishing Company*, 1964.

[134] V. Yang and F.E.C. Culick. On the existence and stability of limit cycles for transverse acoustic oscillations in a cylindrical combiustion chamber. *Combust. Sci. and Tech., Vol. 72, pp. 37-65.*, 1990.

[135] V. Yang, A. Sinha, and Y.T Fung. State-feedback control of combustion instabilities. *J. Propulsion, vol 8, no 1.*, 1990.

[136] K.H. Yu, A. C. Trouv'e, and J.W. Daily. Low-frequency pressure oscillations in a model ramjet combustor. *J. Fluid. Mech., vol. 232, pp. 47-72.*, 1991.

[137] K. Zhou and C.D. Doyle. Essentials of robust control. *Prentice-Hall.*, 1998.

[138] M. Zhu, A.P. Dowling, and K.N.C. Bray. Flame transfer function calculations for combustion oscillations. *ASME 2001-GT-0374, Proc. ASME Turbo Expo 2001, New Orleans, June 4-7.*, 2001.

[139] V.L. Zimont, F. Biagioli, C. Bruno, and A.N. Lipatnikov. Test of an engineering model of premixed turbulent combustion. *4th European conference Industrial Furnaces and Boilers, Espinho, Porto, Portugal, April 1-4*, 1997.